

Aeolian Dust Deposition Rates in South-Western Iran

Dissertation Thesis

Submitted for obtaining the degree of
Doctor of Natural Science
(Dr. rer. nat.)
to the

Fachbereich Geographie

Philipps-Universität Marburg

by

Mansour Ahmadi Foroushani

Marburg, September 2020

Supervisor I: Prof. Dr. Christian Opp

Chair: Physical Geography
Working Group: Hydrology and Soil Science
Faculty of Geography Philipps-Universität Marburg

Supervisor II: Prof. Dr. Jürgen Wunderlich

Department of Physical Geography
Goethe Universität Frankfurt am Main

Not everything that counts can be counted, and not everything that can be counted counts
Albert Einstein

Declaration by the Author

I declared that this thesis is composed of my original work, and contains no material previously published or written by another person except where due reference has been made in the text. I have clearly stated the contribution by others to jointly-authored works that I have included in my thesis.



Mansour Ahmadi Foroushani

Acknowledgement

A special appreciation goes to my first supervisor, Dr. Prof. Christian Opp, for his continuous support and his comments. I was accompanied by his valuable guidance throughout my thesis period, always providing scientific advice and critical comments to my work. His assistance has strongly improved this research. Special thanks to Dr. Michael Groll for his bright comments to this research, which helped make this document come out in a better shape. I would like to show gratitude to deanery department, Prof. Dr. Carina Peter, and Prof. Dr. Dr. Thomas Brenner. To the others namely, Dr. Harnischmacher, Dorenkamp, Göttlicher, and Ralf. To MARA that I was honored to take financial support and lectures from, I thank you all for opening new windows in my academic life in the faculty of Geography, for supporting and providing me all the necessary information needed for this research. Prof. Chiffard, Dr. Thomas Hennig, and Dr. Martin Reiss, I was honoured to take your ideas and comments on my work. I cannot express enough thank to Ms. Katharina Eberling and her colleagues for their continued support and encouragement.

I gratefully acknowledge the NOAA Air Resources Laboratory team (ARL) and MODIS Giovanni and NEO/NASA for their technical assistance and useful data. The Giovanni online data system, developed by the NASA GES DISC, was used to obtain the surface AOT values test. For many memorable evenings and night, I would like to express my gratitude and appreciation to Ilario Emanuele and his colleague [Event Manager Security Services] from Accente who support me financially on available job.

Even though I have not had the opportunity to work with Mr. Nikfall previously, the impact of his model (WRF- Chem model for dust) on my own study is obvious, thanks. I wish to acknowledge the scientific contributions made by Dr. Jens Hahn, Bundesanstalt für Gewässerkunde, Koblenz. Moreover, thanks to the professional laboratory assistance from Nils Jansen, Olga Schechtel, and Nina Zitzer with regard to preparation and the operation of the instruments, respectively. In addition, I would like to thank IRIMO (Iranian Meteorological Organization) for providing observation data for this research, IOPTC for hosting my fieldwork and cooperation utilized by my best friends, experts back-home, NIORDC training quarter for last two years. My sincere thanks go to Ms. Afsaneh Dalvand, who beyond being my colleague in this work is very close family, her personal and professional advice during past 5 years was always been an inspiration to me.

Getting through my thesis required more than academic support, and I have many, people and family to thank for listening to and, at times, having to tolerate me over the research period. I cannot begin to express my gratitude for their friendship. Special thanks to friends for making my academic life in Philipps Universität are namely Babak (Writer) and Nico Küver (Netzproduzenten ® GmbH). Ma Weijing, Meena Kumari Kolli, Hamidreza Abbassi, Neda Abbassi, Anna, Phyto, and Adriana, you were unwavering in your personal and professional support during the time I spent at the University.

None of this could have happened without my friends and family, Mr Arjmand and his family, Noshin, Shirin, and Ziba, very special thanks are certainly due Esmail and his wife Behshad who are very close friend family in Germany, I am forever grateful. Finally yet importantly, I would like to recognize the unrelenting long-distance support from my parents and family. [Parisa and Delaram], this work is dedicated to you.

Mansour Ahmadi Foroushani
May, 2020

Published works by the author incorporated into the thesis

Publication 1: Included as Chapter 4

Mansour A FOROUSHANI, Christian OPP, Michael GROLL. 2020. Spatial and temporal gradients in the rate of dust deposition and aerosol optical thickness in southwestern Iran. *Journal of Arid Land*, <https://doi.org/10.1007/s40333-020-0079-5>.

Publication 2: Included as Chapter 5

Foroushani, M., Opp, C. and Groll, M., 2019. Chemical Characterization of Aeolian Dust Deposition in Southern and Western Iran, *Asian Journal of Geographical Research*, 2(2), pp. 1-22. <https://doi.org/10.9734/ajgr/2019/v2i230081>

Publication 3: Included as Chapter 6

Foroushani, M.A.; Opp, C.; Groll, M.; Nikfal, A. Evaluation of WRF-Chem Predictions for Dust Deposition in Southwestern Iran. *Atmosphere* 2020, 11, 757. <https://doi.org/10.3390/atmos11070757>

Publication 4: Included as Chapter 7

Foroushani, M., Opp C., Groll M., 2020. Investigation of Aeolian Dust Deposition Rates in Different Climate Zones. (*Journal of Aeolin Research*)

Publication 5: Eprint <http://eprints.dbges.de/1226/>

Ahmadi Foroushani, M., Opp, C., & Groll, M., 2017 Determination of dust sources by analyzing the elements correlation within the dust.. In: *Jahrestagung der Deutschen Bodenkundlichen Gesellschaft*, Eprint 04.09.2017: <http://eprints.dbges.de/id/eprint/>

Conference Contribution

Foroushani, M., Opp, C. and Groll, M. 2018. Dust deposition in the south and west of Iran, International Conference, Oral presentation, InDust, Technische Universität Darmstadt. 27-28 November, Darmstadt, Germany.

Foroushani, M., Opp, C. and Groll, M., 2017. Impact on terrestrial exposures from dust elements and dust event Frequency, Oral presentation, Wageningen Soil Conference, 27-29 August Wageningen, the Netherland

Foroushani, M., Opp, C. and Groll, M., 2017. Determination of dust sources by analyzing the elements correlation within the dust, Oral presentation, DBG Jahrestagung der Deutschen Bodenkundlichen Gesellschaft, 2-7. September, Göttingen, Germany, <http://www.dbges.de>

Foroushani, M., Opp, C., 2017. Association among the Dust Elements Concentration and Event Frequency, Oral presentation, Marin desert conference, February, Rauischholzhausen, Germany.

Foroushani, M., Opp, C., 2016. Trace Element Analysis of Dust Samples in Southwestern part of Iran, Oral presentation, 1st International Conference on Dust, 02-04 March Shahid Chameran University, and Ahwaz, Iran

M. A. Foroushani , Christian Opp., 2014, High resolution analysis of elements in dust by mass spectrometry in South- West of Iran, Oral presentation, ISLSCE2014, 15-19 October, University of Gorgan, Iran

M. A. Foroushani, Christian Opp., 2014. Dust Deposition in South–West of Iran, oral presentation, 07-08 February, Rauischholzhausen, Germany

Table of content

1. RESEARCH PROPOSAL.....	5
1.1 INTRODUCTION	5
1.2 DEPOSITION MORPHOLOGY AND GENERALISATION	5
1.3 THE STATE OF THE ART	7
1.4 PROBLEM STATEMENT AND HYPOTHESIS	10
1.5 GOAL AND RESEARCH OBJECTIVES	11
1.6 RESEARCH FRAMEWORK.....	11
1.7 THESIS STRUCTURE.....	12
2. RESEARCH APPROACH	21
2.1 INTRODUCTION	21
2.2 STUDY AREA	21
2.3 SUMMARY.....	30
2.4 CONCLUSION	30
3. METHODS.....	35
3.1 INTRODUCTION	35
3.2 FIELD WORK STATEMENTS	35
3.3 OPTICAL THICKNESS.....	37
3.4 ANALYSIS	38
3.5 IMPEDIMENTS AND PROBLEMS IN THE FIELD WORK	41
3.6 CONCLUSION	41
4. SPATIAL AND TEMPORAL GRADIENTS OF DUST DEPOSITION AND AEROSOL OPTICAL THICKNESS	45
4.1 INTRODUCTION	46
4.2 MATERIALS AND METHODS	47
4.3 RESULTS ANALYSIS AND VALIDATION	48
4.4 DISCUSSION.....	56
4.5 CONCLUSIONS AND REMARKS.....	62
5. CHEMICAL CHARACTERIZATION OF AEOLIAN DUST DEPOSITION.....	71
5.1 INTRODUCTION	71
5.2 MATERIAL AND METHOD.....	72
5.3 RESULTS AND DISCUSSION	73
5.4 STATISTICAL ANALYSIS.....	79
5.5 CONCLUSION	85
6. INVESTIGATION OF EVALUATION OF WRF-CHEM PREDICTION FOR DUST DEPOSITION	89
6.1 INTRODUCTION	90
6.2 MATERIALS AND METHOD	91
6.3 RESULTS AND STATISTICS	93
6.4 MODEL OUTPUT AND DISCUSSION	96
6.5 CONCLUSION	105
7. INVESTIGATION OF AEOLIAN DUST DEPOSITION RATES IN DIFFERENT CLIMATE ZONES.....	117
7.1 INTRODUCTION	118
7.2 MATERIAL AND METHOD.....	121
7.3 RESULTS AND DISCUSSION	121
7.4 CONCLUSIONS AND REMARKS.....	129
8. CONCLUSION AND RECOMMENDATION	137
8.1 INTRODUCTION	137
8.2 CONCLUSIONS.....	137
8.3 LIMITATIONS AND RECOMMENDATION	139

List of Figures

Figure 1.1 Proximal loess accumulation.....	5
Figure 1.2 Sandy loess transition	6
Figure 1.3 Loess accumulation along a climate gradient	6
Figure 1.4 Loess accumulation against a topographic obstacle.....	6
Figure 1.5 Accumulation from two separate sources	7
Figure 1.6 Feasible dust deposition and concentration	8
Figure 1.7 Satellite imagery over Iran.....	8
Figure 1.8 Dust storm had persisted over Iran and the Persian Gulf.	10
Figure 1.9 Research framework, dataset and flow diagram.....	12
Figure 2.1 The dust belt (enclosed by yellow dashes)	21
Figure 2.2 Map of the study area latitude, longitude and elevation.....	22
Figure 2.3 Mapping the LULC on the gauge site distribution	23
Figure 2.4 Time series interannual temperature obtained from study area.....	25
Figure 2.5 Interannual average temperature and monthly precipitation.....	25
Figure 2.6 Histogram of the wind speed in m/s, monthly averages for 2014-2017	26
Figure 2.7 Interannual time series of predominate wind speeds in eastward and northward directions.....	27
Figure 2.8 The seasonal wind-rose for [Bwh] [Csa], and [BSh].....	28
Figure 2.9 Monthly averages deposition rate. MERRA II model M2TMNXAD4- V5.12.4	29
Figure 2.10 Zonal mean of dust deposition rate resolution 0.5 degree left and 1.0 Degree right	30
Figure 3.1 Given circle centered of each gauge	36
Figure 3.2 Installation and sampling technique	37
Figure 4.1 Average Aerosol Optical Depth 550 nm (Dark Target) monthly 0.1 degree	50
Figure 4.2 Average Aerosol Optical Depth 550 nm (Dark Target) monthly 0.1 degree	51
Figure 4.3 Average Aerosol Optical Depth 550 nm.....	52
Figure 4.4 Temporal monthly means of dark-target MODIS AOT	54
Figure 4.5 The model output from HYSPLIT for all sections A, B, and C.....	55
Figure 4.6 Captured from Giovanni MISR 555 nm and applied with a spatial resolution of 0.5 degree	57
Figure.4.7 Captured from Giovanni MISR 555 nm and applied with a spatial resolution of 0.5 degree	58
Figure 4.8 Providing Thickness properties by courtesy of NASA for AOT	59
Figure.4.9 Spatial gradient in AOT compared with the fluctuation rate from ground deposition	Error! Bookmark not defined.
Figure 4.10 Correlation between atmospheric dust loading and dust accumulation.....	61
Figure 4.11 Consistency and variation change between the 3rd and 4th layers, including GDR	62
Figure 5.1 The wind rose speed and direction on data reproduced from IRMO	74
Figure 5.2 Correlation data between the DEF (horizontal) and Wt (vertical)	76
Figure 5.3 Concentration value chart from the southern (top) and western (bottom) of study area	81
Figure 6.1 Simulation domain	93
Figure 6.2 Maps showing the seasonal dust deposition rates (mg/cm ² /month).....	95
Figure 6.3 Seasonal average deposition rate gathered from the GDR	96
Figure 6.4 WRF model outputs for the wind rose diagrams	97
Figure 6.5 WRF-Chem results for concentrations (µg/m ³)	98
Figure 6.6 WRF-Chem results for the load (µg/m ²)	99
Figure 6.7 Hierarchical relationships among the LULC, gauge sites, and climate zones	100
Figure 6.8 Time series of the 10-day average and total average modeled load (µg/ m ²)	101
Figure 6.9 Time series of the 10-day average and the total average modeled concentration (µg/m ³).....	102
Figure 6.10 Correlation plot of the WRF-Chem versus the GDR observation	103
Figure 7.1 Correlation between dust particle and climate factors	119
Figure 7.2 Ground deposition rates (mg/cm ²) from sites G01 to G10 in three climate zones.....	122
Figure 7.3 Overall seasonal deposition rate (mg/cm ²) in the study area.....	123
Figure 7.4 Correlation of surface temperature against the aeolian deposition rate	124
Figure 7.5 Correlation of precipitation against the aeolian deposition rate	125

Figure 7.6 Correlation of wind velocity against the aeolian deposition rate; A. Eastward; B. Northward	127
Figure 7.7 Correlation of Vertical pressure velocity against the aeolian deposition rate	127
Figure 7.8 Mapping high seasonal deposition rates over climate zones.....	129

List of Tables

Table 1.1 Dust storm classification method, after (Hoffmann et al., 2008)	9
Table 1.2 Dust concentration in different regions.....	9
Table 2.1 Climate classification scheme of the study area	24
Table 3.1 Location, altitude and total distance of dust samplers in the study area.....	35
Table 3.2 Titles of Giovanni online data systems developed by NASA GES DISC	38
Table 3.3 Four digestion methods based on USEPA references.....	39
Table 3.4 Data relative to digestive samples.....	39
Table 3.5 interpretation and mass calculation of elements	40
Table 4.1 Dust deposition rates vs dust event frequency (DEF)	49
Table 5.1 Key indicating elements with associated sources	72
Table 5.2 Dust deposition rates vs dust event frequency (DEF)	77
Table 5.3 The total element concentrations in the southern and western parts of the study area (in $\mu\text{g/g}$)	78
Table 5.4 Key indicating elements with associated sources for maximum correlation in the western part	83
Table 5.5 Key indicating elements with associated sources for maximum correlation in the southern part.....	84
Table 6.1 Location, altitude, and total distance of dust samplers	91
Table 6.2 Configuration options for the WRF-Chem model for dust	93
Table 6.3 Land cover in the study area	94
Table 7.1 A few studies on aeolian dust in Iran.....	120
Table 7.2 Observation of dust deposition	121
Table 7.3 Classified the average seasonal deposition rate on the basis of wind pattern	126
Table 7.4 Typical climate patterns relative to the deposition rate	128

Appendix

Appendix I.....	A
Appendix II.....	D

Glossary of term

a.s.l: above sea level	1
AMR: Airborne Metal Regulations	71
AOT: Aerosol Optical Thickness	1, 3
BSh: arid steppe hot	2
BWh: arid desert hot	2
Csa: hot and dry summer	2
DEF: Dust Event Frequency	72
DS: element emanating from Dominant Sources	15
GDR: Ground observation of dust Deposition Rate	1
HYSPLIT: HYbrid Single Particle Lagrangian Integrated Trajectory	1
ICP-MS: Inductively Coupled Plasma - Mass Spectrometry	15
LUCAS: Land Use-Cover Area frame Statistical Survey	24
LULC: 2.2.1 Land Use Land Cover	24
MERRA-2: The second Modern- Era Retrospective-analysis for Research and Applications	15
MODIS: Moderate Resolution Imaging Spectroradiometer	1
NS: element emanating from Natural Sources	15
Std: The standard deviation	27
TSP: Total Suspended Particulate	10
WRF-Chem: Weather Research and Forecasting (WRF) model coupled with Chemistry	2, 15
Wt: Dust Weight	76

Summary

The annual atmospheric dust-load originating in the so-called Dust Belt¹, which ranges from the Sahara desert and the Arabian peninsula to the arid lowlands of Central Asia and the deserts of northern China, impacts the air quality and the climate worldwide. Iran as a whole, and especially the southwestern regions of the country, most affected by dust, with frequent dust storms characterized by annual mean concentrations of more than 100 $\mu\text{g}/\text{m}^3$ of suspended dust. Although aeolian dust is a highly relevant problem in Iran, there is a lack of comprehensive regional studies on this topic. The central aim of the study presented here is therefore the spatiotemporal analyses and classification of dust events, the chemical composition of the dust, and the connections between regional and seasonal climate variation and dust deposition rates in four sub-regions of Iran. This comprehensive approach is based on the maximum mean dust concentration and the seasonality of dust events. The results are provided new and valuable insights into the dust deposition and its related processes in the study area.

The study area covers 8.43% of Iran (about 117,000 km^2), located between 45°30'00" E 35°00'00" N and 49°30'00" E 30°00'00" N including Kermanshah, Lorestan and Khuzestan. The fieldwork area is characterized by the rolling mountainous terrain about 4000 m above sea level (a.s.l) in the north and east, plains and marshlands in the south. Study area has also located in dry climate and hot summer conditions in the south, cold and hot desert climates in the west. The studies on aeolian dust in southwestern Iran are based solely on ground deposition rates from 2014 to 2017.

To address the connections between the Ground observation of dust Deposition Rates (GDR), climate zones, and weather patterns, a comparative analysis with various data sets was conducted. Both gravimetric and directional dust samplers (10 each) were installed to record the monthly GDR between 2014 and 2017. The sampler design was deliberately kept simple to ensure long-term durability and easy maintenance. The collected dust samples were analyzed for their chemical composition using Inductively Coupled Plasma Mass Spectrometry (ICP-MS). The ten sampling sites were also classified by their land use / land cover (LULC) for a more detailed data interpretation. The observation data during two typical dust cases (spring 2014 and winter 2015), have furthermore been compared with the spatiotemporal dust concentration and dust load over the study area. Comparing the results of the monthly mean Aerosol Optical Thickness (AOT) derived from the Moderate Resolution Imaging Spectroradiometer (MODIS) and GDR data, using enhancement algorithms were applied in order to investigate the spatiotemporal distribution of dust events. To demonstrate the aerosol movement, a HYbrid Single Particle Lagrangian Integrated Trajectory (HYSPLIT) model was used for tracing the investigated dust events. The time-space consistency between AOT and GDR, in agreement with the HYSPLIT model output was the basis for an improved estimation of the dust deposition rate from separate thickness layers. Finally, by comparing the high temporal and maximum seasonal deposition rates, using MODIS and GDR data, the impact of the regional climate on the deposition rates of aeolian dust was assessed, which allows insights in potential future dust emission scenarios in times of climate change.

A major finding shows the impact of dust events on the environment and considers the influence of geographical factors, such as weathering, and climate pattern over aeolian dust deposition rates. In more detail, finding to address the first objective suggested that contributors of the elemental concentrations are associated with elements emanating from local industrial and commercial activities (Cr, V, and Cd). The dominant variables (K, Zn) strongly influence the aerosol composition values and

¹ - The dust belt stretches from the Sahara desert in Africa to the Gobi desert in Central and East Asia. Credit: Adapted from Hofer et al., (2017)

represent the dust transport route. Inter –element relationships shows that the highest proportion (80%) of dust samples subjected to Airborne Metals Regulations are formed under local and regional conditions. Besides, the analyses indicate that the WRF-Chem model adequately simulates the evolution, spatial distribution and load of dust over the study area. Hence, the model performance has been evaluated by GDR. It showed different values of GDR highly depending on LULC pattern. Due to the fact, that there is no way to isolate each individual area from the effects of either anthropogenic sources or natural weathering processes, developing guidance on the priorities of expanding projects and preventative actions towards potential dust deposition from natural and dominant sources may be a subject of institutional interest.

The results of direct measurements of dust deposition, which are typically made by passive sampling techniques (ground-based observations), along with analyzed data from AOT, represent the second objective to understand the spatiotemporal pattern of the points with the same variation. The corresponding points headed to find moving air mass trajectories, using HYSPLIT were proven to be a discriminator of their local and regional origin of aeolian dust. Furthermore, the seasonal deposition rate varied from 8.4 g/m²/month in the summer to 3.5 g/m²/month in the spring. Despite all the advances of AOT, under certain circumstances, the ground-based solutions were able to represent aerosol conditions over the research area, tested in the southwestern regions of Iran. And that is when the low number of observations is a commonly acknowledged drawback of GDR.

In addition, the peak of the seasonal deposition rates (t/km²/month) occurred in [arid desert hot-BWh, 8.4], [arid steppe hot-BSh, 6.6], and [hot and dry summer-Csa, 3.5] climate regions. Thus, the third objective response was detected as the highest deposition rates of dust BWh >BSh >Csa throughout the year, once the annual mean deposition rates (t/km²/year) are 100.80 for [BWh], 79.27 for [BSh], and 39.60 for [Csa]. The knowledge gained on the dust deposition processes, together with the feedback from the climate pattern, will provide insights into the records of data for developing new sources, deposition rates and their climate offsets. Taking this in mind, having information about the ground deposition rates in the study region could make the estimations more accurate, while finding an appropriate algorithm is necessary to enhance the affected areas exposed to the dust. In order to assess the impact of dust events on human health, environment and the damage to the various business sectors of the country's economy, additional studies with adequate modelling tools are needed.

Due to this date, the data holding organizations are somewhat reluctant to make their data available to other parties. This work is also a step toward an institutional suggestion to gain benefit from information exchange amongst data holding organizations, providers and users. The need for capacity building and strong policy for implementing user-friendly geo information portal is essential.

Keywords: Dust deposition rate, Climate forcing, Dust deposition rate, AOT, HYSPLIT, ICP-MS, metal concentrations, aeolian dust, WRF_Chem, LULC, climate zone, Iran

Zusammenfassung

Die jährliche atmosphärische Staubbelastung im sog. Staubgürtel, dessen Quellgebiete von der Sahara, der Arabischen Halbinsel, bis nach Zentralasien und Nordchina reichen, hat einen starken Einfluss auf die Luftqualität und das globale Klima. Eine der am stärksten vom atmosphärischen Staub betroffenen Regionen ist der Iran, und hier insbesondere dessen südwestliche Gebiete, die sehr häufig Staubstürmen ausgesetzt sind, bzw. davon beeinflusst werden. Diese können im Jahresmittel Konzentrationen von über $100 \mu\text{g}/\text{m}^3$ erreichen. Trotzdem Staub im Iran ein besonders relevantes Problem darstellt, fehlen bisher Regionalstudien darüber. Das zentrale Ziel dieser Studie ist es deshalb, raum-zeitliche Analysen und eine Klassifikation von Staubereignissen, deren chemische Zusammensetzung und die Beziehungen zwischen regionalen und jahreszeitlichen Klimaschwankungen sowie Staubdepositionen in vier Subregionen mittels der maximalen mittleren Staubkonzentration und der Saisonabhängigkeit der Staubereignisse zu bestimmen. Dieser integrierte Forschungsansatz gestattet es, neue und wertvolle Kenntnisse über Stäube im Untersuchungsgebiet zu gewinnen.

Das Untersuchungsgebiet hat eine Fläche von etwa $117,000 \text{ km}^2$. Das sind 8.43% der Fläche des Iran. Unter Berücksichtigung von Probenentnahmestellen, die sich zwischen $45^\circ 30' 00''$ zu $49^\circ 30' 00''$ E und $30^\circ 00' 00''$ zu $35^\circ 00' 00''$ N in den Provinzen Kermanshah, Lorestan und Khuzestan befinden, wurde das Untersuchungsgebiet abgegrenzt. Das Feldforschungsgebiet ist geprägt von Gebirgen bis etwa 4.000m NN und Gebirgsvorländern im Norden und Osten sowie Flachland und Marschland im Süden. Nördlich des Persischen Golfs, im Südwesten des Iran, erstreckt sich ein Teilgebiet mit trockenem Klima und heißen Sommern, wohingegen das Teilgebiet im Nordwesten des Landes winterkaltes und sommerheißes Wüstenklima aufweist. Die Untersuchungen der äolischen Staubdepositionsraten im Südwesten des Iran wurden zwischen 2014 bis 2017 durchgeführt.

Um die Zusammenhänge zwischen den Staubdepositionsraten in 2 m Höhe bzw. Ground observation of dust Deposition Rate (GDR) und dem Klima, dessen synoptischen Bedingungen und Wettermustern zu untersuchen, wurde eine vergleichende Analyse mit unterschiedlichen Daten durchgeführt. Sowohl gravimetrische als auch ausgerichtete Staubsammler (insgesamt 10) wurden so konstruiert und installiert, dass die Partikelmasse, die sich aus der Luft absetzt, bestimmt werden kann. Die Staubsammlerkonstruktion wurde absichtlich einfach gestaltet, um die Aufrechterhaltung und einfache Wartung des Messbetriebs sicher zu stellen. Bezug nehmend auf das erste Ziel erfolgte die Messung der Staubdepositionen durch eine chemische Analyse mittels induktiv gekoppelter Plasmamassenspektrometrie (ICP-MS). Die 10 Messstellen des Untersuchungsgebietes wurden nach der Flächennutzung bzw. der Bodenbedeckung (LULC) klassifiziert, um diese für Auswertungszwecke nutzen zu können. Die Beobachtungsdaten für zwei typische Staubfallbeispiele (Frühjahr 2014 und Winter 2015) wurden auch mit der räumlich-zeitlichen Staubkonzentration und Staubbelastung über dem Untersuchungsgebiet verglichen. Beim Vergleich der Ergebnisse der monatlich durchschnittlichen Aerosol Optical Thickness (AOT), welche von MODIS (Moderate Resolution Imaging Spectroradiometer) und GDR - Daten abgeleitet wurden, kamen erweiterte Algorithmen zum Einsatz, um die raum-zeitliche Verteilung von Staubereignissen bestimmen zu können. Damit die Aerosolbewegung nachvollzogen werden kann, wurde ein „Hybrid-Einzelpartikel- Lagrangschen-Integriertes-Trajektorie (HYSPLIT) - Modell eingesetzt. Die Zeit-Raum-Konsistenz zwischen AOT und GDR wurde durch Anpassung mit dem Ausgangsmodell, HYSPLIT, erreicht, um Abschätzungen der Staubdepositionsrate aus den einzelnen dicken Schichten (AOT) zu ermöglichen. Schließlich erfolgte ein Vergleich der hohen zeitlichen und maximal saisonalen Deposition mittels MODIS und GDR-Daten, um den Einfluss des Regionalklimas auf die Depositionsraten des äolischen Staubs bewerten zu können. Damit werden neue Erkenntnisse für potentiell zukünftige Staubemissionen in Zeiten des Klimawandels möglich. Eine wichtige Erkenntnis aus dieser Forschung besteht darin, dass

Auswirkungen von Staubereignissen auf die Umwelt und dessen Einflüsse auf geographische Faktoren, wie Verwitterung, Klimamuster und synoptische Bedingungen über äolische Staubdepositionsraten festgestellt werden können.

Bei näherer Betrachtung bezieht sich die Erkenntnis aus dem ersten Ziel darauf, dass die Staubzusammensetzung mit den Elementen, die aus lokalen, industriellen und kommerziellen Aktivitäten (Cr, V, and Cd) stammen, in Verbindung steht. Die dominanten Variablen (K, Zn) beeinflussen die Werte der Aerosolzusammensetzung stark und sind aus dem Staubtransportweg erklärbar. Das Ergebnis zeigt auch, dass der größte Anteil der Staubproben (80%), lokale und regionale Ursprünge hat. Zusätzlich deuten die Analysen darauf hin, dass das WRF-Chem. Modell die Entwicklung, die räumliche Verbreitung und die Staubbelastung im Untersuchungsgebiet angemessen simuliert. Da die Modellleistung durch die GDR überprüft wurde, zeigen sich unterschiedliche Werte der DDR, die sehr stark von den LULC Mustern abhängig sind. Da es nicht möglich ist, einzelne Gebiete vor sowohl anthropogenen Quellen als auch natürlichen Verwitterungs- und Staubbildungsprozessen zu isolieren, stellen die Entwicklung von Handlungsempfehlungen vor allem für neue Projektaktivitäten und präventive Maßnahmen zur Reduzierung der potentiellen Staubbelastung Gegenstände von hohem institutionellem Interesse dar.

Die Ergebnisse direkter Staubdepositionsmessungen mittels passiver Staubsammler (ground-based observations) repräsentieren zusammen mit ausgewerteten Daten aus der AOT das zweite Ziel, um so die raumzeitlichen Muster in ihrer Variabilität zu verstehen. Die korrespondierenden Merkmalspunkte die zur Suche von sich bewegenden Luftmassenbahnen genutzt wurden, verwenden das HYSPLIT - Modell, das es ermöglicht, die lokalen und regionalen Herkunft äolischer Stäube zu unterscheiden. Die jahreszeitliche Depositionsrate variiert zwischen 3.5 g/m²/Monat im Sommer und 8.3 g m²/Monat im Frühling und gibt einen Einblick in die Transportrichtung des Staubes. Ungeachtet der Vorzüge der AOT-Messwerte können bodengestützte Messungen unter bestimmten Umständen die Aerosolbedingungen im Untersuchungsgebiet besser darstellen, obwohl die geringe Anzahl von Beobachtungen ein allgemein anerkannter Nachteil bei der Bestimmung der Staubdepositionsraten ist. Das wurde in den südwestlichen Regionen des Iran getestet.

Der Höhepunkt der saisonalen Ablagerungsrate (g/m²/Monat) tritt in den trockenen Wüsten [heiß- BWh, 8.4], Wüstensteppen [heiß-BSh, 6.6] und heißen und trockenen [Sommer-Csa, 3.5] Klimaregionen auf. Laut des dritten Ziels wurde die höchste Staubdepositionsrate (BWh >BSh >Csa) festgestellt, wenn der jährliche Mittelwert der Depositionsrate (t/km²/ Jahr) für [BWh] 100.80, für [BSh] 79.27, und für [Csa] 39.60 betrug. Die über die Staubablagerungsprozesse gewonnenen Erkenntnisse werden in Verbindung mit den Klimamustern neue Erkenntnisse über Quellen, Depositionsraten und deren klimaabhängigen Schwankungen gewähren. Kenntnisse aus Depositionsmessungen erlauben es, Aussagen über die Staubbelastung im Untersuchungsgebiet viel präziser zu tätigen. Dagegen muss noch ein geeigneter Algorithmus gefunden werden, der die Exposition der vom Staub betroffenen Gebiete besser widerspiegelt. Um die Auswirkungen von Staubereignissen auf die menschliche Gesundheit, die Umwelt und die Schädigung der verschiedenen Wirtschaftszweige des Landes beurteilen zu können, sind zusätzliche Studien mit geeigneten Modellierungsinstrumenten erforderlich. Leider erschweren Organisationen, die ihre Daten anderen nicht zur Verfügung stellen, die Forschung und daraus abzuleitende Lösungen. Diese Arbeit versteht sich auch als ein Schritt in Richtung eines Vorschlags zur Verbesserung des Informationsaustauschs zwischen Datenerfassungsorganisationen, Anbietersektoren und Benutzern. Die Notwendigkeit des Aufbaus von Kapazitäten und einer strengen Politik zur Implementierung eines benutzerfreundlichen Geoinformationsportals, ist von wesentlicher Bedeutung.

Keywords: Dust deposition rate, Climate forcing, AOT, HYSPLIT, ICP-MS, Metal concentrations, Aeolian dust, WRF_Chem, LULC, climate zone, Iran

1. Research Proposal

1.1 Introduction

Aeolian impact and dust storms are the results of strong winds, which are common earth-surface processes for both sediment transportation and deposition. Particles can be moved long distances by, for example, winds from Central Africa to Arctic regions and they can be deposited either by trapping or settling in various places depending heavily on wind direction (Nickling and Brazel, 1984; Sleewaegen et al., 2002) and barriers. Recently, western Asia and the Middle East are regions affected by dust storms causing a reduced visibility (Furman, 2003; Akbari, 2011). The nature of deposition varies according to the proximity and nature of the source material, the terrain, and the conditions responsible for transport and deposition. To address the environment impact of dust process, deposition morphology, previous work within well structured will be discussed in the following.

1.2 Deposition morphology and generalisation

According to the proximity and nature of the source material, the nature of deposition are clarified in 5 scenarios (Roberts, 2008). Scenarios of schematic models to explain the formation of loess- and other related aeolian-deposits source rebuild and determined in figures (1.1-1.5) with courtesy of (Pye, 1995). In the first scenario thick deposition are often found immediately downwind, which were the source of dust (Fig. 1.1).

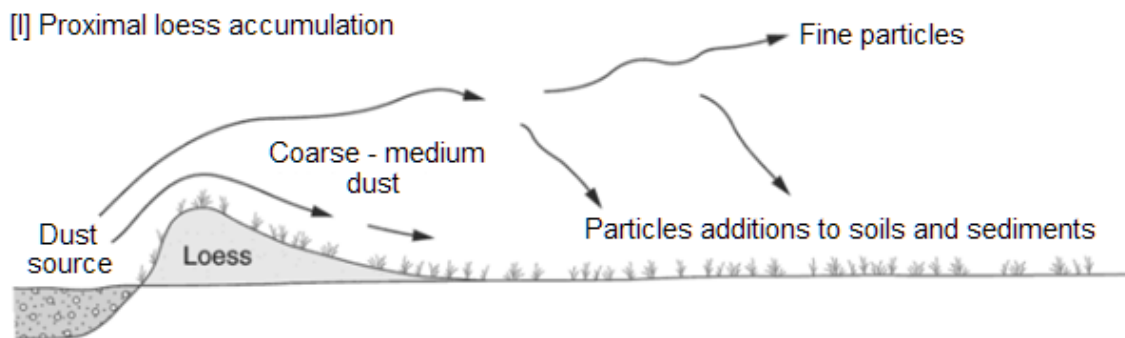


Figure 1.1 Proximal loess accumulation

Where source material consists of a greater range of grain sizes, sediment-sorting processes can also give rise to aeolian sand and loess deposits being found close to each other. Either as one contiguous deposit ranging from sand dunes, to sand sheets, sandy loess, and finally silt and clay-loess (Fig. 1.2) or as sand dunes and loess deposits separated by a clear zone of sediment bypassing (Pye, 1995; Muhs et al., 2003). The third scenario shown in Fig. 1.3 is of a situation in arid zone with both a rainfall gradient and a gradient of vegetation density. According to (Pye, 1995) these conditions can be found in desert margins, in which loess can accumulate in sparsely vegetated areas some considerable distance downwind of the source of the dust. The lack of vegetation in the intermediate area means that most dust particles pass through forward (Fig 1.3). In contrast to the scenario shown in (Fig. 1.2) occurs where there is sufficient moisture and hence vegetation to enable a gradual transition in grain size (down-wind fining), with no zone of sediment bypassing, before the distal transition to loess.

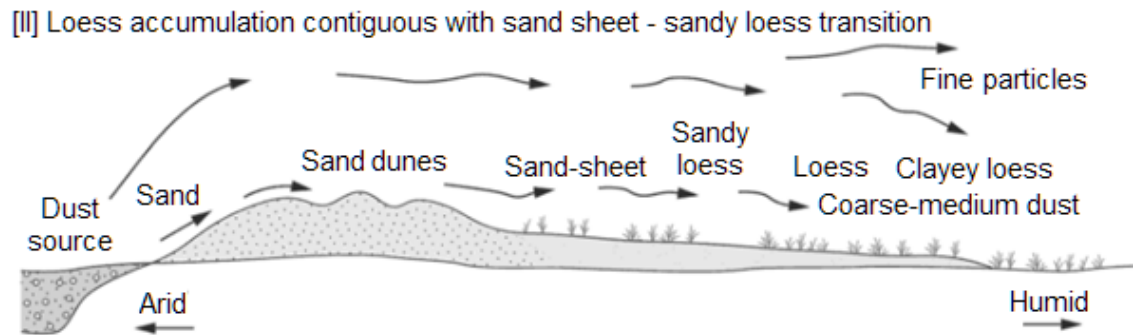


Figure 1.2 Sandy loess transition

Loess may also accumulate against topographic barriers in the fourth scenario. Topographic obstacles interrupt the flow of the wind, potentially leading to enhanced deposition on the windward side of the barrier (Fig. 1.4), but the deposition on the summit and or enhanced preferential deposition in the shelter side of the feature has been observed.

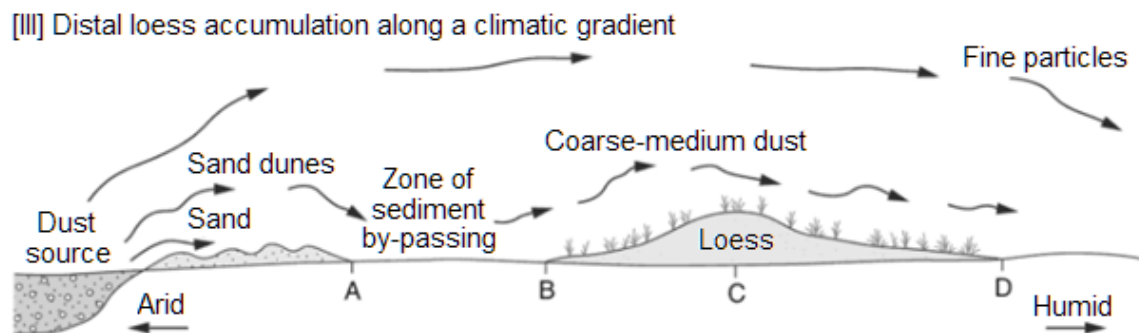


Figure 1.3 Loess accumulation along a climate gradient

The scenario illustrated in figure 1.4 is a single sediment source responsible for the proximal and distal accumulations of aeolian sand and loess (Muhs et al., 2003). Formation of proximal aeolian sand dunes further rise in response to accumulate deposition from local sediment sources. As fifth scenario depicted (Fig. 1.5) a distal sediment source also brings finer-grained sediments which are deposited over a wider area, forming loess deposits which have a distinctly different source to the aeolian sand, and may also have been deposited at very different time.

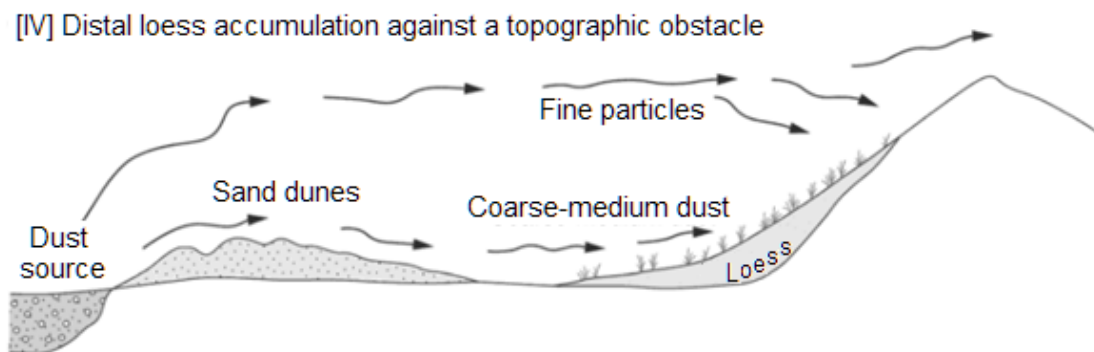


Figure 1.4 Loess accumulation against a topographic obstacle

Schematic models to explain the formation of loess and other related aeolian deposits source rebuild with courtesy of (Muhs et al., 2003). The role of vegetation in all these models of loses accumulation is critical, because obstacles (topographic and vegetation) disrupts the flow and reduces the wind

speed, hence reducing the re entrainment of deposited dust and it also provides a physical trapping mechanism for the dust.

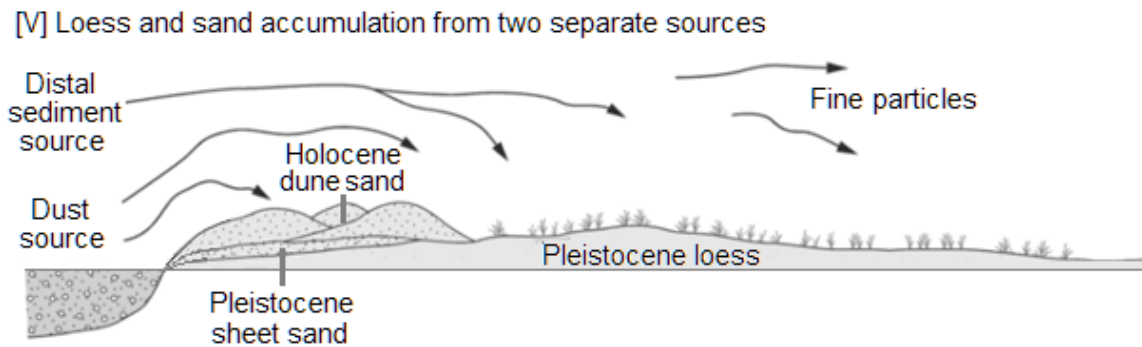


Figure 1.5 Accumulation from two separate sources

1.3 The state of the art

Dust is the most pervasive and essential factor affecting human welfare which derives from the earth's crust (Banerjee, 2003; Yongming et al., 2006). Although natural forces drive dust transport and deposition, dust transport processes can also be substantially constituted through human activities, including off-road driving (Gillies et al., 2005; Goossens et al., 2012), land use change (B. Marticorena et al., 1997; R. Reynolds et al., 2001; J. A. Gillies et al., 2005; J. C. Neff et al., 2008). Small solid and dry particles can remain suspended in the Earth's atmosphere long enough to extensively affect weather and climate (Calvert, 1990; Charlson et al., 1992; Prospero et al., 2002; Song et al., 2008; Rezazadeh et al., 2013). In fact, while particles are airborne, they can affect the radiation balance through scattering and absorbing radiation (Tegen et al., 1997; Haywood and Boucher, 2000; Sokolik et al., 2001; Tegen et al., 2004; Kim et al., 2008). Thus, interact with solar and terrestrial radiation, depending on their mineralogical composition, which is determined by the source of deposition (Okin et al., 2004; Mahowald et al., 2005). Mineral dust aerosols furthermore, influence the climate system directly by scattering and absorbing radiation (Kaufman and Koren, 2006; Alizadeh Choobari et al., 2013). It is associated with alterations in meteorological significance that may change the vertical profiles of temperatures and wind velocity thus, they can be deposited either by trapping or settling in various places depending heavily on wind direction (Alizadeh Choobari et al. 2013). Aside from immediate threats to atmospheric condition and satellite retrievals (Merchant et al., 2006; Amiridis et al., 2013), dust also significantly affects air quality (Claiborn et al., 2000; Liu et al., 2006).

On a global scale the aeolian dust transport cycle and dust loads are closely connected to climate variability and changes (Jouzel et al., 1996; AO, 2001; Goudie, 2009; Huang et al., 2011) and have reciprocal effects (Ramanathan et al., 2005). During transport, dust particles are continuously removed from the atmosphere by processes of dry and/or wet deposition (Lawrence and Neff, 2009). By all means, dislocating aeolian dust material over hundreds of years creates conceivable positive and negative feedback between the dust loads in the atmosphere and climate (Swap et al., 1992) that can be important for terrestrial systems. It provides essential nutrients for plant growth that are contained in the fertilized terrestrial dust, and a series of wet years can trigger rapid re-vegetation of desert surfaces (Falkowski et al., 1998; Jickells et al., 2005).

All the while positive feedback, aeolian dust might also increase soil salinity (Popov, 1998), reduce the photosynthetic efficiency (Razakov and Kosnazarov, 1996), depreciate air quality, and impair human health (Stone, 1999; O'Hara et al., 2000; Wiggs et al., 2003; Opp et al., 2017). With other words, the mass deposition rate of dust particles may cause considerable negative health effects (Roberts, 2008;

Albani et al., 2015; Kharazmi et al., 2018; Sharifi et al., 2015), and infections (Thomson et al., 2006; Díaz et al., 2012; de Longueville et al., 2013). It can effect further, agriculture (Stefanski and Sivakumar, 2009), engines and technical infrastructure (El-Nashar, 2003; Tegen et al., 2004; Elminir et al., 2006; Mahowald et al., 2010; Ohde & Siegel, 2012; Kazem et al., 2014). Moreover, causing severe economic damages (Ai and Polenske, 2008; Miri et al., 2009).



Figure 1.6 Feasible dust deposition and concentration

*Dust deposition [A], Visibility and dust concentration [B], and Turbine Vanes [D,E] are provided by M. A. Foroushani . Desertification [C] provided by Christian Opp

As shown in Fig. 1.6, unlike earthquakes and other natural disasters, the effects can be mitigated, often reversible through the restoration of degraded lands where feasible. However, the economic and social impacts are often underestimated. During the last decades, dust event frequency and intensity have increased significantly in the western parts of Iran (Gerivani et al., 2011). Equally, Cao et al., (2015) identified the main dust sources and areas prone to desertification in southwest (Khuzestan) based on satellite remote sensing, while (Rezazadeh et al., 2013) examined the most dust-affected areas based on visibility data from meteorological stations. Both studies uncovered the most dust-affected areas in southwest (Khuzestan Province) and southeast (Sistan Basin) of Iran.

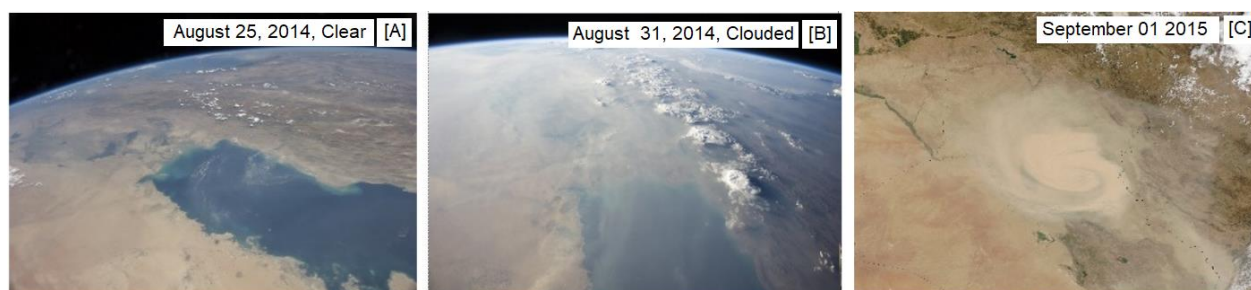


Figure 1.7 Satellite imagery over Iran

*The photos are provided by the ISS Crew Earth Observations Facility and the Earth Science and Remote Sensing (Wilkinson 2014). [a, b] Desert dust in the atmosphere engulfs the Persian Gulf, and [c] the western part of Iran

These regions also were subject of interest to scientific terms of meteorological regimes and the monitoring dust event (Tab. 1.1), such as; total suspended particulate (TSP) and particulate matter concentrations (PM), dust mineralogy, health impacts and socio-economic effects (Miri et al., 2007). Based on the severity of dust events on the classification method of (Hoffmann et al., 2008) the

categories are referred to: Dusty air, Light dust storm, Dust storm, Strong dust storm, and Serious dust storm.

Table 1.1 Dust storm classification method, after (Hoffmann et al., 2008)

Category	Visibility (m)	Wind speed (m/s)	Hourly PM10 ($\mu\text{g}/\text{m}^3$)
Dusty air	Haze	–	50–200
Light dust storm	<2000	–	200–500
Dust storm	<1000	>17	500–2000
Strong dust storm	<200	>20	2000–5000
Serious strong DS	<50	>25	>5000

As shown in Tab. 1.2 dust concentration has been extensively examined in many regions with a wide range of concentrations and documented sources. The World Health Organization (WHO) recently reported the most polluted city based on mean-annual PM10 concentration (Goudie, 2014). An overview of the most relevant literature are emphasised over the following items. In the first place, the changing patterns of human activities (Neff et al., 2008), followed by uncertainties in spatial and temporal patterns, including different measurement techniques (Sokolik et al., 2001) have been addressed. Besides, the concentration of dust in the atmosphere as well as surface features of the environment of the depositional sites (Tegen and Lacis, 1996; Arimoto et al., 1997; Abdou et al., 2005) are studied. In particular, several studies have addressed the dust deposition rate (Schaap et al., 2009; Sorooshian et al., 2011; Balakrishnaiah et al., 2012; Crosbie et al., 2015; Yu et al., 2016). However, the long-term monitoring atmospheric aeolian against ground observation of dust and deposition rate has not been previously investigated in southwestern Iran. This area, frequently encountered with dust events and their problems.

Table 1.2 Dust concentration in different regions

Reference	Year	concentration $\mu\text{g}/\text{m}^3$	Location
(Malm and Sisler, 2000)	2012-2015	30	Across the USA
(Salvador et al., 2011)	2012-2015	40	Madrid- Spain
(Liu et al., 2015)	2004-2012	95	Saudi Arabia- The west-
(Liu et al., 2015)	2004-2012	138.5	Beijing- China
(Gupta et al., 2008)	2008	140.1	Kolkata- India
(Maleki et al., 2016)	2009-2014	315	Iran- Southwest
(Goudie, 2014)	2014	254	Iran- West (Sanandaj
(Goudie, 2014)	2014	229	Iran- West (Kermanshah)
(Goudie, 2014)	2014	215	Iran- Jasouj
(Goudie, 2014)	2014	372	Iran- Ahwaz

Considering the importance of dust phenomenon, subsequent problems, and its impact on various regions, are the main purpose of this study is to determine aeolian dust performed using statistical data, synoptic charts, and remote sensing data for the southwest of Iran.

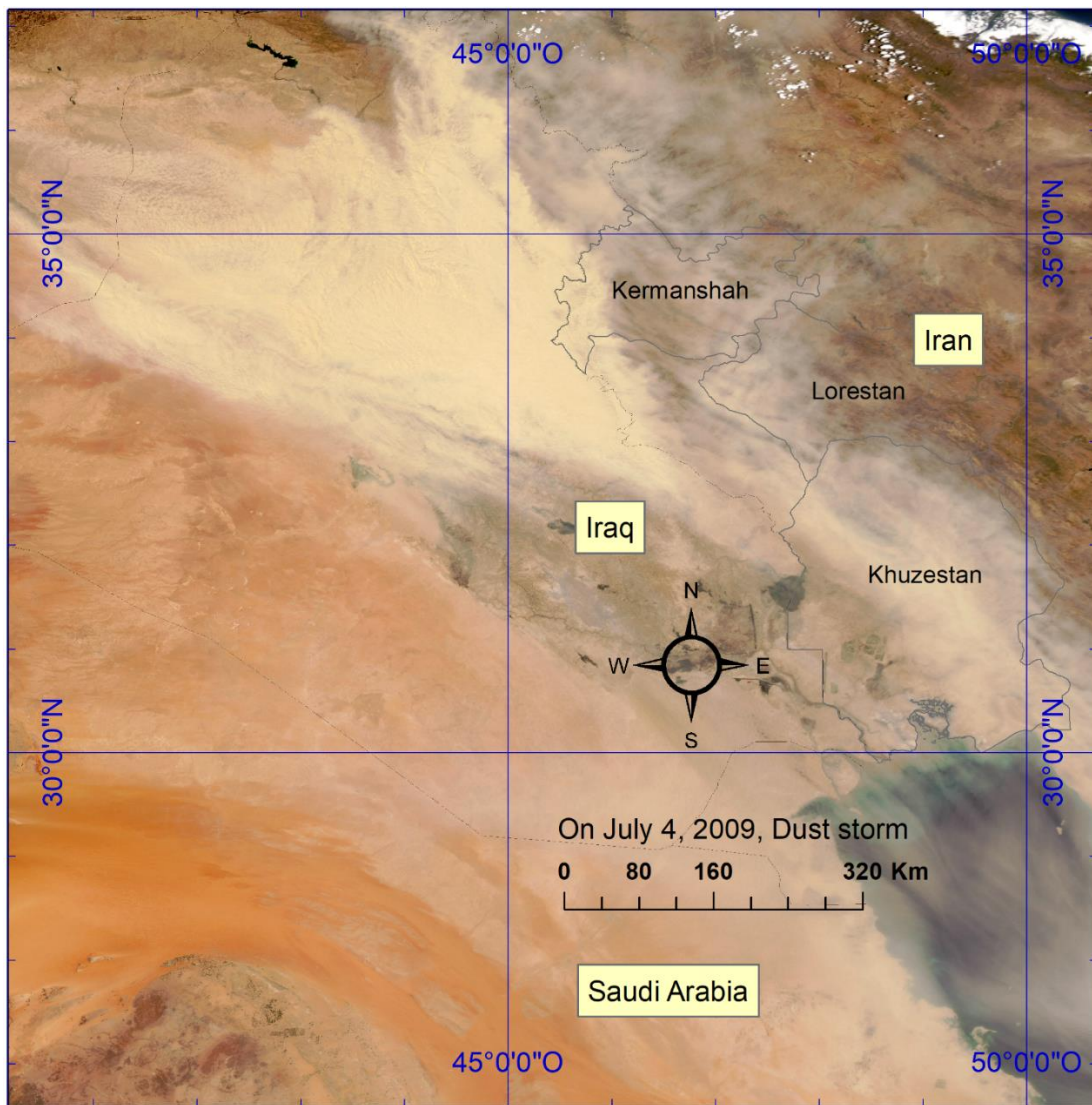


Figure 1.8 Dust storm had persisted over Iran and the Persian Gulf.

*On July 4, 2009, a massive dust storm had persisted over Iraq for a week. The dust storm also spread toward the east and southeast, over Iran and the Persian Gulf. The Moderate Resolution Imaging Spectroradiometer (MODIS) on NASA's Aqua satellite took this natural-color picture the same day

In this research, the study area is southwest of Iran including Kermanshah, Lorestan, and Khuzestan provinces located in the west of mountain ranges of the Zagros foothills and north of Persian Gulf. The study area has a high population density, because of the extraction of gas and oil fields, and cultivation. The climate conditions are semi-arid to semi-humid. The precipitation of the area is under the influence of the Mediterranean raining regime. The most important natural hazards in this area are severe droughts, floods, and dust storms. The results can provide a baseline to use in the future assessments of environmental impact, and to guide mitigation impact in that area.

1.4 Problem statement and Hypothesis

In general, when considering extensive sand and dust deposits in the geological record, plain-land takes considerable amount of aeolian deposits. This amount, particularly in great value on land depends on artificial and natural obstacles. Beyond the state of deposition rate on land, discriminating aeolian sediments in water bodies as a major part of their influences, that could be provided by dust events is extremely difficult (An et al. 2012). This study will provide specific guidance on the evaluation of

deposition rate. Equally, it targets based on prior information over three missing parts of concept in southwest of Iran.

In the first place, there is a lack of consistent references from chemical gradients in that particular area: the result is important to understand if anthropogenic activities can directly affect elemental composition in aeolian particles. Significantly, this reference will deploy for many business purposes that is to say healthcare systems, economy including industry and agriculture.

The next missing part takes into account for observation data in comparison with dust load and dust concentration values that retrieved from instruments. The correlation between data collected from deposition rate and discrimination of dust concentration maintained by instrument, which is still not known. Narrow gapped is to find out rate factor from different observation methods. Due to dust concentrations in the atmosphere can represent the dust deposition factors but not the rate of deposition on the land.

The last missing part is the absence of information about deposition offset and climate zones, climate pattern influence regionally aeolian dust budget. Although the importance of dust deposition as an integral component of terrestrial process is well recognized, few studies have directly addressed regional climate factor associated with dust deposition rate on the land surface. This part addresses this gap by looking at response to the rate closely connected to climate variability.

1.5 Goal and Research Objectives

Having data about the deposition rate are usually used to validate model simulations (Yu et al., 2003) or may provide a useful benchmark. Accordingly, both passive and active sampling techniques can pay off to the lack of information from the deposition rate by ground observations (Taheri Shahraiyni et al., 2015). The general aim of this study will focus on establishing the association between Ground observation of Deposition Rates – GDR- and dust occurrence, chemical gradients, and climate factors including pattern of land surface. Monitoring aeolian dust and improving the understanding of the factors influencing dust deposition is a key scientific challenge. Due to one in different climate might anticipates different result, the connection between climate zones and dust deposition rates is essential. Consequently, climate factors, geographical features, natural and artificial obstruct play an important role in the development of the deposition rate.

The primary purpose of this study is to determine whether there is an evidence to support the hypothesis that the area exposed to aeolian dust is associated with the occurrence of the chemical gradient value. Specifically to determine the inter correlation of elements.

The secondary purpose of this research will interrogate the effect of other confounding factors of dust (dust load, dust concentration, and dust deposition rate) when dust occurred. Monitoring methods and the main factors of association will be investigated. To sum up, response to the following objectives and research questions will be fulfilled the research goals:

- [1] To investigate the spatial and temporal variability of dust deposition rates in the study area
- [2] To discriminate the major contributors of the elemental concentrations associated with elements emanating from natural and dominant sources
- [3] To understand the spatiotemporal pattern of dust distribution and dust concentrations determining the seasonal and spatial variability of the dust deposition rate in relation to the climate zones.

1.6 Research framework

The research framework explains the path of a research firmly based on flow diagram (Fig. 1.9). The process flow is illustrated where data comes from, where it goes and how it presents. Since available

data retrieved from divers, terms of serving sources, all concerns were addressed quality data. The first group which is making the main reference context of data, consisting of a long-term data that is created by NASA with information about the vertical distribution of dust (Aaron van Donkelaar 2010). Moreover, required geo-reference and shape files (Geofabrik 2017) besides a map of climate (Peel et al., 2007). In addition to the associated sources of airborne trace elements from literature (S. Wang et al., 2006) followed by the standard (Geiger and Cooper, 2010), modified annual precipitation report (IRMO 2016) has been retrieved.

The second data group comprises a set of own experimental data retrieved from research practice spatiotemporal data such as data from observation, sampling data, treatment procedures before decomposed by inductively coupled plasma mass spectrometry (ICP-MS) based on standard (ASTM D1356, 2017; ASTM D5111, 2012), including element concentration (ASTM D7439, 2014). The third group of data is presenting calculated correlation and statistics including the registration, geo-processing task and mapping into data obtain from fieldwork boundary using ArcMap.

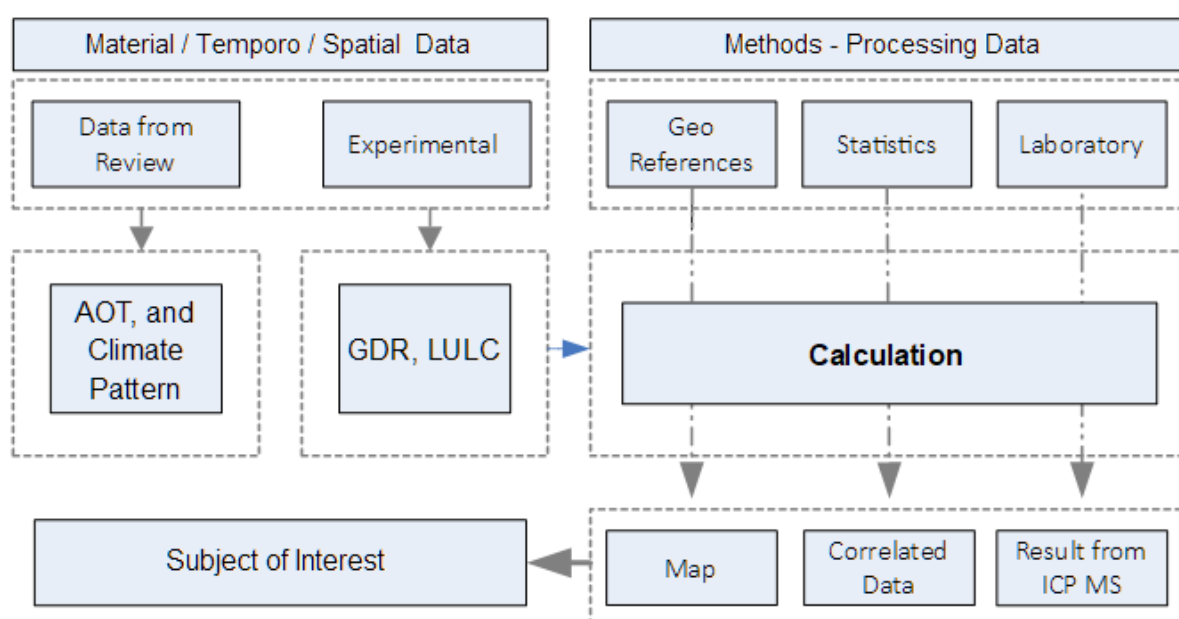


Figure 1.9 Research framework, dataset and flow diagram

1.7 Thesis structure

The thesis structure is described shortly with the research proposal, followed by the research approach, the methods and results, including three publication added into dissertation. They are titled with chemical characterization of GDR, spatiotemporal gradients of GDR and AOT, and spatiotemporal gradients of GDR and AOT. The final chapter consists of research conclusion and some recommendation about future works.

1.7.1 Research proposal

The research proposal structure includes the background and the research context, the problem statement and the research objectives are provided. This chapter also concludes by, primarily express situation as the state of the art, generalization and characterized research question, definition of temporary research framework and finally method definition.

1.7.2 Research approach (Physical setting)

This chapter concludes, the developed research framework based on theory and strategic planning for sampling sites and the process of gathering and measuring data.

1.7.3 Material and methods

This chapter contains the observational study, laboratories and statistics designed to answer the research questions. Objectives addressed to the three following chapters. The first objective addresses in a given article consist of the finding correlations of different strengths between elemental value using ICP-MS data, based on Airborne Metal Regulations called AMR-matrix (Geiger and Cooper, 2010). Certainly, a wide range of chemical compounds have been examined and classified in a range of studies (Mertz, 1981; X. Wang et al., 2006; Kabata-Pendias, 2010). The statements of the next objective conducts to discriminate monthly mean aerosol optical thickness (AOT) from the Moderate Resolution Imaging Spectroradiometer (MODIS) compared with the dust amount variations collected from the ground observation process. Ground observation of Deposition Rates – GDR- therefore, will be introduced as a key factor for finding the relative impact of the dust. Finally, the connection between climate zones and dust deposition rates using a reanalysis tool called MERRA-II (The second modern-era retrospective analysis for research and applications) in combination with GDR between 2014 and 2017 will be demonstrated

1.7.4 Results and discussion

1.7.4.1 Chemical characterization of GDR

To reveal the chemical gradient from collected samples (samples with strong correlations between dust deposition rate and the dust event frequency), ICP-MS analyses have been applied. The element chart was classified based on Airborne Metal Regulations matrix. These findings suggest correlation between wind and element emanating from natural (NS) or dominant (DS) activities. The major contributors in the elemental concentrations is very critical to identify key component which is necessary for turning into products desired air quality objectives that effect a particular area before they become problems. The chemical properties of deposited particles is important to develop proper mitigation strategies. The observation data (GDR) during two typical dust cases (Spring 2014 and winter 2015), were compared with both the spatiotemporal dust concentration and dust load over the study area, simulated by the Weather Research and Forecasting Model coupled with Chemistry (WRF-Chem) for the application into the dust modeling system.

1.7.4.2 Spatiotemporal gradients of GDR and AOT

To investigate the spatiotemporal distribution of dust events in the study area, the monthly mean aerosol optical thickness (AOT) from the Moderate Resolution Imaging Spectroradiometer (MODIS) was compared with the dust amount variations from the Ground observation of Deposition Rates – GDR- . Getting the dust concentration from AOT and GDR including air mass trajectories simulation, the HYbrid Single Particle Lagrangian Integrated Trajectory model (HYSPLIT) was used, in order to discriminate the local and regional origin of dust.

1.7.4.3 Investigation of the GDR in different climate zones

To investigate the seasonal deposition rates ($t/km^2/year$) in climate zone, results will be addressed to the gauge-sites. The highest deposition rates of dust correlated with climate factors will be uncovered. The knowledge gained on the dust deposition processes, together with feedback from the climate pattern, will provide insights into the records of data for developing new sources, deposition rates and their climate offsets. Since the aeolian deposited rate are sensitive over climate zones, even suggesting

that additional observation data from GDR on climate regimes might be performed to obtain precise information on dust plumes.

1.7.5 Conclusion

In this chapter, the research proposal, the morphology and generalization of deposition together with direct and indirect influences of immediate treats to the society are reviewed. Furthermore, significant retrievals in monitoring and results are discussed. Finally, it is realized that the potential environmental and social impact of dust plum ultimately depends on the route (media speed and direction), load, concentration, and deposition rate in real world. Thus, the wide range of affects further can only be assessed case-by-case.

References

- Aaron van Donkelaar, R.M., 2010. Global satellite-derived map of PM_{2.5} averaged over 2001-2006.
- Abdou, W.A., Diner, D.J., Martonchik, J.V., Bruegge, C.J., Kahn, R.A., Gaitley, B.J., Crean, K.A., Remer, L.A., Holben, B., 2005. Comparison of coincident Multiangle Imaging Spectroradiometer and Moderate Resolution Imaging Spectroradiometer aerosol optical depths over land and ocean scenes containing Aerosol Robotic Network sites. *J. Geophys. Res.-Atmospheres* 110. <https://doi.org/Artn D10s07> 10.1029/2004jd004693
- Ai, N., Polenske, K.R., 2008. Socioeconomic Impact Analysis of Yellow-dust Storms: An Approach and Case Study for Beijing. *Econ. Syst. Res.* 20, 187–203. <https://doi.org/10.1080/09535310802075364>
- Akbari, S., 2011. Dust storms, sources in the Middle East and economic model for survey its impacts. *Aust. J. Basic Appl. Sci.* 5, 227–233.
- Albani, S., Mahowald, N.M., Winckler, G., Anderson, R.F., Bradtmiller, L.I., Delmonte, B., Francois, R., Goman, M., Heavens, N.G., Hesse, P.P., Hovan, S.A., Kang, S.G., Kohfeld, K.E., Lu, H., Maggi, V., Mason, J.A., Mayewski, P.A., McGee, D., Miao, X., Otto-Bliesner, B.L., Perry, A.T., Pourmand, A., Roberts, H.M., Rosenbloom, N., Stevens, T., Sun, J., 2015. Twelve thousand years of dust: the Holocene global dust cycle constrained by natural archives. *Clim. Past* 11, 869–903. <https://doi.org/10.5194/cp-11-869-2015>
- Alizadeh Choobari, O., Zawar-Reza, P., Sturman, A., 2013. Low level jet intensification by mineral dust aerosols. *Ann. Geophys.* 09927689 31.
- Amiridis, V., Wandinger, U., Marinou, E., Giannakaki, E., Tsekeri, A., Basart, S., Kazadzis, S., Gkikas, A., Taylor, M., Baldasano, J., Ansmann, A., 2013. Optimizing CALIPSO Saharan dust retrievals. *Atmospheric Chem. Phys.* 13, 12089–12106. <https://doi.org/10.5194/acp-13-12089-2013>
- An, F., Ma, H., Wei, H., Lai, Z., 2012. Distinguishing aeolian signature from lacustrine sediments of the Qaidam Basin in northeastern Qinghai-Tibetan Plateau and its palaeoclimatic implications. *Aeolian Res.* 4, 17–30.
- AO, J.W.Z., 2001. The IPCC Third Assessment Report on the Scientific Basis of Climate Change. *Aust. J. Environ. Manag.* 8, 169–185. <https://doi.org/10.1080/14486563.2001.10648526>
- Arimoto, R., Ray, B.J., Lewis, N.F., Tomza, U., Duce, R.A., 1997. Mass-particle size distributions of atmospheric dust and the dry deposition of dust to the remote ocean. *J. Geophys. Res.-Atmospheres* 102, 15867–15874. <https://doi.org/Doi 10.1029/97jd00796>
- ASTM D1356, 2017. Standard Terminology Relating to Sampling and Analysis of Atmospheres, in: Book of Standards, ASTM D1356. Subcommittee D22.03.
- ASTM D5111, 2012. Standard Guide for Choosing Locations and Sampling Methods to Monitor Atmospheric Deposition at Non-Urban Locations, in: Book of Standards, ASTM D5111 - 12. Subcommittee D22.03.
- ASTM D7439, 2014. Standard Test Method for Determination of Elements in Airborne Particulate Matter by Inductively Coupled Plasma–Mass Spectrometry, in: Book of Standards, ASTM D7439-14. Subcommittee D22.03.
- Balakrishnaiah, G., Reddy, B.S.K., Gopal, K.R., Reddy, R., Reddy, L., Swamulu, C., Ahammed, Y.N., Narasimhulu, K., KrishnaMoorthy, K., Babu, S.S., 2012. Spatio-temporal variations in aerosol optical and cloud parameters over Southern India retrieved from MODIS satellite data. *Atmos. Environ.* 47, 435–445.
- Banerjee, A.D., 2003. Heavy metal levels and solid phase speciation in street dusts of Delhi, India. *Env. Pollut* 123, 95–105. [https://doi.org/10.1016/s0269-7491\(02\)00337-8](https://doi.org/10.1016/s0269-7491(02)00337-8)
- Calvert, J.G., 1990. Glossary of Atmospheric Chemistry Terms. *Pure Appl. Chem.* 62, 2167–2219. <https://doi.org/DOI 10.1351/pac199062112167>
- Cao, H., Liu, J., Wang, G.Z., Yang, G., Luo, L., 2015. Identification of sand and dust storm source areas in Iran. *J. Arid Land* 7, 567–578. <https://doi.org/10.1007/s40333-015-0127-8>
- Charlson, R.J., Schwartz, S.E., Hales, J.M., Cess, R.D., Coakley, J.A., Hansen, J.E., Hofmann, D.J., 1992. Climate forcing by anthropogenic aerosols. *Science* 255, 423–30. <https://doi.org/10.1126/science.255.5043.423>
- Claiborn, C.S., Finn, D., Larson, T.V., Koenig, J.Q., 2000. Windblown Dust Contributes to High PM₂₅ Concentrations. *J. Air Waste Manag. Assoc.* 50, 1440–1445. <https://doi.org/10.1080/10473289.2000.10464179>
- Crosbie, E., Youn, J.-S., Balch, B., Wonaschütz, A., Shingler, T., Wang, Z., Conant, W.C., Betterton, E.A., Sorooshian, A., 2015. On the competition among aerosol number, size and composition in predicting CCN

- variability: a multi-annual field study in an urbanized desert. *Atmospheric Chem. Phys.* 15, 6943–6958. <https://doi.org/10.5194/acp-15-6943-2015>
- de Longueville, F., Ozer, P., Doumbia, S., Henry, S., 2013. Desert dust impacts on human health: an alarming worldwide reality and a need for studies in West Africa. *Int. J. Biometeorol.* 57, 1–19. <https://doi.org/10.1007/s00484-012-0541-y>
- Díaz, J., Tobías, A., Linares, C., 2012. Saharan dust and association between particulate matter and case-specific mortality: a case-crossover analysis in Madrid (Spain). *Environ. Health* 11, 11.
- Elminir, H.K., Ghitas, A.E., Hamid, R.H., El-Hussairly, F., Beheary, M.M., Abdel-Moneim, K.M., 2006. Effect of dust on the transparent cover of solar collectors. *Energy Convers. Manag.* 47, 3192–3203. <https://doi.org/10.1016/j.enconman.2006.02.014>
- El-Nashar, A.M., 2003. Effect of dust deposition on the performance of a solar desalination plant operating in an arid desert area. *Sol. Energy* 75, 421–431. <https://doi.org/10.1016/j.solener.2003.08.032>
- Falkowski, P.G., Barber, R.T., Smetacek, V.V., 1998. Biogeochemical Controls and Feedbacks on Ocean Primary Production. *Science* 281, 200–7. <https://doi.org/10.1126/science.281.5374.200>
- Furman, H.K.H., 2003. Dust storms in the Middle East: sources of origin and their temporal characteristics. *Indoor Built Environ.* 12, 419–426.
- Geiger, A., Cooper, J., 2010. Overview of airborne metals regulations, exposure limits, health effects, and contemporary research. *US Environ. Prot. Agency Accessed* Accessed August 25, 2015.
- Geofabrik, 2017. OpenStreetMap Creative Commons.
- Gerivani, H., Lashkaripour, G.R., Ghafoori, M., Jalali, N., 2011. The Source of Dust Storm in Iran: A Case Study Based on Geological Information and Rainfall Data. *Carpathian J. Earth Environ. Sci.* 6, 297–308.
- Gillies, J.A., Etyemezian, V., Kuhns, H., Nikolic, D., Gillette, D.A., 2005. Effect of vehicle characteristics on unpaved road dust emissions. *Atmos. Environ.* 39, 2341–2347. <https://doi.org/10.1016/j.atmosenv.2004.05.064>
- Goossens, D., Buck, B., McLaurin, B., 2012. Contributions to atmospheric dust production of natural and anthropogenic emissions in a recreational area designated for off-road vehicular activity (Nellis Dunes, Nevada, USA). *J. Arid Environ.* 78, 80–99. <https://doi.org/10.1016/j.jaridenv.2011.10.015>
- Goudie, A.S., 2014. Desert dust and human health disorders. *Env. Int* 63, 101–13. <https://doi.org/10.1016/j.envint.2013.10.011>
- Goudie, A.S., 2009. Dust storms: recent developments. *J. Env. Manage* 90, 89–94. <https://doi.org/10.1016/j.jenvman.2008.07.007>
- Gupta, A., Karar, K., Ayoob, S., John, K., 2008. Spatio-temporal characteristics of gaseous and particulate pollutants in an urban region of Kolkata, India. *Atmospheric Res.* 87, 103–115.
- Haywood, J., Boucher, O., 2000. Estimates of the direct and indirect radiative forcing due to tropospheric aerosols: A review. *Rev. Geophys.* 38, 513–543. <https://doi.org/10.1029/1999rg000078>
- Hofer, J., Althausen, D., Abdullaev, S.F., Makhmudov, A.N., Nazarov, B.I., Schettler, G., Engelmann, R., Baars, H., Fomba, K.W., Müller, K., 2017. Long-term profiling of mineral dust and pollution aerosol with multiwavelength polarization Raman lidar at the Central Asian site of Dushanbe, Tajikistan: case studies. *Atmospheric Chem. Phys.* 17, 14559.
- Hoffmann, C., Funk, R., Sommer, M., Li, Y., 2008. Temporal variations in PM10 and particle size distribution during Asian dust storms in Inner Mongolia. *Atmos. Environ.* 42, 8422–8431. <https://doi.org/10.1016/j.atmosenv.2008.08.014>
- Huang, X.T., Oberhansli, H., von Suchodoletz, H., Sorrel, P., 2011. Dust deposition in the Aral Sea: implications for changes in atmospheric circulation in central Asia during the past 2000 years. *Quat. Sci. Rev.* 30, 3661–3674. <https://doi.org/10.1016/j.quascirev.2011.09.011>
- IRMO, 2016. I.R.OF IRAN Meteorological Organization.
- Jickells, T.D., An, Z.S., Andersen, K.K., Baker, A.R., Bergametti, G., Brooks, N., Cao, J.J., Boyd, P.W., Duce, R.A., Hunter, K.A., Kawahata, H., Kubilay, N., laRoche, J., Liss, P.S., Mahowald, N., Prospero, J.M., Ridgwell, A.J., Tegen, I., Torres, R., 2005. Global iron connections between desert dust, ocean biogeochemistry, and climate. *Science* 308, 67–71. <https://doi.org/10.1126/science.1105959>

- Jouzel, J., Waelbroeck, C., Malaize, B., Bender, M., Petit, J.R., Stievenard, M., Barkov, N.I., Barnola, J.M., King, T., Kotlyakov, V.M., Lipenkov, V., Lorius, C., Raynaud, D., Ritz, C., Sowers, T., 1996. Climatic interpretation of the recently extended Vostok ice records. *Clim. Dyn.* 12, 513–521. <https://doi.org/10.1007/Bf00207935>
- Kabata-Pendias, A., 2010. Trace elements in soils and plants. CRC press.
- Kaufman, Y.J., Koren, I., 2006. Smoke and pollution aerosol effect on cloud cover. *Science* 313, 655–658.
- Kazem, A.A., Chaichan, M.T., Kazem, H.A., 2014. Dust effect on photovoltaic utilization in Iraq: Review article. *Renew. Sustain. Energy Rev.* 37, 734–749. <https://doi.org/10.1016/j.rser.2014.05.073>
- Kharazmi, R., Tavili, A., Rahdari, M.R., Chaban, L., Panidi, E., Rodrigo-Comino, J., 2018. Monitoring and assessment of seasonal land cover changes using remote sensing: a 30-year (1987–2016) case study of Hamoun Wetland, Iran. *Environ. Monit. Assess.* 190, 356. <https://doi.org/10.1007/s10661-018-6726-z>
- Kim, S.W., Yoon, S.C., Kim, J., 2008. Columnar Asian dust particle properties observed by sun/sky radiometers from 2000 to 2006 in Korea. *Atmos. Environ.* 42, 492–504. <https://doi.org/10.1016/j.atmosenv.2007.09.055>
- Lawrence, C.R., Neff, J.C., 2009. The contemporary physical and chemical flux of aeolian dust: A synthesis of direct measurements of dust deposition. *Chem. Geol.* 267, 46–63. <https://doi.org/10.1016/j.chemgeo.2009.02.005>
- Liu, C.M., Young, C.Y., Lee, Y.C., 2006. Influence of Asian dust storms on air quality in Taiwan. *Sci Total Env.* 368, 884–97. <https://doi.org/10.1016/j.scitotenv.2006.03.039>
- Liu, Z., Hu, B., Wang, L., Wu, F., Gao, W., Wang, Y., 2015. Seasonal and diurnal variation in particulate matter (PM₁₀ and PM_{2.5}) at an urban site of Beijing: analyses from a 9-year study. *Environ. Sci. Pollut. Res.* 22, 627–642.
- Mahowald, N.M., Baker, A.R., Bergametti, G., Brooks, N., Duce, R.A., Jickells, T.D., Kubilay, N., Prospero, J.M., Tegen, I., 2005. Atmospheric global dust cycle and iron inputs to the ocean. *Glob. Biogeochem. Cycles* 19. <https://doi.org/10.1029/2004gb002402>
- Mahowald, N.M., Kloster, S., Engelstaedter, S., Moore, J.K., Mukhopadhyay, S., McConnell, J.R., Albani, S., Doney, S.C., Bhattacharya, A., Curran, M.A.J., Flanner, M.G., Hoffman, F.M., Lawrence, D.M., Lindsay, K., Mayewski, P.A., Neff, J., Rothenberg, D., Thomas, E., Thornton, P.E., Zender, C.S., 2010. Observed 20th century desert dust variability: impact on climate and biogeochemistry. *Atmospheric Chem. Phys.* 10, 10875–10893. <https://doi.org/10.5194/acp-10-10875-2010>
- Maleki, H., Sorooshian, A., Goudarzi, G., Nikfal, A., Baneshi, M.M., 2016. Temporal profile of PM₁₀ and associated health effects in one of the most polluted cities of the world (Ahvaz, Iran) between 2009 and 2014. *Aeolian Res.* 22, 135–140. <https://doi.org/10.1016/j.aeolia.2016.08.006>
- Malm, W.C., Sisler, J.F., 2000. Spatial patterns of major aerosol species and selected heavy metals in the United States. *Fuel Process. Technol.* 65, 473–501.
- Martcorena, B., Bergametti, G., Gillette, D., Belpas, J., 1997. Factors controlling threshold friction velocity in semiarid and arid areas of the United States. *J. Geophys. Res.-Atmospheres* 102, 23277–23287. <https://doi.org/10.1029/97jd01303>
- Merchant, C.J., Embury, O., Le Borgne, P., Bellec, B., 2006. Saharan dust in nighttime thermal imagery: Detection and reduction of related biases in retrieved sea surface temperature. *Remote Sens. Environ.* 104, 15–30. <https://doi.org/10.1016/j.rse.2006.03.007>
- Mertz, W., 1981. The essential trace elements. *Science* 213, 1332–1338. <https://doi.org/10.1126/science.7022654>
- Miri, A., Ahmadi, H., Ekhtesasi, M.R., Panjehkeh, N., Ghanbari, A., 2009. Environmental and socio-economic impacts of dust storms in Sistan Region, Iran. *Int. J. Environ. Stud.* 66, 343–355. <https://doi.org/10.1080/00207230902720170>
- Miri, A., Ahmadi, H., Ghanbari, A., Moghaddamnia, A., 2007. Dust storms impacts on air pollution and public health under hot and dry climate. *Int J Energy Env.* 2, 101–105.
- Muhs, D.R., Ager, T.A., Arthur Bettis, E., McGeekin, J., Been, J.M., Begét, J.E., Pavich, M.J., Stafford, T.W., Stevens, D.A.S.P., 2003. Stratigraphy and palaeoclimatic significance of Late Quaternary loess–palaeosol sequences of the Last Interglacial–Glacial cycle in central Alaska. *Loess Dust Indic. Rec. Terr. Mari Ne Palaeoenvironments DIRTMAP Database* 22, 1947–1986. [https://doi.org/10.1016/S0277-3791\(03\)00167-7](https://doi.org/10.1016/S0277-3791(03)00167-7)
- Neff, J.C., Ballantyne, A.P., Farmer, G.L., Mahowald, N.M., Conroy, J.L., Landry, C.C., Overpeck, J.T., Painter, T.H., Lawrence, C.R., Reynolds, R.L., 2008. Increasing eolian dust deposition in the western United States linked to human activity. *Nat. Geosci.* 1, 189–195. <https://doi.org/10.1038/ngeo133>

- Nickling, W., Brazel, A., 1984. Temporal and spatial characteristics of Arizona dust storms (1965–1980). *J. Climatol.* 4, 645–660. <https://doi.org/10.1002/joc.3370040608>
- O'Hara, S.L., Wiggs, G.F., Mamedov, B., Davidson, G., Hubbard, R.B., 2000. Exposure to airborne dust contaminated with pesticide in the Aral Sea region. *Lancet* 355, 627–8. [https://doi.org/10.1016/S0140-6736\(99\)04753-4](https://doi.org/10.1016/S0140-6736(99)04753-4)
- Ohde, T., Siegel, H., 2012. Impacts of Saharan dust and clouds on photosynthetically available radiation in the area off Northwest Africa. *Tellus Ser. B-Chem. Phys. Meteorol.* 64, 17160. <https://doi.org/ARTN 17160 10.3402/tellusb.v64i0.17160>
- Okin, G.S., Mahowald, N., Chadwick, O.A., Artaxo, P., 2004. Impact of desert dust on the biogeochemistry of phosphorus in terrestrial ecosystems. *Glob. Biogeochem. Cycles* 18. <https://doi.org/Artn Gb2005 10.1029/2003gb002145>
- Opp, C., Groll, M., Aslanov, I., Lotz, T., Vereshagina, N., 2017. Aeolian dust deposition in the southern Aral Sea region (Uzbekistan): Ground-based monitoring results from the LUCA project. *Quat. Int.* 429, 86–99. <https://doi.org/10.1016/j.quaint.2015.12.103>
- Peel, M.C., Finlayson, B.L., McMahon, T.A., 2007. Updated world map of the Köppen-Geiger climate classification. *Hydrol. Earth Syst. Sci. Discuss.* 4, 439–473.
- Popov, V.A., 1998. The Role of Salt Migration in Landscape Genesis of the Cis-Aral region.
- Prospero, J.M., Ginoux, P., Torres, O., Nicholson, S.E., Gill, T.E., 2002. Environmental characterization of global sources of atmospheric soil dust identified with the Nimbus 7 Total Ozone Mapping Spectrometer (TOMS) absorbing aerosol product. *Rev. Geophys.* 40, 2–1. <https://doi.org/10.1029/2000RG000095>
- Pye, K., 1995. The nature, origin and accumulation of loess. *Quat. Sci. Rev.* 14, 653–667. [https://doi.org/Doi 10.1016/0277-3791\(95\)00047-X](https://doi.org/Doi 10.1016/0277-3791(95)00047-X)
- Ramanathan, V., Chung, C., Kim, D., Bettge, T., Buja, L., Kiehl, J.T., Washington, W.M., Fu, Q., Sikka, D.R., Wild, M., 2005. Atmospheric brown clouds: impacts on South Asian climate and hydrological cycle. *Proc Natl Acad Sci U A* 102, 5326–33. <https://doi.org/10.1073/pnas.0500656102>
- Razakov, R., Kosnazarov, K., 1996. Dust and salt transfer from the exposed bed of the Aral Sea and measures to decrease its environmental impact, in: *The Aral Sea Basin*. Springer, pp. 95–102.
- Reynolds, R., Belnap, J., Reheis, M., Lamothe, P., Luiszer, F., 2001. Aeolian dust in Colorado Plateau soils: nutrient inputs and recent change in source. *Proc Natl Acad Sci U A* 98, 7123–7. <https://doi.org/10.1073/pnas.121094298>
- Rezazadeh, M., Irannejad, P., Shao, Y., 2013. Climatology of the Middle East dust events. *Aeolian Res.* 10, 103–109. <https://doi.org/10.1016/j.aeolia.2013.04.001>
- Roberts, H.M., 2008. The development and application of luminescence dating to loess deposits: a perspective on the past, present and future. *Boreas* 37, 483–507. <https://doi.org/10.1111/j.1502-3885.2008.00057.x>
- Salvador, P., Artíñano, B., Viana, M.M., Querol, X., Alastuey, A., González-Fernández, I., Alonso, R., 2011. Spatial and temporal variations in PM₁₀ and PM_{2.5} across Madrid metropolitan area in 1999–2008. *Procedia Environ. Sci.* 4, 198–208.
- Schaap, M., Apituley, A., Timmermans, R., Koelemeijer, R., Leeuw, G. de, 2009. Exploring the relation between aerosol optical depth and PM_{2.5} at Cabauw, the Netherlands. *Atmospheric Chem. Phys.* 9, 909–925.
- Sharifi, A., Pourmand, A., Canuel, E.A., Ferer-Tyler, E., Peterson, L.C., Aichner, B., Feakins, S.J., Daryaei, T., Djamali, M., Beni, A.N., Lahijani, H.A.K., Swart, P.K., 2015. Abrupt climate variability since the last deglaciation based on a high-resolution, multi-proxy peat record from NW Iran: The hand that rocked the Cradle of Civilization? *Quat. Sci. Rev.* 123, 215–230. <https://doi.org/10.1016/j.quascirev.2015.07.006>
- Sleewaegen, S., Lorrain, R., Offer, Z., Azmon, E., Fitzsimons, S., Souchez, R., 2002. Trapping of aeolian sediments and build-up of the ice cover of a dry-based Antarctic lake. *Earth Surf. Process. Landf.* 27, 307–315.
- Sokolik, I.N., Winker, D.M., Bergametti, G., Gillette, D.A., Carmichael, G., Kaufman, Y.J., Gomes, L., Schuetz, L., Penner, J.E., 2001. Introduction to special section: Outstanding problems in quantifying the radiative impacts of mineral dust. *J. Geophys. Res.-Atmospheres* 106, 18015–18027. <https://doi.org/Doi 10.1029/2000jd900498>
- Song, C.H., Park, M.E., Lee, K.H., Ahn, H.J., Lee, Y., Kim, J.Y., Han, K.M., Kim, J., Ghim, Y.S., Kim, Y.J., 2008. An investigation into seasonal and regional aerosol characteristics in East Asia using model-predicted and remotely-sensed aerosol properties 8, 8661. <http://dx.doi.org/10.5194/acpd-8-8661-2008>

- Sorooshian, S., AghaKouchak, A., Arkin, P., Eylander, J., Foufoula-Georgiou, E., Harmon, R., Hendrickx, J.M., Imam, B., Kuligowski, R., Skahill, B., 2011. Advanced concepts on remote sensing of precipitation at multiple scales. *Bull. Am. Meteorol. Soc.* 92, 1353–1357.
- Stefanski, R., Sivakumar, M., 2009. Impacts of sand and dust storms on agriculture and potential agricultural applications of a SDSWS. Presented at the IOP Conference Series: Earth and Environmental Science, IOP Publishing, p. 012016.
- Stone, R., 1999. Coming to Grips With the Aral Sea's Grim Legacy. *Science* 284, 30–33. <https://doi.org/10.1126/science.284.5411.30>
- Swap, R., Garstang, M., Greco, S., Talbot, R., Kallberg, P., 1992. Saharan Dust in the Amazon Basin. *Tellus B* 44, 133–149. [https://doi.org/DOI 10.1034/j.1600-0889.1992.t01-1-00005.x](https://doi.org/DOI%2010.1034/j.1600-0889.1992.t01-1-00005.x)
- Taheri Shahraini, H., Karimi, K., Habibi Nokhandan, M., Hafezi Moghadas, N., 2015. Monitoring of dust storm and estimation of aerosol concentration in the Middle East using remotely sensed images. *Arab. J. Geosci.* 8, 2095–2110. <https://doi.org/10.1007/s12517-013-1252-3>
- Tegen, I., Hollrig, P., Chin, M., Fung, I., Jacob, D., Penner, J., 1997. Contribution of different aerosol species to the global aerosol extinction optical thickness: Estimates from model results. *J. Geophys. Res. Atmospheres* 102, 23895–23915. <https://doi.org/10.1029/97JD01864>
- Tegen, I., Lacis, A.A., 1996. Modeling of particle size distribution and its influence on the radiative properties of mineral dust aerosol. *J. Geophys. Res.-Atmospheres* 101, 19237–19244. [https://doi.org/Doi 10.1029/95jd03610](https://doi.org/Doi%2010.1029/95jd03610)
- Tegen, I., Werner, M., Harrison, S., Kohfeld, K., 2004. Relative importance of climate and land use in determining present and future global soil dust emission. *Geophys. Res. Lett.* 31.
- Thomson, M.C., Molesworth, A.M., Djingarey, M.H., Yameogo, K.R., Belanger, F., Cuevas, L.E., 2006. Potential of environmental models to predict meningitis epidemics in Africa. *Trop Med Int Health* 11, 781–8. <https://doi.org/10.1111/j.1365-3156.2006.01630.x>
- Wang, S., Yuan, W., Shang, K., 2006. The impacts of different kinds of dust events on PM 10 pollution in northern China. *Atmos. Environ.* 40, 7975–7982.
- Wang, X., Sato, T., Xing, B., 2006. Size distribution and anthropogenic sources apportionment of airborne trace metals in Kanazawa, Japan. *Chemosphere* 65, 2440–8. <https://doi.org/10.1016/j.chemosphere.2006.04.050>
- Wiggs, G.F.S., O'Hara, S.L., Wegerdt, J., Van der Meer, J., Small, I., Hubbard, R., 2003. The dynamics and characteristics of aeolian dust in dryland Central Asia: possible impacts on human exposure and respiratory health in the Aral Sea basin. *Geogr. J.* 169, 142–157. [https://doi.org/Doi 10.1111/1475-4959.04976](https://doi.org/Doi%2010.1111/1475-4959.04976)
- Wilkinson, M.J., 2014. The Persian Gulf, Clear and Clouded. Johnson Space Center.
- Yongming, H., Peixuan, D., Junji, C., Posmentier, E.S., 2006. Multivariate analysis of heavy metal contamination in urban dusts of Xi'an, Central China. *Sci Total Env.* 355, 176–86. <https://doi.org/10.1016/j.scitotenv.2005.02.026>
- Yu, H., Dickinson, R.E., Chin, M., Kaufman, Y.J., Holben, B.N., Geogdzhayev, I.V., Mishchenko, M.I., 2003. Annual cycle of global distributions of aerosol optical depth from integration of MODIS retrievals and GOCART model simulations. *J. Geophys. Res. Atmospheres* 108. <https://doi.org/10.1029/2002JD002717>
- Yu, X., Lü, R., Kumar, K.R., Ma, J., Zhang, Q., Jiang, Y., Kang, N., Yang, S., Wang, J., Li, M., 2016. Dust aerosol properties and radiative forcing observed in spring during 2001–2014 over urban Beijing, China. *Environ. Sci. Pollut. Res.* 23, 15432–15442. <https://doi.org/10.1007/s11356-016-6727-9>

2. Research Approach

2.1 Introduction

Iran consists of a complex plain and hilly terrain located in Western Asia, between the Oman sea and the Persian Gulf in the south and the Caspian sea in the north. Regions with frequent dust events were found in southwestern Iran over the northern tip of the Persian Gulf and in western Iran. This region is strongly affected by dust storms blown from huge deserts of Iraq, Saudi Arabia, and Syria every year, especially during the hot season (Alizadeh-Choobari et al., 2016). The dust belt (Fig. 2.1) stretches from the Sahara desert in Africa to the Gobi desert in Central and East Asia (Hofer et al., 2017). Comparatively, southwestern Iran is being recognized as one of the global hotspots of aeolian dust (Shen et al., 2016; Taghavi et al., 2017). In like manner aeolian dust is a very common phenomenon and reaches annual mean concentrations of 50-100 $\mu\text{g}/\text{m}^3$ (Wilkinson, 2014; Global Ambient Air Pollution, 2018).

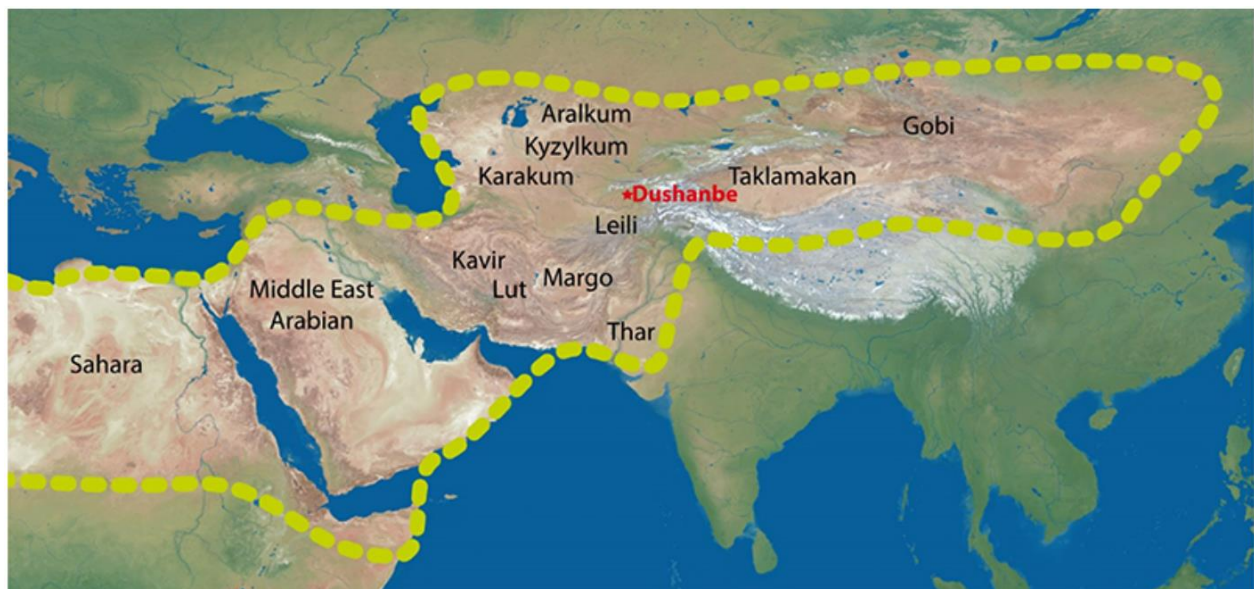


Figure 2.1 The dust belt (enclosed by yellow dashes)

*Stretches from the Sahara desert in Africa to the Gobi desert in central and East Asia. Credit: Adapted from (Hofer et al., 2017)

2.2 Study area

With two major mountains ranges in the north, oriented from west to east [Alborz], and one mountain range stretching from northwest to the south [Zagros], Iran occupies a broad latitudinal range (Fig. 2.2) and diverse geographic setting in the north and west

Airborne dusts travel daily through dust belt conquered southern and southwestern Iran (Zarasvandi et al., 2011; Ghasem et al., 2012; Almasi et al., 2014; Najafi et al., 2014). From summer to cold seasons denote that some areas (Taghavi & Asadi, 2008). Western Iran, is much more prone to dust storms than other areas. Therefore, this area was considered to design sampling sites located between 45° 30' 00" to 49° 30' 00" E and 30° 00' 00" to 35° 00' 00" N in southwest of Iran, covering an area of about 117,000 km² (Statistical Center of Iran, 2018). From south to north, it includes the provinces of

Khuzestan, Lorestan, and Kermanshah. Thus, the area of study is characterized by mountainous in the north and east, the plain and marshland to its south. The altitude ranges from sea level in the southern part to 900 m in the north and to 4,000 m above sea level (a.s.l.) in the east.

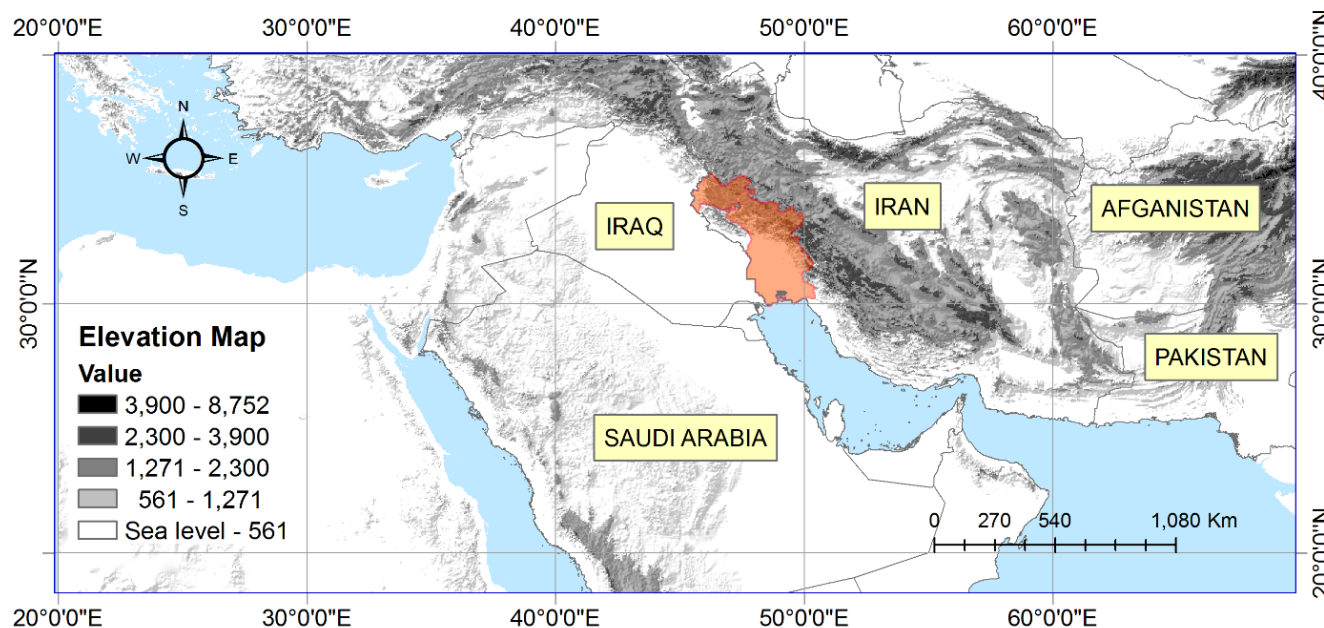


Figure 2.2 Map of the study area latitude, longitude and elevation

*Oranged part is related to the area of study. The reproduced courtesy of the U.S. Geological Survey data explorer.

The study area covers 8.43% of Iran and is located in cold and hot desert climates (Peel et al., 2007). The provinces of Khuzestan, Lorestan, and Kermanshah are 64,000, 28,392, and 24,998 km² in area, respectively (Statoids, 2016). In that order, they also play an important role in the country's economy, as they are ranked 2nd, 26th and 21st in Gross Domestic Product (GDP) among Iran's provinces (MCLSW 2015). The censuses indicate that the population of Khuzestan, Lorestan, and Kermanshah are 4.7, 1.9, and 1.74 million, for a total of 8.34 million (Statistical Center of Iran, 2018). The area's geographic bases information, meteorological data, and climate map adjacent to selecting point will be presented in the following chapter.

2.2.1 Land Use Land Cover (LULC)

The land cover condition in this study was attempted to provide information on the recent LULC pattern of research area were classified each gauge center with respect to Land Use / Cover Area frame Statistical Survey (LUCAS). Additionally, the subject conjointly encompasses research area underneath the foremost five classifications including artificial (6.5%) and industrial (0.05%), wet land (4.5%), vegetation (27%), and bare-land (61%).

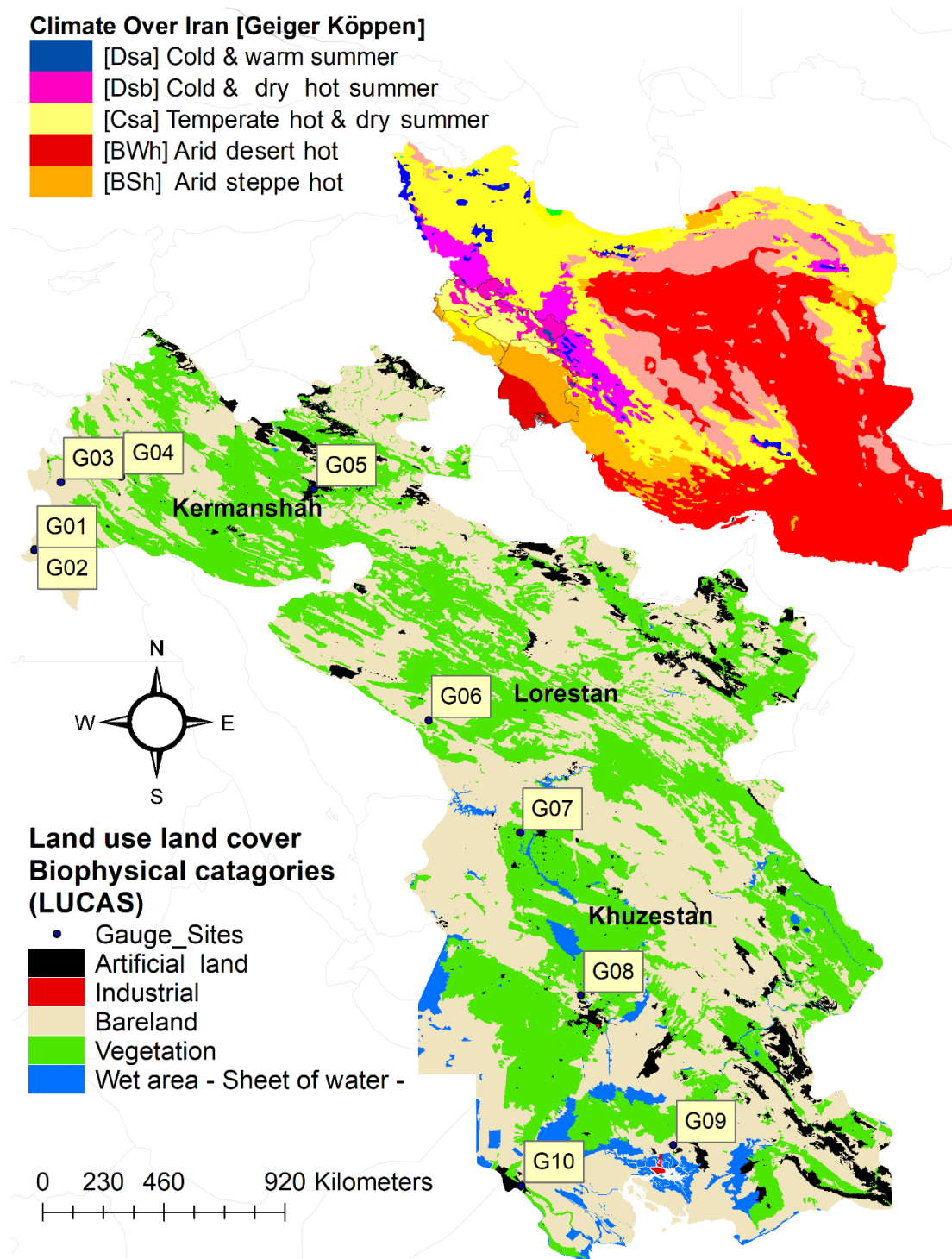


Figure 2.3 Mapping climate and LULC on the gauge site distribution

*A given circle centered (with a radius of 10 km) at each gauge site (G01–G10) represents the spatial pattern of the LULC. This analysis represents the whole area with respect to each sampler at the gauge site.

*The climate map upright: shows climate classification of Iran (Peel et al., 2007). The image retrieved from the Landsat satellite summer 2012 retrieved from The United States Geological Survey (USGS) Earth Explorer, and unsupervised classification using ArcMap. The software finds the spectral classes in the multi-band image (B1-B7) without the analysis intervention. Once the operation done, what the cluster represents (e.g., wet area, bare-land, vegetation, etc.) are discriminated. The classification represents the real world was carried out to determine the quality of information by the means of random sampling method of observation in 10 km circle of given radius

2.2.2 Climate

The climate of the study area varies from a cold and warm summer to an extremely hot zone located between the international boarder in the west, Zagros Mountains in the east and the northern coast of the Persian Gulf in the south. As is shown in the map (Fig. 2.3), following the suggestion of Russell, (1931) in Tab. 2.1, the Geiger and Köppen climate classification scheme was used, with three letters representing world climates divided into five main climate groups at a 1 km resolution (Peel et al., 2007). The study area was classified on the basis of standard zone properties which was also used by previous researchers (Peel et al., 2007; Kriticos et al., 2012; Buchard et al., 2017). This standard is defined in the Köppen climate classification scheme (Tab. 2.1), with three letters representing the world climates divided into five main climate groups at a 1 km resolution. These main groups are as follows: A (tropical), B (dry), C (temperate), D (continental or cold climate) and E (polar). The second letter indicates the seasonal precipitation type for steppe (S) and desert (W). Alternately, (f), (m), (w), and (s) represent rain force, monsoon, savanna-wet and savanna-dry, respectively, while the third letter indicates the level of heat, with cold as (k) and hot as (h). In general, a, b, c, and d represent hot summer (a), warm summer (b), cold summer (c), and very cold winter (d) climates.

Table 2.1 Climate classification scheme of the study area

Type	Description	Criterion
B	Arid climate	$P_{ann} < 10 \text{ Pth}$
BS	Arid steppe climate	$P_{ann} > 05 \text{ Pth}$
BW	Arid desert climate	$P_{ann} \leq 5 \text{ Pth}$
C	Warm temperate climate	$-3 \text{ C} < T_{min} < +18 \text{ C}$
Cs	Warm temperate climate, with dry summer	$P_{smin} < P_{wmin}, P_{wmax} > 2 \text{ P}_{smin}$ and $P_{smin} < 40\text{mm}$
Cw	Warm temperate climate, with dry winter	$P_{wmin} < P_{smin}$ and $P_{smax} > 10 \text{ P}_{wmin}$
Cf	Warm temperate climate, fully humid	Neither Cs nor Cw
D	Snow climate	$T_{min} \leq -3\text{C}$
Ds	Snow climate, with dry summer	$P_{smin} < P_{wmin}, P_{wmax} > 3P_{smin}$ and $P_{smin} < 40\text{mm}$
Dw	Snow climate, with dry winter	$P_{wmin} < P_{smin}$ and $P_{smax} > 10 \text{ P}_{wmin}$
Df	Snow climate, with fully humid	Neither Ds nor Dw

Climate of the study areas were classified using the Köppen climate classification scheme (Kriticos et al., 2012) by those three letters represented worlds climates into five main climate groups at 1km resolution (Peel et al., 2007)

As shown in Fig. 2.3, the study area is categorized into three main climate zones. The arid desert hot [BWh] in the southern region of the northern coastal plains of the Persian Gulf covers the locations of G08, G09, and G10 between the latitudes of 30 N and 31N. An arid steppe hot zone [BSh] in the western areas is indicated over the locations of G01, G02, and G07, which are located in 34N and 32N. The temperate hot summer zone [Csa] is located between 33 N and 34N from the extreme western region G04 and G05 and reaches G06. Again, [BWh] climate zone is plain marshland and coastal plains, [Csa] is a typical complex terrain between high mountains in the east from the north to the south. [BSh] climate however is an open flat terrain area which is connected to complex terrain at the east.

2.2.3 Meteorological setting

Wind, precipitation and temperature characteristics are very important for determining the synoptic conditions responsible for the dust deposition rate. Maximum, minimum, and average temperature were calculated for all climate zones. Figure 2.5 illustrates the average interannual monthly temperature of three climate zones – [BWh], [BSh], and [Csa]. The data compares how the temperature in these three climate zones changes throughout the study period.

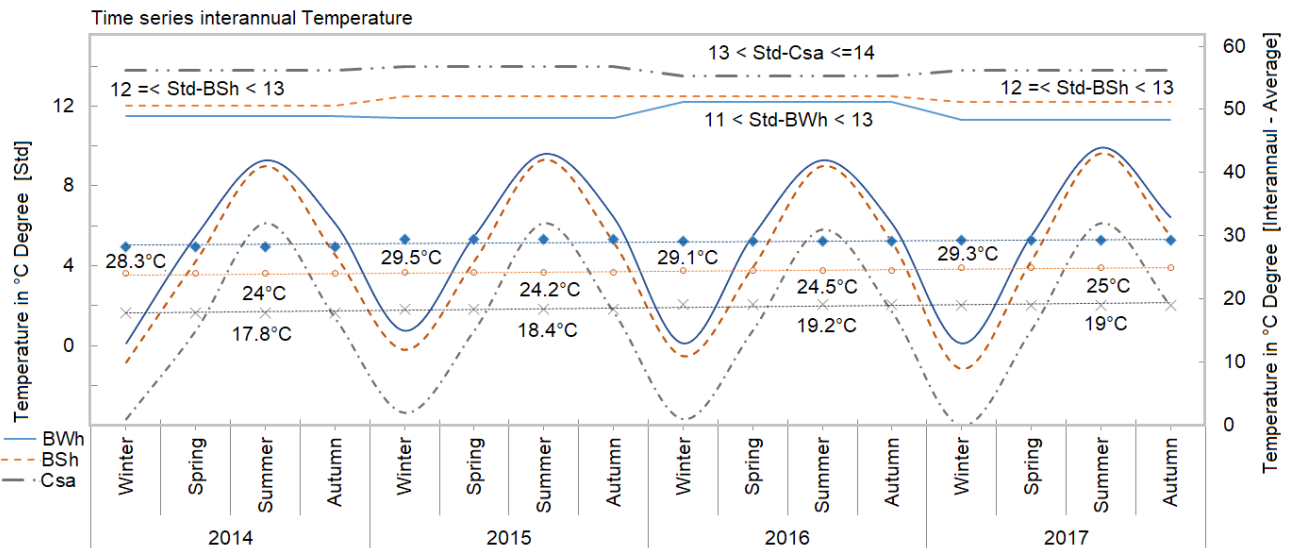


Figure 2.4 Time series interannual temperature obtained from study area

*Represented Std (The standard deviation) which is a measure variation or dispersion of the temperature. The reproduced courtesy of the Iranian Meteorological Organization.

Each of the three climate zones has a maximum average (mean) of [BWh-29.5°C, 2015], [BSh-25°C, 2017], and [Csa-19.2°C, 2016] while the average minimum temperature has remained for desert-hot [BWh-28.3°C], steppe-hot [BSh-24°C], and temperate-hot-summer [Csa-17.8°C] in 2014. The line also demonstrates standard deviation data. A fluctuating trend with the highest Std has recorded for the temperate-hot-summer zone [$13 < \text{Csa} < 14$] degree in Celsius. Besides, for the steppe-hot zone, it remains between 12°C and 13°C. In the given time frame, the desert-hot zone has smaller standard deviation than the other two with dispersion value of [$11 < \text{BWh} < 13$] degree in Celsius far from the average. As the illustration shows (Fig. 2.5), precipitation and average temperature in the three climate zones were calculated for the study period from 2014 to 2017. The seasonal distribution of the precipitation data shows that the highest amounts of rainfall are detected during winter and spring, while the summer months are received hardly any precipitation.

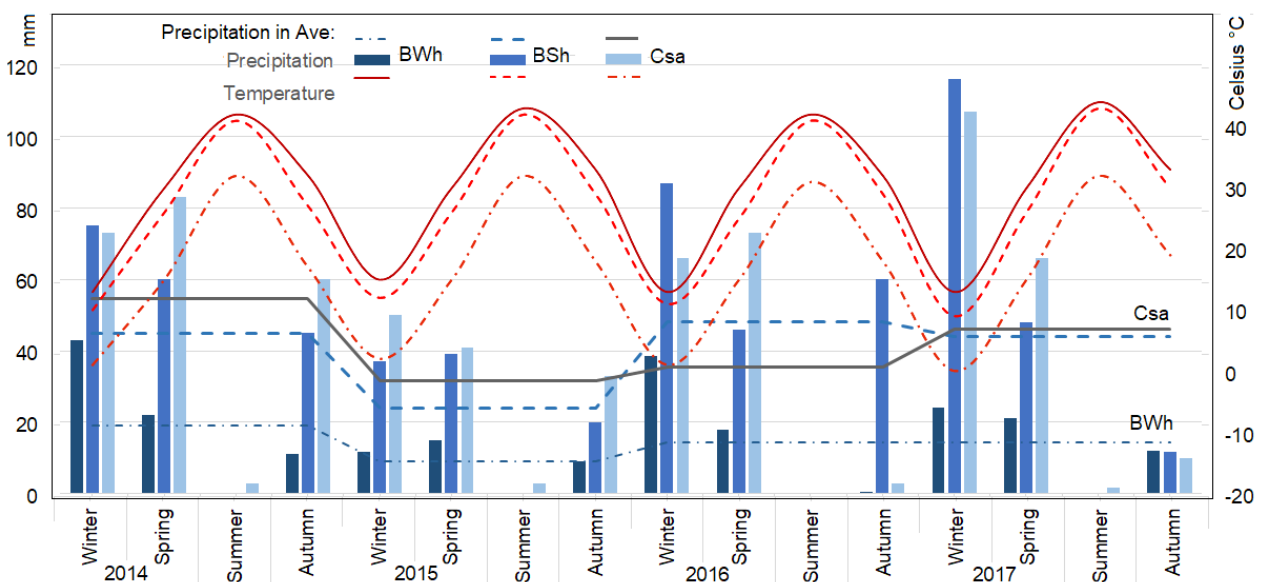


Figure 2.5 Interannual average temperature and monthly precipitation

Plot presented 4 years precipitation and temperature over three climate zones (BWh, BSh, and Csa). The reproduced courtesy of the Iranian Meteorological Organization.

Significantly, an average annual precipitation (mm/year) in hot desert climate [BWh] was between 107 mm in 2015 and 228 mm in 2014. The precipitation in the hot steppe area [BSh] was considerably higher and ranged typically around 540 mm per year, with 2015 being the exception with an average precipitation of only 228 (mm/year). Equally, the warm temperate climate zone (savanna area), [Csa] followed the same trend with a well-below average precipitation in 2015 (381 mm), while 2014 was the wettest year with 667 mm of rainfall. This temporal pattern was also detected by NOAA researchers (Lenssen et al., 2019), with 2015 being the warmest year on record for Asia and South America and a global temperature deviation of 0.90°C above average for the period 1901-2000. New monthly records were set in 2015 for each month except for January and April (Young et al., 2018).

Equally important, the summer of 2015 was the driest season of the time period 1901-2015 in central Europe (Lee et al., 2018). In monsoon influenced regions, on the other hand, more extreme precipitation events related to the temperature anomaly were recorded (Orth et al., 2016).

Recently, the global total precipitation from January 2015 to December 2018 were compared to the data from 1951 to 2010 (Alexander et al., 2019; WMO, 2019). The region eastward of the Persian Gulf (including the study area) was, among other regions (North America, northern South America, Europe, north-east Australia, southern and south-west Africa), characterized by a significant negative precipitation anomaly during recent years. In given time, although this result is indicating non-linear scale of corresponding between precipitation and temperature, clearly is revealed a negative correlation between the summer precipitation and the air temperature.

The wind characteristics are another highly important synoptic parameter, which heavily influences both the temporal distribution and intensity of dust events and dust deposition rates. It just as the precipitation and temperature data there is clear distinctions between the three climate zones.

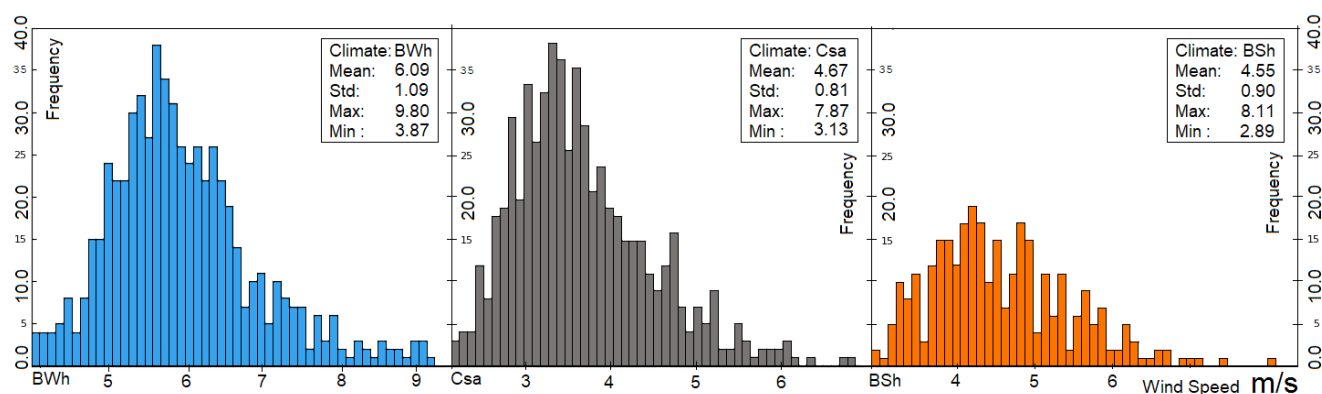


Figure 2.6 Histogram of the wind speed in m/s, monthly averages for 2014-2017

The histograms (Fig. 2.6) show the frequency of the average monthly wind speeds relative to data across all four years of observations. The overall mean wind speed (m/s) for [BWh] was 6.09 m/s, 4.55 m/s for [BSh], and 4.67 m/s for [Csa]. The data distribution is clearly skewed towards lower wind speeds, which means that the most frequent wind speeds are below the mean values. The standard deviation (Std) of the wind speed variation is representative of the unsteadiness of the wind speeds in [BWh], [BSh], and [Csa] which is marked by 1.09, 0.90, and 0.81 m/s, respectively.

According to the directional seasonal wind speed displayed in Fig. 2.7, the eastward and southward winds were characterized by maximum velocities of 4 and 3 m/s in [BWh] summer respectively. If read in fluctuation with the wind speed, it can be seen where the speed of the wind dropped to about 0.2 m/s in [BSh] and fading back towards west in [Csa]. The drop and rise in wind speed are also indicated on the northward wind records.

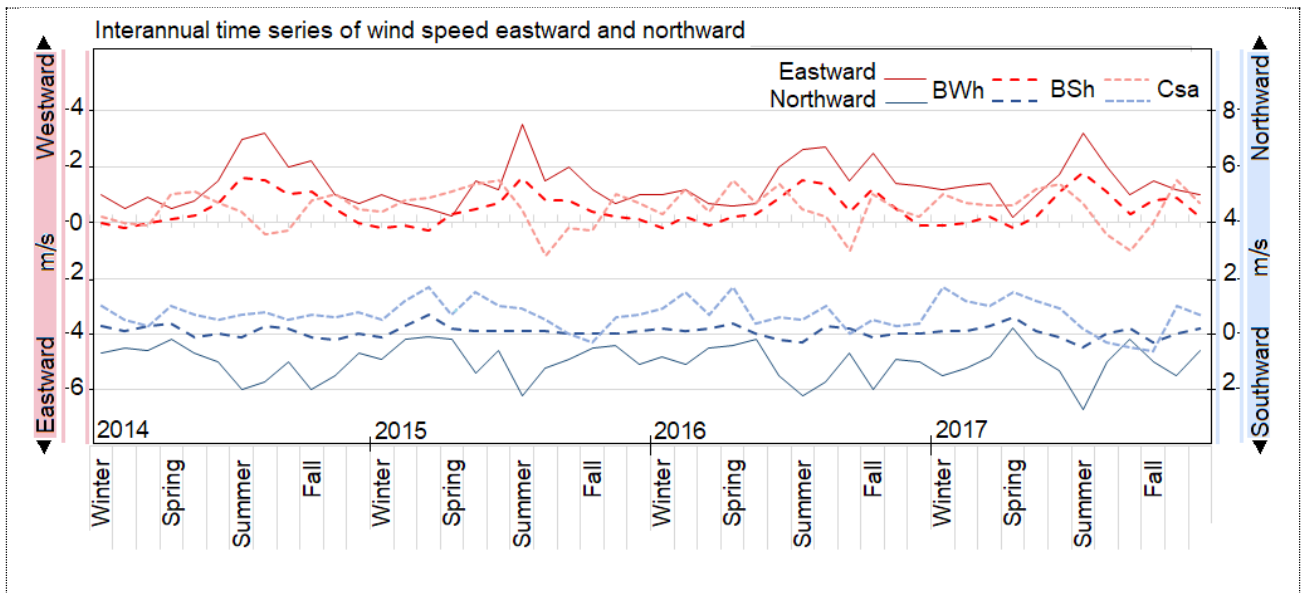


Figure 2.7 Interannual time series of predominate wind speeds in eastward and northward directions

According to the seasonal wind speed in Figure 2.7, westward winds showed a similar seasonal variation pattern in two of the three climate zones (excluding [Csa]), with maximum wind speeds ([BWh] 3.5 m/s, [BSh] 1.8 m/s) during summer and minima during winter and spring. The [Csa] climate, however, was characterized by maximum eastward wind speeds of 1.2 m/s in summer and minima in spring and winter. The Northward wind speed over [Csa] further show a bimodal seasonal variation with two maxima, one during spring and the other during the winter period, while the minima were recorded in fall and summer. Southward wind speeds, in contrast, revealed a complex temporal dynamic with double peaks during spring and summer of 2015 and 2016 and during summer and fall of 2014. During the summer period in 2017, however, an unimodal seasonal variation with one maxima was detected. In order to further illustrate the seasonal differences within and between the three climate zones, seasonal wind roses were designed, using the frequency of different wind speed as a percentage of total winds (Fig. 2.8).

The predominant seasonal wind directions in [BWh] are along the NW axis during all seasons, with average frequencies of 54% (winter), 52% (spring), 50% (summer), and 34% (fall). During summer and fall, southern and southeastern wind directions increased in importance with shares of up to 25%. The average seasonal wind speed (m/s) in [BWh] was lowest during fall (2.0) and winter (2.3) and highest during spring (2.9) and summer (3.0).

In all season, the dominant wind direction in climate zone [Csa] was SE, with an average frequency of 40%, 40%, 39%, and 35% in winter, spring, summer and fall, respectively. Calms and events with no discernable wind direction were relevant in all seasons, with frequencies 18.5% (winter), 18.5% (spring), 9.7% (summer), and 31.8% (fall). The wind rose plots for [Csa] illustrate that the average seasonal wind speed (m/s) were lowest during fall (1.8) and highest (2.5) during spring and summer, followed by winter with 2.3 m/s.

The predominant seasonal wind direction over [BSh] are along the SE axis as well, with frequencies of 52% in fall, and 40% in winter. The most frequent single wind directions, however, were detected during spring (E, 22.5% & W, 20%), and summer (WNW, 50% & NW, 10%). The average wind speed (m/s) was 1.9 during fall, 2.0 in winter, 2.3 in spring, and 3.4 during summer. Calms and events with no discernable wind direction were recorded in all seasons with frequencies of 22.2% (winter), 26.4% (spring), 10% (summer), and 28.9% (fall).



2 - 4
 4 - 6
 6 - 8
 8 - 10
 10 - 12
 12+

Wind Speed [meter / second]
 Calm Values are less than 2.0 m/s
Arrows indicate wind direction

Figure 2.8 The seasonal wind-rose for [Bwh] [Csa], and [BSh]
 Wind-rose plot illustrates the percentage of time that winds blows from particular direction at certain speed.

Statistical comparisons of the mean deposition rate in each season were performed with meteorological functions. Additionally, the high correlation values with statistically significant differences may potentially provide valuable and timely evidence for the discussion on this topic.

2.2.4 Dust event history

The MERRA-II model application data were downloaded and prepared according to the study area coordinate system. To see the time series of the monthly deposition rate against the seasonal variation, the values from MERRA-II were obtained by using statistical calculations. Figure 2.9 illustrates the monthly and annual averaged deposition rates. The maximum deposition rates were observed in spring and summer while the minimums were observed in autumn and winter. In particular, the area average dust deposition rate (in t/km^2) in [BWh] fluctuated between 4.86 and 5.61. Comparatively in the steppe-hot climate [BSh], the year-to-year deposition rate varied from 2.96 to 3.78 on average. The temperate-hot-summer zone [Csa] was characterized by an average deposition rate of less than $2.05 (t/km^2)$, or less than 50% of the deposition rate in the hot-desert zone. An important feature of the seasonal variation patterns over all climate is that terrains follows the same seasonality but different deposition rates.

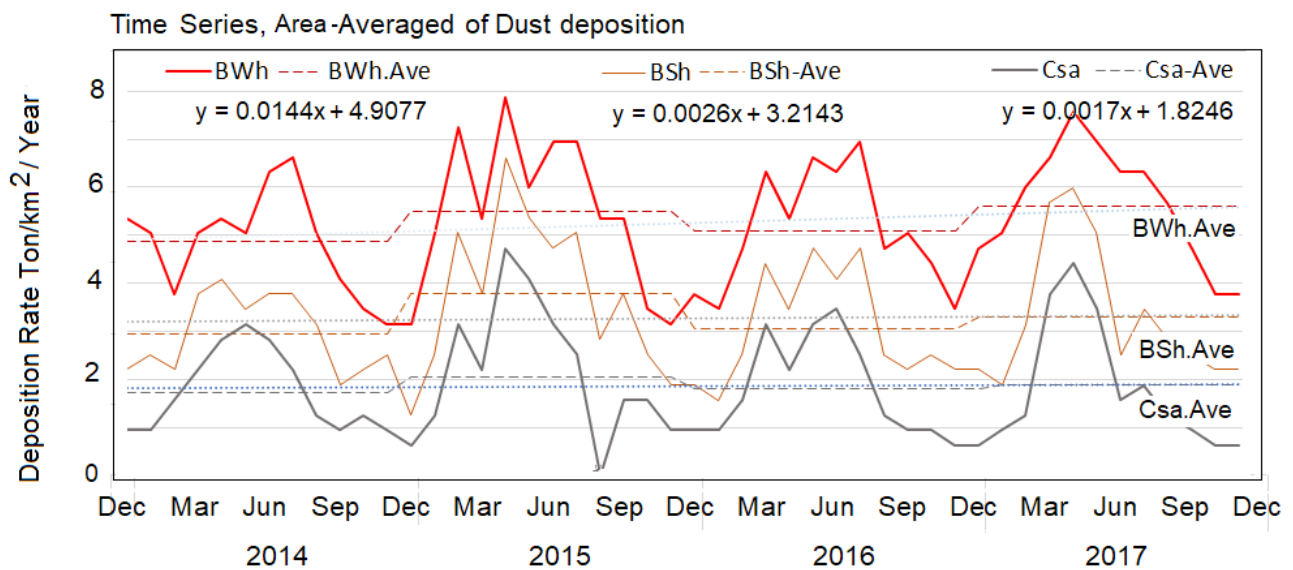


Figure 2.9 Monthly averages deposition rate. MERRA II model M2TMNXAD4- V5.12.4

In fact, the trends of the ground observation rates (GDR) and MERRA II-output agree well with seasonal dust distribution. Both results are provided the same summer maximum deposition rate factor that is consistent with variation in climates pattern. In addition, the study showed that the meteorological factor is associated with the impact of aeolian dust deposition. The large-scale precipitation over land in cold seasons (fall and winter) are provided less deposition rates.

That is to say, the climate variability are closely connected to the deposition rate (Dawson et al., 2014; Feng et al., 2016) and strongly governed by meteorological factors (Duce et al., 1980; Jouzel et al., 1996; AO, 2001; Huang et al., 2011; Goudie, 2014). The connection between the dynamic of the climate factors and the dust deposition rate will be discussed in the next section.

2.3 Summary

As a part of climate, particularly in dry periods, dust events have modified environment and impacted civilizations and currently suffer from dust emissions (Roberts et al., 2011; Albani et al., 2015; Sharifi et al., 2015). For instance the elemental composition of soil surfaces is influenced by aeolian dust transport as well as precipitation, wind speed and direction. Long-term remote sensing observations indicate that the principal directions of dust is from west to east (Modaihsh, 1997; Rifaat et al., 2007). In the last decade, in the southwestern and western provinces of Iran many settlements have been affected (Akbari, 2011; Esmaili et al., 2006; Rifaat et al., 2007; Gerivani et al., 2011). Therefore, the study area is one of the few convenient regions for the research of the aeolian deposition based on geographical setting and due to GDR of aeolian dust during 2000-2014. The illustration (Fig. 2.10) shows represent zonal mean of the dust deposition rate over the area of the northwest to the southeast.

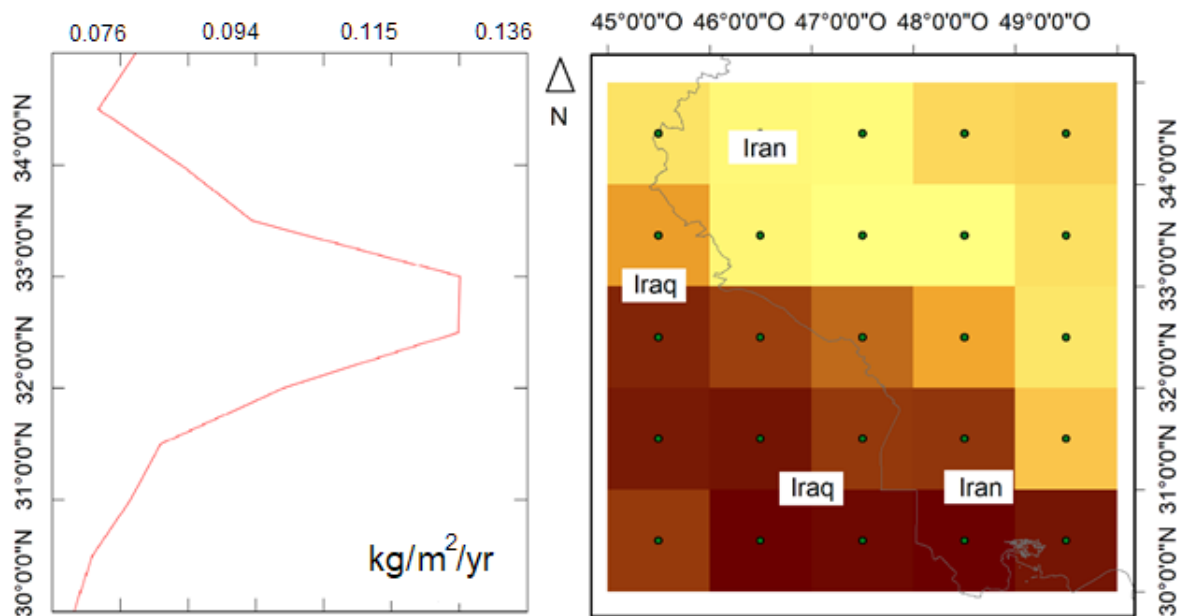


Figure 2.10 Zonal mean of dust deposition rate resolution 0.5 degree left and 1.0-Degree right

* Dust concentrations from west to east shows a dominant direction of dust movement. Moreover, zonal means of the dust deposition rate simulated and observed (red line-left), including GDR and concentrations (dark and light squares-right). In the left side X-axes, denote rates of simulated dust concentrations and Y-axes, represents maximum zonal mean rate (latitude) of the deposition and the concentration occurred from 31N to 33N

2.4 Conclusion

The research setting was suggested that the deposition in the study area was characterized mainly by dust blowing predominantly from the west, south and southwest (Fig. 2.10). Local and regional meteorological data, in addition to the results of relevant investigations, will support spatial deposition, flow and directions. Based on core data, it is possible to argue about the intensity of dust and state of event in the last century. In this research significantly focus is put on the systematically monitoring the GDR. Although monitoring dust concentration and the study about the dust load undoubtedly are an essential part, GDR may indicate correlations among aeolian dust processes, climate factors, and the geographical setting. Thus, in the next chapter the methodology and the setting data collection are highlighted.

References

- Akbari, S. (2011). Dust storms, sources in the Middle East and economic model for survey its impacts. *Australian Journal of Basic and Applied Sciences*, 5(12), 227–233.
- Albani, S., Mahowald, N. M., Winckler, G., Anderson, R. F., Bradtmiller, L. I., Delmonte, B., Francois, R., Goman, M., Heavens, N. G., Hesse, P. P., Hovan, S. A., Kang, S. G., Kohfeld, K. E., Lu, H., Maggi, V., Mason, J. A., Mayewski, P. A., McGee, D., Miao, X., ... Sun, J. (2015). Twelve thousand years of dust: The Holocene global dust cycle constrained by natural archives. *Climate of the Past*, 11(6), 869–903. <https://doi.org/10.5194/cp-11-869-2015>
- Alexander, L. V., Fowler, H. J., Bador, M., Behrangi, A., Donat, M. G., Dunn, R., Funk, C., Goldie, J., Lewis, E., & Rogé, M. (2019). On the use of indices to study extreme precipitation on sub-daily and daily timescales. *Environmental Research Letters*, 14(12), 125008.
- Alizadeh-Choobari, O., Ghafarian, P., & Owlad, E. (2016). Temporal variations in the frequency and concentration of dust events over Iran based on surface observations. *International Journal of Climatology*, 36(4), 2050–2062. <https://doi.org/10.1002/joc.4479>
- Almasi, A., Mousavi, A. R., Bakhshi, S., & Namdari, F. (2014). Dust storms and environmental health impacts. *Journal of Middle East Applied Science and Technology*, 8, 353–356.
- AO, J. W. Z. (2001). The IPCC Third Assessment Report on the Scientific Basis of Climate Change. *Australian Journal of Environmental Management*, 8(3), 169–185. <https://doi.org/10.1080/14486563.2001.10648526>
- Buchard, V., Randles, C. A., da Silva, A. M., Darmenov, A., Colarco, P. R., Govindaraju, R., Ferrare, R., Hair, J., Beyersdorf, A. J., Ziemba, L. D., & Yu, H. (2017). The MERRA-2 Aerosol Reanalysis, 1980 Onward. Part II: Evaluation and Case Studies. *Journal of Climate*, 30(17), 6851–6872. <https://doi.org/10.1175/Jcli-D-16-0613.1>
- Dawson, J. P., Bloomer, B. J., Winner, D. A., & Weaver, C. P. (2014). Understanding the Meteorological Drivers of Us Particulate Matter Concentrations in a Changing Climate. *Bulletin of the American Meteorological Society*, 95(4), 520–532. <https://doi.org/10.1175/Bams-D-12-00181.1>
- Duce, R. A., Unni, C. K., Ray, B. J., Prospero, J. M., & Merrill, J. T. (1980). Long-range atmospheric transport of soil dust from Asia to the tropical north pacific: Temporal variability. *Science*, 209(4464), 1522–1524. <https://doi.org/10.1126/science.209.4464.1522>
- Esmaili, O., Tajrishy, M., & Arasteh, P. D. (2006). Results of the 50 year ground-based measurements in comparison with satellite remote sensing of two prominent dust emission sources located in Iran. 6362, 636209.
- Feng, J., Liao, H., & Li, J. (2016). The impact of monthly variation of the Pacific–North America (PNA) teleconnection pattern on wintertime surface-layer aerosol concentrations in the United States. *Atmospheric Chemistry and Physics*, 16(8), 4927.
- Gerivani, H., Lashkaripour, G. R., Ghafoori, M., & Jalali, N. (2011). The Source of Dust Storm in Iran: A Case Study Based on Geological Information and Rainfall Data. *Carpathian Journal of Earth and Environmental Sciences*, 6(1), 297–308.
- Ghasem, A., Shamsipour, A., Miri, M., & Safarrad, T. (2012). Synoptic and remote sensing analysis of dust events in southwestern Iran. *Natural Hazards*, 64(2), 1625–1638. <https://doi.org/10.1007/s11069-012-0328-9>
- Global ambient air pollution. (2018). [Map]. World Health Organization. <http://maps.who.int/airpollution/>
- Goudie, A. S. (2014). Desert dust and human health disorders. *Environment International*, 63, 101–113. <https://doi.org/10.1016/j.envint.2013.10.011>
- Hofer, J., Althausen, D., Abdullaev, S. F., Makhmudov, A. N., Nazarov, B. I., Schettler, G., Engelmann, R., Baars, H., Fomba, K. W., Muller, K., Heinold, B., Kandler, K., & Ansmann, A. (2017). Long-term profiling of mineral dust and pollution aerosol with multiwavelength polarization Raman lidar at the Central Asian site of Dushanbe, Tajikistan: Case studies. *Atmospheric Chemistry and Physics*, 17(23), 14559–14577. <https://doi.org/10.5194/acp-17-14559-2017>
- Hofer, Julian, Althausen, D., Abdullaev, S. F., Makhmudov, A. N., Nazarov, B. I., Schettler, G., Engelmann, R., Baars, H., Fomba, K. W., & Müller, K. (2017). Long-term profiling of mineral dust and pollution aerosol with multiwavelength polarization Raman lidar at the Central Asian site of Dushanbe, Tajikistan: Case studies. *Atmospheric Chemistry and Physics*, 17(23), 14559.

- Huang, X. T., Oberhansli, H., von Suchodoletz, H., & Sorrel, P. (2011). Dust deposition in the Aral Sea: Implications for changes in atmospheric circulation in central Asia during the past 2000 years. *Quaternary Science Reviews*, 30(25–26), 3661–3674. <https://doi.org/10.1016/j.quascirev.2011.09.011>
- Jouzel, J., Waelbroeck, C., Malaize, B., Bender, M., Petit, J. R., Stievenard, M., Barkov, N. I., Barnola, J. M., King, T., Kotlyakov, V. M., Lipenkov, V., Lorius, C., Raynaud, D., Ritz, C., & Sowers, T. (1996). Climatic interpretation of the recently extended Vostok ice records. *Climate Dynamics*, 12(8), 513–521. <https://doi.org/10.1007/Bf00207935>
- Kriticos, D. J., Webber, B. L., Leriche, A., Ota, N., Macadam, I., Bathols, J., & Scott, J. K. (2012). CliMond: Global high-resolution historical and future scenario climate surfaces for bioclimatic modelling. *Methods in Ecology and Evolution*, 3(1), 53–64. <https://doi.org/10.1111/j.2041-210X.2011.00134.x>
- Lee, D., Min, S. K., Fischer, E., Shiogama, H., Bethke, I., Lierhammer, L., & Scinocca, J. F. (2018). Impacts of half a degree additional warming on the Asian summer monsoon rainfall characteristics. *Environmental Research Letters*, 13(4). <https://doi.org/ARTN 044033 10.1088/1748-9326/aab55d>
- Lenssen, N. J. L., Schmidt, G. A., Hansen, J. E., Menne, M. J., Persin, A., Ruedy, R., & Zyss, D. (2019). Improvements in the GISTEMP Uncertainty Model. *Journal of Geophysical Research-Atmospheres*, 124(12), 6307–6326. <https://doi.org/10.1029/2018jd029522>
- MCLSW. (2015). GDP Report- The Province Index (pp. 5–6) [Annual Report]. Ministry of Cooperative labour and Social welfare. <http://amarkar.ir/handler/getfile.ashx?type=pub&id=655>
- Modaihsh, A. S. (1997). Characteristics and composition of the falling dust sediments on Riyadh city, Saudi Arabia. *Journal of Arid Environments*, 36(2), 211–223. <https://doi.org/10.1006/jare.1996.0225>
- Najafi, M. S., Khoshakhlagh, F., Zamanzadeh, S. M., Shirazi, M. H., Samadi, M., & Hajikhani, S. (2014). Characteristics of TSP Loads during the Middle East Springtime Dust Storm (MESDS) in Western Iran. *Arabian Journal of Geosciences*, 7(12), 5367–5381. <https://doi.org/10.1007/s12517-013-1086-z>
- Orth, R., Zscheischler, J., & Seneviratne, S. I. (2016). Record dry summer in 2015 challenges precipitation projections in Central Europe. *Sci Rep*, 6, 28334. <https://doi.org/10.1038/srep28334>
- Peel, M. C., Finlayson, B. L., & McMahon, T. A. (2007). Updated world map of the Köppen-Geiger climate classification. *Hydrology and Earth System Sciences*, 11(5), 1633–1644. <https://doi.org/10.5194/hess-11-1633-2007>
- Rifaat, A., Basaham, A., El-Mamoney, M., & El-Sayed, M. (2007). Mineralogical and chemical composition of dry atmospheric deposition on Jeddah City, Eastern Coast of the Red Sea. *Journal of King Abdullah University Marine Science*, 19, 167–188.
- Roberts, N., Brayshaw, D., Kuzucuoglu, C., Perez, R., & Sadori, L. (2011). The mid-Holocene climatic transition in the Mediterranean: Causes and consequences. *Holocene*, 21(1), 3–13. <https://doi.org/10.1177/0959683610388058>
- Russell, R. (1931). *Dry Climates of the United States. Part I, The Climatic Map*. Univ. Of California, Publ.
- Sharifi, A., Pourmand, A., Canuel, E. A., Ferer-Tyler, E., Peterson, L. C., Aichner, B., Feakins, S. J., Daryaei, T., Djamali, M., Beni, A. N., Lahijani, H. A. K., & Swart, P. K. (2015). Abrupt climate variability since the last deglaciation based on a high-resolution, multi-proxy peat record from NW Iran: The hand that rocked the Cradle of Civilization? *Quaternary Science Reviews*, 123, 215–230. <https://doi.org/10.1016/j.quascirev.2015.07.006>
- Shen, H., Abuduwalli, J., Samat, A., & Ma, L. (2016). A review on the research of modern aeolian dust in Central Asia. *Arabian Journal of Geosciences*, 9(13), 625.
- Statistical Center of Iran. (2018). National Population and Housing Census [Annual Report]. Vice Presidency Plan and Budget Organization Statistical Centre of Iran. <https://www.amar.org.ir/english/Home/portalid/1>
- Statoids. (2016). Administrative Divisions of Countries (Statics Center of Iran) [Monthly Clearing House]. <http://www.statoids.com/uir.html>
- Taghavi, F., & Asadi, A. (2008). The Persian Gulf 12th April 2007 dust storm: Observation and model analysis. 8–12.
- Taghavi, F., Owlad, E., & Ackerman, S. (2017). Enhancement and identification of dust events in the south-west region of Iran using satellite observations. *Journal of Earth System Science*, 126(2), 28.
- Wilkinson, M. J. (2014). The Persian Gulf, Clear and Clouded (The photos are provided by the ISS Crew Earth Observations Facility and the Earth Science and Remote Sensing Unit,). Johnson Space Center. <https://earthobservatory.nasa.gov/images/84490/the-persian-gulf-clear-and-clouded>

- WMO. (2019). The Global Climate in 2015-2019. World Meteorological Organization.
https://library.wmo.int/doc_num.php?explnum_id=9936
- Young, A. H., Knapp, K. R., Inamdar, A., Hankins, W., & Rossow, W. B. (2018). The International Satellite Cloud Climatology Project H-Series climate data record product. *Earth System Science Data*, 10(1), 583–593.
<https://doi.org/10.5194/essd-10-583-2018>
- Zarasvandi, A., Carranza, E. J. M., Moore, F., & Rastmanesh, F. (2011). Spatio-temporal occurrences and mineralogical–geochemical characteristics of airborne dusts in Khuzestan Province (southwestern Iran). *Geochemistry for Geological-Environmental Studies*, 111(3), 138–151.
<https://doi.org/10.1016/j.gexplo.2011.04.004>

3. Methods

3.1 Introduction

This chapter addresses methodology based on triple aims defined in the first chapter. It is subdivided into five main sections. Each section provides data necessary to further analysis. To begin with the fieldwork setting defining district in which sampling routine must be performed.

The next section contains how data was retrieved from measurements of the dust collection, including the construction of the samplers and equally important dust distribution data from Aerosol optical thickness of study area during the research period. The subsequent essential part is chemical and geo-statistical analysis over the gathered data followed by pitfalls and problem in the fieldwork.

3.2 Field work statements

According to information from long-term dust events over the study area, ten sampling sites were marked (Fig. 3.1). The sites were coded from G01 to G10 and were placed based on the distribution and intensity of the dust events reported by (IRMO, 2016) between 2000 and 2015. The sampler locations were classified with respect to LULC classification. As shown in (Fig. 3.1), a given circle centered (radius 10 km) at each gauge site (G01–G10) represents the spatial pattern of the LULC. This analysis consists of the whole research area with respect to each sampler at the gauge site. The dust deposition rate was measured by positioning 20 the following dust deposit gauges at 10 gauge sites to improve that observation and surveillance quality (Tab. 3.1).

Table 3.1 Location, altitude and total distance of dust samplers in the study area

Classification			Geo-Coordinates			Altitude	Distance
No	Dominance	Code	Latitude [N]	Longitude [E]	Surrounding	(a.s.l.) [m]	Total [km]
1	Rur & Agr & Ind	G01	34.000553	45.497595	Light Ind & Semi Desert	144	0
2	Sub & Ind	G02	34.007182	45.499075	Light Ind & Semi Desert	184	1
3	Rur	G03	34.393584	45.648174	Semi Desert	394	52
4	Agr & Ind	G04	34.423028	45.993753	Road Traffic Load	910	113
5	Urb & Ind	G05	34.353365	47.101335	Densely occupied	1,304	245
6	Rur & Agr & Ind	G06	33.024976	47.759393	Light Ind & village	581	632
7	Rur & Agr & Ind	G07	32.380038	48.282664	Light Ind & village	109	733
8	Rur & Agr & Ind	G08	31.445194	48.632398	Light Ind & village	25	860
9	Sub	G09	30.584651	49.163632	Occupied	6	991
10	Urb & Ind	G10	30.352411	48.292293	Road Traffic Load	2	1,091

*Dust samplers were marked from G01 to G10. The sampler locations were classified with respect to Rural (Rur), Agricultural (Agr), Industrial (Ind), Urban (Urb), and Suburban (Sub) land cover dominance (Levy et al., 2013). Distance of each site-gauge from the one before remarked in the last columns

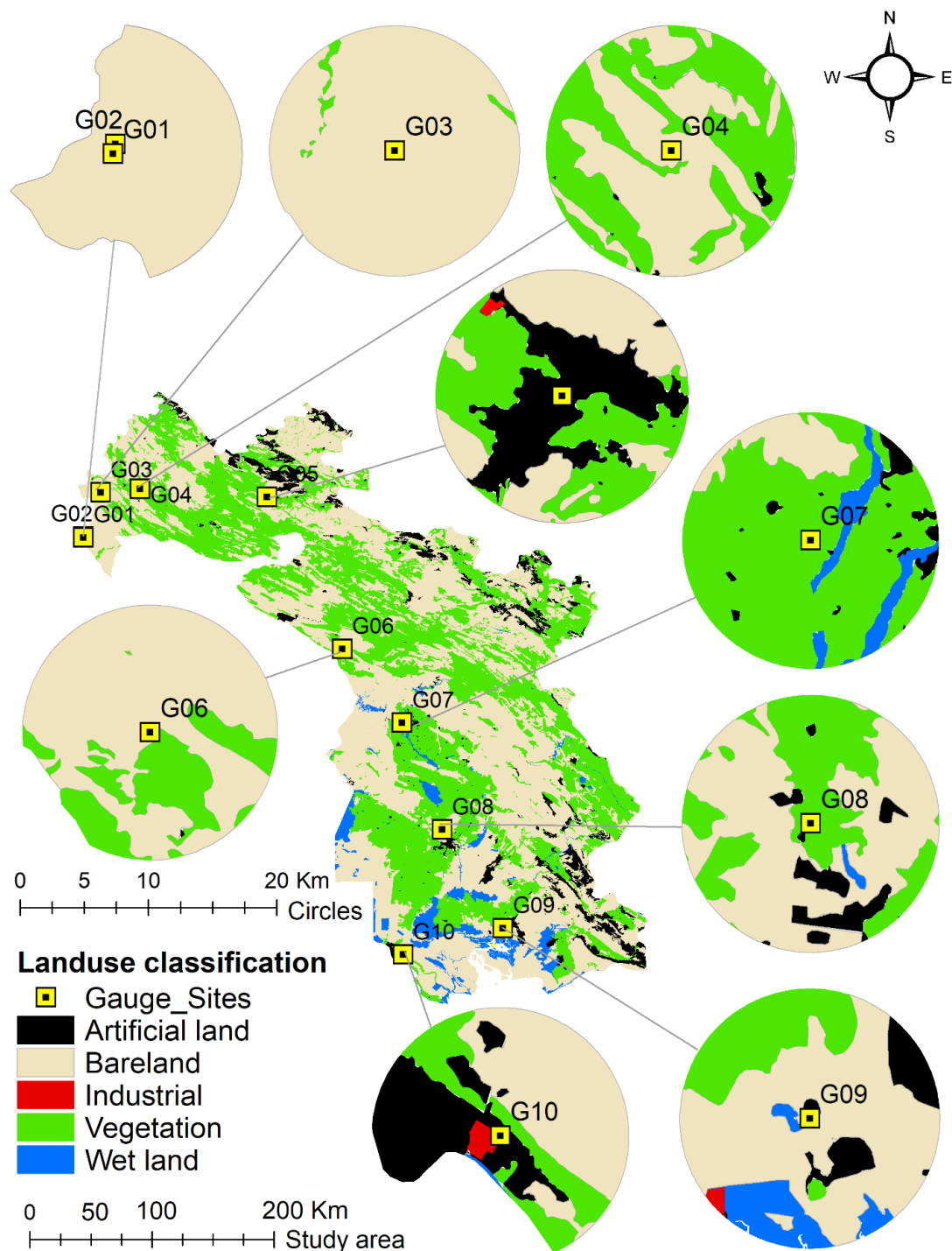


Figure 3.1 Given circle centered of each gauge

*Site representing the LULC for 314 km² Measurement dependence of dust collection

Both gravimetric and directional dust samplers (total = 20) have been deployed to satisfy requirements of ASTM D1356-05 (IHS under license with ASTM, 2010) and have operated since 2014.

3.2.1 Sampler design

The sampling sites were selected based on the following criteria. They were easily accessible and secure against animal intrusion, humans and upwind obstructions, Samplers constructed far from shadow. They were covered with a mesh on top. Accordingly, samplers were installed about 2 m above the ground level. Each collection tray consisted of a circular plastic plate (200 mm in diameter, 20 mm depth) fixed into cylinder with 30 cm height (Fig. 3.2). The surface area is 314 cm² (inverted Frisbee

design) and a paper inlay for the passive dust collection. As illustrated in Tab. 3.1, dust samples were collected monthly for gauges installed at 10 gauge sites. The samplers was deliberately kept simple to ensure long-term durability and easy maintenance.

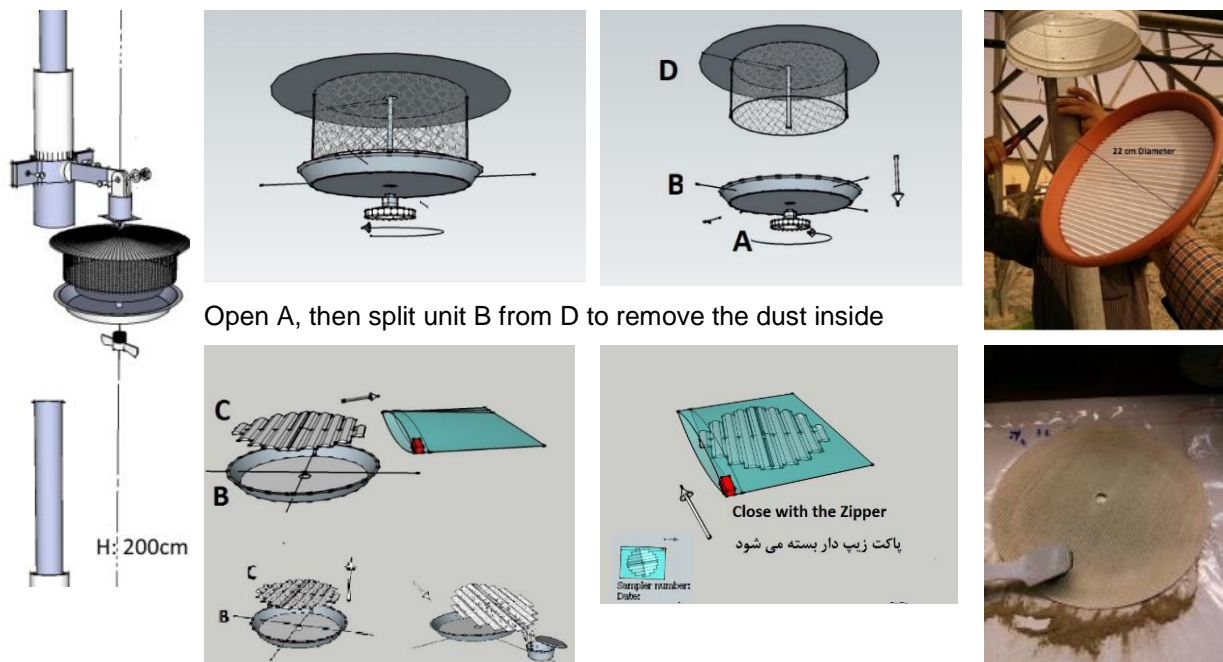


Figure 3.2 Installation and sampling technique

3.2.2 Deposition rate

After each monthly sampling, and after every exposure period, dust samples were removed from the site and sent to the laboratory of the University of Marburg, Germany. Copies of these laboratory reports are presented in the chapter Appendix containing the GDR results.

3.3 Optical thickness

In recent years, several new reanalysis applications, including the National Centers for Environmental Prediction (NCEP) North American Regional Reanalysis (NARR), and MERRA-II have been released (Mesinger et al., 2006; Rienecker et al., 2011). Furthermore, the Aerosol Optical Thickness at 550 nm (AOT) has been obtained from the MODIS instrument onboard the NASA Terra satellite since March 2014. High spatial resolution, level 3, ranging from 250 m to 1 km, allowing for almost daily world coverage collection quality controlled (Q1) MODIS aerosol repository, were aside from different spatial averaging for the southwestern part of the study area.

MODIS AOT data are collected over a larger area of (45.49E, 50.42E) and (30.35N 34.39N) longitude and latitude respectively, as well as regional dust loading points. A very good quality data were flagged to generate AOT statistics over the study area having 0.5 to 1 degree resolution, at 550 nm over dark targets for land only have been selected (Tab. 3.2). Besides, the MERRA-II dataset using the Goddard Earth Observing System Model, Version 5 (GEOS-5, version 5.12.4), also can function extensively with an expanding array of applications areas, such as ecological forecasting, air quality, wind flow patterns, meteorological observations, and dust as part of its routine reports (Gao et al., 1992; Pease et al., 1998).

Table 3.2 Titles of Giovanni online data systems developed by NASA GES DISC

Disciplines: Aerosol, Atmospheric dynamic Measurement: AOT, Dust & meteorological observations					Resolution
DataSet. Sensor, Satellite, Bandwidth	Platform	Availability	Spatial	Temporal	
MOD08-M3-v6.1 at 550 nm Dark Target, for land only	Terra Level 3	03/01/2000	0.1 x 0.1 degree (10x10 km)	Daily, 8 days, and Monthly	
MOD08-M3-v6.1 at 550 nm Deep blue Aerosol, for land only	Terra Level 3	01/02/2000 Giovanni	1 x 1 degree	Monthly	
OD08-M3-v6.1 at 550 nm Deep blue Aerosol, for land and ocean	Terra Level 3	Giovanni	1 x 1 degree	Monthly	
MIL3MAE V4, MISR Aerosol Optical Depth 555 nm	Terra	01/03/2000 Giovanni	0.5 x 0.5 degree	Daily and Monthly	
Satellite systems with numerical models, 550 nm	MERRA-II Model	M2TMNXSLV	0.5 ° x 0.625 °	Hourly & Monthly Giovanni	

*Dark target has separate algorithms for land and ocean. Deep blue in the MODIS aerosol products is a land retrieval only. Land algorithm method works best over dark vegetated targets and does not work over bright land surfaces.

*MERRA-II is a NASA atmospheric reanalysis that begins in 1980 and replaced the original MERRA reanalysis (Rienecker et al., 2011) using an upgraded version of the Goddard Earth Observing System Model, Version 5 (GEOS-5) data assimilation system.

Therefore, the MERRA-II results were used to evaluate the correlation of the dry deposition rates with the climate factors that were obtained during the study period.

3.4 Analysis

Once the data is coded, the research can start identifying themes, and finding relative pattern. The first stage of analyzing data is data preparation, where the aim is to convert raw data into something meaningful and readable. Therefore, it includes preparation and chemical analysis.

After dust samples have been taken from the field, all extraneous material and particulate contaminants (insoluble pieces, high mass loading of surfactants, tissue, etc) have been removed from the samples. Accurate measurement and identical process were done by weighing for one gram of each sample.

3.4.1 Inductively Coupled Plasma Mass Spectrometry (ICP-MS)

The collected material was transferred into plastic bags on a monthly basis between March 2014 and March 2015 and was stored at room temperature before being analyzed using an ICP-MS (ASTM D7439, 2014)). The DIN EN ISO 17294-2 (Beuth, 2004; EN ISO 17294-2, 2016) guideline on quantifying dissolved elements using the ICP-MS was used for determining the elemental composition of the dust samples. Among the following four USEPA (United States Environmental Protection Agency) methods (Chen and Ma, 2001; da Silva et al., 2014) (Tab. 3-3), method 3050 was deliberately chosen.

A representative 1 gram of each sample is digested with 15 and 5 ml respectively additions of Hydro-chloric and Nitric acid in 200 ml Flasks, closed using a vapor recovery glass left at the laboratory hood condition overnight. The samples cooked to ~ 95°C ± 100°C without boiling over one hour until oxidation is finished. Then contained reagents (~30 ml) in the flask was filtered into the 50 ml volumetric-flask, and diluted to a final volume of 50 ml with double deionized water.

Table 3.3 Four digestion methods based on USEPA references

Methods	Reagents	Digestive	Recoveries Strength
3050	HNO3- HCL	Hotplate	-
3051	HNO3	Microwave	-
3051A	HNO3- HCL	Microwave	Zn Hg
3052	HNO3- HCL- HF	Microwave	All elements except Pb - Mg

* United States Environmental Protection Agency - USEPA

Data interpretation from ICP-MS analysis is about the bottom-up calculation. The raw data from the instrument is depicted in ppb concentration (Tab. 3.4). Declaration is prepared in my own draft.

Table 3.4 Data relative to digestive samples

Run	Time	23Na ppb	24Mg ppb	28Si-3V ppb	39K-3V ppb	43Ca ppb	88Sr ppb	138Ba ppb	206Pb ppb
1	10:51:54	4.21	0.065	1.472	0.443	0.576	0.003	0.017	0
2	10:51:57	7.322	0.151	0.151	1.892	3.407	0	0.026	0
3	10:52:01	8.733	0.181	0.181	1.051	2.843	0.005	0.029	0
X		6.755	0.132	0.132	0.49	1.891	0	0.013	0
S		2.314	0.06	0.06	1.751	2.155	0.004	0.026	0
%RSD		34.26	45.5	45.5	356.9	113.9	831.2	202.3	0

*A part of raw data relative to digestive samples from our ICP-MS software

The ppb data from the ICP-MS printed out into an excel format, is contained the dilution information for the sample. Each sample analyzed three times, and the average of the three replicates was calculated, including means and standard. Accuracy and precision in terms of %RSD which stands for relative standard deviation have been determined by the machine.

$$\%RSD = \frac{S(SD)}{X(mean)} \times 100$$

Equation. 1

$$True\ value \xleftarrow{S(SD)} RSD \times \left(\sum_{i=1}^3 Na_i \right) / 3$$

Equation. 2

Tab. 3.4 presents the acceptance criteria for Natrium [Na]. The %RSD value is calculated right 34.26 using equation Eq. (1). Mass true value on the other hands is taken from Eq. (2). Accuracy within the minimum and maximum value, therefore, are obtained from Eq. (3).

$$\min_{Na} value + \overbrace{True\ value}^{SD} \cong \max_{Na} value - \overbrace{True\ value}^{SD} \cong \left(\underbrace{X}_{Na} \left| \left(\sum_{i=1} Na_i / 3 \right) \right. \right)$$

Equation. 3

The result retrieved from ICP-MS is converted to the mass concentration metric using Eq. (4).

$$(ICP - MS^{ppb} \times \overbrace{Tm_1^{ml} \times Tm_2^{ml}}^{Total\ Mass[I] \times [II]}) / (\overbrace{Pm_1^g \times Pm_2^{ml}}^{Mass\ Product\ [I] \times [II]}) = \overbrace{Result\ \mu g/kg}^{Interperting\ Metric}$$

Equation. 4

ICP-MS Measured (ppb). Dilution (ml) /Weighting (g) = Interpreting Result (µg/kg)

Since the samples have been performed 2 dilutions, Interpreting Result (µg/kg) would be recalculated from the above equation and divided by 1,000 unit to get final interpreted of µg/g. Finally, the dilution information from the ICP-MS converted to value of µg/g out into an excel format (Tab. 3.5).

Table 3.5 interpretation and mass calculation of elements

Dilution I g-ml	Dilution II g- ml	Run	23Na ppb	24Mg ppb	28Si-3V ppb	39K-3V ppb	43Ca ppb	138Ba Ppb
Pm I=1	Pm II=1	X	6.755	0.132	0.132	0.49	1.891	0.013
Tm I=50	Tm II=10	mg/l						
	Interpreted Result	3.377	0.066	0.066	0.245	0.9455	0.0065	

1ug/l =1 ppb

3.4.2 Statistical analysis

Following the basic steps of statistical analysis has been applied to evaluate the accuracy for the generated results.

[1] The correlation values of 20 elements to the Dust Event Frequency (DEF) and its weight, as based on the Airborne Metal Regulations index –AMR- (Geiger and Cooper, 2010; Prasad et al., 2018), have been classified into four matrices. Correlation strength may be due to the exposure of aerosol and dust particles to extra elements throughout the dust's travel history. In either case, the correlation strength may be related to distance from the source, the wind direction, the meteorological situation, and industrial and commercial activities nearby.

[2] In accordance with Trenberth et al., (2007), Trenberth, (2011), and Tao et al., (2012), the correlation between the deposition rate and meteorological pattern indicates that, wind velocity, high temperature, and lack of precipitation are the most significant factors behind a high dust deposition rate. Statistical comparisons of the mean deposition rate in each season were performed with meteorological functions. Interestingly, the high correlation values with statistically significant differences may potentially provide valuable and timely evidence for the discussion on this topic.

[3] In line with Shao and Wang, (2003), dust concentrations in the atmosphere could represent the dust deposition rate factors. Therefore, a statistical comparison of the GDR and model result for both the load and concentration values over the study area was performed to reveal the true correlation. The analysis of the time series reveals a potentially promising correlation between the derived thickness layers from AOT and actual deposition rate data from ground surveying.

[4] In order to assess the LULC and climate offset of each gauge site, for analysis, areas with different LULCs were classified under the same climate zone (chapter 6). A dendrogram is the most commonly used method for cluster analysis. Clustering analysis was performed according to Ward's method (Tokalioğlu and Kartal, 2006; Yongming et al., 2006). The study area was classified into three exclusive scenarios based on a combination of internal variables (Lu et al., 2010), such as the climate patterns, and it was applied to identify different LULC groups by clustering sites with similar climate patterns.

[5] After converting the AOT results to points, the kriging interpolation method (Dindaroglu, 2014; Franklin et al., 2018) was applied to the pixel values. Kriging is a geo-statistical interpolation method used to calculate weights for measured points and to derive predicted values for unmeasured locations.

Ultimately, the Iterative Self-Organizing Data Analysis Technique (ISODATA) classification was applied to 550 nm AOT of the monthly images for the period between 2014 and 2015.

3.5 Impediments and problems in the field work

In order to make an appropriate solution to difficulties faced undertaking the works, procedures to manage data retrieved from the study area and analysis should be identified as a part of the planning for the field investigation works.

- [1] Potential climate pattern include weather factors: Wind, heat and cold stress should be considered.
- [2] Introducing contaminants into samples: A procedure to minimize external particles.
- [3] Inappropriate sampling report: Influential of local dust into main samples. E.g. from contaminant exposure of surrounding land.
- [4] Losing the samples: The losing are minimized under certain activities on the site during dry and windy conditions. Establishing the gauges far from the work area, and vehicle access.
- [5] Packaging and transporting samples to the Laboratory: Items from field work should be hand-carried to laboratory.
- [6] Rescheduling this work in more than once due to busy agenda of most respondent, failure happened in technical process and reluctant to sharing data in many cases.
- [7] Although observation from Ground Deposition Rate (GDR) is the best way of conducting an experiment and valid result, this experiment is complex and greatly expensive due to has a number of stages.

3.6 Conclusion

All those methods which are used during the research are termed at a solution for a given problem, the available data and the unknown aspects of the problem been released to make a solution possible. Keeping this in mind, research methods are addressed into the following three groups:

- [1] In the first group those methods were included, which are concerned with the collection of data (GDR). The gauge sites were constructed, where the data already are not sufficient to arrive at the required solution.
- [2] The second group consists of those analytical and statistical techniques, which are used for establishing relationships between the data and the unknowns.
- [3] The third group consists of those methods, which are used to evaluate the accuracy of the results obtained using spatiotemporal data.

Research methods falling in the above stated in three groups are generally taken as sampling methods, data, and the analytical tools of research.

References

- ASTM D7439, 2014. Standard Test Method for Determination of Elements in Airborne Particulate Matter by Inductively Coupled Plasma–Mass Spectrometry, in: Book of Standards, ASTM D7439-14. Subcommittee D22.03.
- Beuth, 2004. Wasserbeschaffenheit - Anwendung der induktiv gekoppelten Plasma-Massenspektrometrie (ICP-MS). 2005-02.
- Chen, M., Ma, L.Q., 2001. Comparison of three aqua regia digestion methods for twenty Florida soils. *Soil Sci. Soc. Am. J.* 65, 491–499. [https://doi.org/DOI 10.2136/sssaj2001.652491x](https://doi.org/DOI%2010.2136/sssaj2001.652491x)
- da Silva, Y.J.A.B., do Nascimento, C.W.A., Biondi, C.M., 2014. Comparison of USEPA digestion methods to heavy metals in soil samples. *Environ. Monit. Assess.* 186, 47–53. <https://doi.org/10.1007/s10661-013-3354-5>
- Dindaroglu, T., 2014. The use of the GIS Kriging technique to determine the spatial changes of natural radionuclide concentrations in soil and forest cover. *J. Environ. Health Sci. Eng.* 12, 130 %U <https://doi.org/10.1186/s40201-014-0130-6>. [https://doi.org/ARTN 130 10.1186/s40201-014-0130-6](https://doi.org/ARTN%20130%2010.1186/s40201-014-0130-6)
- EN ISO 17294-2, 2016. Water quality: Application of inductively coupled plasma mass spectrometry (ICP-MS).
- Franklin, M., Kalashnikova, O.V., Garay, M.J., Fruin, S., 2018. Characterization of Subgrid-Scale Variability in Particulate Matter with Respect to Satellite Aerosol Observations. *Remote Sens.* 10, 623. [https://doi.org/ARTN 623 10.3390/rs10040623](https://doi.org/ARTN%20623%2010.3390/rs10040623)
- Gao, W., Wesely, M.L., Cook, D.R., Hart, R.L., 1992. Air-surface exchange of H₂O, CO₂, and O₃ at a tallgrass prairie in relation to remotely sensed vegetation indices. *J. Geophys. Res.* <https://doi.org/10.1029/91JD03175>
- Geiger, A., Cooper, J., 2010. Overview of airborne metals regulations, exposure limits, health effects, and contemporary research. US Environ. Prot. Agency Accessed August 25, 2015.
- IHS under license with ASTM, 2010. Standard Terminology Relating to Sampling and Analysis of Atmospheres. IHS License ASTM.
- IRMO, 2016. I.R.OF IRAN Meteorological Organization.
- Levy, R.C., Mattoo, S., Munchak, L.A., Remer, L.A., Sayer, A.M., Patadia, F., Hsu, N.C., 2013. The Collection 6 MODIS aerosol products over land and ocean. *Atmos Meas Tech* 6, 2989–3034. <https://doi.org/10.5194/amt-6-2989-2013>
- Lu, X., Wang, L., Li, L.Y., Lei, K., Huang, L., Kang, D., 2010. Multivariate statistical analysis of heavy metals in street dust of Baoji, NW China. *J Hazard Mater* 173, 744–9. <https://doi.org/10.1016/j.jhazmat.2009.09.001>
- Mesinger, F., DiMego, G., Kalnay, E., Mitchell, K., Shafran, P.C., Ebisuzaki, W., Jovic, D., Woollen, J., Rogers, E., Berbery, E.H., Ek, M.B., Fan, Y., Grumbine, R., Higgins, W., Li, H., Lin, Y., Manikin, G., Parrish, D., Shi, W., 2006. North American regional reanalysis. *Bull. Am. Meteorol. Soc.* 87, 343–360. <https://doi.org/10.1175/Bams-87-3-343>
- Pease, P.P., Tchakerian, V.P., Tindale, N.W., 1998. Aerosols over the Arabian Sea: geochemistry and source areas for aeolian desert dust. *J. Arid Environ.* 39, 477–496. [https://doi.org/DOI 10.1006/jare.1997.0368](https://doi.org/DOI%2010.1006/jare.1997.0368)
- Prasad, M.N.V., de Campos Favas, P.J., Maiti, S.K., 2018. Bio-Geotechnologies for Mine Site Rehabilitation. Elsevier.
- Rienecker, M.M., Suarez, M.J., Gelaro, R., Todling, R., Bacmeister, J., Liu, E., Bosilovich, M.G., Schubert, S.D., Takacs, L., Kim, G.-K., 2011. MERRA: NASA's modern-era retrospective analysis for research and applications. *J. Clim.* 24, 3624–3648. <https://doi.org/10.1175/JCLI-D-11-00015.1>
- Shao, Y., Wang, J., 2003. A climatology of Northeast Asian dust events. *Meteorol. Z.* 12, 187–196. <https://doi.org/10.1127/0941-2948/2003/0012-0187>
- Tao, W.K., Chen, J.P., Li, Z.Q., Wang, C., Zhang, C.D., 2012. Impact of Aerosols on Convective Clouds and Precipitation. *Rev. Geophys.* 50. [https://doi.org/Artn Rg2001 10.1029/2011rg000369](https://doi.org/Artn%20Rg2001%2010.1029/2011rg000369)
- Tokaloğlu, Ş., Kartal, Ş., 2006. Multivariate analysis of the data and speciation of heavy metals in street dust samples from the Organized Industrial District in Kayseri (Turkey). *Atmos. Environ.* 40, 2797–2805. <https://doi.org/10.1016/j.atmosenv.2006.01.019>

- Trenberth, K., Jones, P., Ambenje, P., Bojariu, R., Easterling, D., Tank, A.K., Parker, D., Rahimzadeh, F., Renwick, J., Rusticucci, M., 2007. Observations: surface and atmospheric climate change. Chapter 3. *Clim. Change* 235–336.
- Trenberth, K.E., 2011. Changes in precipitation with climate change. *Clim. Res.* 47, 123–138.
<https://doi.org/10.3354/cr00953>
- Yongming, H., Peixuan, D., Junji, C., Posmentier, E.S., 2006. Multivariate analysis of heavy metal contamination in urban dusts of Xi'an, Central China. *Sci Total Env.* 355, 176–86.
<https://doi.org/10.1016/j.scitotenv.2005.02.026>

4. Spatial and temporal gradients of dust deposition and aerosol optical thickness

Abstract

The southwestern Iran is one of the regions that are most prone to dust events. The objective of this study is the analysis of the spatial and temporal distributions of dust deposition rate as a key factor for finding the relative impact of the dust. First, the monthly mean aerosol optical thickness (AOT) from Moderate Resolution Imaging Spectroradiometer (MODIS) was analyzed and compared with the dust amount variations from ground deposition rate (GDR), and the results were further used to investigate the spatial and temporal distributions of dust events in southwestern Iran for the period between 2014 and 2015. Moving air mass trajectories, using the Hybrid Single-Particle Lagrangian Integrated Trajectory (HYSPLIT) model, were proven to be a discriminator of their local and regional origin. The results from GDR analysis produced a correlation coefficient between dust event history and deposition rates at dust magnitudes of >0.93 that is meaningful at the 95% confidence level. Furthermore, the deposition rates varied from 3 g/m² per month in summer to 10 g/m² per month in spring and gave insight into the transport direction of the dust. Within the same time series, AOT correspondences with MODIS on Terra in four aerosol thickness layers (clean, thin, thick, and strong thick) were shown in relation to each other. The deepest mixed layers were observed in spring and summer with a thickness of approximately 3500 m above ground level in the study area. Investigations of ground-based observations were correlated with the same variations for each aerosol thickness layer from MODIS images and they can be applied to discriminate layers of aeolian dust from layers of other aerosols. Together, dust distribution plots from AOT participated to enhance mass calculations and estimation deposition rates from the thick and strong thick aerosol thickness layers using the results from GDR. Despite all the advances of AOT, under certain circumstances, ground-based observations are better able to represent aerosol conditions over the study area, which were tested in southwestern Iran, even though the low number of observations is a commonly acknowledged drawback of GDR.

Keywords: aerosol optical thickness; ground deposition rate; HYSPLIT; dust deposition; Iran

4.1 Introduction

During the last decades, both dust event frequency and intensity have increased significantly in the western parts of Iran (Gerivani et al., 2011). Rezaei et al., (2019) analyzed dust studies in Iran since 2006 and concluded that the southwestern provinces of Iran were characterized by the highest dust deposition rates. Mineral dust aerosols influence the climate system directly by scattering and absorbing radiation (Kaufman and Koren, 2006; Alizadeh Choobari et al., 2013), which is associated with alterations in meteorological significance that may change the vertical profiles of temperatures and wind speeds. During transport, dust particles are continuously removed from the atmosphere by processes of dry and/or wet deposition (Lawrence and Neff, 2009). Several studies have addressed the dust deposition rate (Song et al., 2008; Schaap et al., 2009; Huang et al., 2010; Sorooshian et al., 2011; Balakrishnaiah et al., 2012; Crosbie et al., 2015; Yu et al., 2016). However, given the most attention were the uncertainties in spatial and temporal patterns, depending on changing patterns of human activities (Neff et al., 2008), different measurement techniques (Sokolik et al., 2001), the concentration of dust in the atmosphere, as well as surface features of the environment of the depositional sites (Tegen and Lacis, 1996). In the long run, the mass deposition rate of dust particles influences air quality (Arimoto et al., 1997; Abdou et al., 2005) and may cause considerable negative health effects (de Longueville et al., 2013; Kharazmi et al., 2018). Having data from the rate are usually used to validate model simulations (Yu et al., 2003) or may provide a useful benchmark. Accordingly, both passive and active sampling techniques can pay off to the lack of information from the rate by ground observations (Taheri Shahraini et al., 2015).

The most commonly used passive sampling techniques for collecting dust use a nonreactive collection pan, which serves as the depositional surface (Offer and Goossens, 1994; Reheis and Kihl, 1995). However, active sampling is suggested for particle measurements and for air filtration at or near ground level (Prospero et al., 1987). Estimates of deposition from active sampling are subject to the ability to accurately convert atmospheric dust concentrations to rates of deposition (Wesely and Hicks, 2000). Ground-based observations contribute strongly to a better understanding of the processes of aeolian dust transport and the impact of aeolian dust, e.g. in the form of a long-term research project in the Aral Sea basin from 2003 to 2012 (Groll et al., 2013; Opp et al., 2017). Aerosol optical thickness is usually obtained both from ground-based and satellite observations. Many studies have been performed on the high temporal and spectral resolution measurements from the AErosol RObotics NETwork (AERONET) in comparison with data from space (Prospero et al., 1987; Rubin et al., 2017). AERONET is a NASA network for monitoring and characterizing atmospheric aerosols by ground-based sun photometer (Müller et al., 2012; Cazacu et al., 2018). It has to be pointed out that due to the regional distribution of the AERONET stations (Binietoglou et al., 2015) the quality and representativeness of the AERONET data, which play an important role in the global dust monitoring (Cesnulyte et al., 2014), are strongly dependent on LIDAR instruments, measurement techniques (Lolli et al., 2018), and subsequent data processing methodologies. Based on these dependencies AERONET only represents a small area around the monitoring sites and does not provide data with a great spatial coverage (Rubin et al., 2017). While unlikely, aerosol optical thickness (AOT) predictions from satellites are performed by imaging using a column-integrated measure of the extinction coefficient (Yu et al., 2016) by the quantitative calculation of the effect of the total (anthropogenic plus natural) aerosols. Many algorithms have been applied to NASA's Moderate Resolution Imaging Spectroradiometer (MODIS on Terra and Aqua over the land) to retrieve AOT (Pawan et al., 2005; Kaufman and Koren, 2006). Comparatively, the standard collection product from MODIS has been used in many aerosol studies (Golitsyn and Gillette, 1993; Sorooshian et al., 2011). Experiences from aerosol patterns represented the seasonal climatology of AOT over the Indian subcontinent (Maiti and Prasad, 2016). Included are the long-term AOT variation in eastern China from 2001 to 2010 (Kim et al., 2014) and an application in northern China using the

Multi-angle Imaging SpectroRadiometer (MISR) over a three year period (Qi et al., 2013). In addition, observed concentration, deposition, and aerosol optical thickness measured by satellite instruments can be used to estimate the overall source location, and temporal evolution of the transported material (Bieringer et al., 2017; Hutchinson et al., 2017). Several studies have attempted to make such estimations, using a number of different approaches from model comparisons to field measurements (Chai et al., 2015; Ngan et al., 2015; Stein et al., 2015). To demonstrate the aerosol movement, a HYbrid Single Particle Lagrangian Integrated Trajectory (HYSPLIT) model was used (Ashrafi et al., 2014; Chen et al., 2013; Wang et al., 2011) for the trajectory analysis, and its back trajectory at different heights, to investigate the origin of particles prior to their arrival at a given place (Cazacu et al., 2018). To allow the discrimination of separate layers of aeolian dust from layers of other aerosols (Yasui et al., 2005), HYSPLIT facilitates the development of backward and forward trajectories (Draxler and Hess, 1998) and computes complex dispersions at various altitudes with a resolution of 500 x 500 m and a horizontal grid of 1.5° x 1.5° (Ashraf et al. 2013).

The Ground based Deposition Rate (GDR) can determine key points of dust activity in order to identify the general directions and areas of emission, an essential prerequisite for a better understanding of dust processes. Therefore, this study is focused primarily on direct measurements of dust deposition, made by passive sampling techniques. As has been noted, many studies have been done to evaluate dust deposition rates using different techniques in Iran and in other countries. However, the GDR in southwestern Iran has not been investigated very well. Providing an assessment of dust deposition rates against the relevant criteria such as wind, rain and temperature, evaluating the spatial distribution of the dust deposition, and observing the potential relationship between total dust distribution and aerosol optical thickness (AOT) will address the following research questions: (1) What is the level of dust deposition that is representative for the study area? (2) What spatial variations in dust deposition can be identified? (3) How do the measured dust deposition rates compare to AOT in the period from March of 2014 to March of 2015?

The results from ground-based observations together, along with analyzed data from AOT, were compared for a more detailed monthly dust event over the study area. AOT data were analyzed to understand the spatiotemporal patterns of the points with the same variation and intensity to GDR for the period of 2014–2015. The corresponding points were used in HYSPLIT for the model output.

4.2 Materials and methods

Comparing the results of monthly mean aerosol optical thickness (AOT) from Moderate Resolution Imaging Spectroradiometer (MODIS), and data from weighting ground deposition rate (GDR) using enhancement algorithms are used to investigate the spatiotemporal distribution of dust events in the southwest of Iran for the period between 2014 and 2015. Time-space consistency between AOT and GDR are defined. The results by agreement with model output of HYSPLIT are taken into further calculation to improve estimation of the dust deposition rate from the separate thickness layers.

In this section, I have provided a brief introduction to data and key observation and sampling practice (4.2.2 and 4.2.3) are given in chapter 3.

4.2.1 Testing method

For the GDR method, a correlation function in high magnitude and P-Value <0.05 from mass deposition rate and dust event history in accordance to synoptic report, when visibility has been reduced below 1,000 m, were suggested. Visibility data are obtained from the Iran Meteorological Organization (IRMO 2016) to compare with AOT values. Cases with inconsistent values have been removed from further calculation. For the second sort of dataset from the MODIS, preliminary qualitative comparisons were

taken for all cases selected from the aforementioned process, AOT values were calculated and justified with NASA's Multi-angle Imaging SpectroRadiometer (MISR). MISR images were captured from Giovanni MISR 555 nm and applied with a spatial resolution of 0.5 degrees. The analysis of the time series reveals a potentially promising correlation between the derived thickness layers from AOT and actual deposition rate data from ground surveying. The interpretation of fluctuated values of AOT, derived from the MODIS on Terra measurements, depicted variation of the thickness layers to discriminate separating layers of aeolian dust with the same variation and high correlation relationship from aerosols background.

4.2.2 Measurement dependences of dust collection

The dust deposition rate was measured by positioning 20 dust deposit gauges at 10 gauge sites (G01-G10) to improve that observation and surveillance quality. Since this study covers a vast area in the southwestern part of Iran and encompasses a range of conditions associated with topography and meteorology, the study area is categorized into three section. At this time G01, G02, G03, and G04 are assigned to the first section, [a]. The second section, [b], contains G05 and G06. The last and third section, [c], was assigned to G07, G08, G09, and G10.

4.2.3 Aerosol optical thickness

Twelve months of records of aerosol optical thickness at 550 nm (AOT) have been obtained from the MODIS instrument onboard the NASA Terra satellite since March 2014. High spatial resolution, level 3, ranging from 250 m to 1 km, allowing for almost daily world coverage collection quality controlled (Q1) MODIS aerosol repository, were aside from different spatial averaging for the southwestern part of the study area.

4.2.4 HYSPLIT model trajectory review

Air Research Laboratory provided the tools (see <https://ready.arl.noaa.gov/hypub-bin/trajtype.pl>), of calculating forward or backward trajectories and specifying the start/end point location as well as the period over which to calculate the trajectories. Surface wind observations and air above ground- based level (AGL) trajectories are included using the local wind profile (Rolph et al., 2017; Stein et al., 2015). To obtain the direction and updraft located above ground-based level (AGL) relatively and to reveal the influence of direct or indirect effects of the dust transport on deposition rates, backward trajectories model output (NOAA HYSPLIT) has been applied over three sections, [a], [b], and [c]. During the steady state results from the dust evidence from both AOT and GDR, each section has its own longitude and latitude direction and three trajectories that are simulated from 100 m, 500 m and 1000 m for AGL backward to 90 hours before reaching the points (a, b, and c).

4.3 Results analysis and validation

Monthly GDR were obtained using statistical calculations for approximately 12 months since March, 2014. MODIS monthly AOT onboard Terra satellites (MOD08_M3) data were downloaded according to the study area coordinate system. The pixel values of each image were rebuilt and refined. Correlation coefficients were used to find relationships between dust event frequencies and GDR for selecting justified collections. The MODIS provide data according to decimal degrees; accordingly, all the ground station coordinates were converted to decimal degrees. The zonal statistics trend results from AOT justified collection from GDR run into HYSPLIT model, which provided backward trajectory data from dust transport directions. Variations in both GDR and AOT, based on model output, will be discussed in the discussion section.

4.3.1 Ground monitoring results

Table 4.1 represents dust event frequency (DEF), in concert with the deposition rates. In the given time, total DEF values at G05 and G06 were zero and one while DEF values recorded 19, 17, 16, and 12 times was observed at G01, G02, G10 and G09. It however, the 8 times of dust occurrence at sites G08 and G03. The same magnitudes were also found at sites G01 and G02 during March, April, and May 2014. The average dust deposition rates ranged from 0.3 mg/cm² (G04-G06) to 1.2 mg/cm² (G01), which equals monthly field deposition rates of 3-12 g/m² per month, while the maximum value is between 12 to 30 g/m² per month, recorded in summer, 2014 and spring, 2015. Correlation magnitudes of 0.35, 0.49, and 0.69 were indicated for the rate of deposition at G05, G02, and G08, respectively. Given these points, the high deposition rates (GDR) were observed in March, April, May, 2014 (G01, G02, G03) with significant $p < 0.04$ and correlation values from 73% to 96%. Similarly, with significant $p < 0.05$, high correlation values between 69% to 93% were observed during January and February of 2015 (G10, G09, G08 and G07). Interestingly, the high correlation values with statistically significant differences would be wishful to make remarkable time of evidence into discussion.

Table 4.1 Dust deposition rates vs dust event frequency (DEF)

Collection time		Gauges site, Deposition rate mg/cm ²										Gauge site	
	Months	G10	G09	G08	G07	G06	G05	G04	G03	G02	G01	Total	(M.W)
2014	March	1.00	0.6	0.7	0.20	0.20	0.50	0.20	0.80	0.80	0.60	5.6	G10
	April	0.80	0.90	0.50	1.00	0.20	0.20	2.00	0.50	2.00	2.60	10.70	G01
	May	0.20	0.50	0.20	0.50	0.10	0.30	3.0	0.30	0.50	1.00	6.60	G04
	June	1.00	1.00	0.60	0.50	0.20	1.00	0.20	0.80	0.80	1.50	7.60	G01
	Juli	0.90	1.20	1.90	0.60	0.30	0.90	0.20	0.80	0.50	0.80	8.10	G08
	August	2.10	1.80	2.00	0.30	0.60	2.00	0.00	0.90	1.00	1.50	12.20	G10
	September	0.90	0.90	0.60	0.20	0.00	1.00	0.50	0.90	1.50	1.50	8.00	G01
	October	0.30	0.30	0.30	0.20	0.00	0.10	0.20	0.20	0.60	0.90	3.10	G01
	November	0.20	0.50	0.20	0.20	1.00	0.10	0.20	0.20	0.90	2.00	5.50	G01
	December	1.00	0.30	0.30	0.90	0.20	0.20	0.20	0.10	0.20	1.50	4.90	G01
2015	January	3.10	2.50	2.00	2.50	0.30	0.20	0.60	0.80	1.00	1.80	14.80	G10
	February	1.10	1.50	0.80	1.70	0.10	0.20	0.20	0.60	0.40	0.50	7.10	G07
	March	2.10	0.70	0.90	1.00	0.20	0.60	0.50	0.40	0.30	0.80	7.50	G07
Total DEF	Dust sum	14.70	12.70	11.00	9.80	3.40	7.30	8.00	7.30	10.50	17.00	101.70	mg/cm ²
	Temporal	Jan 2015	Jan 2015	Jan 2015	Jan 2015	Nov 2014	Aug 2014	May 2014	Sep 2014	Apr 2014	Apr 2014		
	Frequency	16	12	8	7	0	1	2	8	17	19		
Statistics	Correlation	74%	93%	69%	85%	-	35%	73%	81%	49%	96%		
	P-Value	0.05	0.05	0.05	0.05	NA	NA	0.05	0.05	0.05	0.05		

4.3.2 Results from aerosol optical thickness

Mapping pixel values of the study area have been calculated and classified into four different layers of aerosol thickness and include Clean [1], Thin [2], Thick [3], and Strong Thick [4] (Fig. 4.1; 4.2; 4.3). Monthly variations and trends in averages, and standard deviation AOT values were analyzed to understand changes in the types of aerosols in the study area (Fig. 4.4). To determine the areas with deposition rates in each month, pixel values which are remarked under 4 layers of classification were taken into consideration.

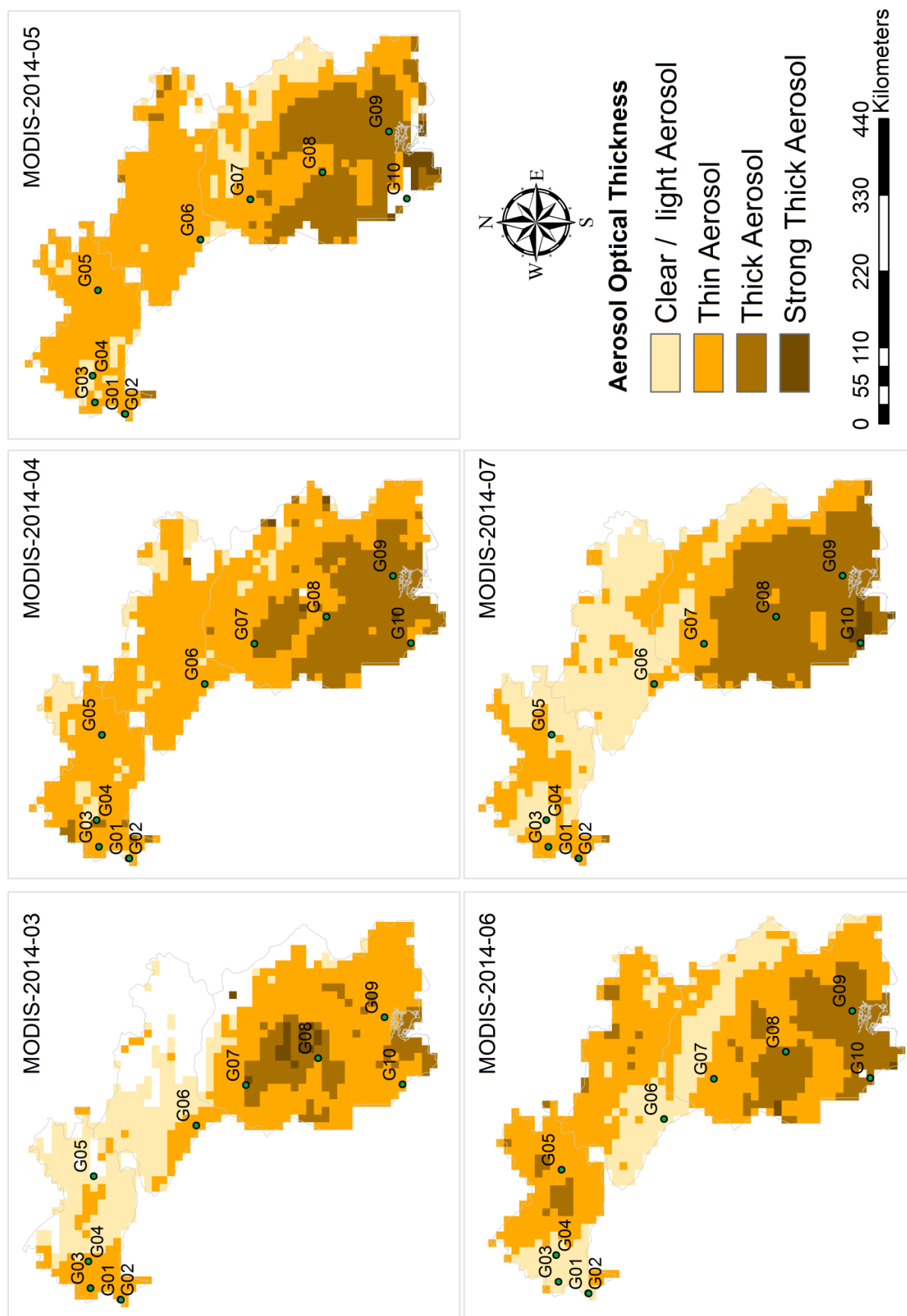


Figure 4.1 Average Aerosol Optical Depth 550 nm (Dark Target) monthly 0.1 degree

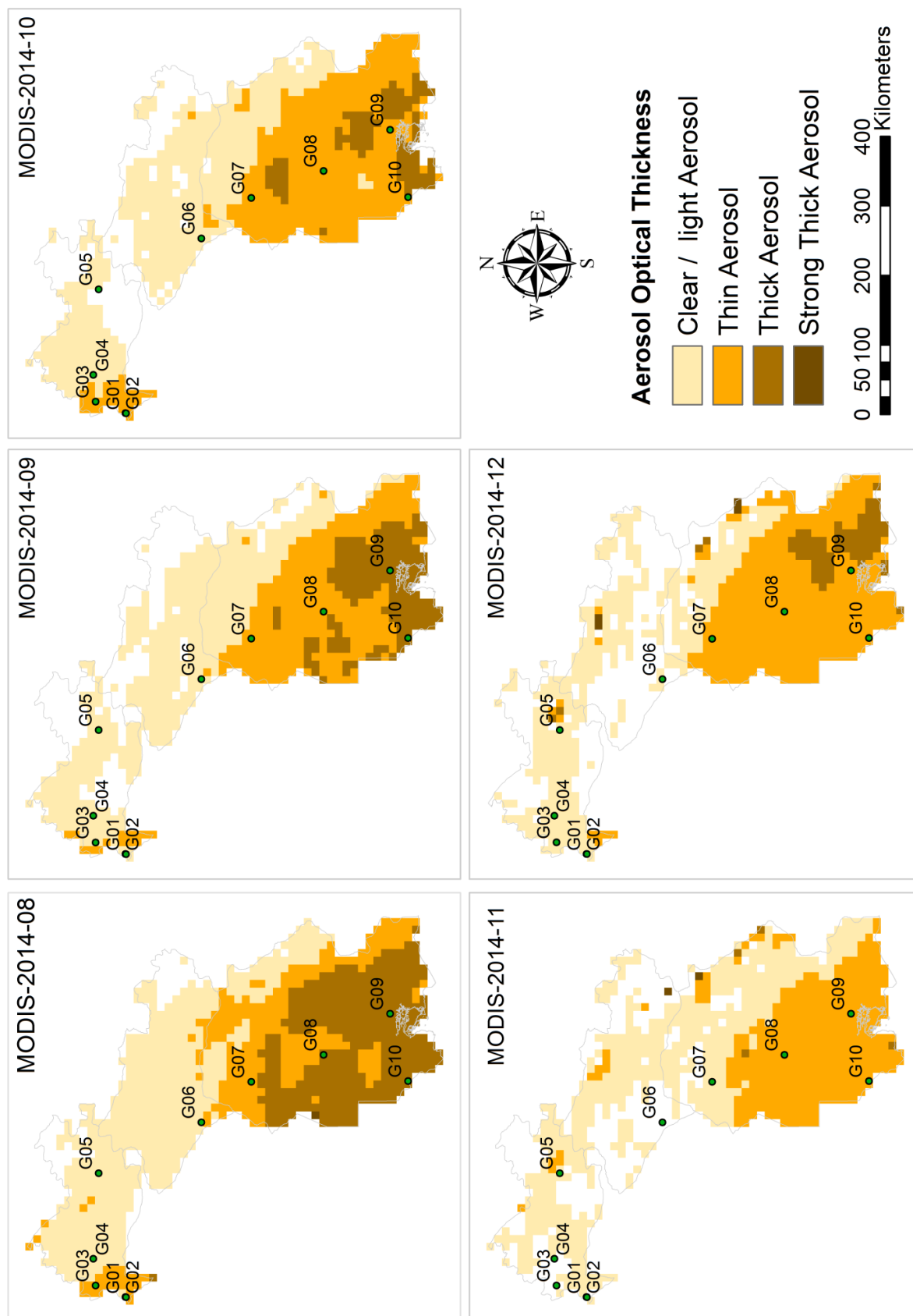


Figure 4.2 Average Aerosol Optical Depth 550 nm (Dark Target) monthly 0.1 degree

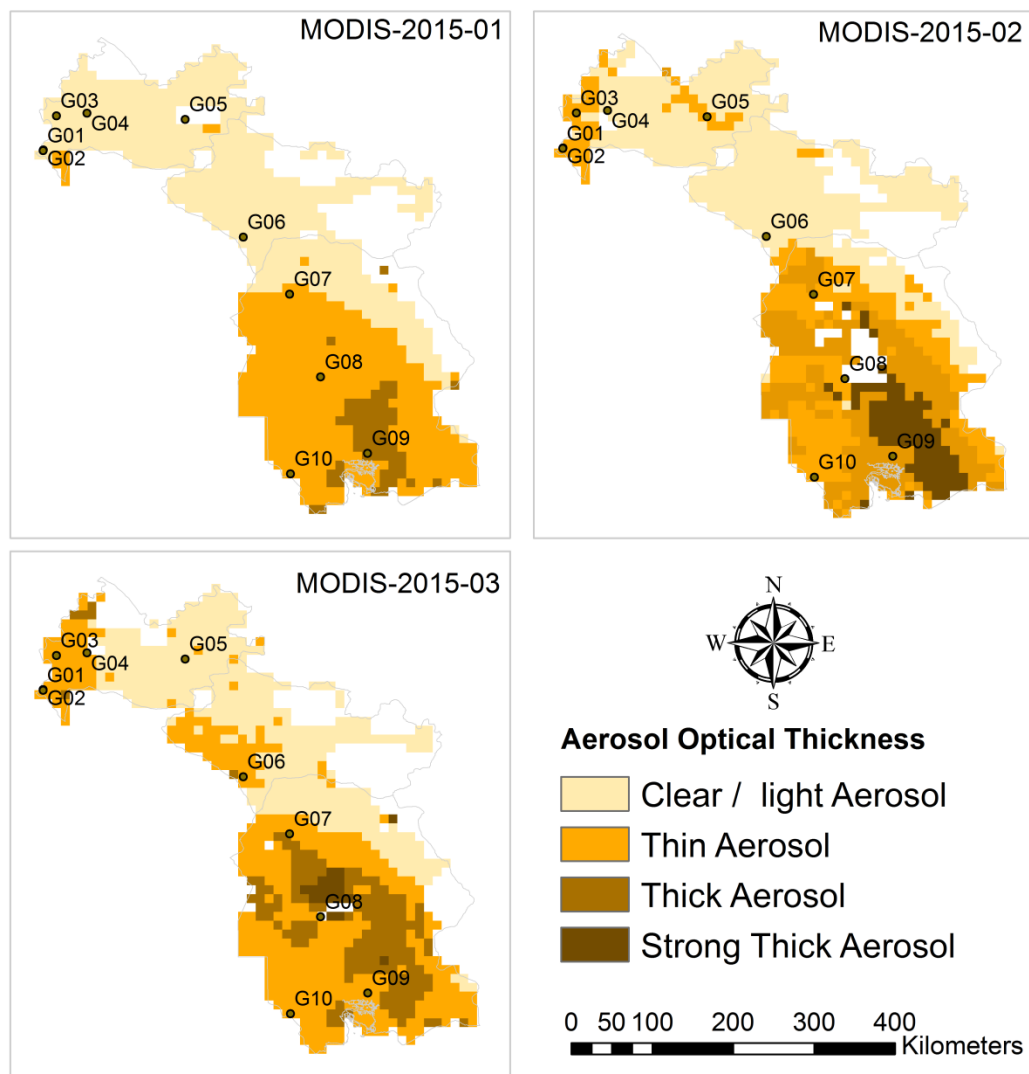
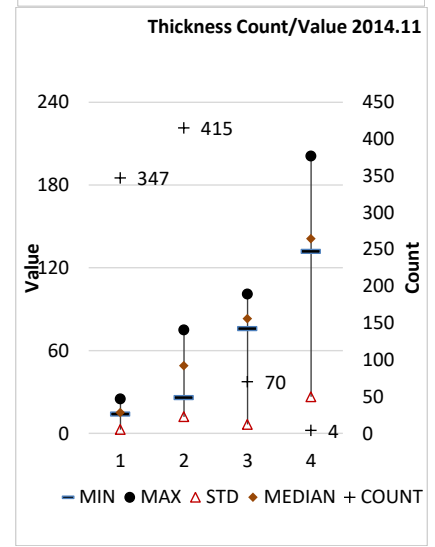
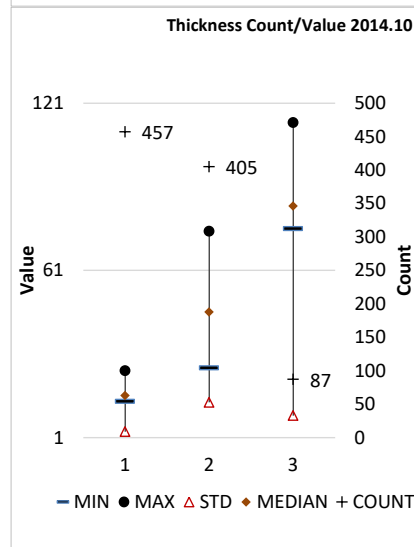
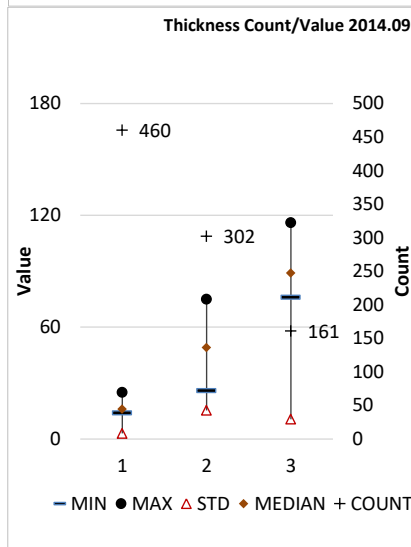
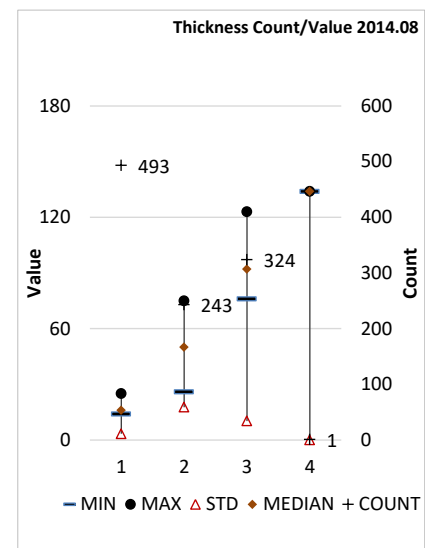
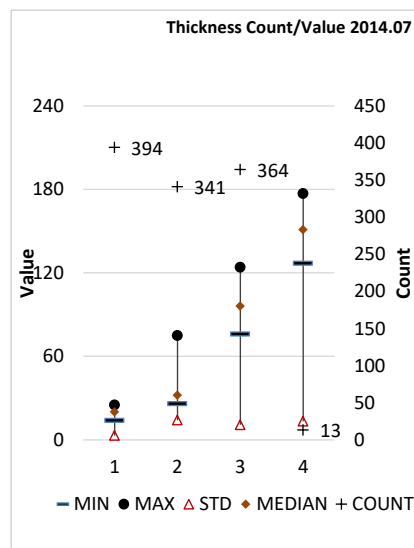
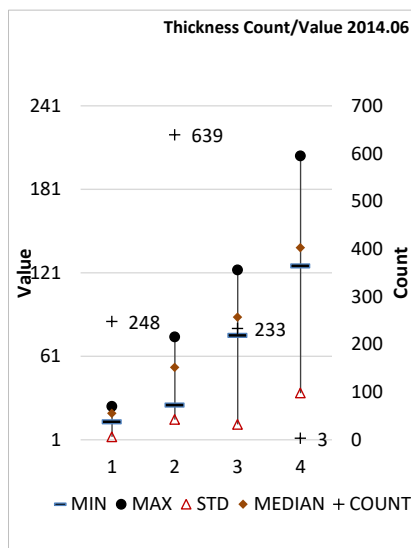
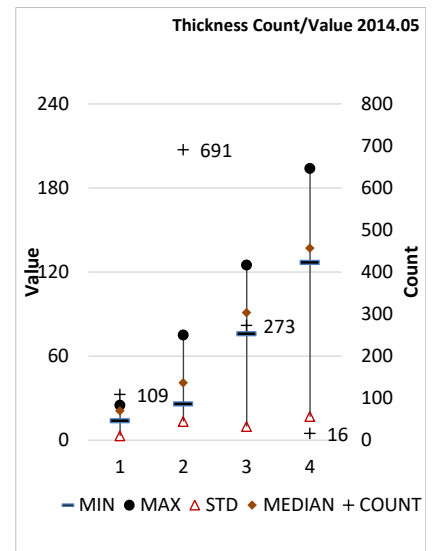
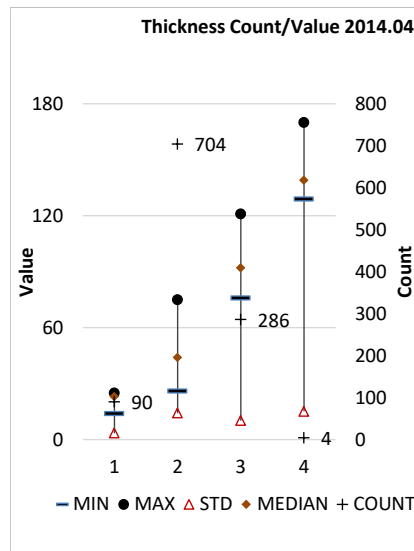
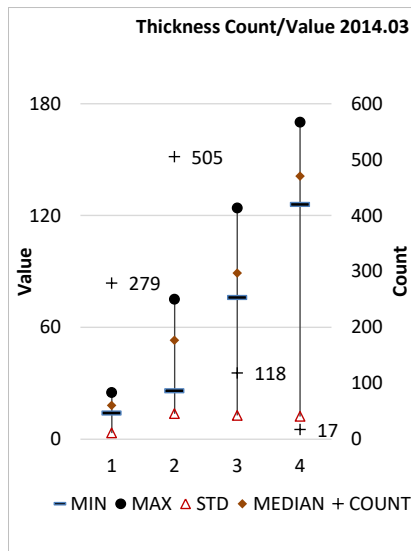


Figure 4.3 Average Aerosol Optical Depth 550 nm

*Whites have no pixel value, Average Aerosol Optical Depth 550 nm (Dark Target) monthly 0.1 degree. [MODIS-Terra MOD08_M3 v6.1] for April, 2014 until March, 2015, Region 45E, 30.0753N, 49.9658E, 36.4474N

Fig. 4.4 shows the count-value fluctuation in the monthly trends of the four thickness layers. It also illustrates the similar trends in AOT values for the Thin [2] and Thick [3] classifications; also illustrated are different variations in terms of extreme dust events such as the Strong Thick [4] or Clean from aerosols [1] in the entire study period. In other words, except for autumn and winter, the study area has experienced different monthly AOT variations with strong thickness aerosols and higher standard deviations that indicate dust events. In spring and summer, the study area exhibited the highest standard deviations, indicating that it is the area at most risk in terms of extreme dust events. In the detail for April, May and June, the standard deviations were relatively high in the area of section [c]. Standard deviations in each group of thickness just reflect the magnitude of variation in the group. The general trend in the standard deviation decreased in most of the gauge sites during the research period. A specific decline occurred in autumn and winter and was most likely due to the relative counted value of thickness layers.



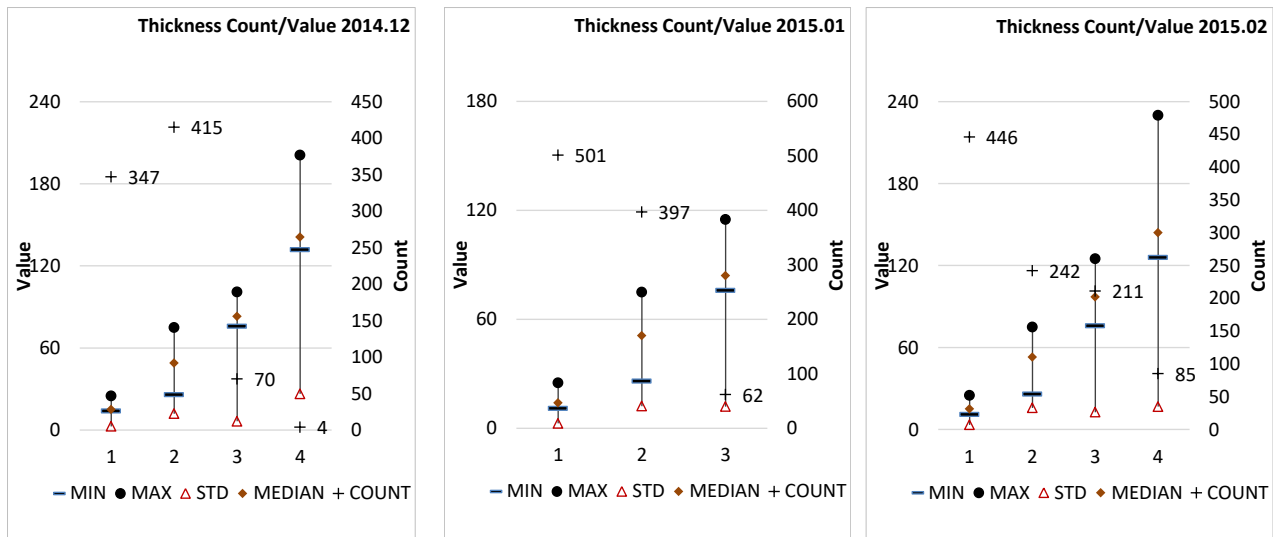


Figure 4.4 Temporal monthly means of dark-target MODIS AOT

*The left Y axis shows modified pixel values which represents min, max, median, and standard deviation values. The right label for vertical bar shows counting pixel values for the thickness classification.

4.3.3 HYSPLIT model output

The same temporal image data from NASA's Multi-angle Imaging SpectroRadiometer, called MISR, are applied to justify AOT. These likely quantified the ability of aerosol optical thickness (AOT) collection to retrieve thickness values from the pixel values of each point and were compared to the monthly data for the ground deposition rate (GDR). In addition to the aforementioned relationship between GDR and the variation of value of the optical thickness layer [4], the model outputs were characterized for summer and spring based on the ground gauge distributions. Therefore, the HYSPLIT model was running for location of endpoints for all sections, [a], [b], and [c] (Fig. 4.5).

As shown in Fig. 4.5, the model output simulated four days backward trajectory in spring and summer based on updrafts loaded for 100 m, 500 m, and 1000 m above ground level (AGL), with respect to the above ground surface level. The transport history relative to dust event frequency is shown to the end at 1000 UTC in 29th March 2014. The transport rate originated from west-north Syria and Mediterranean Sea, moved southward toward the center of Iraq, and reached section [a], section [b], and section [c]. This could also be seen in MODIS AOT retrievals (Fig. 4.6). Thus, it is reasonable to suggest that the high AOT are somehow linked with the backward trajectory from west in May, 2014 but not as clearly in March, 2014.

In contrast, the backward trajectories on 29 April, 2014 show trajectory flow derived from northwest of Saudi Arabia continuing northward to southeast of Iraq and is observed in both sections [a and b], while the backward trajectory flow passed directly over section [c] from section [b], which can be associated with the local influence flow. AOT mapping is not able to represent the deposition rate in section [a], [b], including the intensity of the dust transport rate.

The retrieved aerosol mass rate for January, 2015 has been verified by backward trajectories from the model output. Figure 9 shows the four days backward trajectories. The transport direction was influenced northward from Saudi Arabia at 1,500 m above ground level, crossing the Persian Gulf, and reaching the area of section [c]. The observation can be verified by the high thickness of pixel values from AOT ($AOT > 0.4$), which are linked into section [c]. It therefore seems that the value observations at section [b] and section [c] mainly have been derived from section [a] the same flow with respect to the underlying ground surface and almost zero AGL.

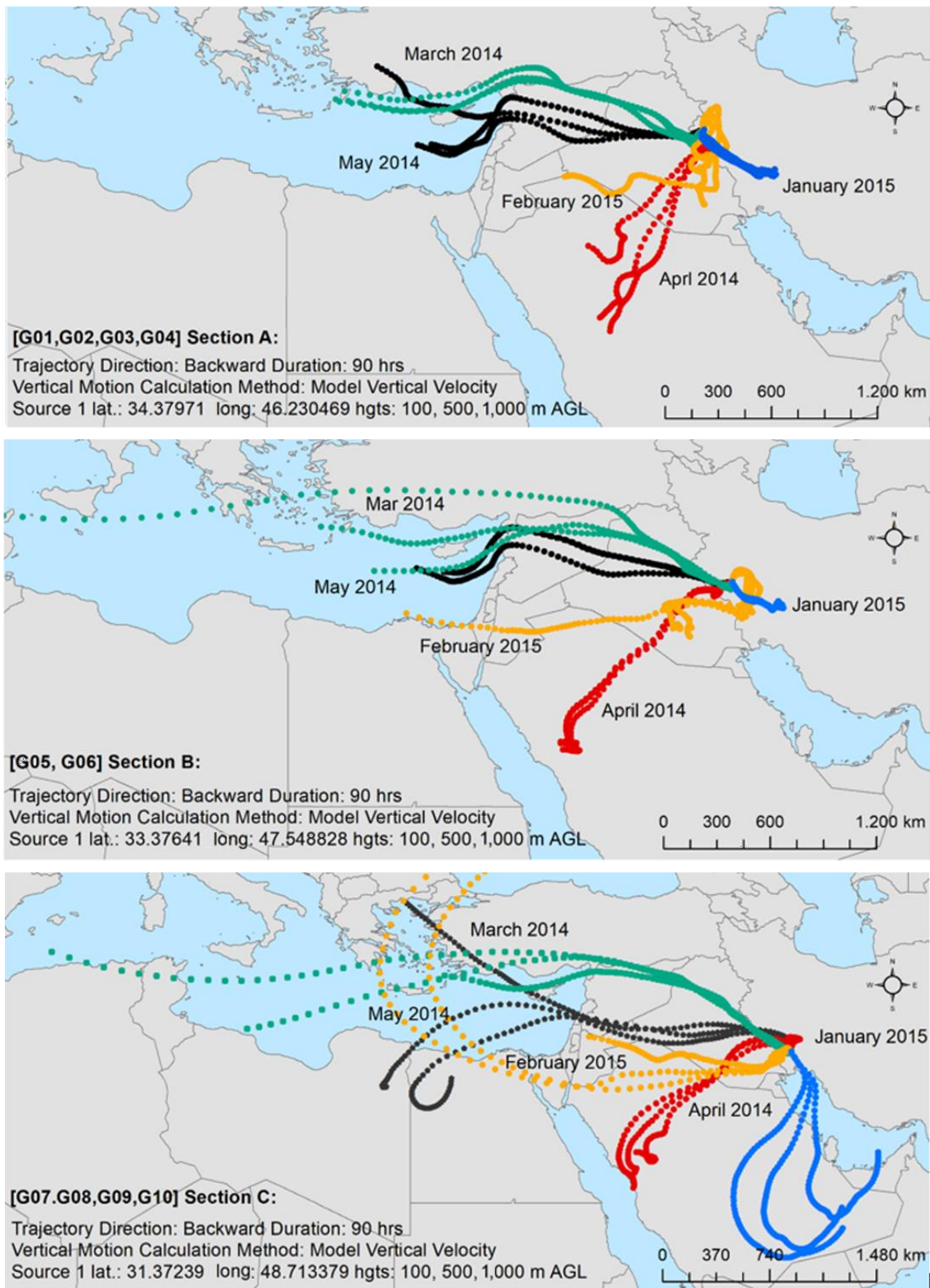


Figure 4.5 The model output from HYSPLIT for all sections A, B, and C

*Transport history relative on dust event frequency has been simulated four days backward trajectories for an ending time at 1000 UTC in 29th January, February 2015 and March , April, and May 2014.

The retrieved aerosol distributions on 22 February 2015 demonstrate that high AOT are linked to the back trajectory at 3,500 m AGL from the Mediterranean Sea, the extreme north of Saudi Arabia and through southern Iraq and reached the area of section [a].

The transport direction confirmed the impact of local dust contributions from southern Iraq adding to the surface layer before deposition in section [b]. This could also illustrate the cause of different dust event situations in section [a]. Maximum AOT values are combined with more intense flow from the north at 1,000 m above ground level (AGL) and dust flow from long distance transports directed from southern Iraq and the Mediterranean Sea.

4.4 Discussion

In this study, MODIS and MISR data are then compared with similar data from sampling periods preceding and following the dust events in order to validate the optical thickness of MODIS and MISR. Accordingly, the results of evaluating these data focusing on the retrieved AOT values, their differences and correlation are represented. MODIS and MISR onboard the Earth Observing System (Diner et al., 1998) have been extensively used for global dust observations (Xiao et al., 2009). In particular, the AOT product retrieved from visible and near infrared data can be used to monitor dust event (Washington et al., 2003; Levy and Hsu, 2015). The general patterns of the global aerosol fields retrieved by MODIS and MISR are remarkably similar (Huanyong, 1990), indicating a high comparability of both data products (Geogdzhayev et al., 2004; Yan et al., 2006; Huang et al., 2007; Guo et al., 2013). The case studies for this can be found for many different dust areas with attention to the Sahara desert (Zhang and Christopher, 2003; Koren et al., 2006; Schepanski et al., 2017), the Persian Gulf (Banks et al., 2017; Liu and Mishchenko, 2008), the Tarim River basin in north-western China (Yan et al., 2006; Huang et al., 2007), as well as the Indian subcontinent (Di Girolamo et al., 2004; Jethva et al., 2005; Tripathi et al., 2005; Prasad and Singh, 2007), including the Southern Hemisphere (Wu et al., 2009; Pinty et al., 2011). In fact, the magnitude of AOT differs between MODIS and MISR (Levy and Hsu, 2015) and its values have apparent seasonal variations (Yan et al., 2006; Huang et al., 2007). The observations from the same locations in different seasons have shown that MODIS performed better particularly in summer due to the relatively higher vegetation cover (Prasad and Singh, 2007). The MODIS aerosol retrieval method is unable to find dark pixels within the surface albedo channel (Levy and Hsu, 2015), while MISR can retrieve optical properties over a variety of terrains (Diner et al., 2001; Martonchik et al., 2004). Equally important, (Diner et al., 2001) showed that MISR AOT has a positive bias of 0.02 and an overestimate of 10% when compared to ground-based observations. That is to say, the MISR mean AOT is systematically larger than the MODIS values, which can be attributed to a relative calibration offset (Liu and Mishchenko, 2008).

With this in mind, Pearson correlation coefficients, using monthly average level 3 MODIS (MOD08 M3) and MISR (MIL3MAE) data have been computed. Monthly seasonal data from January, February, and March of 2015 as well as from March, April, and May of 2014 were used to calculate the correlation coefficients. Fig. 4.6 shows, that the correlation coefficient is relatively high for MODIS-MISR during May (0.71) and moderate in April (0.57), while the correlation is only little more than moderate in March (0.44). In agreement with Prasad and Singh, (2007) and reinforced by Liu and Mishchenko, (2008), the mean of the absolute differences of the averages of MODIS and MISR explains seasonal variation during the March and May compared to MODIS over section C in April.

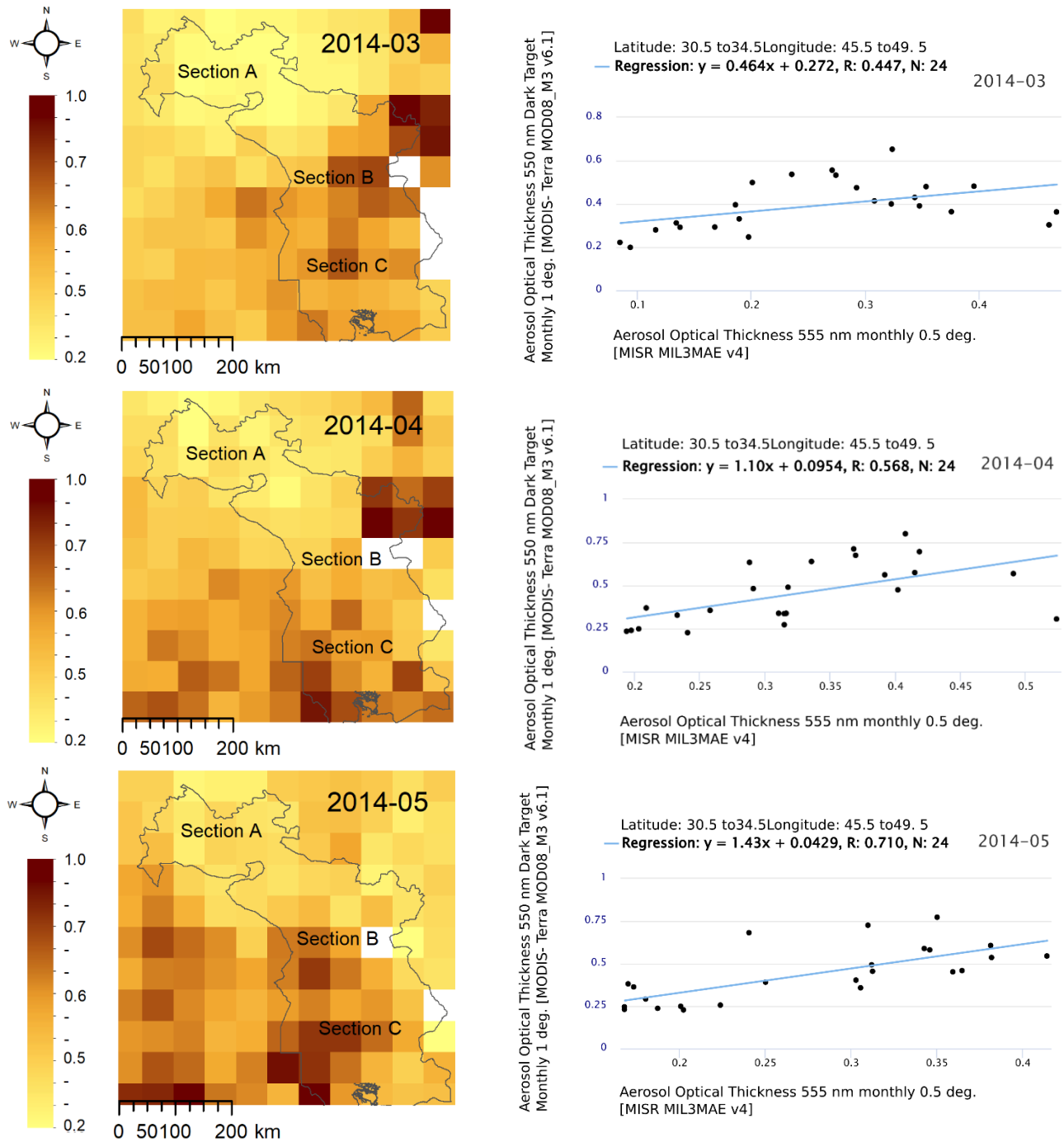


Figure 4.6 Captured from Giovanni MISR 555 nm and applied with a spatial resolution of 0.5 degree

It can also be seen in Fig. 4.7 that the correlation coefficient is relatively high for MODIS-MISR during February (0.75) and March (0.71) of 2015. In addition, the observed correlation data for January (0.64) agree very well with similar findings about seasonal variations retrieved from (Yan et al., 2006; Huang et al., 2007). Similarly, the mean of the absolute differences from the monthly average between both MODIS and MISR is consistent with the MODIS-AOT disability to identify dark pixels (Levy and Hsu, 2015). Also in agreement with Prasad and Singh, (2007), and given the good correlation of the global AOT of MODIS and MISR, MODIS proved to provide better results for this study area in March, April, and May due to high vegetation cover in sections [a], [b], and [c].

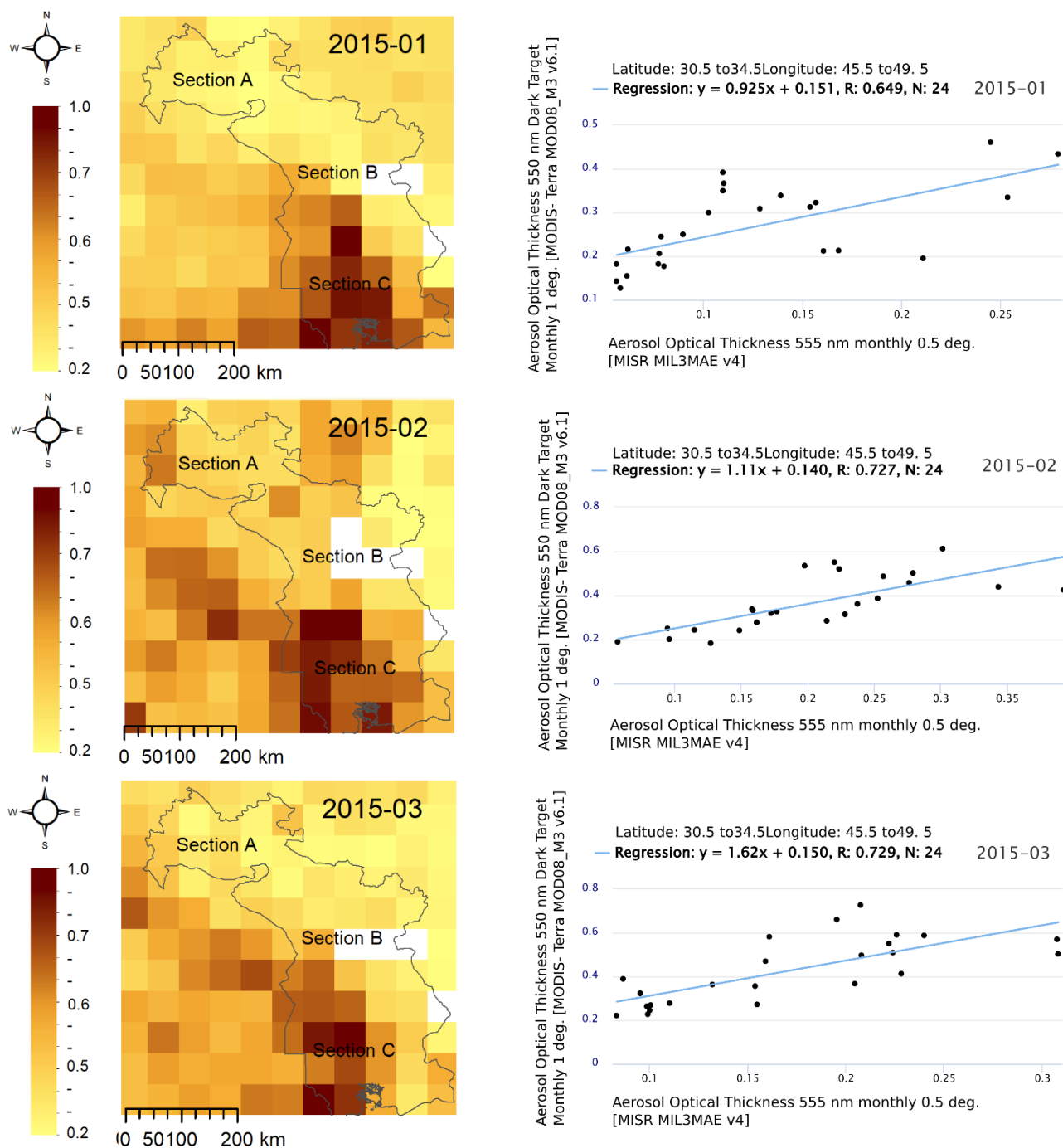


Figure.4.7 Captured from Giovanni MISR 555 nm and applied with a spatial resolution of 0.5 degree

With attention to seasonal ecological changes (Xu and Hu, 1996; Gao, 2000; Yang et al., 2002), results describing seasonal variation of dust events can be related to ecological and climatological characteristics of the environments. Prominent seasonal dust events have been reported during spring and summer in the Sistan region in eastern Iran (Abbasi et al., 2018). Aspiring above and beyond, the highest rates of atmospheric dust fallout in northeastern Iran occurred in summer (Ziyaee et al., 2018). However, recent studies from Central Asia for the period from 2003 to 2012 showed an increase of the seasonal dust deposition rate from spring to fall (Groll et al., 2013; Opp et al., 2017) in the Aral Sea region. Five dust storms have been reported in southwestern Iran during springtime of 2011, 2012 (Najafi et al., 2014), and 2014 (Foroushani et al., 2019). Moreover, dust loads from Africa and Asia were transported into the Arctic (Zwaafink et al., 2016) and deposition reached a maximum rate in spring (Stohl, 2006; Breider et al., 2014). Fiedler et al., (2014) reported that about 25 % of the total dust

emissions from the Sahara occur in spring due to seasonal cyclones over North Africa. As can be seen, in Fig. 4.5, the very similar backward trajectories distribution implies comparable wind directions and dust events in March and May of 2014. Not more than 30% of all air masses in February of 2015 were derived from the Mediterranean Sea, while twice as much has been received from Saudi Arabia and Iraq in April of 2014 and January of 2015.

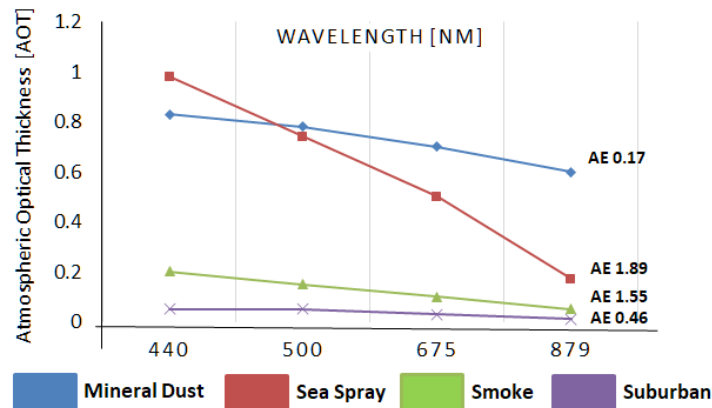


Figure 4.8 Providing Thickness properties by courtesy of NASA for AOT
 *User manual (Levy and Hsu, 2015) Collection 6.0 MODIS data in a publication

According to previous studies (Fig. 4.8), the AOT is classified from 0.1 to 1 in a dusty environment and higher in polluted regions in order to enumerate the principal thickness (Remer et al., 2006; Schaap et al., 2008; Levy and Hsu, 2015). This is a measure of how much light the airborne particles prevent from traveling through the atmosphere (Stockli and Jentoft, 2013). A lower optical thickness likely would have less impact on radiative forcing (Dubovik et al., 2002), while dense aerosols absorb and scatter incoming sunlight more effectively, thus reducing visibility and increasing optical thickness (Schaap et al., 2008). The variance in the layers is consistent with Levy and Hsu, (2015) for an optical thickness of less than 0.1 indicates a clear sky with maximum visibility, whereas a value of 1 indicates the presence of extreme density and very low visibility even at mid-day (Remer et al., 2006). Since the hypothesis behind this exercise is that AOT should show the same variation as GDR values collected in the study period, four layers of aerosol thickness were plotted to identify which one follows the variation in GDR values most closely. Fig. 14 shows the spatial gradient in AOT over the study area as calculated.

Each layer has a group of pixel values (0.0 -1.0) with a classification thickness of [1] for Clean, [2] for Thin, [3] for Thick, and [4] for a Strong thickness. The pixel-value count for each layer has been plotted on the primary Y-axis while GDR values (deposition rate mg/cm^2) are placed on the secondary Y-axis. All layers' thicknesses, derived from AOT, were highest in spring and summer with a maximum of 501 (layer [1]) and 704 (layer [2]), respectively. In autumn, the maximum values (364) were observed in layer [3]. Additionally a strong thickness was detected in layer [4] during spring with a maximum magnitude of 85. In general, the results in Fig. 4.9 reveal that the observed GDR-MODIS correlation from March 2014 to 2015 is indicative of a significant correlation with the thickness increase across study area, especially in layers [3] and [4].

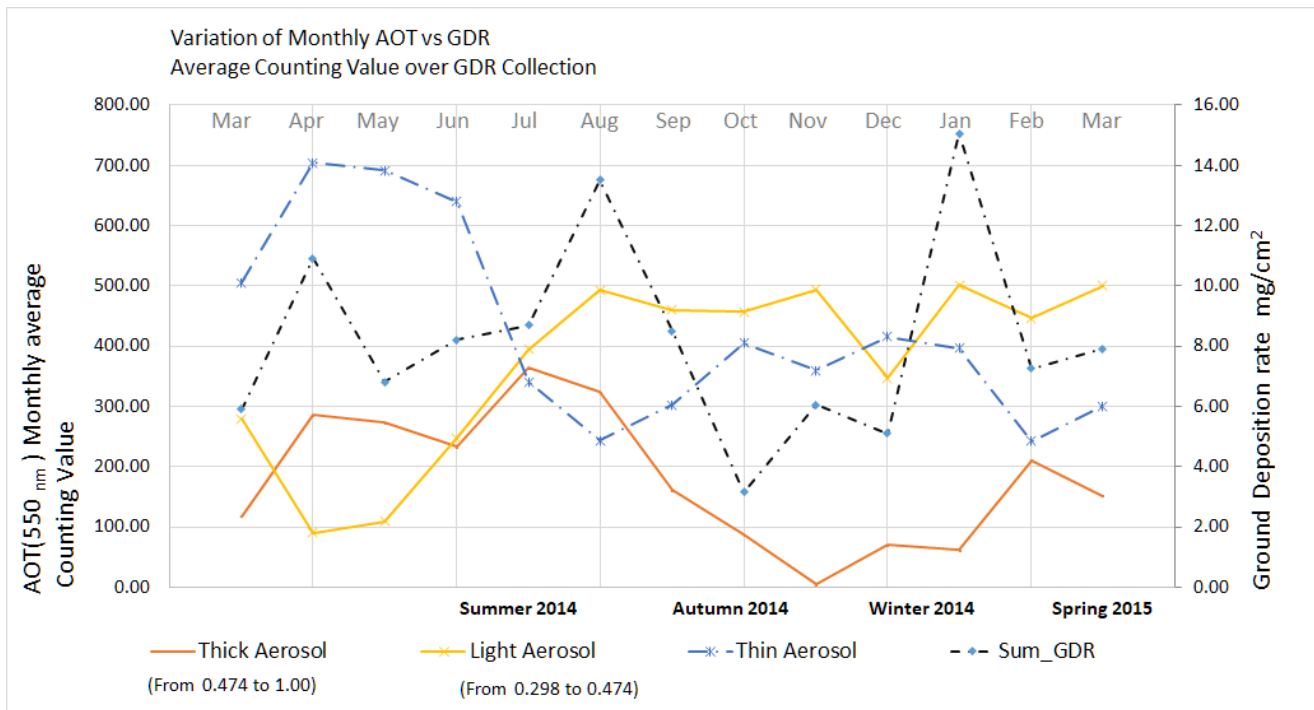


Figure.4.9 Spatial gradient in AOT compared with the fluctuation rate from ground deposition

In accordance with Levy and Hsu, (2015), Remer et al., (2006), and the overall trends illustrated in Fig. 4.10, layers [3] and [4] have notable magnitudes of correlation of 36% and 38% respectively. Whereas, layers [1] and [2] are represented as having almost negative or zero correlation, which is similar to the classification manual by Dubovik et al., (2002) and the MODIS data guidance from (Levy and Hsu, 2015). Results from comparisons of quantitative AOT retrieval could evaluate that the 1st and 2nd layer have some uncertainties in screening the dust deposition rates (GDR). With the results from negative and zero correlation value in layers [1] and [2], respectively, alpha levels were higher than the level of significance ($p > 0.05$ and probability with 98% confidence). Based on that, and in agreement with previous contributions about thickness classifications (Dubovik et al., 2002; Stockli and Jentoft, 2013; Levy and Hsu, 2015), the 1st and 2nd layers of AOT are hence removed from further calculations. Unlike the 1st and 2nd layers, the 3rd layer, together with the 4th, has almost the same variation as has been observed from GDR. As seen in Fig. 4.11, high layer variations were identified in spring and summer while only small changes have been observed in autumn and winter.

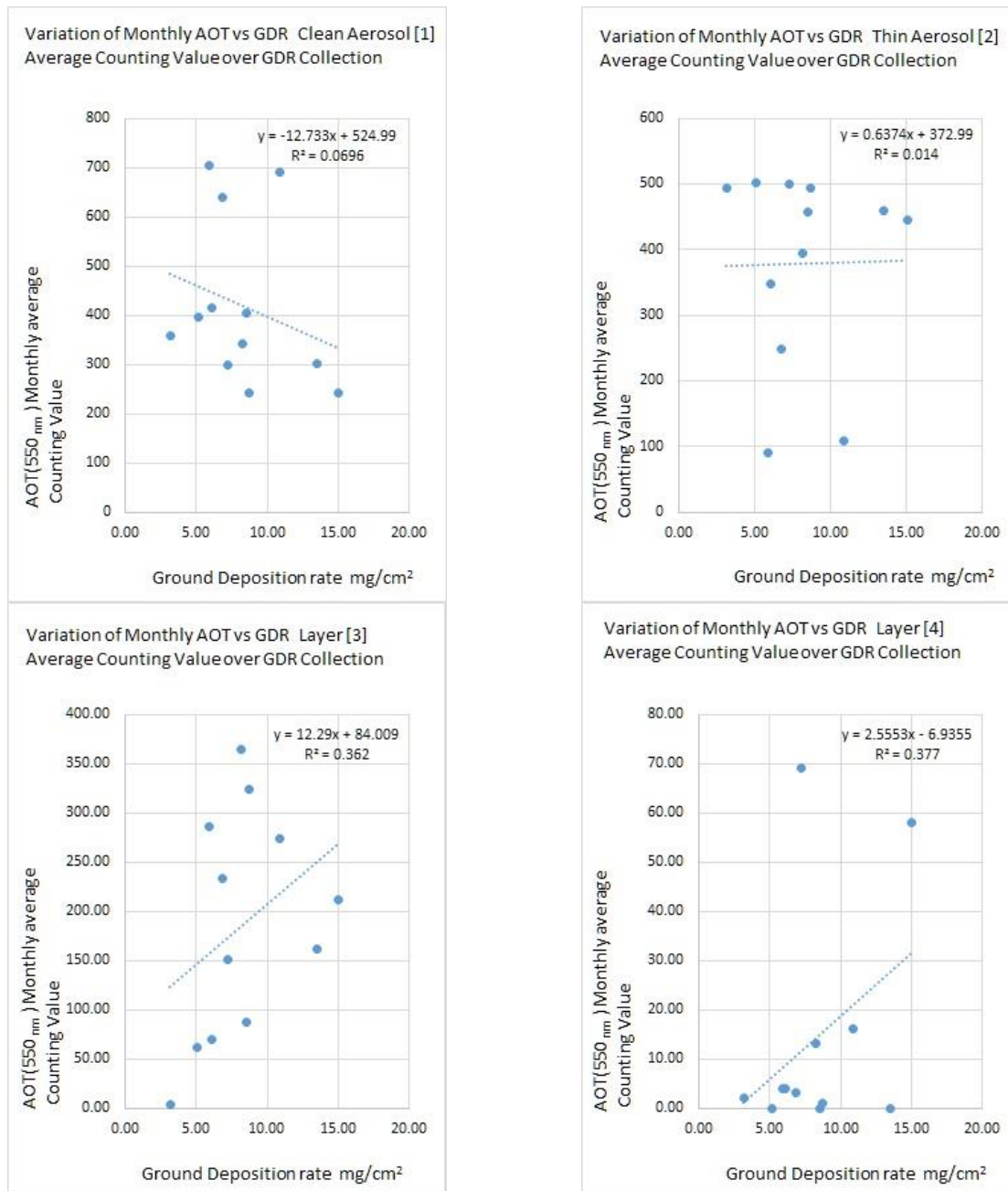


Figure 4.10 Correlation between atmospheric dust loading and dust accumulation

*Given time from March 2014 to 2015,

Differences from the gradient of the 3rd and 4th layers across all four season were identified as the same fluctuation values as for the GDR and showed a high correlation coefficient. This is also supported by the elevated AOT identified during spring and summer in southwestern Iran (Sabetghadam et al., 2018). These result are in great agreement with previously published evidence (Remer et al., 2006; Schaap et al., 2008; Levy and Hsu, 2015) which obtained the annual average AOT values from MODIS. In order to make the best use of satellite data and reduce the uncertainty of aerosol effects on regional and global climate, these satellite measurements need to be validated using ground-based observations. Intercomparison and validation of satellite products from different instruments with ground based observation reveal interesting details and allow building a long term database of aeolian dust deposition rates.

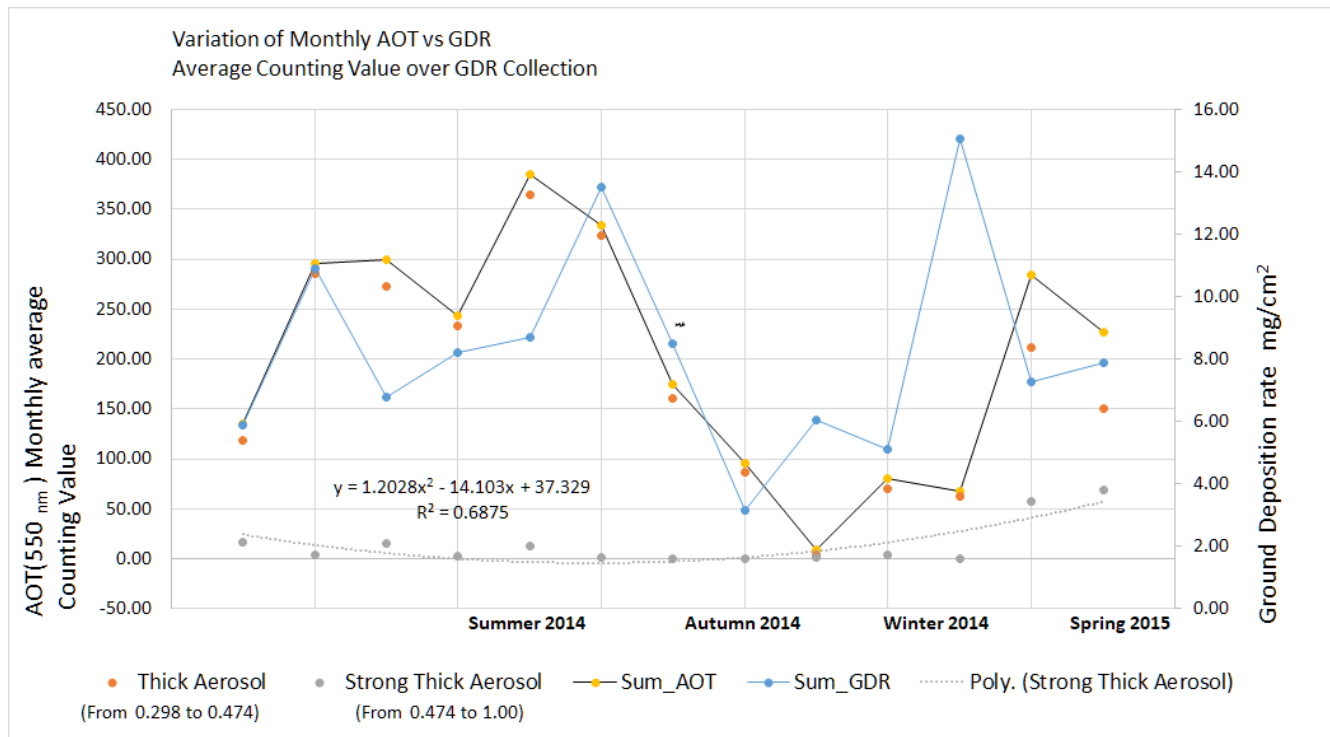


Figure 4.11 Consistency and variation change between the 3rd and 4th layers, including GDR

4.5 Conclusions and remarks

The ground deposition rate and geophysical variation in the dust event frequency, including mass and weight depositions, have been well measured. The composite product data from the MODIS and MISR on Terra satellite has been addressed. The findings suggest that, despite a slightly better estimation from the MISR when the sections [a], [b], and [c] are affected by a number of dust events, MODIS showed the better performance overall. The comparison of MODIS AOT with GDR over the study area shows a good agreement and approximately 65% of GDR falls within AOT limitations with uncertainty. Under the four layer conditions of aerosol thickness: Clean [1], Thin [2], Thick [3] and Strong Thick [4], the standard MODIS aerosol products were applied at regional scales to monitor both dust distributions and transports directions. However, the 1 degree and even the 0.5 degree spatial resolution data are insufficient to depict the deposition rate at local scales due to inherent dust variabilities, as well as the complexity of the land surfaces. In general, AOT retrieval can represent the strong seasonal and geographical variations in the dust deposition rates and their regional distribution. But due to the methodological limitations of these remote sensing approaches significant uncertainties remain and the possibilities to further our knowledge of dust deposition rates and frequencies in a high spatiotemporal resolution are limited. Thus, combining remote sensing and ground-based dust research is, in many cases, vital to estimate real-world effects of dust on the sink regions.

Although high spatial resolution products with a chronological record are suitable basics for the improvement of dust deposition analyses and ecosystem effect assessments, ground surveys are still a key point for analyzing airborne deposition. However, the deposition rate based on space model algorithms (AOT) remain the method of choice, even though they are relatively complicated and less accurate than surface observations (GDR), due to the lack of continuous atmospheric data at required scale over the area of interest. Besides, the development of ground surveying algorithms is necessary to make the estimations of the deposition rate more accurate. Therefore, current detection algorithms could be modified based on the technology of machine learning from physical characteristics, spatial and temporal distribution.

Acknowledgements

The authors would like to thank IRIMO (Iranian Meteorological Organization) for providing observation data for this research and MODIS Giovanni and NEO/NASA for their technical assistance and useful data. The authors gratefully acknowledge the NOAA Air Resources Laboratory team (ARL) for providing the HYSPLIT transport and dispersion model online.

** The Giovanni online data system, developed by the NASA GES DISC, has been used to obtain the surface AOT values test.

References

- Abbasi, H., Opp, C., Groll, M., Rohipour, H., Khosroshahi, M., Khaksarian, F., Gohardoust, A., 2018. Spatial and temporal variation of the aeolian sediment transport in the ephemeral Baringak Lake (Sistan Plain, Iran) using field measurements and geostatistical analyses. *Z. Für Geomorphol.* 61, 315–326.
- Abdou, W.A., Diner, D.J., Martonchik, J.V., Bruegge, C.J., Kahn, R.A., Gaitley, B.J., Crean, K.A., Remer, L.A., Holben, B., 2005. Comparison of coincident Multiangle Imaging Spectroradiometer and Moderate Resolution Imaging Spectroradiometer aerosol optical depths over land and ocean scenes containing Aerosol Robotic Network sites. *J. Geophys. Res.-Atmospheres* 110. <https://doi.org/Artn D10s07> 10.1029/2004jd004693
- Alizadeh Choobari, O., Zawar-Reza, P., Sturman, A., 2013. Low level jet intensification by mineral dust aerosols. *Ann. Geophys.* 09927689 31.
- Arimoto, R., Ray, B.J., Lewis, N.F., Tomza, U., Duce, R.A., 1997. Mass-particle size distributions of atmospheric dust and the dry deposition of dust to the remote ocean. *J. Geophys. Res.-Atmospheres* 102, 15867–15874. <https://doi.org/Doi 10.1029/97jd00796>
- Ashraf, A., Aziz, N., Ahmed, S.S., 2013. Spatio temporal behavior of AOD over Pakistan using MODIS data. Presented at the 2013 International Conference on Aerospace Science & Engineering (ICASE), IEEE, pp. 1–6.
- Ashrafi, K., Shafiepour-Motlagh, M., Aslemand, A., Ghader, S., 2014. Dust storm simulation over Iran using HYSPLIT. *J. Environ. Health Sci. Eng.* 12, 9.
- Balakrishnaiah, G., Kumar, K.R., Reddy, B.S.K., Gopal, K.R., Reddy, R.R., Reddy, L.S.S., Swamulu, C., Ahammed, Y.N., Narasimhulu, K., KrishnaMoorthy, K., Babu, S.S., 2012. Spatio-temporal variations in aerosol optical and cloud parameters over Southern India retrieved from MODIS satellite data. *Atmos. Environ.* 47, 435–445. <https://doi.org/10.1016/j.atmosenv.2011.10.032>
- Banks, J.R., Brindley, H.E., Stenchikov, G., Schepanski, K., 2017. Satellite retrievals of dust aerosol over the Red Sea and the Persian Gulf (2005–2015). *Atmospheric Chem. Phys.* 17, 3987–4003.
- Bieringer, P.E., Young, G.S., Rodriguez, L.M., Annunzio, A.J., Vandenberghe, F., Haupt, S.E., 2017. Paradigms and commonalities in atmospheric source term estimation methods. *Atmos. Environ.* 156, 102–112.
- Biniotoglou, I., Basart, S., Alados-Arboledas, L., Amiridis, V., Argyrouli, A., Baars, H., Baldasano, J.M., Balis, D., Belegante, L., Bravo-Aranda, J., 2015. A methodology for investigating dust model performance using synergistic EARLINET/AERONET dust concentration retrievals [Discussion paper].
- Breider, T.J., Mickley, L.J., Jacob, D.J., Wang, Q., Fisher, J.A., Chang, R.Y., Alexander, B., 2014. Annual distributions and sources of Arctic aerosol components, aerosol optical depth, and aerosol absorption. *J. Geophys. Res. Atmospheres* 119, 4107–4124.
- Cazacu, M.M., Tudose, O., Balanici, D., Balin, I., 2018. Research and development of commercial lidar systems in romania: critical review of the ESYRO lidar systems developed by sc enviroscopy SRL (ESYRO). Presented at the EPJ Web of Conferences, EDP Sciences, p. 11005.
- Cesnulyte, V., Lindfors, A., Pitkänen, M., Lehtinen, K., Morcrette, J.-J., Arola, A., 2014. Comparing ECMWF AOD with AERONET observations at visible and UV wavelengths. *Atmospheric Chem. Phys.* 14, 593–608.

- Chai, T., Draxler, R., Stein, A., 2015. Source term estimation using air concentration measurements and a Lagrangian dispersion model—Experiments with pseudo and real cesium-137 observations from the Fukushima nuclear accident. *Atmos. Environ.* 106, 241–251.
- Chen, B., Stein, A.F., Maldonado, P.G., de la Campa, A.M.S., Gonzalez-Castanedo, Y., Castell, N., Jesus, D., 2013. Size distribution and concentrations of heavy metals in atmospheric aerosols originating from industrial emissions as predicted by the HYSPLIT model. *Atmos. Environ.* 71, 234–244.
- Crosbie, E., Youn, J.-S., Balch, B., Wonaschütz, A., Shingler, T., Wang, Z., Conant, W.C., Betterton, E.A., Sorooshian, A., 2015. On the competition among aerosol number, size and composition in predicting CCN variability: a multi-annual field study in an urbanized desert. *Atmospheric Chem. Phys.* 15, 6943–6958. <https://doi.org/10.5194/acp-15-6943-2015>
- de Longueville, F., Ozer, P., Doumbia, S., Henry, S., 2013. Desert dust impacts on human health: an alarming worldwide reality and a need for studies in West Africa. *Int. J. Biometeorol.* 57, 1–19. <https://doi.org/10.1007/s00484-012-0541-y>
- Di Girolamo, L., Bond, T.C., Bramer, D., Diner, D., Fettingner, F., Kahn, R., Martonchik, J., Ramana, M., Ramanathan, V., Rasch, P., 2004. Analysis of Multi-angle Imaging SpectroRadiometer (MISR) aerosol optical depths over greater India during winter 2001–2004. *Geophys. Res. Lett.* 31.
- Diner, D., Abdou, W., Bruegge, C., Conel, J., Crean, K., Gaitley, B., Helmlinger, M., Kahn, R., Martonchik, J., Pilorz, S., 2001. MISR aerosol optical depth retrievals over southern Africa during the SAFARI-2000 dry season campaign. *Geophys. Res. Lett.* 28, 3127–3130.
- Diner, D.J., Beckert, J.C., Reilly, T.H., Bruegge, C.J., Conel, J.E., Kahn, R.A., Martonchik, J.V., Ackerman, T.P., Davies, R., Gerstl, S.A., 1998. Multi-angle Imaging SpectroRadiometer (MISR) instrument description and experiment overview. *IEEE Trans. Geosci. Remote Sens.* 36, 1072–1087.
- Draxler, R.R., Hess, G., 1998. An overview of the HYSPLIT_4 modelling system for trajectories. *Aust. Meteorol. Mag.* 47, 295–308.
- Dubovik, O., Holben, B., Eck, T.F., Smirnov, A., Kaufman, Y.J., King, M.D., Tanre, D., Slutsker, I., 2002. Variability of absorption and optical properties of key aerosol types observed in worldwide locations. *J. Atmospheric Sci.* 59, 590–608. [https://doi.org/10.1175/1520-0469\(2002\)059<0590:Voaaop>2.0.Co;2](https://doi.org/10.1175/1520-0469(2002)059<0590:Voaaop>2.0.Co;2)
- Fiedler, S., Schepanski, K., Knippertz, P., Heinold, B., Tegen, I., 2014. How important are atmospheric depressions and mobile cyclones for emitting mineral dust aerosol in North Africa? *Atmospheric Chem. Phys.* 14, 8983–9000.
- Gao, Q., 2000. Studies on the springtime dust storm of China. *CHINA Environ. Sci.-Chin. Ed.* 20, 495–500.
- Geogdzhayev, I.V., Mishchenko, M.I., Liu, L., Remer, L., 2004. Global two-channel AVHRR aerosol climatology: effects of stratospheric aerosols and preliminary comparisons with MODIS and MISR retrievals. *J. Quant. Spectrosc. Radiat. Transf.* 88, 47–59. <https://doi.org/10.1016/j.jqsrt.2004.03.024>
- Gerivani, H., Lashkaripour, G.R., Ghafoori, M., Jalali, N., 2011. The source of dust storm in Iran: a case study based on geological information and rainfall data. *Carpathian J. Earth Environ. Sci.* 6.

- Golitsyn, G., Gillette, D.A., 1993. A Joint Soviet-American Experiment for the Study of Asian Desert Dust and Its Impact on Local Meteorological Conditions and Climate - Introduction. *Atmospheric Environ. Part -Gen. Top.* 27, 2467–2470. [https://doi.org/Doi 10.1016/0960-1686\(93\)90017-S](https://doi.org/Doi 10.1016/0960-1686(93)90017-S)
- Groll, M., Opp, Chr., Aslanov, I., 2013. Spatial and temporal distribution of the dust deposition in Central Asia – results from a long term monitoring program. *Aeolian Res.* 9, 49–62. <https://doi.org/10.1016/j.aeolia.2012.08.002>
- Guo, J., Gu, X.F., Yu, T., Cheng, T.H., Chen, H., Xie, D.H., 2013. Trend analysis of the aerosol optical depth over china using fusion of MODIS and MISR aerosol products via adaptive weighted estimate algorithm. *Earth Obs. Syst. Xviii* 8866. <https://doi.org/Artn 88661x 10.1117/12.2024687>
- Huang, J., Minnis, P., Yan, H., Yi, Y., Chen, B., Zhang, L., Ayers, J.K., 2010. Dust aerosol effect on semi-arid climate over Northwest China detected from A-Train satellite measurements. *Atmospheric Chem. Phys.* 10, 6863–6872. <https://doi.org/10.5194/acp-10-6863-2010>
- Huang, J.P., Minnis, P., Yi, Y.H., Tang, Q., Wang, X., Hu, Y.X., Liu, Z.Y., Ayers, K., Trepte, C., Winker, D., 2007. Summer dust aerosols detected from CALIPSO over the Tibetan Plateau. *Geophys. Res. Lett.* 34. <https://doi.org/Artn L18805 10.1029/2007gl029938>
- Huanyong, H., 1990. The distribution, regionalization and prospect of China's population. *Acta Geogr. Sin.* 2, 139–145.
- Hutchinson, M., Oh, H., Chen, W.-H., 2017. A review of source term estimation methods for atmospheric dispersion events using static or mobile sensors. *Inf. Fusion* 36, 130–148.
- IRMO, 2016. I.R.OF IRAN Meteorological Organization.
- Jethva, H., Satheesh, S., Srinivasan, J., 2005. Seasonal variability of aerosols over the Indo-Gangetic basin. *J. Geophys. Res. Atmospheres* 110.
- Kaufman, Y.J., Koren, I., 2006. Smoke and pollution aerosol effect on cloud cover. *Science* 313, 655–8. <https://doi.org/10.1126/science.1126232>
- Kharazmi, R., Tavili, A., Rahdari, M.R., Chaban, L., Panidi, E., Rodrigo-Comino, J., 2018. Monitoring and assessment of seasonal land cover changes using remote sensing: a 30-year (1987–2016) case study of Hamoun Wetland, Iran. *Environ. Monit. Assess.* 190, 356. <https://doi.org/10.1007/s10661-018-6726-z>
- Kim, H.-S., Chung, Y.-S., Kim, J.-T., 2014. Spatio-temporal variations of optical properties of aerosols in East Asia measured by MODIS and relation to the ground-based mass concentrations observed in central Korea during 2001~ 2010. *Asia-Pac. J. Atmospheric Sci.* 50, 191–200.
- Koren, I., Kaufman, Y.J., Washington, R., Todd, M.C., Rudich, Y., Martins, J.V., Rosenfeld, D., 2006. The Bodélé depression: a single spot in the Sahara that provides most of the mineral dust to the Amazon forest. *Environ. Res. Lett.* 1, 014005.
- Lawrence, C.R., Neff, J.C., 2009. The contemporary physical and chemical flux of aeolian dust: A synthesis of direct measurements of dust deposition. *Chem. Geol.* 267, 46–63. <https://doi.org/10.1016/j.chemgeo.2009.02.005>
- Levy, R., Hsu, C., 2015. MODIS atmosphere L2 aerosol product. NASA MODIS Adapt. Process. Syst.
- Liu, L., Mishchenko, M.I., 2008. Toward unified satellite climatology of aerosol properties: Direct comparisons of advanced level 2 aerosol products. *J. Quant. Spectrosc. Radiat. Transf.* 109, 2376–2385. <https://doi.org/10.1016/j.jqsrt.2008.05.003>

- Lolli, S., Madonna, F., Rosoldi, M., Campbell, J.R., Welton, E.J., Lewis, J.R., Gu, Y., Pappalardo, G., 2018. Impact of varying lidar measurement and data processing techniques in evaluating cirrus cloud and aerosol direct radiative effects. *Atmospheric Meas. Tech.* 11, 1639–1651. <https://doi.org/10.5194/amt-11-1639-2018>
- Maiti, D., Prasad, B., 2016. Revegetation of fly ash—a review with emphasis on grass-legume plantation and bioaccumulation of metals. *Appl. Ecol. Environ. Res.* 14, 185–212.
- Martonchik, J.V., Diner, D.J., Kahn, R., Gaitley, B., Holben, B.N., 2004. Comparison of MISR and AERONET aerosol optical depths over desert sites. *Geophys. Res. Lett.* 31. <https://doi.org/Artn L16102> 10.1029/2004gl019807
- Müller, D., Lee, K., Gasteiger, J., Tesche, M., Weinzierl, B., Kandler, K., Müller, T., Toledano, C., Otto, S., Althausen, D., 2012. Comparison of optical and microphysical properties of pure Saharan mineral dust observed with AERONET Sun photometer, Raman lidar, and in situ instruments during SAMUM 2006. *J. Geophys. Res. Atmospheres* 117.
- Najafi, M.S., Khoshakhllagh, F., Zamanzadeh, S.M., Shirazi, M.H., Samadi, M., Hajikhani, S., 2014. Characteristics of TSP loads during the Middle East springtime dust storm (MESDS) in Western Iran. *Arab. J. Geosci.* 7, 5367–5381.
- Neff, J.C., Ballantyne, A.P., Farmer, G.L., Mahowald, N.M., Conroy, J.L., Landry, C.C., Overpeck, J.T., Painter, T.H., Lawrence, C.R., Reynolds, R.L., 2008. Increasing eolian dust deposition in the western United States linked to human activity. *Nat. Geosci.* 1, 189–195. <https://doi.org/10.1038/ngeo133>
- Ngan, F., Stein, A., Draxler, R., 2015. Inline coupling of WRF–HYSPLIT: Model development and evaluation using tracer experiments. *J. Appl. Meteorol. Climatol.* 54, 1162–1176.
- Offer, Z.Y., Goossens, D., 1994. The Use of Topographic Scale Models in Predicting Eolian Dust Erosion in Hilly Areas - Field Verification of a Wind-Tunnel Experiment. *CATENA* 22, 249–263. [https://doi.org/Doi 10.1016/0341-8162\(94\)90036-1](https://doi.org/Doi 10.1016/0341-8162(94)90036-1)
- Opp, C., Groll, M., Aslanov, I., Lotz, T., Vereshagina, N., 2017. Aeolian dust deposition in the southern Aral Sea region (Uzbekistan): Ground-based monitoring results from the LUCA project. *Quat. Int.* 429, 86–99. <https://doi.org/10.1016/j.quaint.2015.12.103>
- Pawan, Remer, Lorraine A., Levy, Gaitley, Remer, L.A., Holben, B., 2005. Pawan; Remer, Lorraine A.; Levy, Robert C; Mattoo, Shana. *Atmospheric Measurement Techniques; Katlenburg-Lindau Vol. 11, Iss. 5, (2018): 3145-3159. DOI:10.5194/amt-11-3145-2018. J. Geophys. Res. Atmospheres* 110. <https://doi.org/10.1029/2004JD004693>
- Pinty, B., Taberner, M., Haemmerle, V.R., Paradise, S.R., Vermote, E., Verstraete, M.M., Gobron, N., Widlowski, J.-L., 2011. Global-scale comparison of MISR and MODIS land surface albedos. *J. Clim.* 24, 732–749.
- Prasad, A.K., Singh, R.P., 2007. Comparison of MISR-MODIS aerosol optical depth over the Indo-Gangetic basin during the winter and summer seasons (2000–2005). *Multi-Angle Imaging SpectroRadiometer MISR Spec. Issue* 107, 109–119. <https://doi.org/10.1016/j.rse.2006.09.026>
- Prospero, J.M., Nees, R.T., Uematsu, M., 1987. Deposition rate of particulate and dissolved aluminum derived from saharan dust in precipitation at Miami, Florida. *J. Geophys. Res. Atmospheres* 92, 14723–14731. <https://doi.org/10.1029/JD092iD12p14723>

- Qi, Y.L., Ge, J.M., Huang, J.P., 2013. Spatial and temporal distribution of MODIS and MISR aerosol optical depth over northern China and comparison with AERONET. *Chin. Sci. Bull.* 58, 2497–2506. <https://doi.org/10.1007/s11434-013-5678-5>
- Reheis, M.C., Kihl, R., 1995. Dust deposition in southern Nevada and California, 1984–1989: Relations to climate, source area, and source lithology. *J. Geophys. Res. Atmospheres* 100, 8893–8918.
- Remer, L.A., Tanré, D., Kaufman, Y.J., Levy, R., Mattoo, S., 2006. Algorithm for remote sensing of tropospheric aerosol from MODIS: Collection 005. *Natl. Aeronaut. Space Adm.* 1490.
- Rezaei, M., Farajzadeh, M., Mielonen, T., Ghavidel, Y., 2019. Analysis of spatio-temporal dust aerosol frequency over Iran based on satellite data. *Atmospheric Pollut. Res.* 10, 508–519. <https://doi.org/10.1016/j.apr.2018.10.002>
- Rolph, G., Stein, A., Stunder, B., 2017. Real-time environmental applications and display system: READY. *Environ. Model. Softw.* 95, 210–228.
- Rubin, J.I., Reid, J.S., Hansen, J.A., Anderson, J.L., Holben, B.N., Xian, P., Westphal, D.L., Zhang, J., 2017. Assimilation of AERONET and MODIS AOT observations using variational and ensemble data assimilation methods and its impact on aerosol forecasting skill. *J. Geophys. Res. Atmospheres* 122, 4967–4992. <https://doi.org/10.1002/2016JD026067>
- Sabetghadam, S., Khoshsima, M., Alizadeh-Choobari, O., 2018. Spatial and temporal variations of satellite-based aerosol optical depth over Iran in Southwest Asia: Identification of a regional aerosol hot spot. *Atmospheric Pollut. Res.* 9, 849–856. <https://doi.org/10.1016/j.apr.2018.01.013>
- Schaap, M., Apituley, A., Timmermans, R., Koelemeijer, R., Leeuw, G. de, 2009. Exploring the relation between aerosol optical depth and PM 2.5 at Cabauw, the Netherlands. *Atmospheric Chem. Phys.* 9, 909–925.
- Schaap, M., Timmermans, R.M.A., Koelemeijer, R.B.A., de Leeuw, G., Builtjes, P.J.H., 2008. Evaluation of MODIS aerosol optical thickness over Europe using sun photometer observations. *Atmos. Environ.* 42, 2187–2197. <https://doi.org/10.1016/j.atmosenv.2007.11.044>
- Schepanski, K., Heinold, B., Tegen, I., 2017. Harmattan, Saharan heat low, and West African monsoon circulation: modulations on the Saharan dust outflow towards the North Atlantic. *Atmos Chem Phys* 17, 10223–10243. <https://doi.org/10.5194/acp-17-10223-2017>
- Sokolik, I.N., Winker, D.M., Bergametti, G., Gillette, D.A., Carmichael, G., Kaufman, Y.J., Gomes, L., Schuetz, L., Penner, J.E., 2001. Introduction to special section: Outstanding problems in quantifying the radiative impacts of mineral dust. *J. Geophys. Res.-Atmospheres* 106, 18015–18027. <https://doi.org/10.1029/2000jd900498>
- Song, C.H., Park, M.E., Lee, K.H., Ahn, H.J., Lee, Y., Kim, J.Y., Han, K.M., Kim, J., Ghim, Y.S., Kim, Y.J., 2008. An investigation into seasonal and regional aerosol characteristics in East Asia using model-predicted and remotely-sensed aerosol properties 8, 8661. <http://dx.doi.org/10.5194/acpd-8-8661-2008>
- Sorooshian, S., AghaKouchak, A., Arkin, P., Eylander, J., Foufoula-Georgiou, E., Harmon, R., Hendrickx, J.M.H., Imam, B., Kuligowski, R., Skahill, B., Skofronick-Jackson, G., 2011. Advanced Concepts on Remote Sensing of Precipitation at Multiple Scales. *Bull. Am. Meteorol. Soc.* 92, 1353–1357. <https://doi.org/10.1175/2011bams3158.1>
- Stein, A., Draxler, R.R., Rolph, G.D., Stunder, B.J., Cohen, M., Ngan, F., 2015. NOAA's HYSPLIT atmospheric transport and dispersion modeling system. *Bull. Am. Meteorol. Soc.* 96, 2059–2077.

- Stockli, R., Jentoft, M., 2013. Monthly MODIS aerosol optical thickness. *Natl. Aeronaut. Space Adm.*
- Stohl, A., 2006. Characteristics of atmospheric transport into the Arctic troposphere. *J. Geophys. Res. Atmospheres* 111.
- Taheri Shahraiyni, H., Karimi, K., Habibi Nokhandan, M., Hafezi Moghadas, N., 2015. Monitoring of dust storm and estimation of aerosol concentration in the Middle East using remotely sensed images. *Arab. J. Geosci.* 8, 2095–2110. <https://doi.org/10.1007/s12517-013-1252-3>
- Tegen, I., Lacis, A.A., 1996. Modeling of particle size distribution and its influence on the radiative properties of mineral dust aerosol. *J. Geophys. Res.-Atmospheres* 101, 19237–19244. <https://doi.org/10.1029/95jd03610>
- Tripathi, S., Dey, S., Chandel, A., Srivastava, S., Singh, R.P., Holben, B., 2005. Comparison of MODIS and AERONET derived aerosol optical depth over the Ganga Basin, India. Presented at the *Annales Geophysicae*, pp. 1093–1101.
- Wang, Y., Stein, A.F., Draxler, R.R., Jesús, D., Zhang, X., 2011. Global sand and dust storms in 2008: Observation and HYSPLIT model verification. *Atmos. Environ.* 45, 6368–6381.
- Washington, R., Todd, M., Middleton, N.J., Goudie, A.S., 2003. Dust-storm source areas determined by the total ozone monitoring spectrometer and surface observations. *Ann. Assoc. Am. Geogr.* 93, 297–313.
- Wesely, M.L., Hicks, B.B., 2000. A review of the current status of knowledge on dry deposition. *Atmos. Environ.* 34, 2261–2282. [https://doi.org/10.1016/S1352-2310\(99\)00467-7](https://doi.org/10.1016/S1352-2310(99)00467-7)
- Wu, D.L., Ackerman, S.A., Davies, R., Diner, D.J., Garay, M.J., Kahn, B.H., Maddux, B.C., Moroney, C.M., Stephens, G.L., Veefkind, J.P., Vaughan, M.A., 2009. Vertical distributions and relationships of cloud occurrence frequency as observed by MISR, AIRS, MODIS, OMI, CALIPSO, and CloudSat. *Geophys. Res. Lett.* 36. <https://doi.org/10.1029/2009gl037464>
- Xiao, N.C., Shi, T., Calder, C.A., Munroe, D.K., Berrett, C., Wolfenbarger, S., Li, D.M., 2009. Spatial characteristics of the difference between MISR and MODIS aerosol optical depth retrievals over mainland Southeast Asia. *Remote Sens. Environ.* 113, 1–9. <https://doi.org/10.1016/j.rse.2008.07.011>
- Xu, Q., Hu, J., 1996. Features of spatial and temporal distributions of the dust storms in northwest China. *Q. J. Appl. Meteorol.* 7, 479–482.
- Yan, H., Jiao, M., Bi, B., Zhang, C., 2006. Observation on sand dust aerosol in center of Taklimakan Desert. *J Desert Res* 26, 389–393.
- Yang, D., Yan, P., Xu, X., 2002. Characteristics of aerosols under dust and sand weather in Beijing. *J Appl Meteorol* 13, 185–194.
- Yasui, M., Zhou, J.X., Liu, L.C., Itabe, T., Mizutani, K., Aoki, T., 2005. Vertical profiles of aeolian dust in a desert atmosphere observed using lidar in Shapotou, China. *J. Meteorol. Soc. Jpn.* 83a, 149–171. <https://doi.org/10.2151/jmsj.83A.149>
- Yu, H., Dickinson, R.E., Chin, M., Kaufman, Y.J., Holben, B.N., Geogdzhayev, I.V., Mishchenko, M.I., 2003. Annual cycle of global distributions of aerosol optical depth from integration of MODIS retrievals and GOCART model simulations. *J. Geophys. Res. Atmospheres* 108. <https://doi.org/10.1029/2002JD002717>

- Yu, X., Lü, R., Kumar, K.R., Ma, J., Zhang, Q., Jiang, Y., Kang, N., Yang, S., Wang, J., Li, M., 2016. Dust aerosol properties and radiative forcing observed in spring during 2001–2014 over urban Beijing, China. *Environ. Sci. Pollut. Res.* 23, 15432–15442. <https://doi.org/10.1007/s11356-016-6727-9>
- Zhang, J., Christopher, S.A., 2003. Longwave radiative forcing of Saharan dust aerosols estimated from MODIS, MISR, and CERES observations on Terra. *Geophys. Res. Lett.* 30.
- Ziyadeh, A., Karimi, A., Hirmas, D.R., Kehl, M., Lakzian, A., Khademi, H., Mechem, D.B., 2018. Spatial and temporal variations of airborne dust fallout in Khorasan Razavi Province, Northeastern Iran. *Geoderma* 326, 42–55. <https://doi.org/10.1016/j.geoderma.2018.04.010>
- Zwaaftink, C.G., Grythe, H., Skov, H., Stohl, A., 2016. Substantial contribution of northern high-latitude sources to mineral dust in the Arctic. *J. Geophys. Res. Atmospheres* 121, 13–678.

5. Chemical Characterization of Aeolian Dust Deposition

Abstract

In the last decade, the southwestern and western provinces of Iran have been heavily affected by aeolian dust deposition. As a result, the elemental composition of soil surfaces is influenced by dust transport as well as precipitation, wind speed and direction. The relationship between daily recorded dust events and the elemental composition of the dust is studied in this paper. Strong correlations were detected between dust deposition rate from most deposition sites (G01-G10, except for G05, G06) and the dust event frequency. Correlations of different strengths have been revealed between the dust event frequencies (DEF), and the elemental classification matrix based on Airborne Metal Regulations.

As expected, high correlation values indicate high concentration contributions of elemental values to the aerosol, such as Na, Mn, As, Pb, from large-scale depositions in the south including Cr and V in the west. These findings also suggest that the major contributors of V, Cr, Co, Ni, Cu, Zn, As, Se, Cd, Ba, and Pb in the elemental concentrations may depend on the meteorological situation and correlation magnitude are associated with elements emanating from local anthropogenic activities.

Keywords: Dust composition; ICP-MS; metal concentrations; aeolian dust; Iran.

5.1 Introduction

Small solid and dry particles below 75 μm in diameter can be projected easily into the air by natural forces (Calvert, 1990) and remain suspended in the Earth's atmosphere long enough to substantially affect weather and climate (Prospero et al., 2002). In fact, while particles are airborne, they impact the regional and global climate (Tegen & Lacis, 1996; Wu et al., 2006; Carslaw et al., 2010) and interact with solar and terrestrial radiation, depending on their mineralogical composition, which is determined by the source of deposition (Okin et al., 2004; Mahowald et al., 2005, 2010). Although natural forces drive dust transport and deposition, dust transport processes can also be substantially constituted through human activities, including off-road driving (Gillies et al., 2005; Goossens et al., 2012), land use change (Reynolds et al., 2001; Gillies et al., 2005; Neff et al., 2008), and anthropogenic activities in general (Tegen et al., 2004; Mahowald et al., 2010). In the long run, airborne dust is slowly removed from the atmosphere under the influence of gravity, land shape, land cover (Slinn, 1982) such as vegetation that can obstruct dust movement effectively (Visser & Sterk, 2007), and dry deposition, which consists of all deposition that accounts for gravitational settling not associated with precipitation (Williams, 1982). In a similar manner, airborne particles function as condensation cores in the water cycle (Carslaw et al., 2010; Tao et al., 2012) and influence soil properties when they are deposited (Tegen & Lacis, 1996; Roth & Okada, 1998; Wu et al., 2006; Morman & Plumlee, 2013). Aeolian dust can also contribute to the spreading of viruses (Gerivani et al., 2011) that also have large-scale effects on the soil, vegetation, animals, and humans (Larssen & Carmichael, 2000; Basta & McGowen, 2004; Muhs & Benedict, 2006). Aside from immediate threats to the water cycle and soil properties, aeolian dust also causes considerable impairments in social (Opp et al., 2017) and commercial activities. As a result, the reduced visibility disrupts transport while the subsequent dust can damage engines and technical infrastructure, thus causing severe economic damages (Ai & Polenske, 2008; Miri et al., 2009). The sources and impacts of a wide range of chemical compounds have been examined and

classified in a range of studies (Mertz, 1981; Wang et al., 2006; Kabata-Pendias, 2010), while a comprehensive list of sources compiled for key elements (Geiger & Cooper, 2010) called the Airborne Metals Regulations (AMR) in aeolian particles worldwide (Table 5.1).

Table 5.1 Key indicating elements with associated sources

	Marine Aerosol; Crustal - Geologic	Vegetative Burning	Iron & steel industry; Oil combustion	Smelter; Automotive; Coal combustion
Indicating element	Na; Na, Mg, Al, Si, K, Ca, Mn, Fe, and Sr,	K, Zn Organic carbon, Elemental carbon	Fe, Cr, Ni, and Mg (fine PM) V and Ni	Cu, As, Cd, Pb, Ni; Br, Pb (fine PM), As, Se, Ba, and B
Source	NS	DS	DS	DS
Associate	DS (Na)	NS (K, Zn)	NS (Fe, Mg)	NS (Crustal elements)

*Example of key indicating elements with associated sources reproduced from Geiger and Cooper (2010)

Chemical gradients are constituted through natural sources (NS) such as Na, Mg, Al, Si, Ca, Mn, Fe, and Sr. Having signature from NS are referred as geologic origin and can thus be classified as coming from NS (Geiger & Cooper, 2010). It however, including local soils, weathered materials, and crustal minerals (El-Fadel & Hashisho, 2001; Geiger & Cooper, 2010) while elements such as Ni, Br or Pb have been classified as dominant sources (DS) mostly associated with industrial and commercial. With the same result further off-road driving are investigated (Charlesworth et al., 2003; Kreider et al., 2010; Evan et al., 2014). Residential fossil fuel burning such as Fe, Cr, Ni, Mg (fine PM), V, and Ni (Bilos et al., 2001; Schleicher et al., 2011) classified as coming from DS. Human activities, including, land use change (Marticorena et al., 1997; Richard Reynolds et al., 2001; Gillies et al., 2005; Neff et al., 2008) are indicated as NS and DS. According to the Airborne Metals Regulations(AMR), Na, Mg, Al, Si, Ca, Mn, Fe, and Sr is mainly of geologic origin and can thus be classified as coming from natural sources (NS), while elements such as Ni, Br or Pb are mostly associated with industrial and commercial activities, which have been classified as so-called dominant sources (DS) (Geiger & Cooper, 2010).

In either case, detailed knowledge of the dust source and of its activation process, dust event characteristics, dust transport routes, and deposition is crucial to fully understand this complex matter (Schepanski et al., 2017). Ultimately, synthesized dust observations need to examine the correlation among atmospheric dust functions, which is invoked the rate of dust deposition and dust event frequency (DEF) relation. Uncertainty has been evaluated for sampling and treatment result after chemical analysis carried out using ICP-MS. Later, attempt to identify the connections between the proximity to potential sources, including NS and DS by means of the element composition. This information is important to understand how anthropogenic activities can directly affect the elemental composition of aeolian particles. The results presented here are the products of a complex study from the west to the southwest of Iran located between latitudes 47.101335° and 49.163632°E, longitudes 34.353365° and 30.584651°N.

5.2 Material and method

Large correlation data sets of dust event history and deposition rate based on true-table are obtained per month. In with deposition rate and event history relation, inter-element correlation of chemical characteristics of samples addressed effect to aerosol from dominant and natural sources regarding Airborne Metal Regulation (AMR).

5.2.1 Measurement dependence of dust collection

Both gravimetric and directional dust samplers were constructed and installed from G01 to G10 at a 2 m height above ground (Chapter 3, 3.2.1) to observe deposited particulate matter that settles from the air. The sampler design was deliberately kept simple to ensure long-term durability and easy maintenance. Each sampler consisted of a plastic container with a surface area of 314 cm² (inverted Frisbee design) and a paper inlay for the passive dust collection.

5.2.2 Chemical composition

After dust sample taken from the field, all extraneous material and particulate contaminants (insoluble pieces, high mass loading of surfactants, tissue, etc) removed from samples. The DIN EN ISO 17294-2 (Beuth, 2004); (EN ISO 17294-2, 2016) guideline on quantifying dissolved elements using the ICP-MS was used for determining the elemental composition of the dust samples. Accurate measurement and identical process are done by weighing for one gram of each sample (Chapter 3, 3.4.2).

5.2.3 Statistical analysis

The inter-element correlation values of 20 elements to the DEF and its weight as based on the Airborne Metal Regulations index has been classified into four matrices. Correlation strength may be due to the exposure of aerosol and dust particles to extra elements throughout the dust's travel history. In either case, the correlation strength may be related to distance from the source, the wind direction, the meteorological situation, and industrial and commercial activities nearby.

5.3 Results and discussion

5.3.1 Contribution of wind aspects

The wind roses show the time ratio where winds blow from a particular direction at a certain speed (Fig. 5.1). To emphasize this dynamic, the direction has been marked using an external arc with a different colour. Exterior red arcs from G01 to G10 illustrate that the maximized key-direction between 180 and 360 degrees comprised 50% to 100% of all monthly wind direction from northwest to southwest, with an exception at G08 where the wind almost altered 360 degrees at a maximum speed value of 2 (m/s). However, winds from eastern directions were rarely detected at a maximum speed value of 1 (m/s) at G03, G04 and almost 2 (m/s) at G07 and G08. As shown in Fig.6, a strong key direction is indicated a speed value of 4 (m/s) at G01 and G02 for southwest winds, while northwest winds were coupled with the same speed value at G09 and G10. In addition, winds from the north and west blew up to 3 (m/s) at G06, whereas the same strong value for wind speed was also indicated at G07 from the west. The key-directions at G05 illustrated the wind blew up to 2 (m/s) from the northwest.

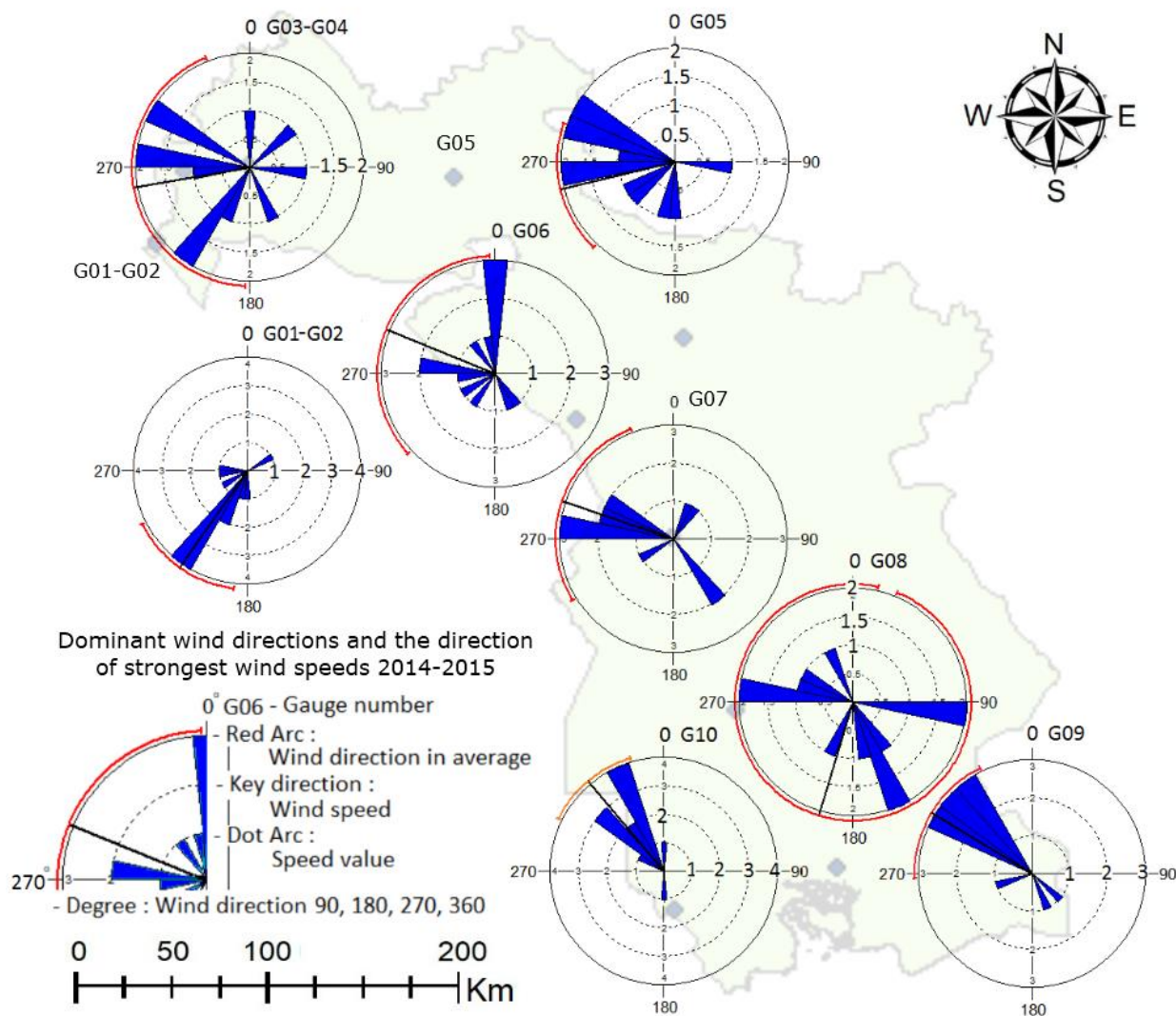
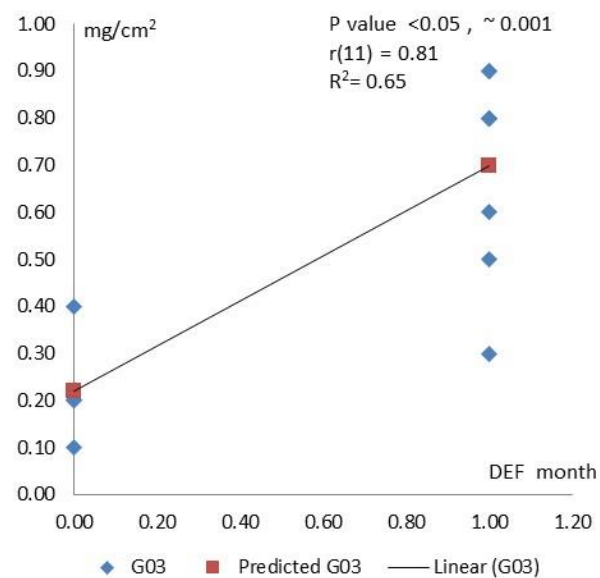
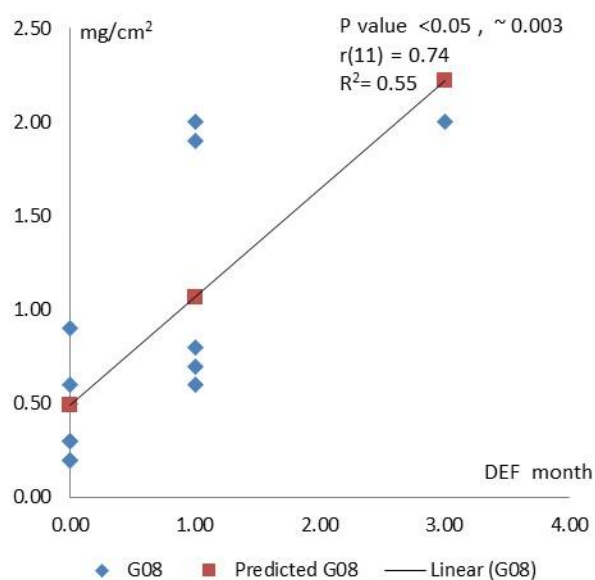
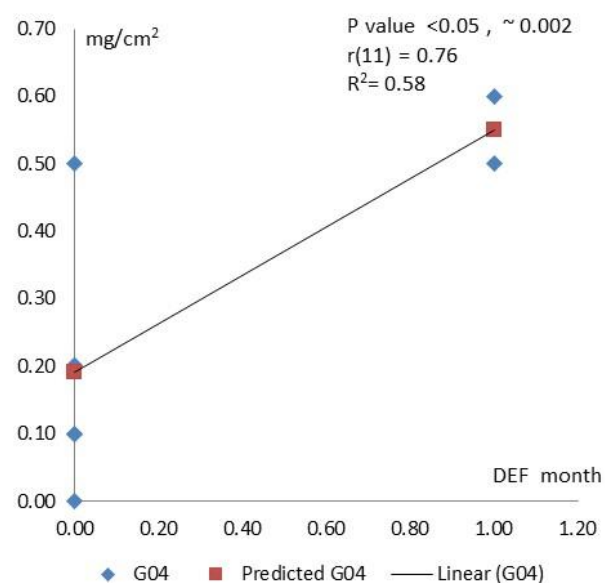
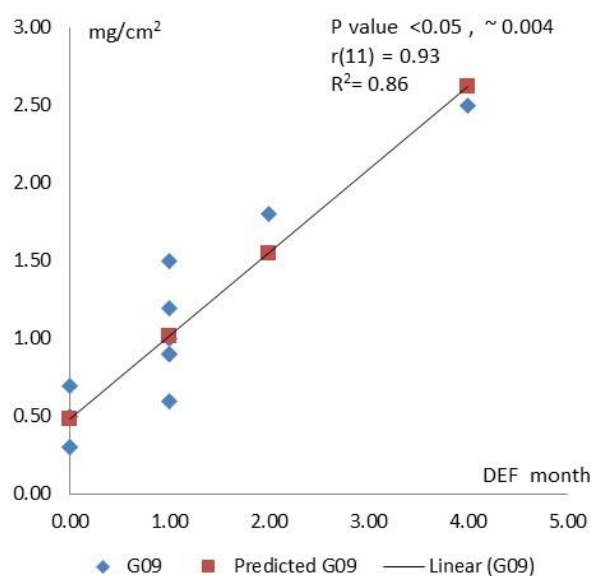
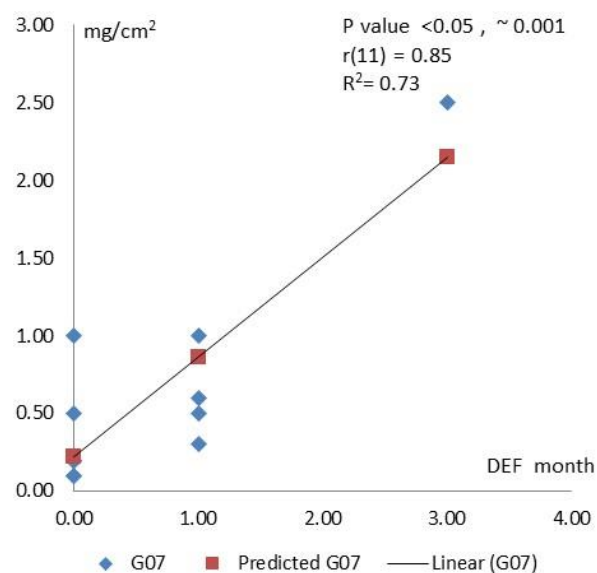
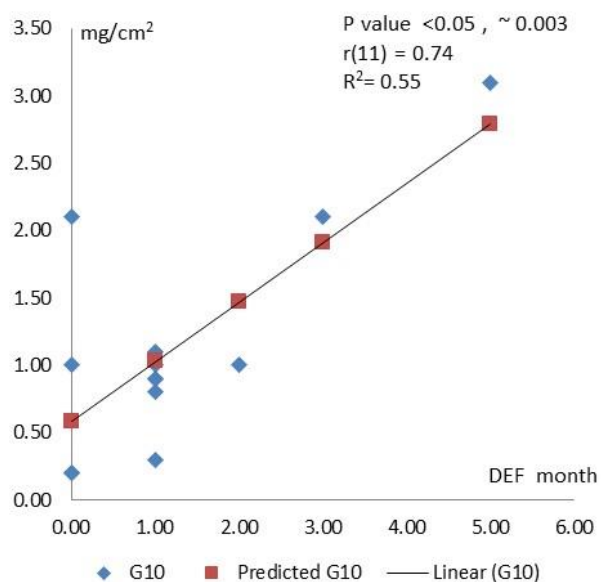


Figure 5.1 The wind rose speed and direction on data reproduced from IRMO

5.3.2 Deposition Rate and Dust Event History

Dust event frequency in concert with the deposition rate is represented in Table 5.2. While DEF values increased to 2, 3, or 5 times evidence of dust per month in the south and west, the DEF values at G05 and G06 were zero. The high magnitude of DEF was observed in the south for G09 and G10 during January and February 2015. The same values were also found in the west for G01 and G02 during March, April, and May 2014.



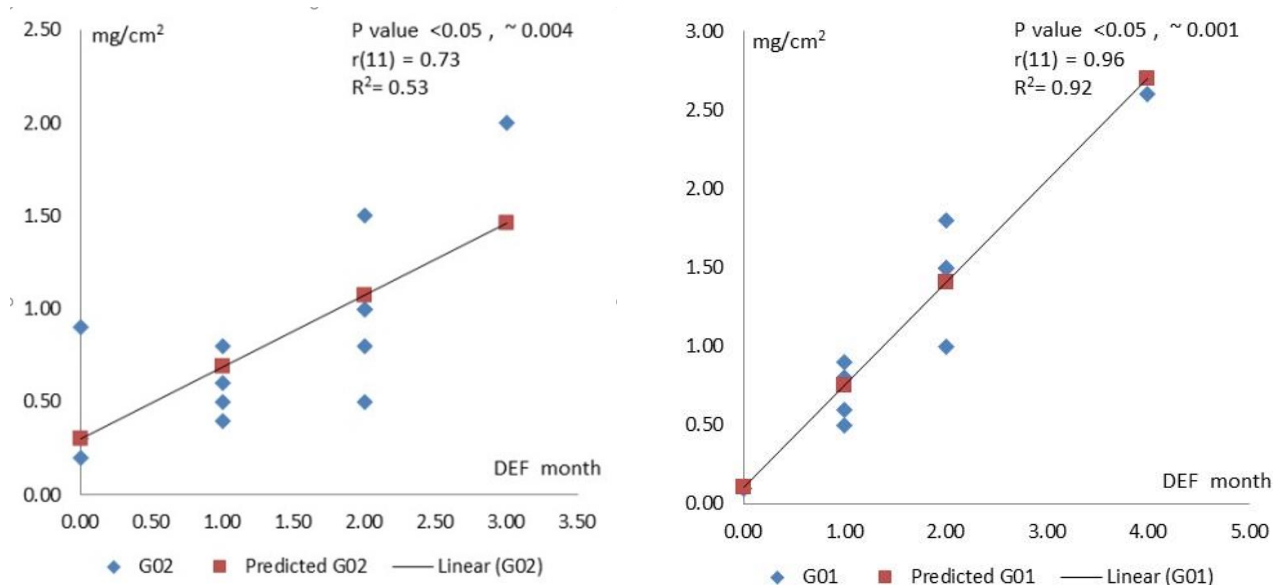


Figure 5.2 Correlation data between the DEF (horizontal) and Wt (vertical)

*Predicted lines were presented in April and May 2014 for G01 and G02, January and February 2015 for G09 and G10.

The average dust deposition rates ranged from 0.3 (mg/cm²) (G04-G06, Table 6) to 1.2 (mg/cm²) (G01), which equals the monthly field deposition rates of 30-120 (kg ha⁻¹), while most stations, recorded a maximum between 2 and 3 (mg/cm²) (Table 5.2). Therefore, the correlation values of DEF and the observation report from the dust deposition value can be considered. The monthly report from sites G01, G03, G04, G07, G08, G09, G10 indicated a strong correlation between DEF values and Dust Weight (Wt). Correlation magnitudes of 0.35, 0.49, and 0.69 were indicated for the Wt numbers of G05, G02, and G08, respectively.

For all gauges site in the red block, significant and correlation value are shown in Fig. 5.2. We note that more correlative data between the DEF and Wt were presented in April and May 2014 for G01 and G02 significantly with $P=0.001$, and $P=0.004$ similarly, in with significant at $P=0.004$, and $P=0.003$ a high correlation value was observed during January and February 2015 at G09 and G10.

5.3.3 Chemical Characterization of Samples

Results from these ICP-MS analyses must be split into four groups to support the value and interpretation of the elements, as well as find any deviation from anthropogenic activities. As shown in Table 5.3, results from the characterized chemical value based on AMR were deployed through the measurement point to articulate the spatial and temporal classifications that were made by characterizing the chemical composition of particle matter.

Table 5.2 Dust deposition rates vs dust event frequency (DEF)

Chronic		Sample sites G01-G10 (mg cm ⁻²)																			
Month	Year	G01	DEF	G02	DEF	G03	DEF	G04	DEF	G05	DEF	G06	DEF	G07	DEF	G08	DEF	G09	DEF	G10	DEF
Mar	2014	0.6	1	0.8	1	0.2	0	0.2	0	0.5	0	0.2	0	0.2	0	0.7	1	0.6	1	1.0	2
Apr	2014	2.6	4	2.0	3	0.5	1	*2	0	0.2	0	0.2	0	1.0	0	0.5	0	0.9	1	0.8	1
May	2014	1.0	2	*0.5	2	0.3	1	*3	0	0.3	0	0.1	0	0.5	0	0.2	0	0.5	0	0.2	0
Jun	2014	1.5	2	*0.8	2	0.8	1	0.2	0	1.0	0	0.2	0	0.5	1	0.6	1	1.0	1	1.0	1
Jul	2014	0.8	1	0.5	1	0.8	1	0.2	0	0.9	0	0.3	0	0.6	1	1.9	1	1.2	1	0.9	1
Aug	2014	1.5	2	1.0	2	0.9	1	0.0	0	2	0	0.6	0	0.3	1	*2	1	1.8	2	2.1	3
Sep	2014	1.5	2	1.5	2	0.9	1	0.5	0	1	0	*15.9	0	0.2	0	0.6	0	0.9	1	0.9	1
Oct	2014	0.9	1	0.6	1	0.2	0	0.2	0	0.1	0	*9.5	0	0.2	0	0.3	0	0.3	0	0.3	1
Nov	2014	*2	0	0.9	0	0.2	0	0.2	0	0.1	0	1.0	0	0.2	0	0.2	0	0.5	0	0.2	0
Dec	2014	*1.5	0	0.2	0	0.1	0	0.2	0	0.2	0	0.2	0	*0.9	0	0.3	0	0.3	0	1.0	0
Jan	2015	1.8	2	1.0	2	0.8	1	0.6	1	0.2	0	0.3	0	2.5	3	2.0	3	2.5	4	3.1	5
Feb	2015	0.5	1	0.4	1	0.6	1	0.2	0	0.2	0	0.1	0	*1.7	0	0.8	1	1.5	1	1.1	1
Mar	2015	0.8	1	0.3	0	0.4	0	0.5	1	0.6	1	0.2	0	1.0	1	0.9	0	0.7	0	2.1	0
Average		1.20		0.80		0.50		0.30		0.30		0.30		0.70		0.80		1.00		1.10	
Min		0.50		0.20		0.10		0.00		0.10		0.10		0.20		0.20		0.30		0.20	
Max		2.60		2.00		0.90		3.00		2.00		15.9		2.50		2.00		2.50		3.10	
Total		17.0	19	10.5	17	6.7	8	8.0	2	7.3	1	28.8	0	9.8	7	11.0	8	12.7	12	14.7	16
Correlation		0.96		0.49		0.81		0.73		0.35		0.00		0.85		0.69		0.93		0.74	
P-Value<		0.05		0.05		0.05		0.05		NA		NA		0.05		0.05		0.05		0.05	
R Square		0.55		0.86		0.55		0.73						0.58		0.68		0.53		0.92	

*Dust deposition rates (Wt. in mg cm⁻²) and dust event frequency (DEF) in the grey columns (events/month) from the sites G01 to G10 during March 2014 and March 2015, as well as the Pearson correlation for each station. Unusual values are highlighted in a “~” prefix, are removed from the calculation and are not influence on results.

Table 5.3 The total element concentrations in the southern and western parts of the study area (in µg/g)

Elements/ samples		*West-2014/01/04-05		*South-2015/01/01-02		Element concentrations (µg/g)				
		W14104	W14105	S15101	S15102	Ave	S.D	Max	Min	Mean(SD)
Matrice	EF	3.42	2.00	4.87	1.15	1.34	1.16	4.87	0.00	1.34±1.16
AMR	Wt mg/cm ²	2.48	0.94	3.15	1.47	1.19	0.69	3.15	0.23	1.19±0.69
1	Na	4.23	2.97	5.13	1.28	4.20	1.79	9.12	1.28	4.20±1.79
	Mg	86.01	62.64	52.08	37.52	62.28	20.04	104.75	30.38	62.28±20.04
	Al	39.32	34.33	30.98	21.02	29.86	8.29	41.15	16.08	29.86±8.29
	Si	11.58	3.62	2.20	2.27	4.46	4.26	14.05	-0.06	4.46±4.26
	K	19.37	16.58	13.08	7.42	14.85	5.52	31.25	6.14	14.85±5.52
	Ca	694.62	554.38	235.30	147.70	400.91	238.83	725.00	110.50	400.91±238.83
	Mn	1.72	1.48	1.54	1.24	1.47	0.41	2.90	0.90	1.47±0.41
	Fe	92.57	77.23	75.92	56.99	70.98	18.30	98.45	43.00	70.98±18.30
	Sr	14.08	12.42	0.88	0.48	0.00	0.01	0.01	0.00	0.00±0.01
2	K	19.37	16.58	13.08	7.42	14.85	5.52	31.25	6.14	14.85±5.52
	Zn	2.04	0.00	5.29	1.15	1.74	1.61	5.29	0.00	1.74±1.61
3	Cr	0.43	0.17	0.24	0.15	0.29	0.13	0.65	0.11	0.29±0.13
	Fe	92.57	77.23	75.92	56.99	70.98	18.30	98.45	43.00	70.98±18.30
	Mg	86.01	62.64	52.08	37.52	62.28	20.04	104.75	30.38	62.28±20.04
	Co	0.05	0.05	0.04	0.03	0.04	0.02	0.10	0.01	0.04±0.02
	Ni	0.44	0.36	0.38	0.21	0.32	0.09	0.45	0.16	0.32±0.09
	V	0.15	0.15	0.12	0.11	0.15	0.05	0.30	0.08	0.15±0.05
4	Cu	0.22	0.08	0.16	0.10	0.15	0.06	0.30	0.08	0.15±0.06
	As	0.00	0.00	0.01	0.02	0.02	0.02	0.06	0.00	0.02±0.02
	Cd	0.01	0.01	0.05	0.05	6.92	6.39	14.17	0.43	6.92±6.39
	Ba	0.51	0.34	0.36	0.49	0.42	0.12	0.70	0.21	0.42±0.12
	Pb	0.05	0.05	0.21	0.05	0.08	0.05	0.21	0.03	0.08±0.05

*The next two digits number come after West (represented W) and South (represented S) likewise W14 and S15 are indicated an event in the west 2014 and south 2015 respectively. The next number "1" is shown the first day of each month followed by the last two digits in the west (04, 05) and south (01, 02) which are represented (April, May) and (Jan, Feb). AMR can be seen in the first column abbreviated of Airborne Metal Regulation, average as Ave, standard deviation as S.D., maximum as Max, and minimum as Min including plus/minus value for Means (SD).

5.4 Statistical analysis

As shown in Fig. 5.3, from left to right, important to trace elements from crustal geologic sources were placed in the first group. Vegetative burning sources were placed in the second group, iron and steel industry-coal combustion sources were placed in the third group, followed by smeltery, automotive and coal combustion sources in the final group. The highest values (in $\mu\text{g/g}$) of elements in the study area were obtained in April 2014 for Mg (86.10), Al (39.32), Si (11.58), K (19.37), Mn (1.72), Fe (92.57), and Sr (14.08) in the west, however, in January 2015 the value for Na (5.13) was an exception to this finding in the southern study area. The minimum elemental levels in the southern part of the study area were found for February 2015. Namely, minimum values (in $\mu\text{g/g}$) are indicated for Na (1.28), Mg (37.52), Al (21.02), Si (2.20), K (7.42), Mn (1.24), Fe (56.99), and Sr (0.48).

Although the element concentrations of the first group are indicated as being below the maximum values, clearly above average values were nonetheless observed in the western part of the study area for this group. The values for Na, Al, Mn, K and Fe however, were exceptions to this finding, as they were equal to the average of all values in the southern study area. The ratio of standard deviation to average values for this group is less than 50%, that is, 5:10, which is equivalent to the ratio 1:2. The bigger the value of the coefficient of variation represents the greater the level of dispersion around the means value, or make the less precise the estimate.

Over second group of AMR however, the minimum values (in $\mu\text{g/g}$) of Zn (0, 1.1) and K (16, 7.42) in May and February were observed in both the western and the southern parts of the study area. Moreover, the maximum values (in $\mu\text{g/g}$) of K (19.37, 13) and Zn (2, 5.29) are observed in April and January in the same locations. Concordantly, the K values are revealed to be 3 times and 2 times above the minimum values (6.14) in April and May were observed in the western part of the study area, whereas in the southern part the Zn value is equal to the maximum of all values in January. The coefficient of variance for vegetative burning is K (0.37) and Zn (0.92), that is, 37:100 for K and almost 1 for Zn. A remarkable increase in the values of K and Zn may influence the deliberate burning of agricultural residues that occur in the southern part of the study area.

The impact caused by the iron and steel industries, including emissions from oil combustion, influences the third group of Airborne Metals Regulations with attention to; Cr, Fe, Mg, Co, Ni, and V. The concentration of Cr both in the western and southern parts of the study area has been revealed to be below average in May, January, and February. Instead, the observational value in the western part of the study area in April is an exception, with a substantially above average result of $0.43\mu\text{g/g}$. Further, the concentration magnitude of Fe and Ni is increased by almost a maximum of all values ($92.57\mu\text{g/g}$ and $0.44\mu\text{g/g}$, respectively) and is likely 30% above average in the western part. However, in the southern part, they hardly pass the average in January and stayed below average in February. By the same token, the highest values for Mg ($86.01\mu\text{g/g}$ and 62.64) areas above the average ($61.72\mu\text{g/g}$) of all values in the western part in April and May. Moreover, the January and February concentrations were not levelled up any greater than average. Similarly, the concentration values (in $\mu\text{g/g}$) of Co (0.04) and V (0.12) remain slightly below average in the south for January and February but above average in the west. Vanadium reaches the same value of average in April and May in the west. The ratio of the standard deviation to average values for the 3rd group is less than 40%, that is, 4:10, which is equivalent to the ratio 2:5.

The smelter, Automotive, and Coal combustion sources comprise the fourth group. As has been noted, Cu ($0.22\mu\text{g/g}$) was almost 3 times above the minimum magnitude in April, although shortly after Cu ($0.08\mu\text{g/g}$) decreased the value by the minimum magnitude ($0.08\mu\text{g/g}$) and 50% of the average in May. In the south, however, Cu ($0.16\mu\text{g/g}$) showed an average value and was levelled by 50% of the maximum. Conversely, Cu ($0.10\mu\text{g/g}$) decreased the magnitude by 3 times below the maximum ($0.30\mu\text{g/g}$) in February. Near zero results were obtained for As and Cd in the west and the south. Moreover,

the Ba (0.51 μ g/g) value in April is close to the average (0.42 μ g/g) magnitude but was nevertheless over double the minimum (0.21 μ g/g) in May. In January and February, the concentration values (in μ g/g) of Ba (0.36 and 0.49) were twice as large as the minimum (0.21) and withdrawal average. In the same way, the maximum magnitude of Ba for all samples remained below (0.70). Although a steady magnitude was observed for Pb (0.05 μ g/g) in the west during April and May, in the south only Pb (0.21 μ g/g) experienced a maximum value in January.

5.4.1 Chemical Characterization and Calculation

As Table 5.4 shows, the strong uphill correlation in the western part of the study area is caused by geological influences that are dependent upon many factors from the DEF and Wt. A positive relationship is articulated from K and Fe to Al equally from Fe to K. In the same way, a strong positive correlation is represented among the elements of the first group, except for the moderate positive correlations from Si to Na (55%), Mg (66%), Al (53%), from Sr to Si (57%) and Mn (66%), and from Fe to Si (54%). To this end, weak but still positive correlations from Sr to Na (34%) and Mn to Si (49%) are recognized. A strong correlation magnitude is shown from K (73%) to the DEF and Wt, as well as a moderate positive correlation from Zn (50%) to dust weight.

There was a lack of correlation from Zn (18%) to DEF. In fact, no correlation is observed from Zn to elements from the first group such as Mg (6%), Al (-14%), K (-10%), Ca (-9%), Mn (-7%), and Fe (8%). However, a weak positive correlation is indicated for Na (33%) and Si (58%), and a weak negative correlation to Sr (-33%) is included.

A high correlation value is depicted in the 3rd group of Airborne Metals Regulations with a given strong correlation magnitude from DEF and Wt to Cr, Fe, Mg, Co, Ni, as well as an exception of a moderate positive relationship from V (53%). A perfect positive relationship can be seen between Fe and Ni to Al and K. Although a strong correlation value is given to K from the 2nd group, zero relationships are expressed from the group elements to Zn, albeit not for the weak correlation from Cr to Zn (58%).

As the same manner, there is a strong correlation from Cr (88%) to Si, a moderate correlation from Fe (54%), Ni (58%), and Mg (66%) to Si, and weak positive correlations from Co (42%) and V (31%) to Si. Moreover, a strong, positive individual correlation can be seen between Fe or Ni to Al and K. A strong positive relationship from Cu and Ba to DEF and the Wt. is revealed, excluding an uphill negative correlation from As and Cd (-82%) to the dust event frequency. At the same time, a moderate negative relationship is indicated from the Wt correlation for As (-56%) and Cd (-54%).

A strong positive relationship to Cu and Ba from the first, second and third groups can be recognized; however, there are negative relationships with As and Cd and a close to zero relationships with Pb. In addition to the negative relationships, a strong negative correlation can be seen between Ba to As and Cd. Notwithstanding the strong relationship of DEF and Wt. to the elements from matrices based on Airborne Metals Regulations, a moderate but positive correlation can be found to Na, Mn, Sr, Co, and V. Conversely, strong negative correlations are shown with As and Cd followed by near zero relationships to Zn and Pb.

In the southern study area (Table 5.5) correlation matrices of monthly concentrations represent strong uphill relation values from Na (76, 70%) and/or Sr (83, 93%) to DEF and Wt., respectively. Conversely, null and moderate negative relationship values occur with Ca (-8, -18%) and Si (-57, -74%). Similarly, a strong positive correlation is represented among the elements of the first matrix with the exception of a significant negative correlation to Sr (-93%). Furthermore, there are moderate negative relationships from Si to Mn (-45%), Fe (-43%), and Ca (-52%), and zero relationships are revealed from Si to Na (-5%), and Mg (-6%).

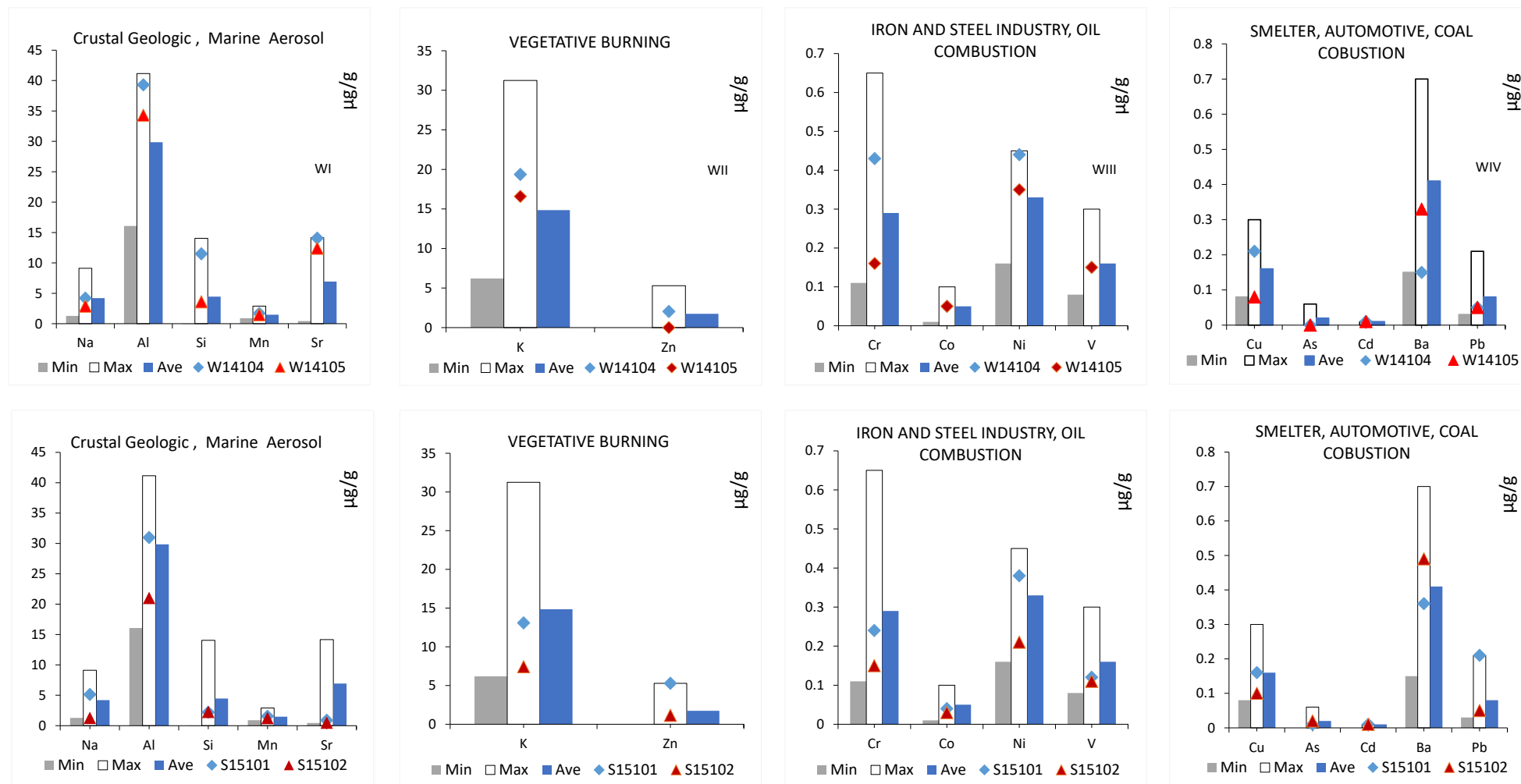


Figure 5.3 Concentration value chart from the southern (top) and western (bottom) of study area
 *Study area in four groups after Geiger and Cooper (2010) [left to right]

Positive relationships with DEF and Wt. are articulated in the second matrix. Significantly positive correlation values are observed from K to Na (89%), Mg (97%), Al (92%), Ca (71%), Mn (84%), and Fe (86), as well as from Zn to Na (79%), and Sr (77%). The exceptions are an almost zero correlation to Ca (-100%) and a negative correlation to Si (-48%). Although a strong correlation is observed from Ni (71, 79%) and Fe (71%) to the DEF and Wt., in general, a moderate positive relationship characterizes the correlation from the third matrix to DEF and Wt. There are perfect positive relationships from Co to Al (100%), and from Fe to Mn (100%), while there are almost zero correlation states from Cr to Sr, and from Mg to Si. Weak to moderately negative relationships from V (14%), Ni (37%), Co (25%), and Fe (43%) to Si are shown.

The high correlation value is depicted from the final matrix to Wt values. Relationship values are strongly positive for Pb (95%) and Cu (72%). In contrast, strong negative correlations are shown with Cd (-73%), and As (-95%) with a weak positive correlation with Ba (33%). Correlations of the matrix to dust event frequency (DEF) show a perfect and moderate negative value to As (100%) and Cd (55%), respectively, and almost no relationship to Ba (7%). In contrast, strong and moderately positive values are articulated to Pb (99%) and Cu (64%), respectively. In addition to the relationship among elements and dust event frequency, no correlation was observed from Cu and As to Si and Ca, respectively. By the same token, zero correlation is expressed from Cd to Na, Mg, K, Co, and V. There was also zero correlation from Ba to Na, Ca, Zn and As. A strong negative correlation is also shown from As to Sr (-85%), Zn (-99%), from Pb to As (-98%), and from Cd to Sr (-92%). Weak negative correlations are shown from Cd to Al (-33%), Mn (-45%), Fe (-44%), Zn (-46%), and Ni (-36%).

A moderate negative correlation is shown for Pb coupled with Ba to Si (50%), and Cd (50%). Aside from the moderate relationship of DEF and Wt to the matrices of the elements, a high positive correlation for these objects can be found with Fe, Sr, Zn, Ni, Cu, and Pb; conversely, an exceptional perfect negative correlation is found with As. Furthermore, a weak to near zero correlation can be seen with Ba, Ca and V.

Henceforth, differential correlations between the southern and western parts of the study are from Si, Ca, Al and Mg to DEF and Wt, as adjacent to local weathering (wind speed and wind direction, land cover based on Table 5.2, discrimination of the first group elemental concentration value) suggest that: Si, Ca, Al and Mg may have higher local impacts on the atmosphere rather than globally. Consequently, the nearby source contributors of the first matrix (Crustal Geologic and Aerosol Marine) should be monitored to predict the concentration values of these elements within soil and water. As an illustration, the addition of Si decreased the values of Mn, Cu, Fe, and Zn.

Moreover, some elements tend to be depleted (e.g., Zn, Fe, Cu, Mn) or enriched (e.g., Si, Mg, Na, K), which may occur as a result of soil weathering processes and anthropogenic factors. Meanwhile, the efficacy of Airborne Metal Regulations in the second matrix can be proven in the west and south parts of the study area revealing the lack of any strong correlation from Zn and K to DEF and Wt, respectively. Similarly, elemental values of Kalong with Zinc deficiency are related to the vegetative burning activities after or during the harvesting season. Although Chromium and Magnesium levels declined in the southern part of the study area, the contributions of iron-steel industries and oil combustion located there have shown a proven disruption of correlation values in the 3rd matrix. Thus, this relationship should be included in conversations about outcomes from anthropogenic activities and media from different geographical regions regardless of concentration level. Notably, with Chromium, the concentrations of Vanadium are slightly elevated from oil combustion sources.

Table 5.4 Key indicating elements with associated sources for maximum correlation in the western part

Capacitance measurement of dust												Elements (Correlation %)																																			
Variable			Elements (Correlation %)																																												
W	DEF	GDR	Na	Mg	Al	Si	K	Ca	Mn	Fe	Sr	K	Zn	Cr	Fe	Mg	Co	Ni	V	Cu	As	Cd	Ba	Pb																							
DEF	1.00																																														
GDR	0.92	1.00																																													
Na	0.56	0.73	1.00																																												
Mg	0.81	0.82	0.89	1.00																																											
Al	0.75	0.70	0.84	0.98	1.00																																										
Si	0.90	0.97	0.55	0.66	0.52	1.00																																									
K	0.77	0.73	0.85	0.99	1.00	0.55	1.00																																								
Ca	0.92	0.82	0.68	0.94	0.93	0.71	0.94	1.00																																							
Mn	0.68	0.69	0.90	0.98	0.99	0.49	0.99	0.88	1.00																																						
Fe	0.75	0.73	0.87	0.99	1.00	0.54	1.00	0.93	0.99	1.00																																					
Sr	0.87	0.63	0.34	0.72	0.76	0.57	0.76	0.92	0.66	0.73	1.00																																				
K	0.77	0.73	0.85	0.99	1.00	0.55	1.00	0.94	0.99	1.00	0.76	1.00																																			
Zn	0.18	0.50	0.33	0.06	-0.14	0.58	-0.10	-0.09	-0.07	-0.08	-0.33	-0.10	1.00																																		
Cr	0.80	0.96	0.87	0.84	0.72	0.88	0.74	0.74	0.74	0.75	0.45	0.74	0.58	1.00																																	
Fe	0.75	0.73	0.87	0.99	1.00	0.54	1.00	0.93	0.99	1.00	0.73	1.00	-0.08	0.75	1.00																																
Mg	0.81	0.82	0.89	1.00	0.98	0.66	0.99	0.94	0.98	0.99	0.72	0.99	0.06	0.84	0.99	1.00																															
Co	0.71	0.60	0.73	0.93	0.98	0.42	0.98	0.93	0.96	0.97	0.81	0.98	-0.30	0.59	0.97	0.93	1.00																														
Ni	0.78	0.75	0.85	0.99	1.00	0.58	1.00	0.95	0.99	1.00	0.77	1.00	-0.08	0.76	1.00	0.99	0.97	1.00																													
V	0.53	0.53	0.86	0.91	0.96	0.31	0.95	0.79	0.98	0.96	0.57	0.95	-0.19	0.62	0.96	0.91	0.94	0.94	1.00																												
Cu	0.77	0.95	0.88	0.84	0.71	0.87	0.74	0.72	0.74	0.75	0.42	0.74	0.60	1.00	0.75	0.84	0.58	0.75	0.62	1.00																											
As	-0.82	-0.56	-0.30	-0.70	-0.75	-0.50	-0.75	-0.90	-0.65	-0.72	-1.00	-0.75	0.41	-0.38	-0.72	-0.70	-0.82	-0.75	-0.58	-0.36	1.00																										
Cd	-0.82	-0.54	-0.25	-0.66	-0.71	-0.50	-0.71	-0.87	-0.61	-0.68	-0.99	-0.71	0.42	-0.36	-0.68	-0.66	-0.78	-0.71	-0.53	-0.33	1.00	1.00																									
Ba	0.73	0.82	0.97	0.98	0.94	0.64	0.95	0.85	0.96	0.96	0.57	0.95	0.20	0.89	0.96	0.98	0.86	0.95	0.91	0.89	-0.54	-0.49	1.00																								
Pb	-0.42	-0.11	0.52	0.11	0.09	-0.27	0.09	-0.24	0.23	0.13	-0.58	0.09	0.29	0.17	0.13	0.11	0.00	0.08	0.33	0.21	0.58	0.62	0.29	1.00																							

Strong and Perfect relationship

Negative

Zero

Positive

Strong and Perfect relationship

Negative
Zero
Positive

Zero relationships. Up to 30%, A weak relationship. Up to 50%, A moderate relationship. Up to 70%, Strong and perfect relationship Up to 100

Table 5.5 Key indicating elements with associated sources for maximum correlation in the southern part

Capacitance measurement of dust																																															
Variable			Elements (Correlation %)																																												
S	DEF	GDR	Na	Mg	Al	Si	K	Ca	Mn	Fe	Sr	K	Zn	Cr	Fe	Mg	Co	Ni	V	Cu	As	Cd	Ba	Pb																							
DEF	1.00																																														
GDR	0.95	1.00																																													
Na	0.76	0.69	1.00																																												
Mg	0.37	0.47	0.78	1.00																																											
Al	0.57	0.69	0.80	0.96	1.00																																										
Si	-0.57	-0.74	-0.05	-0.06	-0.33	1.00																																									
K	0.47	0.50	0.89	0.97	0.92	0.04	1.00																																								
Ca	-0.08	-0.18	0.57	0.62	0.39	0.73	0.71	1.00																																							
Mn	0.51	0.68	0.67	0.92	0.98	-0.45	0.84	0.25	1.00																																						
Fe	0.55	0.71	0.72	0.93	0.99	-0.43	0.86	0.28	1.00	1.00																																					
Sr	0.83	0.93	0.38	0.22	0.49	-0.93	0.20	-0.52	0.54	0.55	1.00																																				
K	0.47	0.50	0.89	0.97	0.92	0.04	1.00	0.71	0.84	0.86	0.20	1.00																																			
Zn	0.99	0.92	0.79	0.37	0.54	-0.48	0.49	-0.01	0.46	0.51	0.77	0.49	1.00																																		
Cr	0.38	0.39	0.86	0.96	0.87	0.16	0.99	0.79	0.78	0.80	0.07	0.99	0.40	1.00																																	
Fe	0.55	0.71	0.72	0.93	0.99	-0.43	0.86	0.28	1.00	1.00	0.55	0.86	0.51	0.80	1.00																																
Mg	0.37	0.47	0.78	1.00	0.96	-0.06	0.97	0.62	0.92	0.93	0.22	0.97	0.37	0.96	0.93	1.00																															
Co	0.56	0.66	0.83	0.97	1.00	-0.25	0.95	0.47	0.96	0.97	0.43	0.95	0.54	0.91	0.97	0.97	1.00																														
Ni	0.71	0.79	0.87	0.91	0.98	-0.37	0.91	0.36	0.94	0.96	0.58	0.91	0.69	0.85	0.96	0.91	0.98	1.00																													
V	0.23	0.40	0.61	0.97	0.93	-0.14	0.88	0.50	0.94	0.93	0.22	0.88	0.21	0.87	0.93	0.97	0.93	0.85	1.00																												
Cu	0.64	0.72	0.88	0.95	0.99	-0.27	0.95	0.46	0.94	0.96	0.48	0.95	0.63	0.91	0.96	0.95	0.99	0.99	0.89	1.00																											
As	-1.00	-0.95	-0.73	-0.33	-0.54	0.59	-0.43	0.13	-0.48	-0.52	-0.85	-0.43	-0.99	-0.33	-0.52	-0.33	-0.52	-0.68	-0.20	-0.61	1.00																										
Cd	-0.55	-0.73	-0.04	-0.06	-0.33	1.00	0.04	0.74	-0.45	-0.44	-0.92	0.04	-0.46	0.16	-0.44	-0.06	-0.25	-0.36	-0.15	-0.27	0.58	1.00																									
Ba	0.07	0.35	0.16	0.67	0.72	-0.50	0.48	-0.03	0.84	0.80	0.38	0.48	-0.01	0.44	0.80	0.67	0.68	0.61	0.82	0.60	-0.05	-0.51	1.00																								
Pb	0.99	0.95	0.84	0.48	0.65	-0.50	0.59	0.05	0.58	0.62	0.78	0.59	0.99	0.50	0.62	0.48	0.65	0.78	0.34	0.73	-0.98	-0.48	0.11	1.00																							

Strong and Perfect relationship

Negative

Zero

Positive

Strong and Perfect relationship

Negative
Zero
Positive

Zero relationships. Up to 30%, A weak relationship. Up to 50%, A moderate relationship. Up to 70%, Strong and perfect relationship Up to 100

Identically, the correlation among elements from the 4th matrix to the dust's physical properties shows a clear reduction in lead concentrations in the western part of the study area. Although at least two sites show a contribution of lead from industrial stations nearby, the only possible explanation for the overall reduction appears to be the absence of a lead from industrial emissions. The concentrations of cadmium are low in the west and elevated in the south, which is probably due to the wind direction and seasonal rains.

5.5 Conclusion

Dust events originate predominantly in arid or semiarid areas and cover approximately 33% of the global land area (Duce, 1995) and 58% of the study area. The rates of dust deposition observed across the study area vary at almost 250 g in square meters per year. The sites receiving dust deposition were classified into broad categories based on natural and anthropogenic features. The element concentration analysis is carried out with the help of an Inductively Coupled Plasma-Mass Spectrometer (ICP-MS) for 20 elements. Geometric values for each element in the southern part (n=50) and the western part (n=50) of the study area were compared. Specifically, positive, zero and negative correlations among elements and the physical parameters of dust samples adjacent to the four matrices of Airborne Metals Regulations are observed. This study comprises a perfect complement to the lessons learned from (Larssen & Carmichael, 2000; D. R. Muhs & Benedict, 2006) in finding dust sources by using texture similarities in dust accumulation in the area of research (G01 to G02; G09 to G10). At the same time, correlations from atmospheric reports and DEF can prove that the highest proportion of dust subjected to Airborne Metals Regulations associated with dominant sources (DS) are formed at local and regional scales rather than globally.

To summarize, weathering combined with anthropogenic change influences the composition of dust travelling from the source region to local deposition; however, this composition cannot be easily controlled. Although in some cases a severity in correlation without a resulting change in the value of the element composition has been observed, elemental correlations of individual matrices are nonetheless the marked effects of dominant sources. An impediment arises from the fact that there is no way to isolate each individual matrix or the environment from the effects of either anthropogenic sources or natural weathering processes. Given this point, developing guidance on the priorities of expanding projects and preventative actions towards potential dust deposition from natural and dominant sources may be a subject of institutional interest.

Acknowledgement

I wish to acknowledge field work cooperation utilized by my best friends, experts back-home, and the scientific contributions made by Dr Jens Hahn, Department of Geography; Koblenz University. Moreover, thanks to the professional laboratory assistance from Nils Jansen, Olga Schechtel and Nina Zitzer with regards to preparation and the operation of the instruments, respectively.

Funding sources

This research didn't receive any specific grant from funding agencies in the public, commercial, or not-for-profit sector.

References

- Ai, N., & Polenske, K. R. (2008). Socioeconomic Impact Analysis of Yellow-dust Storms: An Approach and Case Study for Beijing. *Economic Systems Research*, 20(2), 187–203. <https://doi.org/10.1080/09535310802075364>
- Basta, N., & McGowen, S. (2004). Evaluation of chemical immobilization treatments for reducing heavy metal transport in a smelter-contaminated soil. *Environmental Pollution*, 127(1), 73–82.
- Beuth. (2004). Wasserbeschaffenheit—Anwendung der induktiv gekoppelten Plasma-Massenspektrometrie (ICP-MS). 2005-02, DIN EN ISO 17294-2. <https://www.beuth.de/de/norm/din-en-iso-17294-2/76161035>
- Bilos, C., Colombo, J., Skorupka, C., & Presa, M. R. (2001). Sources, distribution and variability of airborne trace metals in La Plata City area, Argentina. *Environmental Pollution*, 111(1), 149–158.
- Calvert, J. G. (1990). Glossary of Atmospheric Chemistry Terms. *Pure and Applied Chemistry*, 62(11), 2167–2219. <https://doi.org/DOI 10.1351/pac199062112167>
- Carslaw, K. S., Boucher, O., Spracklen, D. V., Mann, G. W., Rae, J. G. L., Woodward, S., & Kulmala, M. (2010). A review of natural aerosol interactions and feedbacks within the Earth system. *Atmospheric Chemistry and Physics*, 10(4), 1701–1737. <https://doi.org/10.5194/acp-10-1701-2010>
- Charlesworth, S., Everett, M., McCarthy, R., Ordonez, A., & De Miguel, E. (2003). A comparative study of heavy metal concentration and distribution in deposited street dusts in a large and a small urban area: Birmingham and Coventry, West Midlands, UK. *Environment International*, 29(5), 563–573.
- Duce, R. (1995). Sources, distributions, and fluxes of mineral aerosols and their relationship to climate. *Aerosol Forcing of Climate*, 6, 43–72.
- El-Fadel, M., & Hashisho, Z. (2001). Vehicular emissions in roadway tunnels: A critical review. *Critical Reviews in Environmental Science and Technology*, 31(2), 125–174.
- EN ISO 17294-2. (2016). Water quality: Application of inductively coupled plasma mass spectrometry (ICP-MS). Beuth Verlag GmbH. <https://www.beuth.de/en/standard/din-en-iso-17294-2/76161035>
- Evan, A. T., Flamant, C., Fiedler, S., & Doherty, O. (2014). An analysis of aeolian dust in climate models. *Geophysical Research Letters*, 41(16), 5996–6001.
- Geiger, A., & Cooper, J. (2010). Overview of Airborne Metals Regulations, Exposure Limits, Health Effects, and Contemporary Research. US Environmental Protection Agency. Accessed on August, 25, 2015.
- Gerivani, H., Lashkaripour, G. R., Ghafoori, M., & Jalali, N. (2011). The Source of Dust Storm in Iran: A Case Study Based on Geological Information and Rainfall Data. *Carpathian Journal of Earth and Environmental Sciences*, 6(1), 297–308.
- Gillies, J. A., Etyemezian, V., Kuhns, H., Nikolic, D., & Gillette, D. A. (2005). Effect of vehicle characteristics on unpaved road dust emissions. *Atmospheric Environment*, 39(13), 2341–2347. <https://doi.org/10.1016/j.atmosenv.2004.05.064>
- Goossens, D., Buck, B., & McLaurin, B. (2012). Contributions to atmospheric dust production of natural and anthropogenic emissions in a recreational area designated for off-road vehicular activity

(Nellis Dunes, Nevada, USA). *Journal of Arid Environments*, 78, 80–99. <https://doi.org/10.1016/j.jaridenv.2011.10.015>

Kabata-Pendias, A. (2010). *Trace elements in soils and plants*. CRC press.

Kreider, M. L., Panko, J. M., McAtee, B. L., Sweet, L. I., & Finley, B. L. (2010). Physical and chemical characterization of tire-related particles: Comparison of particles generated using different methodologies. *Science of the Total Environment*, 408(3), 652–659.

Larssen, T., & Carmichael, G. R. (2000). Acid rain and acidification in China: The importance of base cation deposition. *Environ Pollut*, 110(1), 89–102. [https://doi.org/10.1016/s0269-7491\(99\)00279-1](https://doi.org/10.1016/s0269-7491(99)00279-1)

Mahowald, N. M., Baker, A. R., Bergametti, G., Brooks, N., Duce, R. A., Jickells, T. D., Kubilay, N., Prospero, J. M., & Tegen, I. (2005). Atmospheric global dust cycle and iron inputs to the ocean. *Global Biogeochemical Cycles*, 19(4). <https://doi.org/10.1029/2004gb002402>

Mahowald, N. M., Kloster, S., Engelstaedter, S., Moore, J. K., Mukhopadhyay, S., McConnell, J. R., Albani, S., Doney, S. C., Bhattacharya, A., Curran, M. A. J., Flanner, M. G., Hoffman, F. M., Lawrence, D. M., Lindsay, K., Mayewski, P. A., Neff, J., Rothenberg, D., Thomas, E., Thornton, P. E., & Zender, C. S. (2010). Observed 20th century desert dust variability: Impact on climate and biogeochemistry. *Atmospheric Chemistry and Physics*, 10(22), 10875–10893. <https://doi.org/10.5194/acp-10-10875-2010>

Marticorena, B., Bergametti, G., Gillette, D., & Belnap, J. (1997). Factors controlling threshold friction velocity in semiarid and arid areas of the United States. *Journal of Geophysical Research-Atmospheres*, 102(D19), 23277–23287. <https://doi.org/10.1029/97jd01303>

Mertz, W. (1981). The essential trace elements. *Science*, 213(4514), 1332–1338. <https://doi.org/10.1126/science.7022654>

Miri, A., Ahmadi, H., Ekhtesasi, M. R., Panjehkeh, N., & Ghanbari, A. (2009). Environmental and socio-economic impacts of dust storms in Sistan Region, Iran. *International Journal of Environmental Studies*, 66(3), 343–355. <https://doi.org/10.1080/00207230902720170>

Morman, S. A., & Plumlee, G. S. (2013). The role of airborne mineral dusts in human disease. *Aeolian Research*, 9, 203–212. <https://doi.org/10.1016/j.aeolia.2012.12.001>

Muhs, D. R., & Benedict, J. B. (2006). Eolian additions to late Quaternary alpine soils, Indian Peaks Wilderness Area, Colorado Front Range. *Arctic Antarctic and Alpine Research*, 38(1), 120–130. [https://doi.org/10.1657/1523-0430\(2006\)038\[0120:EatIqa\]2.0.Co;2](https://doi.org/10.1657/1523-0430(2006)038[0120:EatIqa]2.0.Co;2)

Muhs, Daniel R, & Benedict, J. B. (2006). Eolian additions to late quaternary alpine soils, Indian peaks wilderness area, Colorado front range. *Arctic, Antarctic, and Alpine Research*, 38(1), 120–130.

Neff, J. C., Ballantyne, A. P., Farmer, G. L., Mahowald, N. M., Conroy, J. L., Landry, C. C., Overpeck, J. T., Painter, T. H., Lawrence, C. R., & Reynolds, R. L. (2008). Increasing eolian dust deposition in the western United States linked to human activity. *Nature Geoscience*, 1(3), 189–195. <https://doi.org/10.1038/ngeo133>

Okin, G. S., Mahowald, N., Chadwick, O. A., & Artaxo, P. (2004). Impact of desert dust on the biogeochemistry of phosphorus in terrestrial ecosystems. *Global Biogeochemical Cycles*, 18(2). <https://doi.org/10.1029/2003gb002145>

- Opp, C., Groll, M., Aslanov, I., Lotz, T., & Vereshagina, N. (2017). Aeolian dust deposition in the southern Aral Sea region (Uzbekistan): Ground-based monitoring results from the LUCA project. *Quaternary International*, 429, 86–99. <https://doi.org/10.1016/j.quaint.2015.12.103>
- Prospero, J. M., Ginoux, P., Torres, O., Nicholson, S. E., & Gill, T. E. (2002). Environmental characterization of global sources of atmospheric soil dust identified with the Nimbus 7 Total Ozone Mapping Spectrometer (TOMS) absorbing aerosol product. *Reviews of Geophysics*, 40(1), 2–1.
- Reynolds, R., Belnap, J., Reheis, M., Lamothe, P., & Luiszer, F. (2001). Aeolian dust in Colorado Plateau soils: Nutrient inputs and recent change in source. *Proc Natl Acad Sci U S A*, 98(13), 7123–7127. <https://doi.org/10.1073/pnas.121094298>
- Reynolds, Richard, Belnap, J., Reheis, M., Lamothe, P., & Luiszer, F. (2001). Aeolian dust in Colorado Plateau soils: Nutrient inputs and recent change in source. *Proceedings of the National Academy of Sciences*, 98(13), 7123–7127.
- Roth, B., & Okada, K. (1998). On the modification of sea-salt particles in the coastal atmosphere. *Atmospheric Environment*, 32(9), 1555–1569. [https://doi.org/10.1016/S1352-2310\(97\)00378-6](https://doi.org/10.1016/S1352-2310(97)00378-6)
- Schepanski, K., Heinold, B., & Tegen, I. (2017). Harmattan, Saharan heat low, and West African monsoon circulation: Modulations on the Saharan dust outflow towards the North Atlantic. *Atmos. Chem. Phys.*, 17(17), 10223–10243. <https://doi.org/10.5194/acp-17-10223-2017>
- Schleicher, N. J., Norra, S., Chai, F., Chen, Y., Wang, S., Cen, K., Yu, Y., & Stüben, D. (2011). Temporal variability of trace metal mobility of urban particulate matter from Beijing—A contribution to health impact assessments of aerosols. *Atmospheric Environment*, 45(39), 7248–7265.
- Slinn, W. G. N. (1982). Estimates for the long-range transport of air pollution. *Water, Air, and Soil Pollution*, 18(1), 45–64. <https://doi.org/10.1007/BF02419402>
- Tao, W. K., Chen, J. P., Li, Z. Q., Wang, C., & Zhang, C. D. (2012). Impact of Aerosols on Convective Clouds and Precipitation. *Reviews of Geophysics*, 50. <https://doi.org/10.1029/2011rg000369>
- Tegen, I., & Lacis, A. A. (1996). Modeling of particle size distribution and its influence on the radiative properties of mineral dust aerosol. *Journal of Geophysical Research-Atmospheres*, 101(D14), 19237–19244. <https://doi.org/10.1029/95jd03610>
- Tegen, I., Werner, M., Harrison, S., & Kohfeld, K. (2004). Relative importance of climate and land use in determining present and future global soil dust emission. *Geophysical Research Letters*, 31(5).
- Visser, S., & Sterk, G. (2007). Nutrient dynamics—Wind and water erosion at the village scale in the Sahel. *Land Degradation & Development*, 18(5), 578–588.
- Wang, Y. S., Xin, J. Y., Li, Z. Q., Wang, P. C., Wang, S. G., Wen, T. X., & Sun, Y. (2006). AOD and angstrom parameters of aerosols observed by the Chinese sun hazemeter network from August to December 2004. *Huan Jing Ke Xue*, 27(9), 1703–1711.
- Williams, R. M. (1982). A model for the dry deposition of particles to natural water surfaces. *Atmospheric Environment* (1967), 16(8), 1933–1938.
- Wu, J., Xu, Y., Fu, C., Zhang, R., Dai, M., & Zhu, Y. (2006). Comparison of simulating mineral dust aerosols in East Asia by two emission schemes. *China Particuology*, 4(06), 293–299.

6. Investigation of evaluation of WRF-Chem prediction for dust deposition

Abstract

The relationships between monthly recorded ground deposition rates (GDRs) and the spatiotemporal characteristics of dust concentrations in southwest Iran are investigated in this paper. A simulation by the Weather Research and Forecasting Model coupled with the Chemistry modeling system (WRF-Chem) is conducted for dust deposition during 2014–2015. The monthly dust deposition values observed at 10 different gauge sites (G01–G10) are mapped to show the seasonal and spatial variations in dust episodes at each location.

An analysis of the dust deposition samples, however, confirms that the region along the deposition sites is exposed to the highest monthly dust load, which has a mean value of 2.4 mg/cm². In addition, the study area is subjected to seasonally varying deposition, which follows the trend: spring > summer > winter > fall. The modeling results further demonstrate that the increase in dust emissions is followed by a windward convergence over the region (particularly in the spring and summer). Based on the maximum likelihood classification of land use land cover, the modeling results are consistent with observation data at gauge sites for three scenarios [S.I, S.II, and S.III].

The WRF model, in contrast with the corresponding observation data, reveals that the rate factor decreases from the southern [S.III- G08, G09, and G10] through [S.II- G04, G05, G06, G07] to the northern points [S.I-G01, G02, G03]. A narrower gap between the modeling results and GDRs is indicated if there is an increase in the number of dust particles moving to lower altitudes or an increase in the dust resident time at high altitudes. The quality of the model forecast is altered by the deposition rate and is sensitive to land surface properties and interactions among land and climate patterns. Using GDRs that correspond with adequate information about the transport and deposition characteristics in the model improves the prediction by 20% for [S.I] in winter 2015 and by 15% for [S.II] in spring 2014.

Keywords: Dust deposition rate, WRF-Chem, climate zone, Iran

6.1 Introduction

Small solid and dry particles can remain suspended in the Earth's atmosphere for a sufficiently long time to extensively affect the weather and climate (Calvert, 1990; Charlson et al., 1992; Prospero et al., 2002; Song et al., 2008; Rezazadeh et al., 2013). When particles are airborne, they can affect the radiation balance by scattering and absorbing radiation (Haywood and Boucher, 2000; Sokolik et al., 2001; Tegen et al., 2004; Kim et al., 2008), in addition to the immediate threat they pose to the atmosphere and satellite retrievals (Merchant et al., 2006; Amiridis et al., 2013). Dust also significantly affects air quality (Claiborn et al., 2000; Liu et al., 2006) and causes considerable impairments to societal health, specifically human health, (Kwon et al., 2002; Chen et al., 2004; Groll et al., 2013; Opp et al., 2017) and infection (Thomson et al., 2006; Díaz et al., 2012; De Longueville et al., 2013). Moreover, dust can affect agriculture (Stefanski & Sivakumar, 2009), engines, and technical infrastructure (Elminir et al., 2006; El-Nashar, 2003; Kazem et al., 2014; Ohde & Siegel, 2012), thereby causing severe economic damages (Ai and Polenske, 2008; Miri et al., 2009). Models that predict dust behavior can improve our understanding of dust process and its effects. However, a detailed knowledge of how dust is activated, including the characteristics of activation, dust transport routes, and deposition processes, is crucial to fully understand its complexity (Schepanski et al., 2017).

The dynamical core of the Weather Research and Forecasting (WRF) model includes several numerical approaches, such as model initialization, boundary conditions, physics options, and grid-nesting techniques (Skamarock et al., 2008). Physical and Planetary Boundary Layer (PBL) parameterization is required to model small-scale processes, such as precipitation, which generally cannot be numerically discretized by the model (Mandal et al., 2004; Dalin Zhang & Anthes, 1982). The WRF coupled with the Chemistry modeling system (WRF-Chem) can be configured to include indirect aerosol effects, which can enhance the results for precipitation (Carvalho et al., 2014; Kai Wang et al., 2015). This option is particularly beneficial for modeling the spatiotemporal behavior of gaseous particles in urban areas (Arghavani et al., 2019; Y. Zhang et al., 2012) (e.g. acid rain simulation). Geological and terrain features, such as the soil texture and land use, are the leading causes of dust emission (Hahnenberger & Nicoll, 2014; J. Huang et al., 2014). However, considering the details of the life of dust particles, WRF-Chem models have also been used to simulate and investigate dust-climate interactions (Gong et al., 2003; Zhang et al., 2008; Sun et al., 2012; Wang et al., 2012; Chen et al., 2013; Li et al., 2016). Recently, great progress has been made in understanding dust processes by modeling the dust source function (Nabavi et al., 2017) and numerically simulating dust events (Hamidi et al., 2014; Zhang et al., 2015) in West Asia. Many researchers have attempted to evaluate model simulation data using air quality station (Teixeira et al., 2016; Chen et al., 2014) data and AOT (aerosol optical thickness) observations over the AERONET (AERosol RObotic NETwork) or retrieved from satellites with in situ measurements (Huang et al., 2008). In other studies, dust emission fluxes in atmospheric models have been mainly parameterized by several atmospheric and geological factors (Beres et al., 2005; Mihailović & Kallos, 1997), such as the wind speed and soil structure. In wind simulations, good performance of the WRF numerical model for dust emissions is vital and consequently influences the model results of dust concentrations (Carvalho et al., 2012; Mattar & Borvarán, 2016).

Furthermore, soil erodibility is a crucial factor for identifying dust sources and estimating the dust emission flux from the surface (Nichols and Hirst, 1998; Koren et al., 2006; Todd et al., 2008). A higher erodibility could make the soil more susceptible to erosion, which would lead to a larger dust emission (Bullard et al., 2011). In numerous dust models, a global dust source function, presented by Ginoux et al. (2001), is used. This source function, $S(Z_i)$, is based on the topography and estimates the probability that soil sediments will accumulate at a specific location as follows:

$$S = \left(\frac{Z_{max} - Z_i}{Z_{max} - Z_{min}} \right)^5,$$

Equation (1)

Global dust source function: where Z_i is the altitude that is normalized by the Z_{max} and Z_{min} heights over an area of $10^\circ \times 10^\circ$ around the i th grid point. S is the erodibility factor for the i th grid of the model.

The southwestern part of Iran is exposed to aeolian dust (Wilkinson, 2014; Boloorani et al., 2014; Daniali and Karimi, 2019; Gerivani et al., 2011; Ghasem et al., 2012; Heidarian et al., 2018). Recently, numerous studies have evaluated the dust deposition rates and the physical and chemical characteristics of dust in Iran (Zarasvandi et al., 2011a; Rashki et al., 2013; Gholampour et al., 2014; Froushani et al., 2019) and worldwide (A. S. Goudie & Middleton, 2001; Ta et al., 2004; X. Lu et al., 2009; Shah & Shaheen, 2010; Schleicher et al., 2011; Al-Harbi, 2015). Previous studies have indicated influences of the PBL and the land surface on the calculation of aeolian feedback (Choobari et al., 2012) and these relationships were used to determine the soil moisture and its corresponding relationships with atmosphere, land, and transport processes.

Although previous research compared the impacts of model processes from WRF-Chem prediction relative to those from different methods of observation, very few works have reported on the effectiveness of using ground deposition rates (GDRs) as ground-based observations combined with model outputs from WRF-Chem. Given the lack of existing literature, this study aims to provide ground-based observations based on more detailed information about the dust episode in the region. The second aim, however, is to demonstrate the beneficial impact of GDR observations on the output of the WRF-Chem model.

The outline of this paper is as follows. In (chapter 3), the study area is illustrated, and the land surface and climate maps, which include the experimental design of the gauge sites (geo-coordination), are explained. The approaches and methodology of sampling and the model simulation are clarified in section 6.3.1. The mean results and climate factors of the dust sampling analysis are provided in section 6.4. The seasonal and spatial variations in the dust deposition and concentration rates were extensively investigated. An evaluation of the model based on quantifying the dust load and dust concentration and a discussion of the climate factor and dust behavior is given in the next section.

6.2 Materials and method

Table 6.1 shows that the sites were coded as G01 to G10 and located based on the distribution and intensity of the dust events reported in the annual report of IRMO (2016). Twenty samplers were constructed and placed in 10 gauge sites and the dominant local features were observed.

Table 6.1 Location, altitude, and total distance of dust samplers

No	LULC based on LUCAS	Code	Geo-Coordinate		Climate
1	Bare & Artificial	G01	34.000553,	45.497595	Arid Steppe Hot [BSh]
2	Bare	G02	34.007182,	45.499075	Arid Steppe Hot [BSh]
3	Bare	G03	34.393584,	45.648174	Arid Steppe Hot [BSh]
4	Bare & Vegetation	G04	34.423028,	45.993753	Temperate Hot [Csa]
5	Bare & Vegetation & Artificial	G05	34.353365,	47.101335	Temperate Hot [Csa]
6	Bare & Vegetation	G06	33.024976,	47.759393	Temperate Hot [Csa]
7	Vegetation & Wet area	G07	32.380038,	48.282664	Arid Steppe Hot [Bsh]
8	Bare & Wet area & Vegetation	G08	31.445194,	48.632398	Arid Desert Hot [BWWh]
9	Bare & Water & Artificial	G09	30.584651,	49.163632	Arid Desert Hot [BWWh]
10	Bare & Artificial	G10	30.352411,	48.292293	Arid Desert Hot [BWWh]

To understand the impact of the physical distribution of dust in southwest Iran, the sampling sites over the LULC of the study area were classified. The GDR data, coupled with the WRF-Chem model, revealed the severity of the physical distribution of the aeolian dust over the study area.

6.2.1 Data sampling method and analysis

From chapter 3, the sampler design was deliberately kept simple to ensure long-term durability and easy maintenance (ASTM D1356, 2017; IHS under license with ASTM, 2010). Each sampler consisted of a plastic container with a surface area of 314 cm² and a paper inlay for passive dust collection.

6.2.2 Gauge site over LULC

The global environment, ecological functions, and structures are affected by the LULC. Thus, the LULC illustrates the evolution of the ecological function in a human–environment system (Bates & Rudel, 2000; Verburg et al., 2004). In this system, numerous drivers interact with different feedbacks, and the consequent interactions affect the development pattern (Lambin & Geist, 2008; Verburg et al., 2004). In several cases of aeolian dust in North Africa, South-west Asia, South-west USA, and China (inner Mongolia), repeated droughts and possible consequences of climate variability, such as desertification, are of interest to numerous scientists (Jamalizadeh et al., 2008; Taghavia & Mohammadi, 2008; Thomas et al., 1997). In south-west Asia, several areas, such as west Iran, are much more prone to dust storms than other areas due to differences in soils and climate (Taghavi et al., 2017). To enhance the identification of dust events in the study area using GDR data, various biophysical categories were distinguished, such as: The areas of vegetation (e.g., trees, bushes, crops, grasses, and herbs), artificial land (building, industries, and road), bare soil, or bare land (rock, sand, and areas with no dominant vegetation cover on at least 90% of the area) cover, and wet areas and bodies of water (sheets of water, watercourses, and wetland). As shown in chapter 3 (Figure 3.1) a given circle centered (with a radius of 10 km) at each gauge site (G01–G10) represents the spatial pattern of the LULC. This analysis represents the whole area with respect to each sampler at the gauge site.

6.2.3 WRF-Chem model simulation

Several atmospheric and environmental variables, such as the dust concentration and dust load, as well as the wind direction and speed over the deposition sites, were simulated by the WRF-Chem model (V3.9.1) (Grell et al., 2005; Skamarock et al., 2008). Under the planetary and boundary layer conditions required to run the WRF model, the reanalysis product of the European Center for Medium–Range Weather Forecasts, called the ERA-Interim data (Dee et al., 2011), which has a spatial resolution of 0.75° × 0.75°, were acquired to run the WRF-Chem model. ERA-Interim data is a global atmospheric reanalysis dataset available for the period from 1979 to 31 August 2019 and is provided by the models and data assimilation systems of the European Centre for Medium-Range Weather Forecasts. For this study, dust-only simulations were performed for two periods: March to April 2014 and January to February 2015. Figure 6.1 shows the simulation domains. The spatial resolutions of the main domain and subdomain are 30 km × 30 km and 10 km × 10 km, respectively.

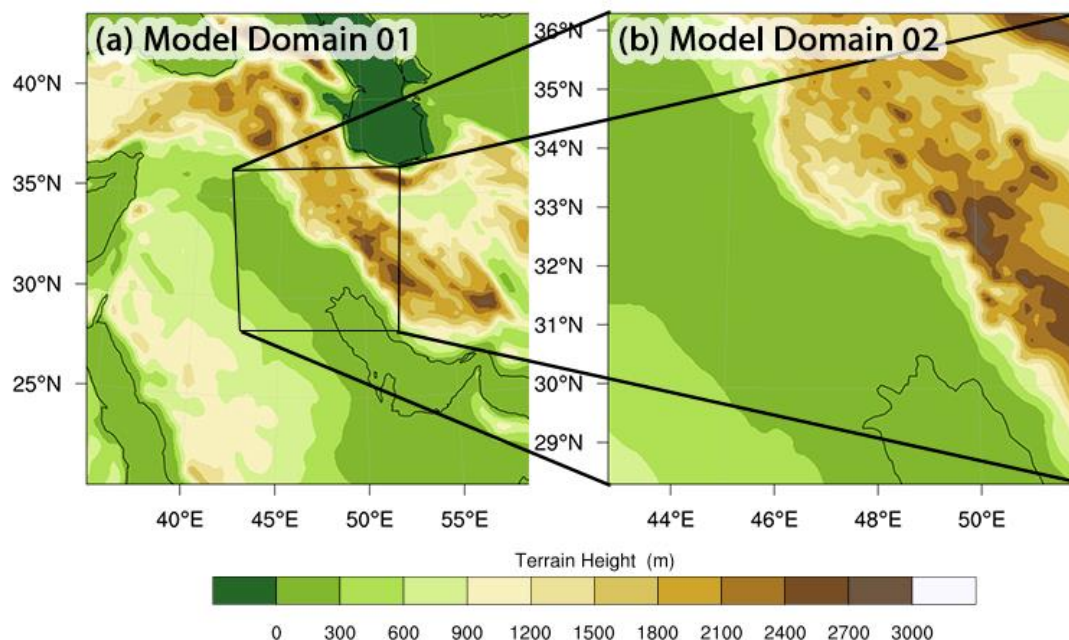


Figure 6.1 Simulation domain

*The spatial resolution of the main domain is 30 km × 30 km (left) and that of the subdomain is 10 km × 10 km (right)

Several physical options that have been highly tested and have produced reasonable results were set as the physical options of the WRF model (Table 6.2). These standard options were introduced in the WRF model as the physics suites, beginning in version 3.9.

Table 6.2 Configuration options for the WRF-Chem model for dust

Physical option	Setting
Microphysics	New Thompson et al. scheme
Cumulus Parameterization	Tiedtke scheme (U. of Hawaii version)
Longwave Radiation	RRTMG (Rapid Radiative Transfer Model for GCMs) scheme
Shortwave Radiation	RRTMG (Rapid Radiative Transfer Model for GCMs) shortwave
Surface Layer	Eta similarity
Land Surface	Noah Land Surface Model
Planetary Boundary layer	Mellor-Yamada-Janjic scheme

6.3 Results and statistics

As shown in Table 6.3, the gauge sites were subclassified into three main climate zones: [BWh], [BSh], and [Csa]. Arid desert climates and hot [BWh] climates are represented in the northern coastal plains of the Persian Gulf between the latitudes of 30°N and 31°N. The next climate zone represents an arid steppe hot zone [BSh], which is located between 34°N and 32°N. A temperate climate with a warm and hot summer zone [Csa] is located between 33°N and 34°N, starting in the extreme western region. Additional results were calculated to improve estimations of the dust load, concentration, and deposition and are described in the Discussion section.

Table 6.3 Land cover in the study area

Sampler and Gauge site number Land cover in total area of study (%)										
Longitude	E45-46	45-46	45-46	46-47	47-48	47-48	48-49	48-49	49-50	48-49
Latitude	N33-34	33-34	33-34	33-34	33-34	32-33	32-33	31-32	30-31	30-31
Climate	BSh	BSh	BSh	BSh	Csa	Csa	BSh	BWh	BWh	BWh
Gauge sites	G01	G02	G03	G04	G05	G06	G07	G08	G09	G10
Artificial	0.07	0.07	0.00	0.95	32.49	0.11	4.33	8.18	9.09	24.81
Bareland	99.93	99.93	98.85	50.90	33.11	72.90	10.32	57.94	60.41	36.43
Industrial	0.00	0.00	0.00	0.00	0.47	0.00	0.00	0.00	0.68	1.58
Vegetation	0.00	0.00	1.56	48.66	34.22	27.00	77.48	33.10	19.07	14.91
Wet land	0.00	0.00	0.00	0.00	0.00	0.00	8.40	0.79	10.76	22.27
Total	100	100	100	100	100	100	100	100	100	100
Accuracy	0.00	0.00	+0.40	+0.50	+0.30	0.00	+0.50	0.00	0.00	0.00

*The gauge sites, area for each site with a radius of 10 km

In the following section, we authentically represent the relative atmospheric state using GDR data, including the wind magnitude, precipitation, and temperature (Duce, 1995; AO, 2001; Andrew S Goudie, 2009; X. Huang et al., 2011). These parameters have been hypothesized to reflect the increase or decrease in the aeolian deposition rate under the LULC classification.

In general, wind speed data for March 2014 to 2015 show that the highest wind speeds occurred in the late spring, summer, and early autumn in the eastward direction (1.0–2.5 m/s). In contrast, the lowest speeds occurred in the winter and spring. The wind speed in the winter was approximately zero in the northward direction, whereas it exceeded that of the eastward direction (1.5 m/s) in the spring throughout the study area. An existing study about an Asian dust storm showed that dust events can be recognized on the basis of the total suspended dust particulate matter (TSP) in combination with the visibility and wind speed (Hoffmann et al., 2008). The study suggested that a wind threshold of 17 m/s can decrease visibility to 1000 m if the TSP is less than 2000 $\mu\text{g}/\text{m}^3$. In addition, Song et al., (2007) identified a wind threshold of 5 to 10 m/s on TSP ($<500 \mu\text{g}/\text{m}^3$) and visibility (2000 m) from a study on northeast Asian Dust. In addition to wind thresholds, our results are also in agreement with a finding from Ta et al., (2004), in which the reported that eastward and southward wind speeds varied from 1 to 6 m/s during dust events.

The mean value of the monthly precipitation was 37.70 mm (Historical climate data, 2016; Iran Meteorological Organization, 2014), whereas the precipitation per month was notably below average in the summer and winter and above that in the spring and fall. Based on rain taxonomy (Thanh, 2019), the precipitation in June, July, and August can be classified as zero-rain (0-1.8 mm/month) when deficits in precipitation occurred (Abdulrazzaq et al., 2019). However, light rain (18-180 mm/month) events, where the precipitation was below the mean value, were recorded in May, September and October. In contrast, the rainfall in November, December, February, March, and April indicated a value of approximately 50 mm, which is above average.

Ambient monthly temperatures were observed during nearly the entire fieldwork period. The mean temperature was generally much higher than 16 °C. A long period of high temperature points fluctuated between 29 °C and 43 °C in the summer. The annual minimum temperature was also warmer than the minimum temperature in the winter, which experienced a minimum value of -8 °C. This temporal pattern was also detected by National Oceanic and Atmospheric Administration (NOAA) researchers (Lenssen et al., 2019). Furthermore, this study is, thus, in accordance with the results of Alizadeh-Choozari and Najafi, (2018), which are as important as the aforementioned results and state that a rise in temperature is associated with a decrease in total annual precipitation. Higher temperatures are generally associated with lower precipitation amounts and vice versa. This observation is expected because the [G10, G09, G08, G07] and [G06, G04] regions are associated with more sunshine and less evaporative cooling.

6.3.1 Ground observation of deposition rates

Ordinary inverse distance weighted (IDW) interpolation technique was applied to identify the average seasonal magnitude of the GDRs obtained from the 10 gauge sites in Fig. 6.2; it demonstrates that the average seasonal GDRs ranged from 0.3 to 2.0 mg/cm², which corresponds to monthly field deposition rates in the range of 3–20 t/km². In general, higher deposition rates occurred in the spring, summer, and winter.

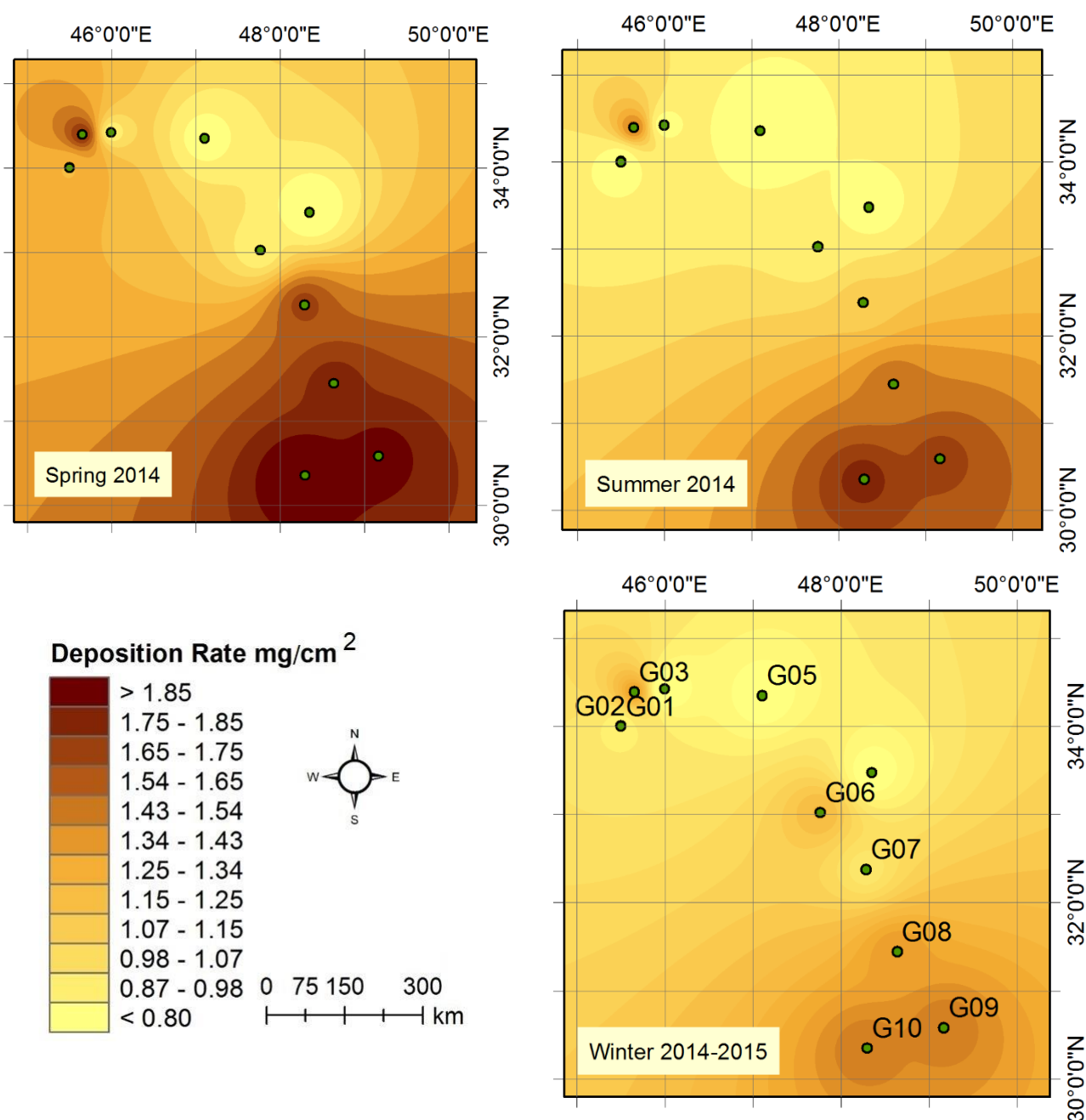


Figure 6.2 Maps showing the seasonal dust deposition rates (mg/cm²/month).

Overall, the seasonal adjustment shows that after February 2014, the deposition rate (mg/cm²) rose sharply to 1.3, increased to 1.4 in March and April, and remained constant in May (1.3). The GDR values fluctuated between 1.3 and 1.4 mg/cm² during the spring and summer and dropped sharply to 0.7 mg/cm² in September. Again, the deposition rate rose slowly in October, and then steadily declined,

reaching minima in December. In January 2015, it underwent a sudden increase, and the deposition rate almost recovered to its maximum rate of 1.5 in February. Finally, the rate dropped by 1.2 mg/cm² in March. By all means, the highest deposition rate occurred in the spring, and the lowest in the fall, based on the high negative correlation between the GDR and precipitation. This contribution is consistent with the observations of Trenberth (2011), which is revealed the highest dust deposition rates in early summer could be caused by dusty winds and low humidity. In addition, the lowest dust deposition rates occurred in autumn when heavy rainfalls occurred during the sampling time. In line with the highest deposition rate in the Gansu province of China (Ta et al., 2004) occurred in the spring. However, with a slight offset, the highest seasonal deposition rate in northern Kuwait (Al-Dousari & Al-Awadhi, 2012, 2012) occurred in the winter, with the rates in spring, summer, and autumn decreasing in that order.

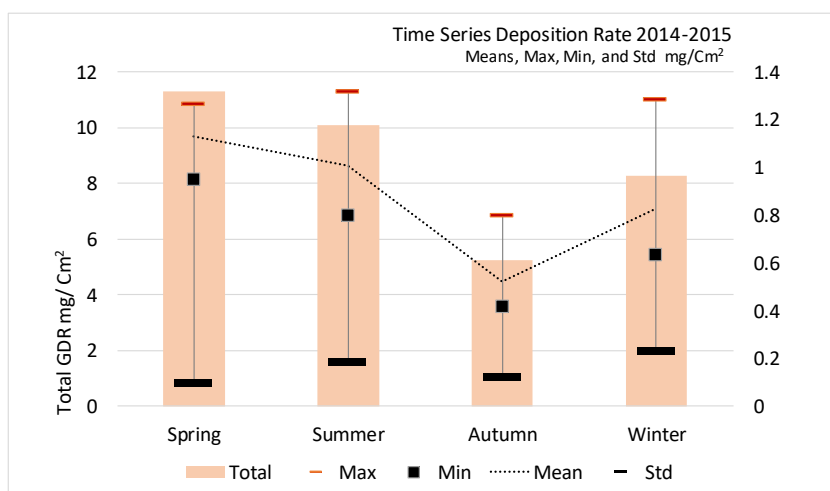


Figure 6.3 Seasonal average deposition rate gathered from the GDR

The seasonal deposition trend is as follows: spring > summer > winter > fall. This trend is depicted in Fig. 6.5. The highest GDR value was exhibited in spring (11 mg/cm²), and the fall season showed deposition rates (mg/cm²) ranging from 0.67 to 7.44, which constitute the lowest recorded rate. No statistically significant difference was observed between the GDR values in the late winter, spring and summer; however, the mean differences between the fall and winter seasons were statistically significant.

6.4 Model output and discussion

Figure 6.4 shows the WRF-modeled wind rose diagrams for the deposition sites for the two simulation periods in 2014 and 2015. The general patterns of the wind rose diagrams for both the simulation periods are reasonably similar. The predominant wind directions can be noticed along the northwest to the southeast, particularly for G08, G09, and G10, which are located in the depositional plain of the south. These predominant wind directions are consistent with the simulated dust concentration by the WRF-Chem model.

Figure 6.5 illustrates the contour maps of the simulated dust concentrations (µg/m³) over the second domain (subdomain) of the WRF model. Outputs of the weather simulations are set with an interval of 1 h; however, to enhance the existing data visualization, each image in Fig. 6.5 represents a 20-day average value of the dust concentration.

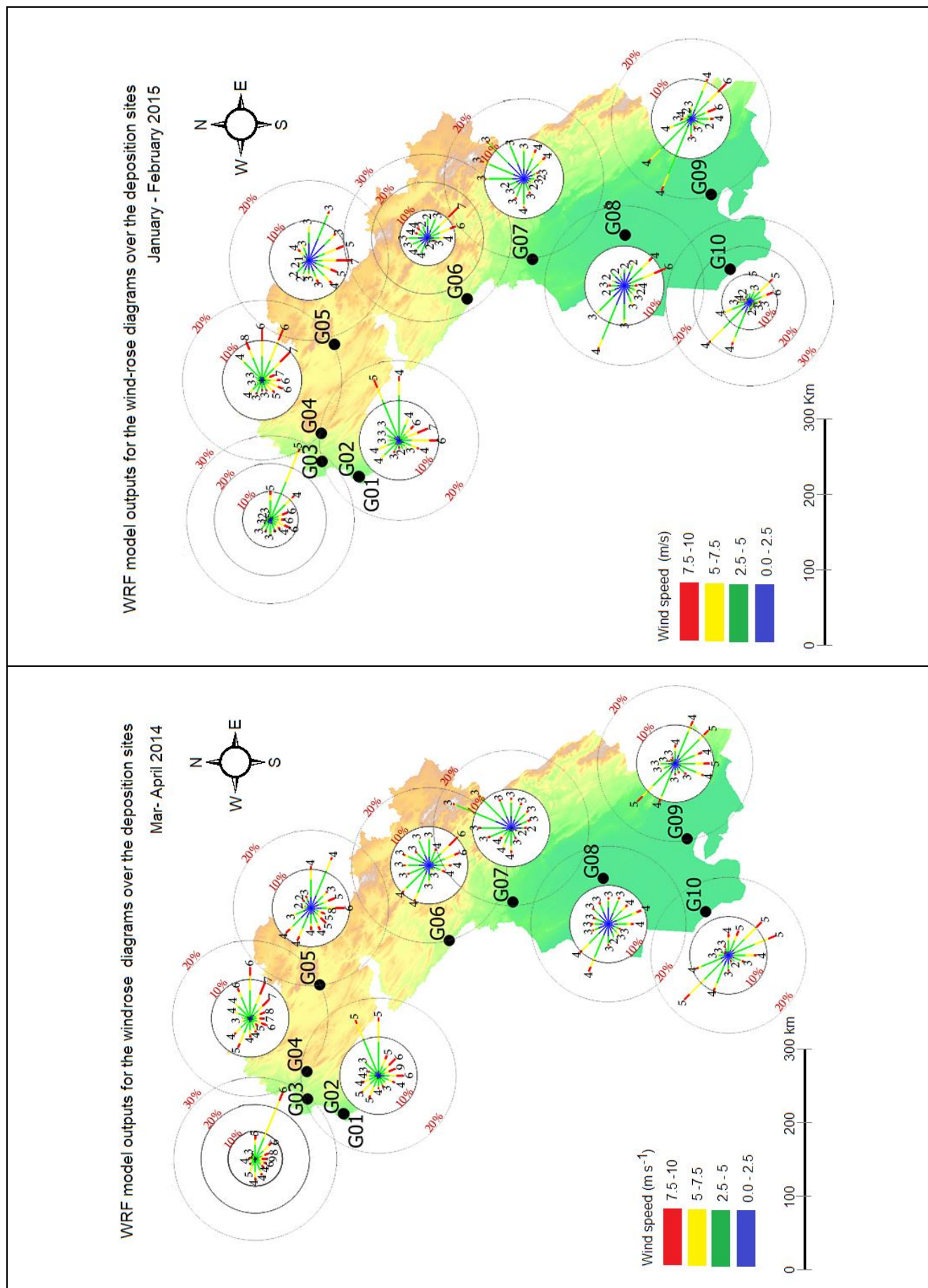


Figure 6.4 WRF model outputs for the wind rose diagrams

From (a) to (f), regions with higher dust concentrations, depicted as red contours, are noticeable over the southern parts of the second simulation domain in G10, G09, G08, and G07. A reason for this pattern may be the soil erosion fields, which cover considerably large areas in the south. In comparison, in the northern parts with mountainous terrains and high altitudes, the soil sediments of the aeolian and fluvial processes cannot be accumulated, and hence, dust sources are not expected to form in such regions.

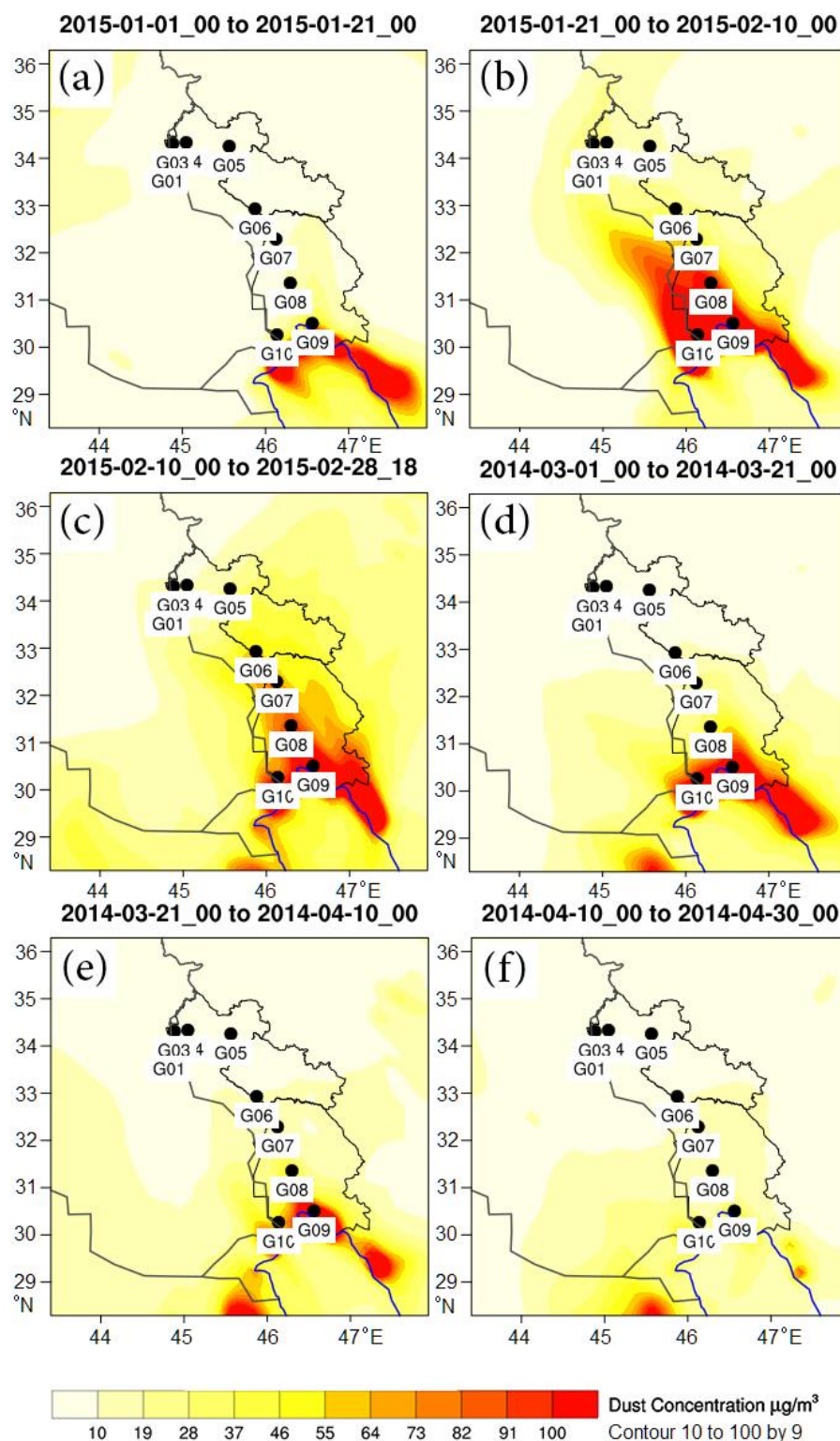


Figure 6.5 WRF-Chem results for concentrations ($\mu\text{g}/\text{m}^3$)

For further investigation of the WRF-Chem results and variations in the simulated dust load, the time series of the modeled dust concentration for the two simulation periods are depicted in Fig. 6.6 from (a) to (f).

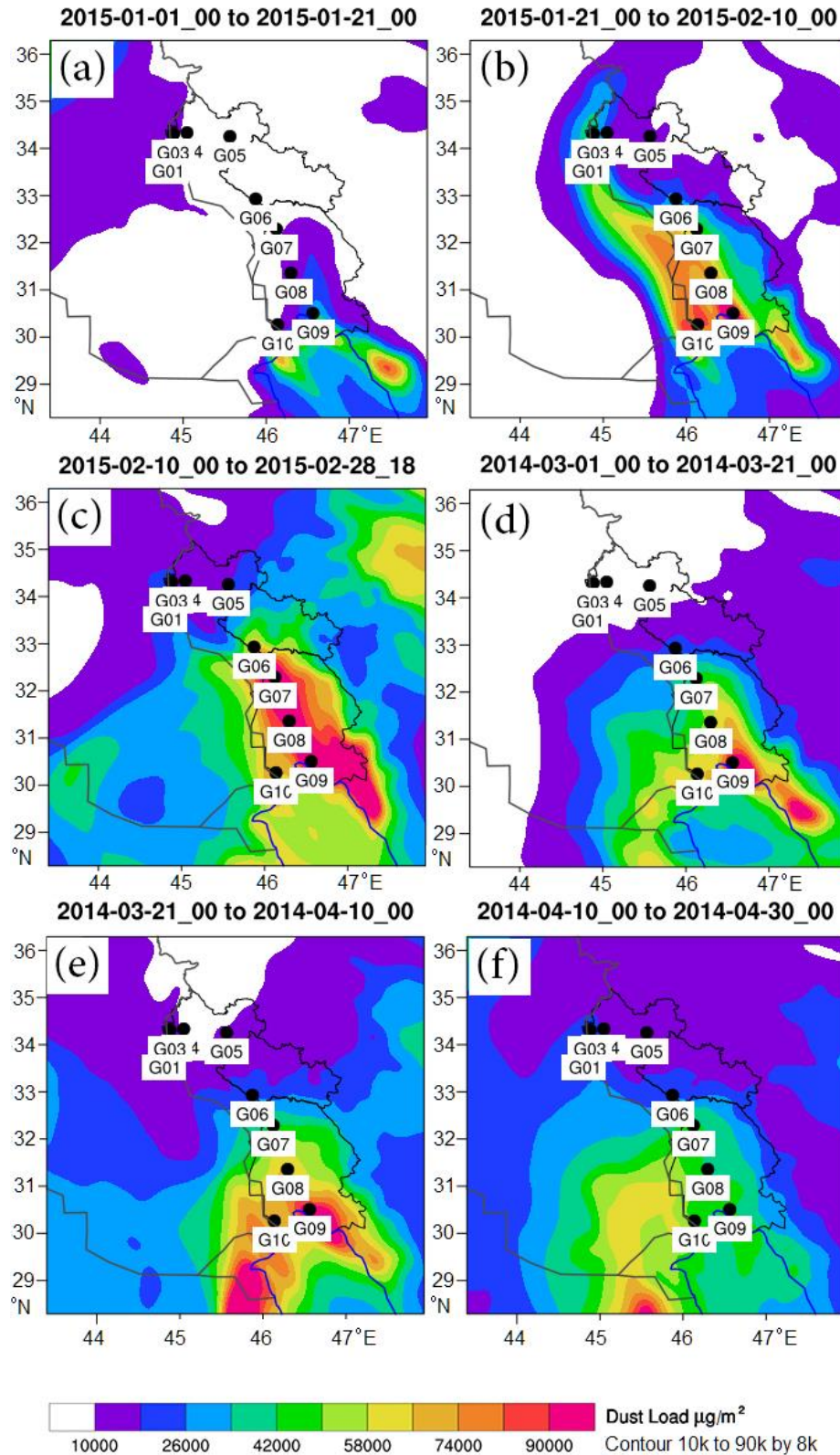


Figure 6.6 WRF-Chem results for the load ($\mu\text{g}/\text{m}^2$)

Regions with a higher dust load ($100\text{k } \mu\text{g}/\text{m}^2$) are noticeable over the southern parts of the study area. The dust load increased from B to C in 2015 and increased slightly from (d) to (e) in 2014. However, in

the northern parts, the dust load barely increased to 26k $\mu\text{g}/\text{m}^2$. In Fig. 6.6, dust loads are grouped by a time series composed of ten days in a chronological order, in March, April 2014 and January, February 2015.

This section discusses the deposition rates based on the LULC classification, climate factors, and GDR data, and provides a better interpretation of the overall influence of the deposition rate on the WRF-Chem model output under the three scenarios. To assess the LULC and climate offset for each gauge site, areas with the same climate zone were classified for analysis. A dendrogram is the most commonly used method for cluster analysis.

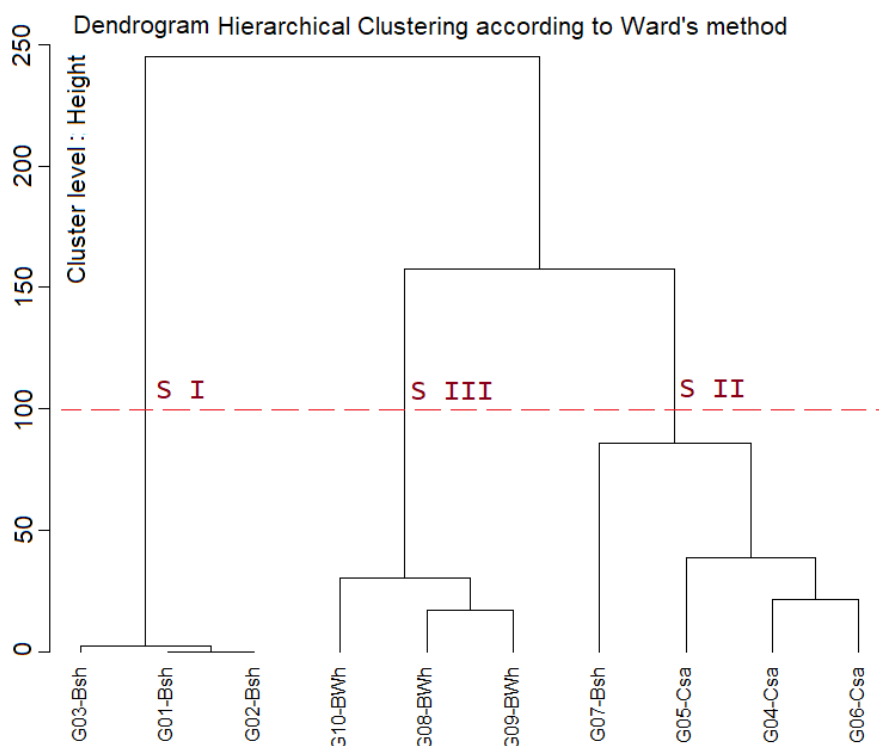


Figure 6.7 Hierarchical relationships among the LULC, gauge sites, and climate zones

*Clustering analysis was performed following Ward's method (Tokaloğlu & Kartal, 2006; Yongming et al., 2006). The study area was classified into three exclusive scenarios based on a combination of internal variables, such as the climate patterns, and this classification was applied to identify different LULC groups by clustering sites with similar climate patterns.

Based on the maximum likelihood classification (Fig. 6.7), the first scenario, S.I, for the three gauges is considered as [S.I- G01, G02, G03] under the BSh Climate. The Csa climate zone in the second scenario (S.II) covers four gauge sites, depicted as [S.II- G04, G05, G06, G07]. For the third scenario (S.III), however, [S.III- G08, G09, and G10] are clustered in the BWh climate zone.

Seasonal ground-based observations showed that the highest dust deposition rates ranged from 1.45 to 1.7 mg/cm^2 , with a mean value of 1.1 mg/cm^2 occurring in the spring (April) and that of 1.45 mg/cm^2 in late winter at [S.III- G09, G10]. The maximum mean of the GDR values was recorded in the following order: (1.2), summer (1.0), winter (0.8), and autumn (< 0.5). The lowest deposition rates, of 0.35 mg/cm^2 , in autumn were reported for September and November and were located at [S.I -G01 to G03] and [S.II -G06, G07].

In the spring, while the highest value (1.49 mg/cm^2) was recorded in April for [S.III -G08, G09] and the lowest value (0.85 mg/cm^2) was recorded in May for [S.I -G03]. Similarly, in summer, for S.III, the maximum values of 1.49 and 1.45 mg/cm^2 were obtained in June and July, respectively, whereas the

minimum amount (0.6 mg/cm^2) was observed in August. The minimum value remained the same from the late summer onward. Subsequently, it slightly increased in the autumn months, resulting in a maximum value (0.8 mg/cm^2) at G10 and a minimum value (0.3 mg/cm^2) in September and November at [S.II- G06 and G07]. Similarly, in winter, a high deposition rate (1.2 mg/cm^2) was observed in [S.III- G09] in January, with the exception of a heavy dust event in late winter. In contrast, a minimum amount (0.35 mg/cm^2) was recorded in December at [S.II- G07 and G06].

As is shown in Fig. 6.8 and Fig. 6.9, because of the short geographical distance between G01 and G02, the same grid point can represent both G01 and G02; therefore, they are expected to show the same values in the plot of the dust load and concentration.

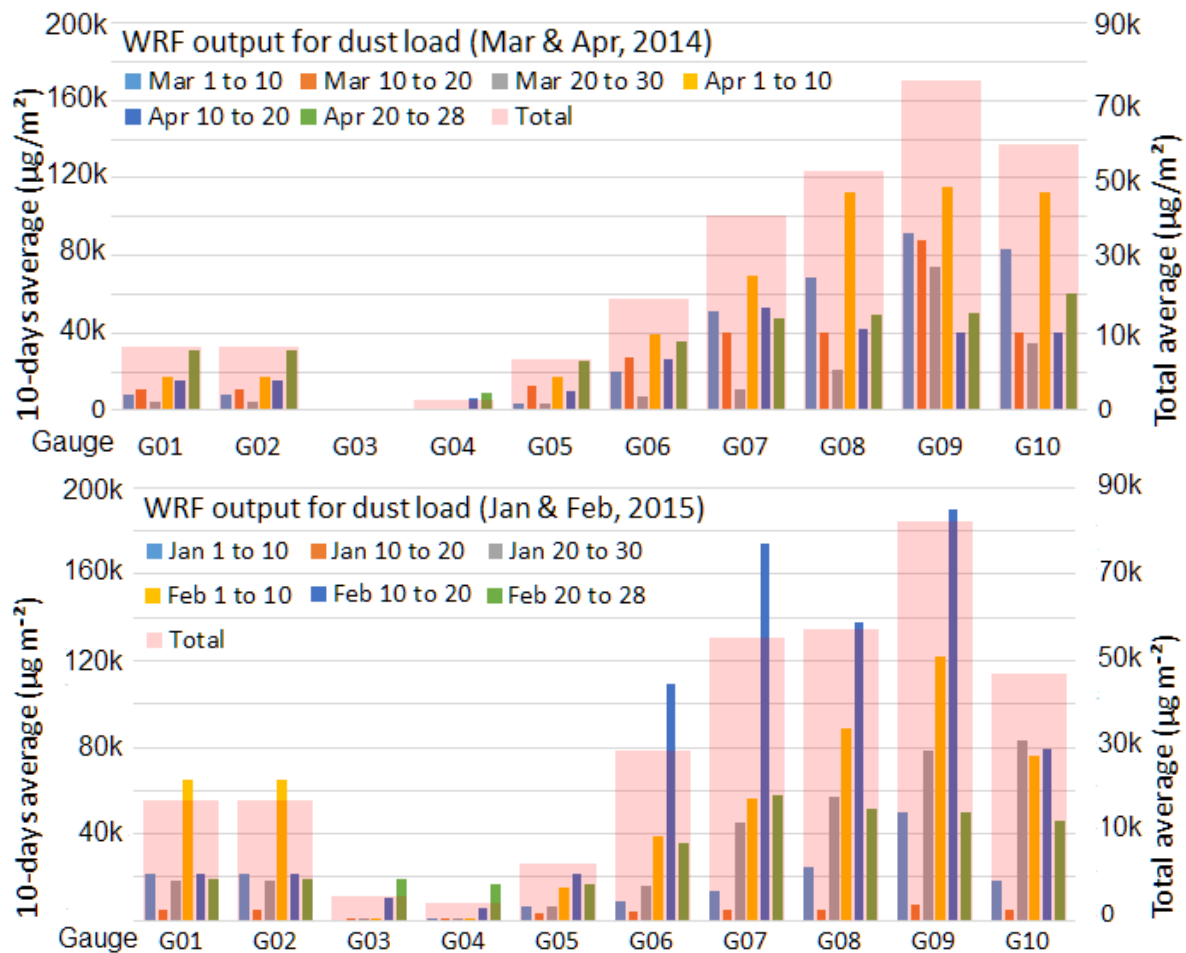


Figure 6.8 Time series of the 10-day average and total average modeled load ($\mu\text{g}/\text{m}^2$)

*The time series plot of the modeled dust load and dust concentration is extracted from the WRF outputs using the nearest point method. The main Y-axis (left) represents the ten-day average values, whereas the secondary Y-axis (right) denotes the total average values

The lowest dust load values [S.I- G03], [S.II- G04, and G05] were in the northernmost deposition sites, and the highest dust load values [S.III- G08, G09, and G10] were in the southernmost deposition sites. The investigation of the dust load revealed that on the time series plot over any of the individual deposition sites, [S.II-G06, G07], and [S.III- G08, G09, and G10] showed approximately the same patterns for the variations in the dust loads, and could be classified in the same group. For example, the blue column (Feb 10 to 20) and yellow column (Apr 1 to 10) correspond to the period with the highest dust load for almost all of the aforementioned sites. However, [S.I - G01, G02, and indeed G03] show different variations in the dust load values. This contrast can be explained by the different geographical regions of these deposition sites, LULC, and climate patterns, which cause them to experience different dust episodes. Therefore, the WRF-Chem model may slightly underestimate the measured dust over

the load area with a soil less susceptible to erosion (Nichols and Hirst, 1998; Koren et al., 2006; Todd et al., 2008; Bullard et al., 2011). Consistent with Trenberth (2011) and Tao et al. (2012), the correlation between the deposition rate and meteorological pattern indicates that high temperatures and lack of precipitation are the most significant factors behind a high dust deposition rate. Therefore, in the autumn and early winter seasons, the lower values of the meteorological parameters, such as temperature, and comparative wind direction, appear to be responsible for the lower deposition.

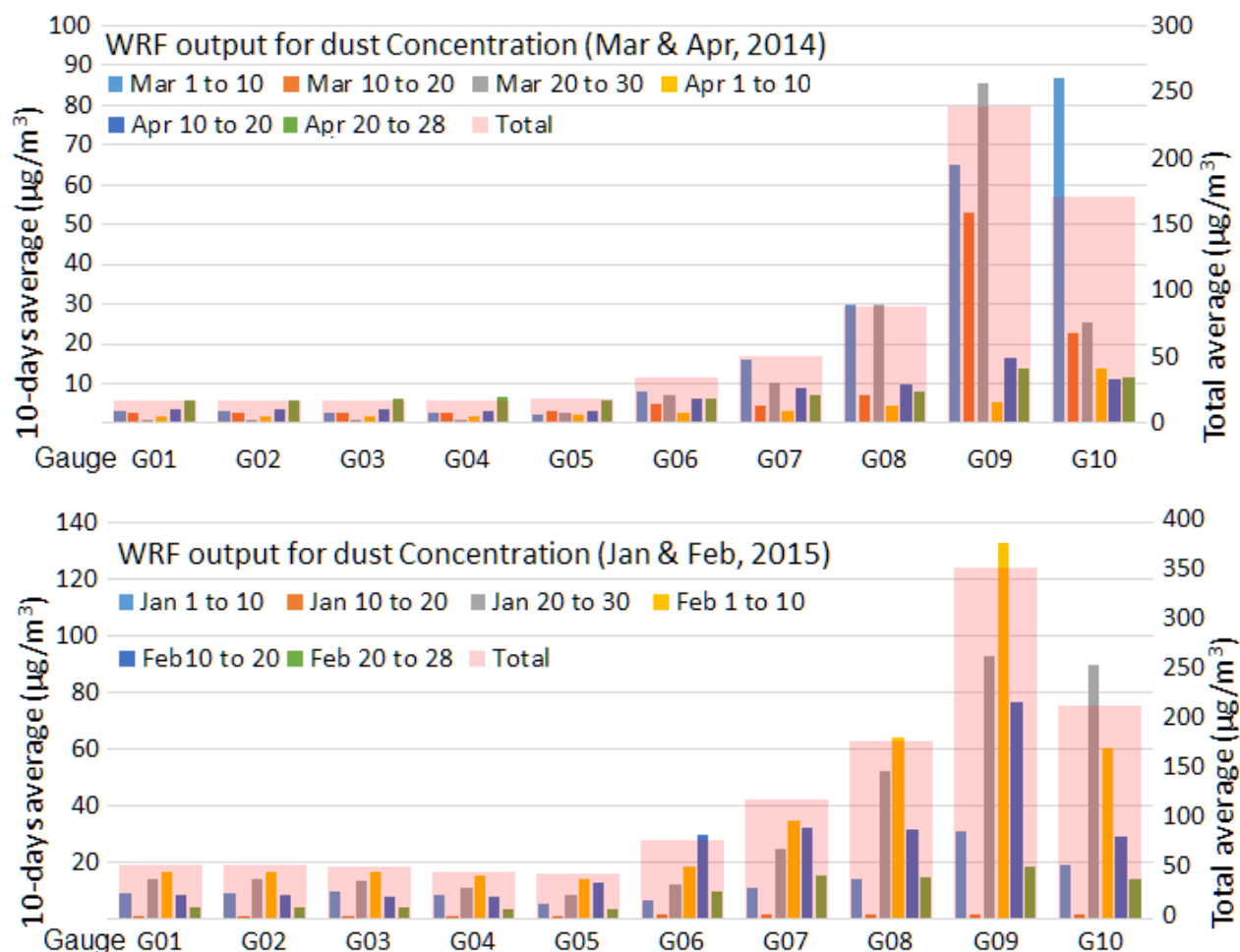


Figure 6.9 Time series of the 10-day average and the total average modeled concentration ($\mu\text{g}/\text{m}^3$)

As is shown in Fig. 6.9, the variation in the concentration values indicates the following sequence: [S.I- G01, G02, G03] < [S.II- G04, G05, G06, G07] < [S.III- G08, G09, G10]. The lowest rates occurred in March and April 2014 for [S.I] (less than $10 \mu\text{g}/\text{m}^3$), [S.II] (slightly above $10 \mu\text{g}/\text{m}^3$), and [S.III] (approximately $160 \mu\text{g}/\text{m}^3$). Similarly, with the same trend in January and February 2015, the lowest rates were approximately $20 \mu\text{g}/\text{m}^3$ for [S.I], slightly less than $40 \mu\text{g}/\text{m}^3$ for [S.II], and approximately $250 \mu\text{g}/\text{m}^3$ for [S.III-].

A statistical comparison of the GDR and model results for both the load and concentration values over the study area was performed to reveal the true correlation and evaluate the rate factor from the model output. A strong positive correlation was presented by the WRF-Chem model for the dust load in January–February 2015 (80%), at 0.004 (p-value). The probability level and correlation lines showed a line-wise match (a perfect match line). In contrast, in the winter, the correlation coefficient between the GDR and WRF-Chem data for March–April 2014 (62%) was calculated to have a p-value of 0.032. This contribution is consistent with previous research, suggesting that different land surface and the climate patterns influence the regional aeolian dust budget and its interaction in the climate system (Li et al., 2016; Carvalho et al., 2012; Mattar and Borvarán, 2016). Moreover, as is illustrated in Fig. 6.10B, the correlation coefficients between the GDR data and WRF-Chem model for the dust concentration in January–February 2015 (75%) and March–April 2014 (76%) have p-values of 0.012 and 0.009 (Fig. 6.10D), respectively. This contribution is reinforced by the rate factor of the dust deposition and by the correlation coefficient between the dust-in-suspension level (WRF-Chem for dust) and the deposition rate (GDR). This rate is altered when dust travels from the south points to the northwest points.

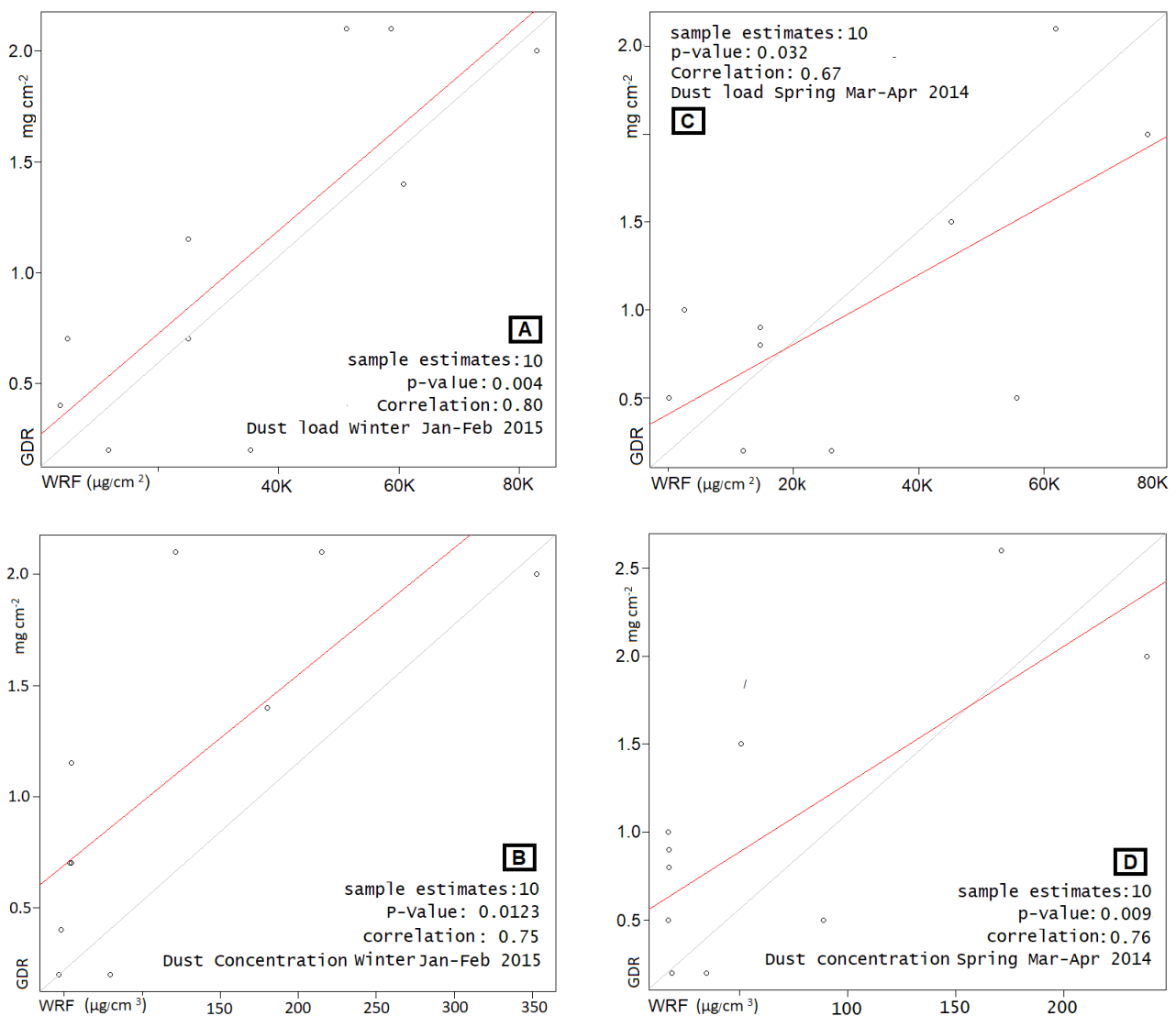


Figure 6.10 Correlation plot of the WRF-Chem versus the GDR observation

*Scatter plot between GDRs (observation) and WRF-Chem (model output) illustrates that for the dust load (A) and dust concentrations (B) in January 2015 on the left and the correlation coefficient value in spring 2014 for the dust load (C) and concentration (D) on the right side

Atmospheric variables, such as temperature and precipitation, are sensitive to land–surface properties and land–atmosphere interactions (Hartig et al., 1997; Shao and Wang, 2003; McMichael et al., 2006). Chronological changes over the land surface are presented under all the conditions, as determined by natural and artificial forcing factors (Camuffo et al., 1999). Yap and Oke (1974) suggested that a reasonable heat flux was mainly determined by the differential temperature, emitting from the land surface to the atmosphere (Rizwan et al., 2008; Lu et al., 2010). Overall, the interactions between the various attributes, such as the climate pattern and topology, are influenced by the deposition rate. Therefore, the dust deposition rates and climate are expected to differ in different regions (Arimoto, 2001). The production and movement of the aeolian material through the atmosphere vary in response to large-scale climatic features (Dawson et al., 2014; Feng et al., 2016). In particular, topology factors, e.g., the vicinity to high-elevated and mountainous areas in the east and north, result in biased deposition rates in the north. In addition, with LULC, bare lands, wet lands, urbanization, and vegetation can be used to subjectively define the rate at the dust sampling sites. Locations close to construction or far from roads appear to affect the quantity and quality of the dust. Therefore, for the given three scenarios (S.I, S.II, S.III), a combination of climate variables is applied to the gauge sites.

The first scenario [S.I- G01, G02, and G03], with an average of 40 °C in the summer and an annual precipitation of 170 mm, is mostly comprised of eastward dusty winds. The prevailing wind directions are west to east, with northwest and southwest fluctuations (IRIMO, 2013; Doabi et al., 2017). This scenario reveals that more than 99% of the land is bare land and land that extends within the borders of Iraq follows the same pattern. As the dust load and concentration increase, the rate factor poorly represents the deposition rate over the gauge sites [S.I- G01, G02, G03]. The high speed eastward wind may have impacted the reading from the model output.

The second scenario [S.II- G04, G05, G06, and G07] covers a part of the study area in the south (G07), which has been suffering from significant increases in dust. G04, G05, and G06 had only small dust events. Despite the identical climate over S.II, various land use land surfaces are present. Although G04 and G06 are represented by bare land (48%) and vegetation (27%), G05 contains 32%, 33%, and 34% of vegetation, artificial, and bare lands, respectively. G07 is an exception, as it is represented by mixed vegetation (77%), waterbodies (8%), and artificial land (4%). Numerous studies have focused on the influence of LULC on atmospheric properties and their processes, e.g., boundary layer dynamics (Niyogi et al., 1999), convection (Pielke Sr, 2001), cloud properties (Ray et al., 2003), and precipitation (Douglas et al., 2009; Marshall et al., 2004; Pielke Sr et al., 2007; Ray et al., 2006).

The impact of the land surface on precipitation is complex (Mahmood et al., 2010) and tends to induce both increased and decreased precipitation. For the urbanization scenario, the simulation shows that the average temperature will be increased by 1.2 °C to 4 °C if the study area is entirely urbanized (Lampthey et al., 2005; Li et al., 2018).

Thus, urbanization influences the exchange values of water and energy between the land and atmosphere, due to changes in the surface roughness and soil moisture. In addition, large aerosol emissions in urban areas absorb a large amount of solar shortwave radiation and lead to reduced albedo (Weng et al., 2004). Therefore, the low albedo can be a major reason for changes in the temperature (Betts, 2001; Myhre & Myhre, 2003). Albedo further refers to the fraction of the solar energy reflected from the land surface to the atmosphere (Royer et al., 1988). Kueppers et al. (2008) suggested that urbanization would significantly impact the heat fluxes between the land and atmosphere. Wetland areas have substantially altered evapotranspiration and runoff, which influences the heat exchange (Kalnay & Cai, 2003). This can cause shifts of land use to croplands, i.e., the structure and function of the vegetation layer can change and the energy flux in the climate system is influenced (Carrington et al., 2001; Kutzbach et al., 1998; Stohlgren et al., 1998). This change is consistent with that observed previous studies that suggested that irrigation could potentially increase precipitation (DeAngelis et al., 2010; Trusilova et al., 2008). During the period with increasing dust load, a narrow gap between the

dust concentration and deposition rates over the gauge sites [S.II] was weak. The high-altitude Zagros Mountains, however, have negatively affected the impact of the deposition rate at the gauge sites [S.II-G07, G06, G05, G04].

In the third scenario (S.III), frequent dust events occurring over decades were attributed by the spatial analysis that showed that the dust pattern extended across the area from a dusty region in Iraq, Saudi Arabia, and Syria and reached southwest Iran every year, particularly during the hot season (Mashayekhi et al., 2009; Moorthy et al., 2016). Aeolian dust was blown from beyond the national border and the aeolian deposition rate has continued to be a major crisis caused by the low topography and extremely warm and arid climate, (Zarasvandi et al., 2011) which reaches over 55 °C in the summer with an annual (100–150 mm) deficit of rainfall. While one third of the area over G10 is bare land (36%), the remaining is composed of vegetation (15%), artificial (25%), and wetlands (22%). The covered areas serve as obstacles for dust and trap dust when the wind is not sufficiently strong. As can be seen in the last scenario, the areas in G08 and G09 include vegetation (33%, 19%), artificial areas (8%, 9% of total), and bare lands (58%, 60% of total). Consistent with the results of Daniali and Karimi, (2019b), as the dust load increases, a positive ratio exists between the dust concentration and deposition rate over the gauge sites [S.III- G10, G09, G08].

6.5 Conclusion

The seasonal dust deposition rate was investigated using the WRF-Chem model to predict the deposition rate of the dust load and the concentration of dust over southwest Iran between 2014 and 2015. The model simulation results were combined with the GDRs and surface meteorological variables at 10 gauge sites. The results of the deposition rate for the three scenarios [S.I, S.II, and S.III] is discussed. S.III exhibited the highest amount of dust, whereas the minimum value was recorded over S.I and S.II.

The analyses indicate that the WRF-Chem model adequately simulates the evolution and spatial distributions of the rate factor over the study area. Although this contribution demonstrates that the WRF-Chem model has significant potential to simulate dust storms, the results reveal decreasing amount of dust load from the southern to the northern points. This indicates a narrowing of the gap between the modeling results and GDR data. The dust concentration and dust load poorly represent the increase in dust particles when moving to lower altitudes or the increase in the dust resident time at high altitudes. The results provide useful guidance for early warnings systems and risk reduction of dust events under various environmental conditions.

The strongest positive correlation between the WRF-Chem model results and GDR data was found for the concentration in the spring, with a correlation coefficient of 76% and $p = 0.0123$. Similarly, a strong correlation for the dust load in the winter (80%) was noted, with $p = 0.004$. This combination is an important data source and can be a relevant subject for studies in this field. In practice, however, unlike with corresponding observations from dust deposition rates (GDRs), the WRF-Chem results show decreases in the dust load and concentrations from the southwest [S.III] to the northwest [S.I] due to the model prediction of dust movement at higher altitudes; for example, the rate factor in [S.II] was higher and the rate factor in [S.I] was lower rate compared with the dust deposition rate captured from GDRs.

The results from this study are consistent with those of previous reviews and show that physical characteristics and gradient distributions are not well known; therefore, a consistent effort is needed to improve our predictions. The capacity of the WRF-Chem to model dust based on GDRs over a study area suggests that future investigations can accurately predict GDRs from the prediction model. Therefore, GDR data can increase the accuracy of the estimations, whereas an appropriate algorithm is necessary to enhance the affected area exposed to dust.

Acknowledgment

I wish to acknowledge the cooperation of IOPTC, experts at home country during the conduction of the fieldwork. We also wish to acknowledge Alireza Rezaei Barmi and his scientific contributions to the preparation and operation of the instruments.

Funding sources

This work did not receive any specific grant from funding agencies in the public, commercial, or not-for-profit sectors.

References

- Abdulrazzaq, Z. T., Hasan, R. H., & Aziz, N. A. (2019). Integrated TRMM Data and Standardized Precipitation Index to Monitor the Meteorological Drought. *Civil Engineering Journal*, 5(7), 1590–1598.
- Ai, N., & Polenske, K. R. (2008). Socioeconomic impact analysis of yellow-dust storms: An approach and case study for Beijing. *Economic Systems Research*, 20(2), 187–203.
- Al-Dousari, A. M., & Al-Awadhi, J. (2012). Dust fallout in northern Kuwait, major sources and characteristics. *Kuwait Journal of Science*, 39(2A), 171–187.
- Al-Harbi, M. (2015). Characteristics and composition of the falling dust in urban environment. *International Journal of Environmental Science and Technology*, 12(2), 641–652.
- Alizadeh-Choozari, O., & Najafi, M. (2018). Extreme weather events in Iran under a changing climate. *Climate Dynamics*, 50(1–2), 249–260.
- Amiridis, V., Wandinger, U., Marinou, E., Giannakaki, E., Tsekeri, A., Basart, S., Kazadzis, S., Gkikas, A., Taylor, M., & Baldasano, J. (2013). Optimizing Saharan dust CALIPSO retrievals. *Atmos. Chem. Phys. Discuss*, 13, 14749–14795.
- AO, J. W. Z. (2001). The IPCC Third Assessment Report on the Scientific Basis of Climate Change. *Australian Journal of Environmental Management*, 8(3), 169–185. <https://doi.org/10.1080/14486563.2001.10648526>
- Arghavani, S., Malakooti, H., & Bidokhti, A. A. (2019). Numerical evaluation of urban green space scenarios effects on gaseous air pollutants in Tehran Metropolis based on WRF-Chem model. *Atmospheric Environment*, 116832.
- Arimoto, R. (2001). Eolian dust and climate: Relationships to sources, tropospheric chemistry, transport and deposition. *Earth-Science Reviews*, 54(1–3), 29–42.
- ASTM D1356. (2017). Standard Terminology Relating to Sampling and Analysis of Atmospheres. In *Book of Standards*. Subcommittee D22.03. <https://www.astm.org/Standards/D1356.htm>
- Bates, D., & Rudel, T. K. (2000). The political ecology of conserving tropical rain forests: A cross-national analysis. *Society & Natural Resources*, 13(7), 619–634.
- Beres, J. H., Garcia, R. R., Boville, B. A., & Sassi, F. (2005). Implementation of a gravity wave source spectrum parameterization dependent on the properties of convection in the Whole Atmosphere Community Climate Model (WACCM). *Journal of Geophysical Research: Atmospheres*, 110(D10).
- Betts, R. A. (2001). Biogeophysical impacts of land use on present-day climate: Near-surface temperature change and radiative forcing. *Atmospheric Science Letters*, 2(1-4), 39–51.
- Bolloorani, A. D., Nabavi, S. O., Bahrami, H. A., Mirzapour, F., Kavosi, M., Abasi, E., & Azizi, R. (2014). Investigation of dust storms entering Western Iran using remotely sensed data and synoptic analysis. *Journal of Environmental Health Science and Engineering*, 12(1), 124.
- Bullard, J. E., Harrison, S. P., Baddock, M. C., Drake, N., Gill, T. E., McTainsh, G., & Sun, Y. (2011). Preferential dust sources: A geomorphological classification designed for use in global dust-cycle models. *Journal of Geophysical Research: Earth Surface*, 116(F4).
- Calvert, J. G. (1990). Glossary of atmospheric chemistry terms (Recommendations 1990). *Pure and Applied Chemistry*, 62(11), 2167–2219.

- Camuffo, D., Sturaro, G., & Valentino, A. (1999). Thermodynamic exchanges between the external boundary layer and the indoor microclimate at the Basilica of Santa Maria Maggiore, Rome, Italy: The problem of conservation of ancient works of art. *Boundary-Layer Meteorology*, 92(2), 243–262.
- Carrington, D. P., Gallimore, R. G., & Kutzbach, J. E. (2001). Climate sensitivity to wetlands and wetland vegetation in mid-Holocene North Africa. *Climate Dynamics*, 17(2–3), 151–157.
- Carvalho, D., Rocha, A., Gómez-Gesteira, M., & Santos, C. (2012). A sensitivity study of the WRF model in wind simulation for an area of high wind energy. *Environmental Modelling & Software*, 33, 23–34.
- Carvalho, D., Rocha, A., Gómez-Gesteira, M., & Santos, C. S. (2014). WRF wind simulation and wind energy production estimates forced by different reanalyses: Comparison with observed data for Portugal. *Applied Energy*, 117, 116–126.
- Charlson, R. J., Schwartz, S., Hales, J., Cess, R. D., Coakley, J. J., Hansen, J., & Hofmann, D. (1992). Climate forcing by anthropogenic aerosols. *Science*, 255(5043), 423–430.
- Chen, S., Huang, J., Zhao, C., Qian, Y., Leung, L. R., & Yang, B. (2013). Modeling the transport and radiative forcing of Taklimakan dust over the Tibetan Plateau: A case study in the summer of 2006. *Journal of Geophysical Research: Atmospheres*, 118(2), 797–812.
- Chen, Y.-S., Sheen, P.-C., Chen, E.-R., Liu, Y.-K., Wu, T.-N., & Yang, C.-Y. (2004). Effects of Asian dust storm events on daily mortality in Taipei, Taiwan. *Environmental Research*, 95(2), 151–155.
- Choobari, O. A., Zawar-Reza, P., & Sturman, A. (2012). Feedback between windblown dust and planetary boundary-layer characteristics: Sensitivity to boundary and surface layer parameterizations. *Atmospheric Environment*, 61, 294–304.
- Claiborn, C. S., Finn, D., Larson, T. V., & Koenig, J. Q. (2000). Windblown dust contributes to high PM25 concentrations. *Journal of the Air & Waste Management Association*, 50(8), 1440–1445.
- Climate Change Knowledge Portal (The World Bank Group). (2016). Climatic Research Unit (CRU) University of East Anglia (UEA). http://sdwebx.worldbank.org/climateportal/index.cfm?page=country_historical_climate&ThisCCode=IRN
- Daniali, M., & Karimi, N. (2019a). Spatiotemporal analysis of dust patterns over Mesopotamia and their impact on Khuzestan province, Iran. *Natural Hazards*, 1–23.
- Daniali, M., & Karimi, N. (2019b). Spatiotemporal analysis of dust patterns over Mesopotamia and their impact on Khuzestan province, Iran. *Natural Hazards*, 1–23.
- Dawson, J. P., Bloomer, B. J., Winner, D. A., & Weaver, C. P. (2014). Understanding the meteorological drivers of US particulate matter concentrations in a changing climate. *Bulletin of the American Meteorological Society*, 95(4), 521–532.
- De Chazal, J., & Rounsevell, M. D. (2009). Land-use and climate change within assessments of biodiversity change: A review. *Global Environmental Change*, 19(2), 306–315.
- De Longueville, F., Ozer, P., Doumbia, S., & Henry, S. (2013). Desert dust impacts on human health: An alarming worldwide reality and a need for studies in West Africa. *International Journal of Biometeorology*, 57(1), 1–19.

- DeAngelis, A., Dominguez, F., Fan, Y., Robock, A., Kustu, M. D., & Robinson, D. (2010). Evidence of enhanced precipitation due to irrigation over the Great Plains of the United States. *Journal of Geophysical Research: Atmospheres*, 115(D15).
- Dee, D. P., Uppala, S., Simmons, A., Berrisford, P., Poli, P., Kobayashi, S., Andrae, U., Balmaseda, M., Balsamo, G., & Bauer, P. (2011). The ERA-Interim reanalysis: Configuration and performance of the data assimilation system. *Quarterly Journal of the Royal Meteorological Society*, 137(656), 553–597.
- Díaz, J., Tobías, A., & Linares, C. (2012). Saharan dust and association between particulate matter and case-specific mortality: A case-crossover analysis in Madrid (Spain). *Environmental Health*, 11(1), 11.
- Doabi, S. A., Afyuni, M., & Karami, M. (2017). Multivariate statistical analysis of heavy metals contamination in atmospheric dust of Kermanshah province, western Iran, during the spring and summer 2013. *Journal of Geochemical Exploration*, 180, 61–70.
- Dong, L., Wang, W., Ma, M., Kong, J., & Veroustraete, F. (2009). The change of land cover and land use and its impact factors in upper key regions of the Yellow River. *International Journal of Remote Sensing*, 30(5), 1251–1265.
- Douglas, E., Beltrán-Przekurat, A., Niyogi, D., Pielke Sr, R., & Vörösmarty, C. (2009). The impact of agricultural intensification and irrigation on land–atmosphere interactions and Indian monsoon precipitation—A mesoscale modeling perspective. *Global and Planetary Change*, 67(1–2), 117–128.
- Duce, R. (1995). Sources, distributions, and fluxes of mineral aerosols and their relationship to climate. *Aerosol Forcing of Climate*.
- Elminir, H. K., Ghitas, A. E., Hamid, R., El-Hussainy, F., Beheary, M., & Abdel-Moneim, K. M. (2006). Effect of dust on the transparent cover of solar collectors. *Energy Conversion and Management*, 47(18–19), 3192–3203.
- El-Nashar, A. M. (2003). Effect of dust deposition on the performance of a solar desalination plant operating in an arid desert area. *Solar Energy*, 75(5), 421–431.
- Feng, J., Liao, H., & Li, J. (2016). The impact of monthly variation of the Pacific–North America (PNA) teleconnection pattern on wintertime surface-layer aerosol concentrations in the United States. *Atmospheric Chemistry and Physics*, 16(8), 4927.
- Foroushani, M. A., Opp, C., & Groll, M. (2019). Chemical Characterization of Aeolian Dust Deposition in Southern and Western Iran. 1–22. <https://doi.org/10.9734/ajgr/2019/v2i230081>
- Gerivani, H., Lashkaripour, G. R., Ghafoori, M., & Jalali, N. (2011). The source of dust storm in Iran: A case study based on geological information and rainfall data. *Carpathian Journal of Earth and Environmental Sciences*, 6.
- Ghasem, A., Shamsipour, A., Miri, M., & Safarrad, T. (2012). Synoptic and remote sensing analysis of dust events in southwestern Iran. *Natural Hazards*, 64(2), 1625–1638.
- Gholampour, A., Nabizadeh, R., Yunesian, M., Naseri, S., Taghipour, H., Rastkari, N., Nazmara, S., & Mahvi, A. H. (2014). Physicochemical characterization of ambient air particulate matter in Tabriz, Iran. *Bull Environ Contam Toxicol*, 92(6), 738–744. <https://doi.org/10.1007/s00128-014-1276-8>

- Gong, S., Zhang, X., Zhao, T., McKendry, I., Jaffe, D., & Lu, N. (2003). Characterization of soil dust aerosol in China and its transport and distribution during 2001 ACE-Asia: 2. Model simulation and validation. *Journal of Geophysical Research: Atmospheres*, 108(D9).
- Goudie, A. S., & Middleton, N. J. (2001). Saharan dust storms: Nature and consequences. *Earth-Science Reviews*, 56(1–4), 179–204. [https://doi.org/Doi 10.1016/S0012-8252\(01\)00067-8](https://doi.org/Doi 10.1016/S0012-8252(01)00067-8)
- Goudie, Andrew S. (2009). Dust storms: Recent developments. *Journal of Environmental Management*, 90(1), 89–94.
- Grell, G. A., Peckham, S. E., Schmitz, R., McKeen, S. A., Frost, G., Skamarock, W. C., & Eder, B. (2005). Fully coupled “online” chemistry within the WRF model. *Atmospheric Environment*, 39(37), 6957–6975.
- Groll, M., Opp, Chr., & Aslanov, I. (2013). Spatial and temporal distribution of the dust deposition in Central Asia – results from a long term monitoring program. *Aeolian Research*, 9, 49–62. <https://doi.org/10.1016/j.aeolia.2012.08.002>
- Hahnenberger, M., & Nicoll, K. (2014). Geomorphic and land cover identification of dust sources in the eastern Great Basin of Utah, USA. *Geomorphology*, 204, 657–672.
- Hamidi, M., Kavianpour, M. R., & Shao, Y. (2014). Numerical simulation of dust events in the Middle East. *Aeolian Research*, 13, 59–70.
- Hartig, E. K., Grozev, O., & Rosenzweig, C. (1997). Climate change, agriculture and wetlands in Eastern Europe: Vulnerability, adaptation and policy. *Climatic Change*, 36(1–2), 107–121.
- Haywood, J., & Boucher, O. (2000). Estimates of the direct and indirect radiative forcing due to tropospheric aerosols: A review. *Reviews of Geophysics*, 38(4), 513–543.
- Heidarian, P., Azhdari, A., Joudaki, M., Khatooni, J. D., & Firoozjaei, S. F. (2018). Integrating Remote Sensing, GIS, and Sedimentology Techniques for Identifying Dust Storm Sources: A Case Study in Khuzestan, Iran. *Journal of the Indian Society of Remote Sensing*, 46(7), 1113–1124.
- Hoffmann, C., Funk, R., Sommer, M., & Li, Y. (2008). Temporal variations in PM10 and particle size distribution during Asian dust storms in Inner Mongolia. *Atmospheric Environment*, 42(36), 8422–8431.
- Huang, J., Wang, T., Wang, W., Li, Z., & Yan, H. (2014). Climate effects of dust aerosols over East Asian arid and semiarid regions. *Journal of Geophysical Research: Atmospheres*, 119(19), 11–398.
- Huang, J., Zhang, W., Zuo, J., Bi, J., Shi, J., Wang, X., Chang, Z., Huang, Z., Yang, S., & Zhang, B. (2008). An overview of the semi-arid climate and environment research observatory over the Loess Plateau. *Advances in Atmospheric Sciences*, 25(6), 906.
- Huang, X., Oberhänsli, H., Von Suchodoletz, H., & Sorrel, P. (2011). Dust deposition in the Aral Sea: Implications for changes in atmospheric circulation in central Asia during the past 2000 years. *Quaternary Science Reviews*, 30(25–26), 3661–3674.
- IHS under license with ASTM. (2010). Standard Terminology Relating to Sampling and Analysis of Atmospheres. IHS under License with ASTM. <https://wenku.baidu.com/view/8324a4b765ce050876321358>
- Iran Meteorological Organization. (2014). Precipitation Map. <http://www.irimo.ir/index.php?newlang=eng>

- IRMO. (2016). I.R.O.F IRAN Meteorological Organization. Dust National Center. <http://www.irimo.ir/far/index.php>
- Jamalizadeh, M., Moghaddamnia, A., Piri, J., Arbabi, V., Homayounifar, M., & Shahryari, A. (2008). Dust Storm Prediction Using ANNs Technique (A Case Study: Zabol City) 1.
- Kalnay, E., & Cai, M. (2003). Impact of urbanization and land-use change on climate. *Nature*, 423(6939), 528.
- Kazem, A. A., Chaichan, M. T., & Kazem, H. A. (2014). Dust effect on photovoltaic utilization in Iraq. *Renewable and Sustainable Energy Reviews*, 37, 734–749.
- Kim, S.-W., Yoon, S.-C., & Kim, J. (2008). Columnar Asian dust particle properties observed by sun/sky radiometers from 2000 to 2006 in Korea. *Atmospheric Environment*, 42(3), 492–504.
- Koren, I., Kaufman, Y. J., Washington, R., Todd, M. C., Rudich, Y., Martins, J. V., & Rosenfeld, D. (2006). The Bodélé depression: A single spot in the Sahara that provides most of the mineral dust to the Amazon forest. *Environmental Research Letters*, 1(1), 014005.
- Kueppers, L. M., Snyder, M. A., Sloan, L. C., Cayan, D., Jin, J., Kanamaru, H., Kanamitsu, M., Miller, N. L., Tyree, M., & Du, H. (2008). Seasonal temperature responses to land-use change in the western United States. *Global and Planetary Change*, 60(3–4), 250–264.
- Kutzbach, J., Gallimore, R., Harrison, S., Behling, P., Selin, R., & Laarif, F. (1998). Climate and biome simulations for the past 21,000 years. *Quaternary Science Reviews*, 17(6–7), 473–506.
- Kwon, H.-J., Cho, S.-H., Chun, Y., Lagarde, F., & Pershagen, G. (2002). Effects of the Asian dust events on daily mortality in Seoul, Korea. *Environmental Research*, 90(1), 1–5.
- Lambin, E. F., & Geist, H. J. (2008). *Land-use and land-cover change: Local processes and global impacts*. Springer Science & Business Media.
- Lenssen, N. J., Schmidt, G. A., Hansen, J. E., Menne, M. J., Persin, A., Ruedy, R., & Zyss, D. (2019). Improvements in the GISTEMP uncertainty model. *Journal of Geophysical Research: Atmospheres*, 124(12), 6307–6326.
- Li, N., Long, X., Tie, X., Cao, J., Huang, R., Zhang, R., Feng, T., Liu, S., & Li, G. (2016). Urban dust in the Guanzhong basin of China, part II: A case study of urban dust pollution using the WRF-Dust model. *Science of the Total Environment*, 541, 1614–1624.
- Li, X., Mitra, C., Dong, L., & Yang, Q. (2018). Understanding land use change impacts on microclimate using Weather Research and Forecasting (WRF) model. *Physics and Chemistry of the Earth, Parts A/B/C*, 103, 115–126.
- Liu, C.-M., Young, C.-Y., & Lee, Y.-C. (2006). Influence of Asian dust storms on air quality in Taiwan. *Science of the Total Environment*, 368(2–3), 884–897.
- Lu, X., Wang, L., Lei, K., Huang, J., & Zhai, Y. (2009). Contamination assessment of copper, lead, zinc, manganese and nickel in street dust of Baoji, NW China. *J Hazard Mater*, 161(2–3), 1058–1062. <https://doi.org/10.1016/j.jhazmat.2008.04.052>
- Lu, Xinwei, Wang, L., Li, L. Y., Lei, K., Huang, L., & Kang, D. (2010). Multivariate statistical analysis of heavy metals in street dust of Baoji, NW China. *Journal of Hazardous Materials*, 173(1–3), 744–749.
- Mahmood, R., Pielke Sr, R. A., Hubbard, K. G., Niyogi, D., Bonan, G., Lawrence, P., McNider, R., McAlpine, C., Etter, A., & Gameda, S. (2010). Impacts of land use/land cover change on climate and future research priorities. *Bulletin of the American Meteorological Society*, 91(1), 37–46.

- Mandal, M., Mohanty, U., & Raman, S. (2004). A study on the impact of parameterization of physical processes on prediction of tropical cyclones over the Bay of Bengal with NCAR/PSU mesoscale model. *Natural Hazards*, 31(2), 391–414.
- Marshall, C. H., Pielke Sr, R. A., Steyaert, L. T., & Willard, D. A. (2004). The impact of anthropogenic land-cover change on the Florida peninsula sea breezes and warm season sensible weather. *Monthly Weather Review*, 132(1), 28–52.
- Mashayekhi, R., Irannejad, P., Feichter, J., & Bidokhti, A. (2009). Implementation of a new aerosol HAM model within the Weather Research and Forecasting (WRF) modeling system. *Geoscientific Model Development Discussions*, 2(2), 681–707.
- Mattar, C., & Borvarán, D. (2016). Offshore wind power simulation by using WRF in the central coast of Chile. *Renewable Energy*, 94, 22–31.
- McMichael, A. J., Woodruff, R. E., & Hales, S. (2006). Climate change and human health: Present and future risks. *The Lancet*, 367(9513), 859–869.
- Merchant, C., Embury, O., Le Borgne, P., & Bellec, B. (2006). Saharan dust in nighttime thermal imagery: Detection and reduction of related biases in retrieved sea surface temperature. *Remote Sensing of Environment*, 104(1), 15–30.
- Mihailović, D. T., & Kallos, G. (1997). A sensitivity study of a coupled soil-vegetation boundary-layer scheme for use in atmospheric modeling. *Boundary-Layer Meteorology*, 82(2), 283–315.
- Miri, A., Ahmadi, H., Ekhtesasi, M. R., Panjehkeh, N., & Ghanbari, A. (2009). Environmental and socio-economic impacts of dust storms in Sistan Region, Iran. *International Journal of Environmental Studies*, 66(3), 343–355. <https://doi.org/10.1080/00207230902720170>
- Moorthy, K. K., Satheesh, S., Sarin, M., & Panday, A. K. (2016). South Asian aerosols in perspective: Preface to the special issue. *Atmospheric Environment*, 125, 307–311.
- Myhre, G., & Myhre, A. (2003). Uncertainties in radiative forcing due to surface albedo changes caused by land-use changes. *Journal of Climate*, 16(10), 1511–1524.
- Nabavi, S. O., Haimberger, L., & Samimi, C. (2017). Sensitivity of WRF-chem predictions to dust source function specification in West Asia. *Aeolian Research*, 24, 115–131.
- Nichols, G. J., & Hirst, J. P. (1998). Alluvial fans and fluvial distributary systems, Oligo-Miocene, northern Spain; contrasting processes and products. *Journal of Sedimentary Research*, 68(5), 879–889.
- Niyogi, D. S., Raman, S., & Alapaty, K. (1999). Uncertainty in the specification of surface characteristics, part II: Hierarchy of interaction-explicit statistical analysis. *Boundary-Layer Meteorology*, 91(3), 341–366.
- Ohde, T., & Siegel, H. (2012). Impacts of Saharan dust and clouds on photosynthetically available radiation in the area off Northwest Africa. *Tellus B: Chemical and Physical Meteorology*, 64(1), 17160.
- Opp, C., Groll, M., Aslanov, I., Lotz, T., & Vereshagina, N. (2017). Aeolian dust deposition in the southern Aral Sea region (Uzbekistan): Ground-based monitoring results from the LUCA project. *Quaternary International*, 429, 86–99.
- Parsa, V. A., Yavari, A., & Nejadi, A. (2016). Spatio-temporal analysis of land use/land cover pattern changes in Arasbaran Biosphere Reserve: Iran. *Modeling Earth Systems and Environment*, 2(4), 1–13.

- Pielke Sr, R. A. (2001). Influence of the spatial distribution of vegetation and soils on the prediction of cumulus convective rainfall. *Reviews of Geophysics*, 39(2), 151–177.
- Pielke Sr, R. A., Adegoke, J., Beltraán-Przekurat, A., Hiemstra, C. A., Lin, J., Nair, U. S., Niyogi, D., & Nobis, T. E. (2007). An overview of regional land-use and land-cover impacts on rainfall. *Tellus B: Chemical and Physical Meteorology*, 59(3), 587–601.
- Prospero, J. M., Ginoux, P., Torres, O., Nicholson, S. E., & Gill, T. E. (2002). ENVIRONMENTAL CHARACTERIZATION OF GLOBAL SOURCES OF ATMOSPHERIC SOIL DUST IDENTIFIED WITH THE NIMBUS 7 TOTAL OZONE MAPPING SPECTROMETER (TOMS) ABSORBING AEROSOL PRODUCT. *Reviews of Geophysics*, 40(1), 2-1-2–31. <https://doi.org/10.1029/2000RG000095>
- Rashki, A., Eriksson, P. G., Rautenbach, C. J., Kaskaoutis, D. G., Grote, W., & Dykstra, J. (2013). Assessment of chemical and mineralogical characteristics of airborne dust in the Sistan region, Iran. *Chemosphere*, 90(2), 227–236. <https://doi.org/10.1016/j.chemosphere.2012.06.059>
- Ray, D. K., Nair, U. S., Lawton, R. O., Welch, R. M., & Pielke Sr, R. A. (2006). Impact of land use on Costa Rican tropical montane cloud forests: Sensitivity of orographic cloud formation to deforestation in the plains. *Journal of Geophysical Research: Atmospheres*, 111(D2).
- Ray, D. K., Nair, U. S., Welch, R. M., Han, Q., Zeng, J., Su, W., Kikuchi, T., & Lyons, T. J. (2003). Effects of land use in Southwest Australia: 1. Observations of cumulus cloudiness and energy fluxes. *Journal of Geophysical Research: Atmospheres*, 108(D14).
- Rezazadeh, M., Irannejad, P., & Shao, Y. (2013). Climatology of the Middle East dust events. *Aeolian Research*, 10, 103–109.
- Rizwan, A. M., Dennis, L. Y., & Chunho, L. (2008). A review on the generation, determination and mitigation of Urban Heat Island. *Journal of Environmental Sciences*, 20(1), 120–128.
- Royer, A., Charbonneau, L., & Bonn, F. (1988). Urbanization and Landsat MSS albedo change in the Windsor-Quebec corridor since 1972. *Remote Sensing*, 9(3), 555–566.
- Schepanski, K., Heinold, B., & Tegen, I. (2017). Harmattan, Saharan heat low, and West African monsoon circulation: Modulations on the Saharan dust outflow towards the North Atlantic. *Atmos. Chem. Phys.*, 17(17), 10223–10243. <https://doi.org/10.5194/acp-17-10223-2017>
- Schleicher, N. J., Norra, S., Chai, F., Chen, Y., Wang, S., Cen, K., Yu, Y., & Stüben, D. (2011). Temporal variability of trace metal mobility of urban particulate matter from Beijing—A contribution to health impact assessments of aerosols. *Atmospheric Environment*, 45(39), 7248–7265.
- Shah, M. H., & Shaheen, N. (2010). Seasonal behaviours in elemental composition of atmospheric aerosols collected in Islamabad, Pakistan. *Atmospheric Research*, 95(2–3), 210–223.
- Shao, Y., & Wang, J. (2003). A climatology of Northeast Asian dust events. *Meteorologische Zeitschrift*, 12(4), 187–196.
- Skamarock, W. C., Klemp, J. B., Dudhia, J., Gill, D. O., Barker, D. M., Wang, W., & Powers, J. G. (2008). A description of the Advanced Research WRF version 3. NCAR Technical note-475+STR.
- Sokolik, I., Winker, D., Bergametti, G., Gillette, D., Carmichael, G., Kaufman, Y., Gomes, L., Schuetz, L., & Penner, J. (2001). Introduction to special section: Outstanding problems in quantifying the radiative impacts of mineral dust. *Journal of Geophysical Research: Atmospheres*, 106(D16), 18015–18027.

- Song, C., Park, M., Lee, K., Ahn, H., Lee, Y., Kim, J., Han, K., Kim, J., Ghim, Y., & Kim, Y. (2008). An investigation into seasonal and regional aerosol characteristics in East Asia using model-predicted and remotely-sensed aerosol properties. *Atmospheric Chemistry and Physics*, 8(22), 6627–6654.
- Song, Z., Wang, J., & Wang, S. (2007). Quantitative classification of northeast Asian dust events. *Journal of Geophysical Research: Atmospheres*, 112(D4).
- Stefanski, R., & Sivakumar, M. (2009). Impacts of sand and dust storms on agriculture and potential agricultural applications of a SDSWS. 7, 012016.
- Stohlgren, T. J., Chase, T. N., Pielke, R. A., Kittel, T. G., & Baron, J. S. (1998). Evidence that local land use practices influence regional climate, vegetation, and stream flow patterns in adjacent natural areas. *Global Change Biology*, 4(5), 495–504.
- Sun, H., Pan, Z., & Liu, X. (2012). Numerical simulation of spatial-temporal distribution of dust aerosol and its direct radiative effects on East Asian climate. *Journal of Geophysical Research: Atmospheres*, 117(D13).
- Ta, W., Xiao, H., Qu, J., Xiao, Z., Yang, G., Wang, T., & Zhang, X. (2004). Measurements of dust deposition in Gansu Province, China, 1986–2000. *Geomorphology*, 57(1–2), 41–51.
- Taghavi, F., Owlad, E., & Ackerman, S. (2017). Enhancement and identification of dust events in the south-west region of Iran using satellite observations. *Journal of Earth System Science*, 126(2), 28.
- Taghavia, F., & Mohammadi, H. (2008). The survey of linkage between climate changes and desertification using extreme climate index software. *Desert*, 13(1), 9–17.
- Tao, W., Chen, J., Li, Z., Wang, C., & Zhang, C. (2012). Impact of aerosols on convective clouds and precipitation. *Reviews of Geophysics*, 50(2).
- Tegen, I., Werner, M., Harrison, S., & Kohfeld, K. (2004). Relative importance of climate and land use in determining present and future global soil dust emission. *Geophysical Research Letters*, 31(5).
- Tegen, Ina, Hollrig, P., Chin, M., Fung, I., Jacob, D., & Penner, J. (1997). Contribution of different aerosol species to the global aerosol extinction optical thickness: Estimates from model results. *Journal of Geophysical Research: Atmospheres*, 102(D20), 23895–23915. <https://doi.org/10.1029/97JD01864>
- Teixeira, J., Carvalho, A., Tuccella, P., Curci, G., & Rocha, A. (2016). WRF-chem sensitivity to vertical resolution during a saharan dust event. *Physics and Chemistry of the Earth, Parts A/B/C*, 94, 188–195.
- Thanh, N. T. (2019). Evaluation of Multi-Precipitation Products for Multi-Time Scales and Spatial Distribution During 2007-2015. *Civil Engineering Journal*, 5(1), 255–267.
- Thomas, D. S., Stokes, S., & Shaw, P. A. (1997). Holocene aeolian activity in the southwestern Kalahari Desert, southern Africa: Significance and relationships to late-Pleistocene dune-building events. *The Holocene*, 7(3), 273–281.
- Thomson, M. C., Molesworth, A. M., Djingarey, M. H., Yameogo, K., Belanger, F., & Cuevas, L. E. (2006). Potential of environmental models to predict meningitis epidemics in Africa. *Tropical Medicine & International Health*, 11(6), 781–788.
- Todd, M. C., Bou Karam, D., Cavazos, C., Bouet, C., Heinold, B., Baldasano, J., Cautenet, G., Koren, I., Perez, C., & Solmon, F. (2008). Quantifying uncertainty in estimates of mineral dust flux: An

- intercomparison of model performance over the Bodélé Depression, northern Chad. *Journal of Geophysical Research: Atmospheres*, 113(D24).
- Tokaloğlu, Ş., & Kartal, Ş. (2006). Multivariate analysis of the data and speciation of heavy metals in street dust samples from the Organized Industrial District in Kayseri (Turkey). *Atmospheric Environment*, 40(16), 2797–2805.
- Trenberth, K. E. (2011). Changes in precipitation with climate change. *Climate Research*, 47(1–2), 123–138.
- Trusilova, K., Jung, M., Churkina, G., Karstens, U., Heimann, M., & Claussen, M. (2008). Urbanization impacts on the climate in Europe: Numerical experiments by the PSU–NCAR Mesoscale Model (MM5). *Journal of Applied Meteorology and Climatology*, 47(5), 1442–1455.
- Verburg, P. H., Schot, P. P., Dijst, M. J., & Veldkamp, A. (2004). Land use change modelling: Current practice and research priorities. *GeoJournal*, 61(4), 309–324.
- Wang, K., Zhang, Y., Nenes, A., & Fountoukis, C. (2012). Implementation of dust emission and chemistry into the Community Multiscale Air Quality modeling system and initial application to an Asian dust storm episode. *Atmospheric Chemistry & Physics*, 12(21).
- Wang, Kai, Zhang, Y., Yahya, K., Wu, S.-Y., & Grell, G. (2015). Implementation and initial application of new chemistry-aerosol options in WRF/Chem for simulating secondary organic aerosols and aerosol indirect effects for regional air quality. *Atmospheric Environment*, 115, 716–732.
- Weng, Q., Lu, D., & Schubring, J. (2004). Estimation of land surface temperature–vegetation abundance relationship for urban heat island studies. *Remote Sensing of Environment*, 89(4), 467–483.
- Wilkinson, M. J. (2014). The Persian Gulf, Clear and Clouded (The photos are provided by the ISS Crew Earth Observations Facility and the Earth Science and Remote Sensing Unit.). Johnson Space Center. <https://earthobservatory.nasa.gov/images/84490/the-persian-gulf-clear-and-clouded>
- Yap, D., & Oke, T. R. (1974). Sensible heat fluxes over an urban area—Vancouver, BC. *Journal of Applied Meteorology*, 13(8), 880–890.
- Yongming, H., Peixuan, D., Junji, C., & Posmentier, E. S. (2006). Multivariate analysis of heavy metal contamination in urban dusts of Xi'an, Central China. *Science of the Total Environment*, 355(1–3), 176–186.
- Zarasvandi, A., Carranza, E. J. M., Moore, F., & Rastmanesh, F. (2011a). Spatio-temporal occurrences and mineralogical–geochemical characteristics of airborne dusts in Khuzestan Province (southwestern Iran). *Geochemistry for Geological-Environmental Studies*, 111(3), 138–151. <https://doi.org/10.1016/j.gexplo.2011.04.004>
- Zhang, Dalin, & Anthes, R. A. (1982). A high-resolution model of the planetary boundary layer—Sensitivity tests and comparisons with SESAME-79 data. *Journal of Applied Meteorology*, 21(11), 1594–1609.
- Zhang, DF, Zakey, A., Gao, X., & Giorgi, F. (2008). Simulation of dust aerosol and its regional feedbacks over East Asia using a regional climate model.
- Zhang, Y., Chen, Y., Sarwar, G., & Schere, K. (2012). Impact of gas-phase mechanisms on Weather Research Forecasting Model with Chemistry (WRF/Chem) predictions: Mechanism

implementation and comparative evaluation. *Journal of Geophysical Research: Atmospheres*, 117(D1).

7. Investigation of Aeolian Dust Deposition Rates in different Climate Zones

Abstract

Monitoring aeolian dust and improving our understanding of the factors influencing dust deposition is a key scientific challenge, as the changing climate might result in the formation of new/additional dust source regions. Therefore, the connections between climate zones in southwestern Iran and dust deposition rates have been investigated between 2014 and 2017 using the second modern-era retrospective analysis for research and applications (MERRA-II) reanalysis tool in combination with aeolian ground deposition rates (GDR) in southwestern Iran. In addition, the surface meteorological records for the same period, including the wind patterns favoring the occurrence of dust events, were examined. Arid desert hot [BWh], arid steppe hot [BSh], and temperate hot and dry summer [Csa] climates are the three dominant climate regions with the highest average dust deposition rates in the research area. The regions of [BSh] and [Csa] were associated with the seasonal cycle of dust events in the months of March, April, and May during the study period, as the dominant meteorological conditions in the study area are responsible for the dust deposition rates. Simultaneously, the peak of the seasonal deposition rates ($\text{mg}/\text{cm}^2/\text{month}$) occurred in the [BWh, 0.84], [BSh, 0.66], and [Csa, 0.35] climate regions, which correspond to the gauge-sites [G10, G09, G08], [G01, G02, G07], and [G03, G04, G05, G06] respectively. The highest deposition rates of dust were detected throughout the year in the southern parts of the research area, with annual mean deposition rates ($\text{t}/\text{km}^2/\text{year}$) of 100.8 for [BWh], 79.27 for [BSh], and 39.6 for [Csa]. The knowledge gained on the dust deposition processes, together with feedback from the climate pattern, will provide insights into the records of data for developing new sources, deposition rates and their climate offsets. Since aeolian deposited rate are sensitive over climate zones, even suggesting that additional observation data from GDR on climate regimes might be performed to obtain precise information on dust plumes.

Keywords: GDR, Climate forcing, Dust deposition, Iran

7.1 Introduction

Dislocating aeolian dust material over hundreds of years creates conceivable positive and negative feedback between the dust loads in the atmosphere and climate (Swap et al., 1992) that can be important for terrestrial systems. While positive feedback provides essential nutrients for plant growth that are contained in the fertilized terrestrial dust, and a series of wet years can trigger rapid revegetation of desert surfaces (Falkowski et al., 1998; Jickells et al., 2005), aeolian dust might also increase soil salinity (Popov, 1998), reduce the photosynthetic efficiency (Razakov and Kosnazarov, 1996), depreciate air quality, and impair human health (Stone, 1999; O'hara et al., 2000; Wiggs et al., 2003; Groll et al., 2013; Opp et al., 2017). On a global scale the aeolian dust transport cycle and dust loads are closely connected to climate variability and changes (Duce, 1995; Jouzel et al., 1996; AO, 2001; Goudie, 2009; Huang et al., 2011) and have reciprocal effects (Ramanathan et al., 2005). On the one hand, variations in meteorological episodes have an influence on dust concentration (Dawson et al., 2014; Feng et al., 2016), and on the other hand, the amount of mineral dust suspended in the atmosphere influences the climate (Claiborn et al., 2000; Wei et al., 2004). One specific climate constellation, which favors dust emission are cold and dry conditions, like large parts of the northern hemisphere experienced during the Pleistocene (Idso et al., 1972, 1981; Penner et al., 1994; Sokolik and Toon, 1996; Muhs et al., 2014; von Holdt et al., 2019). Other studies put an emphasize on arid and semi-arid regions, where dust events originate with high frequencies throughout the year (Duce et al., 1980; Tegen and Fung, 1994; Miller and Tegen, 1998; Léon and Legrand, 2003; Griffin et al., 2007), but the time of the intra-annual peak of the dust activity differs in from region to region (Furman, 2003). Furthermore, over the past century, the correlation between historical climate changes (mainly air temperature, aridity and wind speed) have been the subject of a wide range of studies (Katz and Brown, 1992; Duce, 1995; Jouzel et al., 1996; Smalley et al., 2001; Prospero and Lamb, 2003; Trenberth et al., 2007; Goudie, 2009; Huang et al., 2011; Lucas et al., 2014). Due to changes in environmental policies, aerosol concentration changes are expected to be the dominant responses to climate variations (Westervelt et al., 2016). Recent model simulations have concluded that the global average annual dust transported to higher altitudes (Kipling et al., 2016) will determine the impacts of the overall aeolian dust transport on ecosystems (McTainsh and Strong, 2007) with the most important effects on dust concentrations and source variability (Tegen and Miller, 1998). According to (Orlovsky et al., 2005), aeolian transport is controlled by the complex interaction of several atmospheric parameters and it is characterized by strong temporal and spatial dynamics. Related to atmospheric stability, aerosols can be transported over long distances to remote continents before they are removed from the atmosphere by dry and/or wet deposition (Peng et al., 2016), thus modifying growth and the atmospheric lifetimes of the particles. Therefore, the transport variability becomes increasingly important as the distance from the dust sources increases (Tegen and Miller, 1998). Even a slightly increased particle load (Tegen et al., 1997; Haywood and Boucher, 2000; Sokolik et al., 2001; Kim et al., 2008) can influence the Earth's climate by altering the global energy budget (Lambert et al., 2013; Allen et al., 2016). In other words, Mineral dust in the atmosphere influences the radiative balance by directly scattering and absorbing incoming solar radiation (Haywood et al., 2005) or indirectly changing the optical properties of clouds (Fiedler et al., 2015). The scattering and absorption of incoming radiation impacts the lithosphere and hydrosphere in a variety of complex and interactive ways (Duce et al., 1980; Prospero, 1981; Pye, 1987;). Therefore, changing optical properties (Levin et al., 1996; Wurzler et al., 2000) may possibly push the climate system toward warmer and wetter conditions (Maley, 1982; Martin and Gordon, 1988) or may serve to amplify sudden climate fluctuations (Prospero, 1999; Goudie and Middleton, 2001; Prospero and Lamb, 2003; Shinn et al., 2003). In addition, a multi-model climate study showed that climate change is associated with a negative impact of aeolian dust, which is explained by a decrease

in the large-scale precipitation over land in a warmer climate with less wet deposition, thus increasing aerosol lifetimes (Allen et al., 2016).

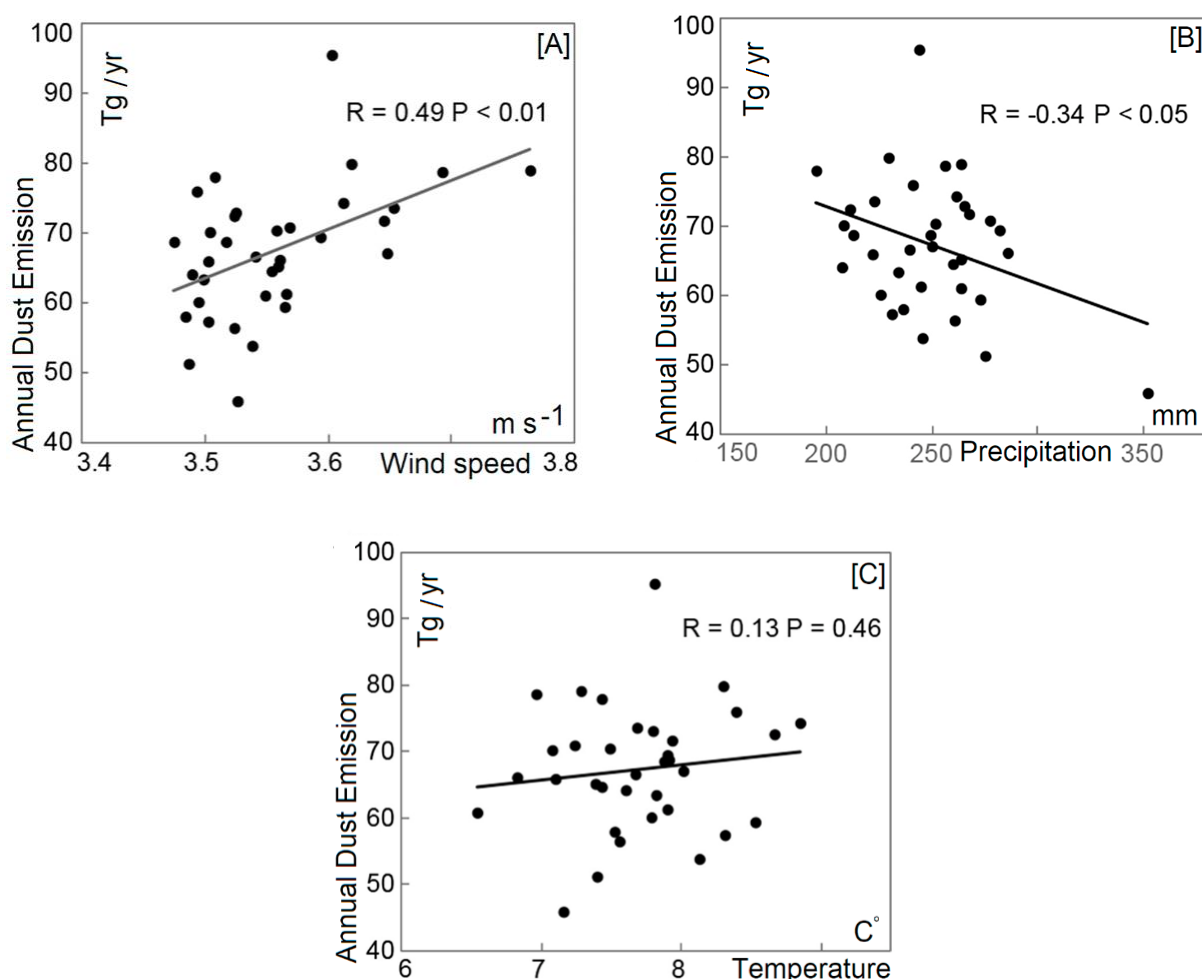


Figure 7.1 Correlation between dust particle and climate factors

As shown in Fig. 7.1, correlations between [A] annual dust emissions and wind speed, [B] annual dust emissions and precipitation, and [C] annual dust emissions and temperature over dust source regions in China and Mongolia from 1980 to 2015. Credit: Adapted from (Song et al., 2017).

*** Tg is the SI unit of mass equal to 10¹² gram

In particular, the burden of atmospheric aerosols depends on several factors, including emissions, chemistry and weather patterns (Jacob and Winner, 2009). However, for a more comprehensive discussion, global precipitation increases slightly due to enhanced evaporation from the oceans but there is considerable regional variability (Christensen et al., 2007). Precipitation increases in the northern parts of North America and Europe but decreases in the southern parts, it increases in northern Asia but decreases in the Middle East. Models agree in general that high latitudes will become wetter and subtropical latitudes drier (Christensen et al., 2007).

Changing radiative balance can in turn alter regional winds and precipitation (Evan et al., 2016), accordingly dust emissions, transport, and deposition processes (Zender and Kwon, 2005; Evan et al., 2016). For one thing, alter regional winds given the exposure of saline deposits combined with the hot and arid climate causes severe ecological problems from salt dust plumes (Prospero et al., 2002). In either case, most studies to date have focused on the mechanisms of dust production, the dust load source regions, and the process of transportation (Prospero, 1981; Péwé and American Association for the Advancement of Science, 1981; Pye, 1987; Duce, 1995). According to Tegen and Fung (1994), the annual atmospheric dust load originating in Sahara Desert, the Arabian Peninsula, Central Asia,

Northern China, and Australia is estimated at more than 200 million tons. This much concentration impact the air quality (Griffin et al., 2007) and the global climate (Swap et al., 1992; Moulin et al., 1997; Prospero, 1999; Tucker and Nicholson, 1999; Goudie and Middleton, 2001; Prospero and Lamb, 2003). Within the Middle East, as one of the regions most affected by dust (Furman, 2003), the Arabian Peninsula is one of the major dust sources (Barkan et al., 2004), ranking in the global top five of the most significant dust source regions (Goudie and Middleton, 2001; Rezazadeh et al. 2013). With this in mind, few studies on aeolian dust in Iran have been conducted.

Table 7.1 A few studies on aeolian dust in Iran

Reference	Method	Period	Area
Rezazadeh et al. (2013)	Analyzing the surface meteorological records	1998 – 2003	Middle East
Bayat et al., (2013)	Data recorded by a polarized sun-photometer	Feb 2010 - Dec 2012	Zanjan 36° 70' N and 48° 51' E
Masoumi et al., (2013)	Data recorded by a polarized sun-photometer	Oct 2006 - Oct 2008 Jan 2010 - Sep 2010	Zanjan 36° 70' N and 48° 51' E
Khoshshima et al., (2014)	Data recorded by a polarized sun-photometer	Dec 2009 - Oct 2010	Zanjan 36° 70' N and 48° 51' E
Maleki et al., (2016)	Pm10 Pm2.5	2009 – 2014	Ahwaz 31° 32' N and 48° 68' E
Doabi et al., (2017)	Ground Deposition Rate -Surface area of 800 cm2 -Opening on top	Mar 2013 to Aug 2013	Kermanshah 33° 40' N and 45° 24' E
Rashki et al., (2017)	IRIMO Dataset	1990–2013	Kerman, Sistan Baluchistan
Norouzi et al., (2017)	Ground Deposition Rate -Surface area of 1 m2 -Opening on top	Jun 2012 - May 2013	Esfahan: 4,500 km2 Central Plateau 32° 26 N and 51° 30E

As illustrated in Table 7.1, the first contribution attempted to determine the climatology of dust events in four sub-regions of the Middle East based on the maximum mean dust concentration and the seasonality of dust events. Rezazadeh et al. (2013) suggested that major sources of dust in the Middle East can be identified by analyzing the surface meteorological records at each station which is retrieved as: $DE = DIS + BD + DS + SDS$

They used synoptic records of land surface observations from 1998 to 2003. Thus, the study area has been classified into four regions (Shao and Dong, 2006), based on the maximum number of dust events (DE) under conditions of :

- DIS: widespread dust in suspension, not raised at or near the station at the time of observation; visibility is usually not greater than 10 km
- BD: raised dust or sand at the time of observation, reducing visibility to 1 to 10 km
- DS: winds lift large quantities of dust particles, reducing visibility to between 200 and 1000m
- SDS: Severe Dust Storm: very strong winds lift large quantities of dust particles, reducing visibility to less than 200 m

In addition to draw dust concentration in the atmosphere, deposition rate is also comparatively essential point to identify aeolian activity and environmental quality (Simonson, 1995; Lin and Feng, 2015; Varga et al., 2016). Besides, deposition has been measured directly at only a few sites (Tab 7.2); therefore, reliable dust deposition data are lacking around the world (Pye, 1987b; Prospero, 1999; Mahowald et al., 2008; Zhang et al., 2010; Huneus et al., 2010; Shao et al., 2011).

Despite the existence of many studies about examining dust concentrations (Maleki et al., 2016; Rashki et al., 2017), mineralogy and chemical composition of dust (Doabi et al. 2017; Norouzi et al. 2017) via different techniques in western and southwestern Iran, the connection between ground deposition rates and climate patterns have hardly been utilized as a data source in this region.

Table 7.2 Observation of dust deposition

Location	Period	Deposition rate (t/km ² /yr)	References
Israel	1968–1973	57–217	(Yaalon and Ganor, 1975)
Kuwait	1982	2600	(Khalaf and Al-Hashash, 1983)
Saudi Arabia	1991–1992	4704	(Modaihsh, 1997)
Lanzhou, China	1988–1991	108	Derbyshire et al. (1998)
Urumqi, China	1981–2004	284.5	(Zhang et al., 2010)
Iran	2008–2009	72–120	(Hojati et al., 2012)
Uzbekistan	2003–2010	8365	(Groll et al., 2013)

By doing so here, this study provides new and valuable insights into the spatial and temporal dynamics of the dust cycle in southwestern Iran. Detailed meteorological data and GDR datasets from ten stations in southwestern Iran were analyzed for the period from 2014 to 2017 in order to assess the spatial and temporal distribution and seasonality of the dust deposition rates. These ten stations represent five main climate categories based on the Köppen-Geiger classification system (Beck et al. 2018).

The main objectives of this study were: [1] to investigate the spatial and temporal variability of dust deposition rates in the study area; [2] to determine the seasonal and spatial variability of the dust deposition rate in relation to the climate zones; and [3] to identify the correlation of the most relevant climate patterns and the weather parameters for the deposition rate. Analyzing the seasonal and spatial variability of the dust activity in different climate zones is important not only for managing the impact of aeolian dust but also for developing proper LULC (land use land cover) strategies in order to mitigate the potential future dust impacts. And as climate change will also affect the spatial distribution of the climate zones, this analysis might also contribute to the estimation of future dust sources and the overall future dust activity in southwestern Iran and the Middle East, as long as the ground deposition rate remains the main factor for determining deposition trends.

7.2 Material and method

To understand the impact of the climate region on the deposition rates in southwestern Iran, dusty days are defined as days with at least one report of a dust event. In addition to this, the ground-based deposition rate was also recorded and classified in 4 climate zones present in the study area. Data used for this study includes monthly average of the ground deposition rate (GDR), the wind speed and direction (northward and eastward wind), precipitation and temperature during the measuring period from 2014 to 2017. In order to evaluate the correlation between the deposition rates and the climate zones, the results from the ten dust sampling sites were reclassified using climate gradients. The rate distinguished with seasonal variation responses to the regional climate provided using the MERRA-II model output with comparable accuracy. By applying this relationship, the high temporal (model output) and seasonal rate (from GDR), the spatio-temporal pattern of the dust deposition rate over different climate zones revealed the probable uncertainty of the deposition rate.

7.3 Results and discussion

The detailed description of dust deposition rate data and analyze their connections with weather pattern will be done in the following section.

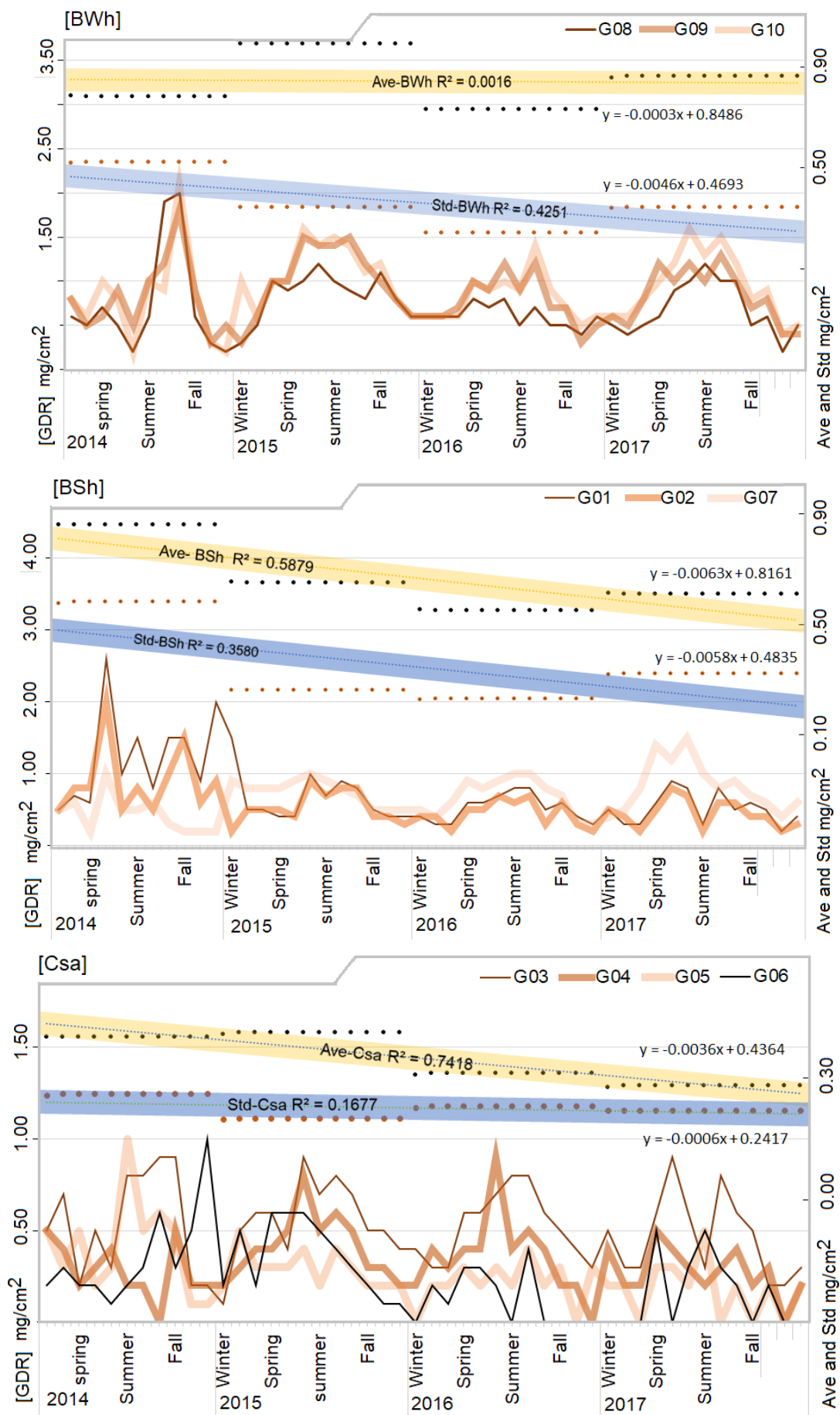


Figure 7.2 Ground deposition rates (mg/cm²) from sites G01 to G10 in three climate zones

Figure 7.2 shows the seasonal deposition rate in study region. In given time, the high deposition rate is found over [BWh], whereas the minimum rate is noted over [Csa]. So [BWh] > [BSh] > [Csa] are where the rate deposited over climate zones in descending order. In 2014 however ground deposition rate is observed over [BSh] > [BWh] > [Csa]. The spatial distribution of GDR was calculated using the seasonal average of the rate per climate zone. In the first place, summer deposition rate over [BWh] was higher in the 2014 and 2017, and stayed level with the rate of deposition in spring 2015. Compared to spring, the rate value is slightly decreased in summer of 2016.

Over [Bsh], GDR is recorded the maximum rate in summer [2015, 2016] and spring [2014, 2017], followed by winter and fall. After all, the spring deposition rate with low fluctuation is found over [Csa] in 2015, 2016 and 2017, but in summer 2014 with an exception, [Csa] is witness of high deposition rate. After all, due to specific role of the local, regional topography and meteorological pattern are mainly related to controlling the dust deposition rate, it is not surprising that the results of this contribution indicate a non-uniform seasonal deposition trend as is shown in Figure 7.2

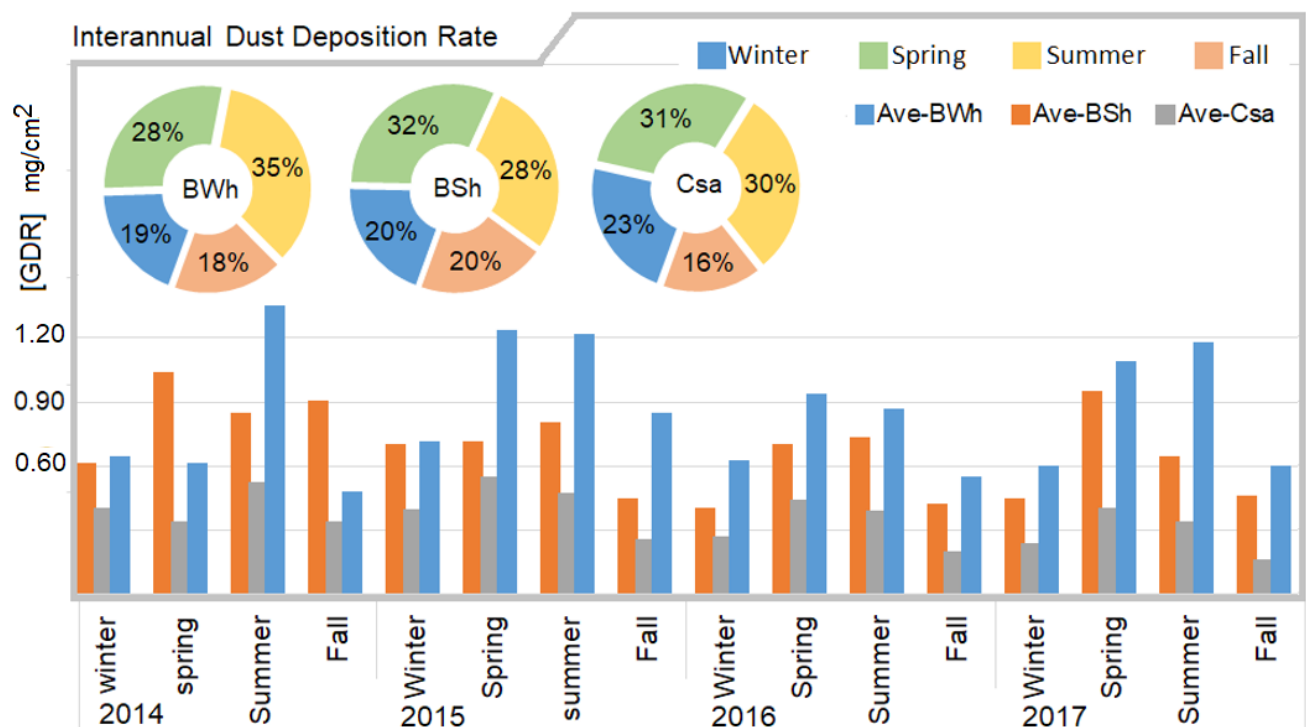


Figure 7.3 Overall seasonal deposition rate (mg/cm²) in the study area
Monthly variations and trends in averages for high values are analyzed to understand the changes in the types of deposition rates in the study area

In spring and summer, while the seasonal maximum deposition rate compare favorably to observed value over different climate zones, the minimum rate over [BWh], [Bsh], and [Csa] were occurred in fall and winter. A more detail from Figure 7.3 illustrates that the dust deposition reached its maximum value in spring and summer over the [BWh], [Bsh], and [Csa]. The peaked percentage of deposition rate, with 35%, 28%, and 30% of the annual deposition are accumulated during spring. In summer further, the peak monthly dust deposition rate with 28%, 32%, and 31% are observed in [BWh], [Bsh], and [Csa] respectively.

This seasonal contribution rate is in-line with findings from studies in eastern Iran and western Afghanistan (Rashki et al., 2017; Abbasi et al., 2018), as well as with previous studies in Khuzestan (Alizadeh Choobari et al., 2013; Rashki et al., 2013). Ta et al. (2004) also presented similar results for the Gansu Province and the Gobi Desert (China), where the highest deposition rates were registered during spring (32.51%), and the lowest values in the fall. A study in Shuwaikh city (Al-Harbi, 2015) further showed a similar pattern of monthly deposition rates in summer (July and August, 2009). Conversely, western Taiwan (Lin et al., 2018) and, Northwest Spain (Oduber et al., 2019), observed evidence of unusual winter dust. Although during fall and winter, the rate of maximum deposition is not very frequent and doesn't reach in northern Kuwait, the investigated seasonal deposition rate (Al-Dousari and Al-Awadhi, 2012) revealed a maximum quantity in late winter (January), and fall (November). During the sampling period, the correlation coefficients obtained between the meteorological parameters (such as the wind direction, precipitation and relative temperature) and the GDR values are demonstrated in Figures 7.4 to 7.7, and are identified as the major factors affecting GDR in different seasons. Ultimately, correlation values of 62%, -28%, and 36% were indicated with statistical significance ($p < 0.05$) for the connections between the deposition rate and the temperature, wind, and precipitation, respectively. Given these results, a high GDR was observed in areas with high temperature, low precipitation and an around zero vertical pressure velocity (VPV). This result is supported by findings from Reheis and Kihl (1995), who showed the major effects of decreasing rainfall on the dust deposition rates.

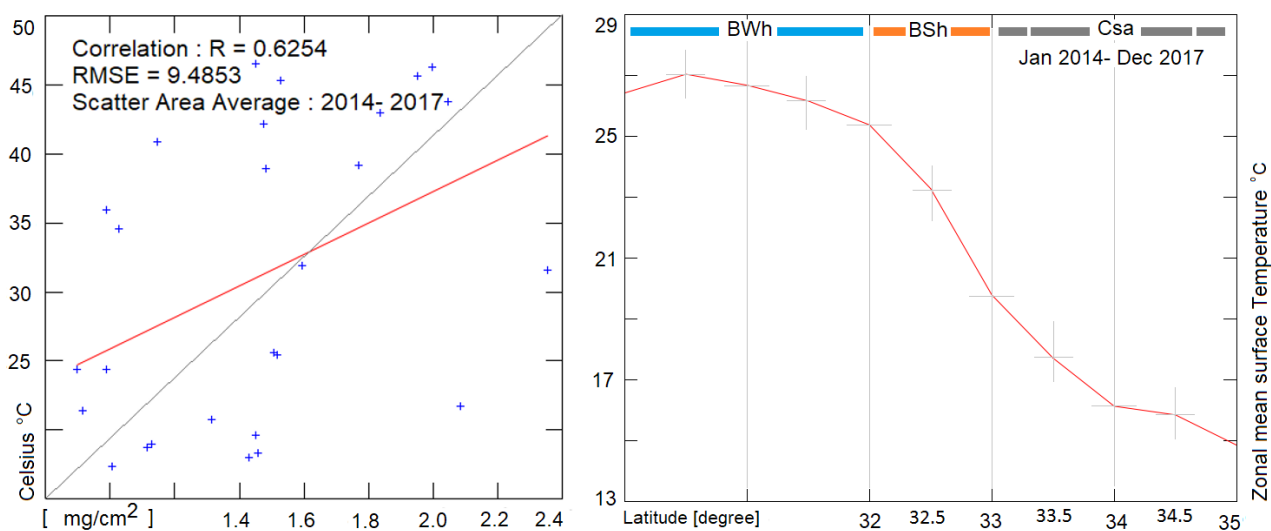


Figure 7.4 Correlation of surface temperature against the aeolian deposition rate

In the given plot of correlation (Fig. 7.4), the positive and statistically significant correlations were detected from the deposition rate to temperature ($R=62\%$, $p<0.01$). Discrimination of the relative variation in GDR of the aeolian dust is also evident in the observed trends of minimum and maximum temperatures and precipitation over the zonal surface. The correlation coefficient and relative RMSE between the dust deposition and maximum temperatures are 62% and 9.48, respectively. In spite of the variation of temperature caused by climate variability, statistically significant positive trends are identified, which may be consistent with results of Groll et al., (2013) who found that increase the dust deposition fluxes considerably for the correlation ($R=53\%$) between the average monthly air temperature and the monthly dust deposition. Additionally this study is, thus, in accordance with the results of Alizadeh-Choobari and Najafi, (2018) who found that a rise in temperature is associated with a decrease in total annual precipitation. Higher temperatures are generally associated with lower precipitation amounts and vice versa. This observation is expected because the [BWh] and [Csa] regions are associated with more sunshine and less evaporative cooling.

As Fig. 7.5 illustrates, a statistically significant negative correlation exists between the monthly deposition rate and monthly precipitation ($R=-0.48\%$, $p<0.01$) due to the dry deposition rate being minimized in the same period with precipitation (Shao and Lu, 2000). This phenomenon may respond to the dry and wet deposition rate when delivered back to the surface through rain or by gravity.

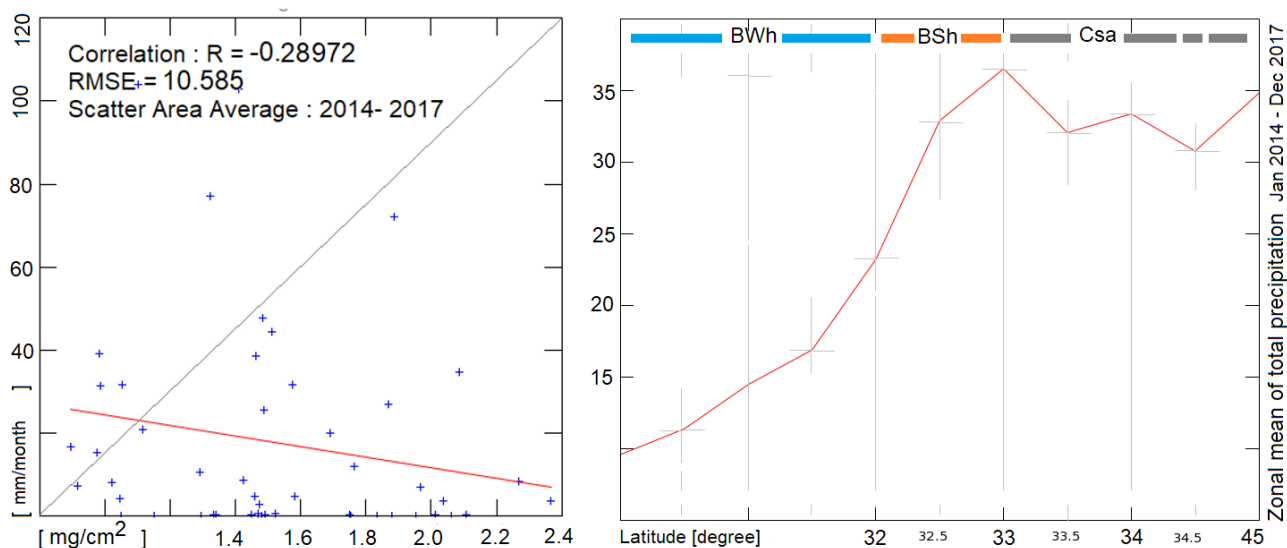


Figure 7.5 Correlation of precipitation against the aeolian deposition rate

The correlation analysis suggests that a strong negative correlation exists between the deposition rate and precipitation over the climate zone, with a correlation coefficient of -0.28 (statistically significant at the 0.01 level) and an RMS of 10.58. In other words, higher precipitation is generally associated with lower deposition amounts and vice versa. This relationship is expected because the [BWh] regions are associated with less precipitation in comparison with [Csa] and [Bsh]. The average annual precipitation varies from more than 35 mm per month at high-altitude (45.90E 33.00N) to less than 10 mm in the arid zone (47.60E 29.97N). This study justified the lowest dust rate collection amounts for the fall and winter seasons and the highest being recorded in the spring and summer. This finding is consistent with the finding of a previous contribution in that dry deposition does not occur simultaneously with rainfall (Shao and Lu, 2000; Shao and Wang, 2003).

Table 7.3 illustrates the average seasonal deposition rate out into three climate regions related to the wind velocity which can be interpreted as follow: 1. [BWh] correspond to the case with eastward wind speed ($v \leq 3.0$ m/s), witnessed the maximum rates of deposition revealed by GDR (34.5 t/km²) and model-output (6.2 t/km²). 2. [BSh] related to the westward wind speed ($v \leq 2.5$ m/s) with the average deposition rate observed from GDR (24.9 t/km²) and model-output (3.3 t/km²). 3. [Csa] correspond to the case with eastward and westward wind speed ($v \leq 3.4$ m/s) that is characterized by the lower dust portion when compared to [BWh] and [BSh]. As can be seen wind velocity correlated well with the seasonal observed deposition rates.

The considerable contributions are determined the entrainment threshold for different soil texture classification (Gillette et al., 1980; Helgren and Prospero, 1987; Belnap et al., 2007), as reviewed by Webb et al., (2016). However, Gillette, (1988) classified wind velocity to find out in which term particles will be set in motion. Threshold velocities for agricultural soils also were measured for a wide variety of conditions in order to quantify a model of dust emissions for the United States (Gillette, 1988). Moreover, Webb et al., (2016) evaluates threshold wind velocity dynamics to figure out the characteristics of threshold dynamics relative to sediment transportation.

Table 7.3 Classified the average seasonal deposition rate on the basis of wind pattern

Criteria		Seasonal Deposition Rates		Wind velocity		
Climate	Seasons	GDR t/ km ²	Model output t/ km ²	Wind less than 2 m/ s	Wind Speed m/ s	Wind Direction
BWh	Winter	18.9	4.8	25.8%	2.3	WNW
	Spring	28.5	6.2	15.5%	2.9	WNW
	Summer	34.5	6.1	10.7%	3.0	WNW
	Fall	18	4	25.4%	2.0	SE-NW
Bsh	Winter	15.6	2.4	18.5%	2.3	SE
	Spring	24.9	4.7	16.0%	2.5	ESE
	Summer	22.2	3.3	9.7%	2.5	ESE
	Fall	16.2	3.3	31.8%	1.8	SE
Csa	Winter	9.3	1.2	27.2%	2.0	SE-E
	Spring	12.3	3.2	26.4%	2.3	W-E
	Summer	12.3	3.6	10.0%	3.4	WNW
	Fall	6.6	2.4	28.9%	1.9	SE

The comparison between the model-output and GDR were carried out for the given time and the corresponding wind velocity near the surface. These data indicates that the agreement between model output and GDR ranges. A consistency index of wind speed ($2.0 < v < 3.5$ m/s), westward wind direction, and minimum peak percentage of calm event are found for three climate zones.

The threshold velocity however, could vary widely from place to place and time to time (Helgren and Prospero, 1987) due to soil properties and aerodynamic of surface can be quite variable (Gillette et al., 1980). On the on hand, the intensity of dust was calculated using combination of visibility and wind speed (Hoffmann et al., 2008). Ta et al., (2004) suggested that the total suspended particles (TSP) concentration increased with increasing wind speed. Meanwhile, contribution over Northeast Asian Dust (Song et al., 2007) identified wind velocity of 5 to 10 m/s on TSP ($< 500 \mu\text{g}/\text{m}^3$) and decreased visibility (2000 meters). On the other hand, an attempt was made to find the threshold friction velocity using temporal variability of particle size distribution and wind speed. Threshold friction velocity for local dust emission was identified between 0.6 m/s and 0.65 m/s Fine dust particles smaller than $10 \mu\text{m}$ however, were only deposited by gravitation when the horizontal wind speed was lower than 0.15 m/s (Hoffmann et al., 2008). Our results are also in agreement with a finding from Hoffmann et al., (2008) where, significant deposition is occurred through gravitation when the wind speed is usually weak (Fig. 7.6).

Finally, wind threshold is also comparatively essential point to identify aeolian activity and environmental quality. The previous result from study over Asian dust storm realized dust event on the basis of Total Suspended dust Particulate matters (TSP) in combination with the visibility and wind speed (Hoffmann et al., 2008). He suggested wind threshold of 17 m/s which can be decreased visibility to 1000 meters on the basis of TSP less than $2000 \mu\text{g}/\text{m}^3$. Meanwhile, (Song et al., 2007) identified wind threshold of 5 to 10 m/s on TSP ($< 500 \mu\text{g}/\text{m}^3$) and visibility (2000 meters) from study over Northeast Asian Dust. In addition to wind thresholds arguments, our results are also in agreement with a finding from (Ta et al., 2004), where the reported eastward and southward wind speeds varied from 1 to 6 m/s during dust events.

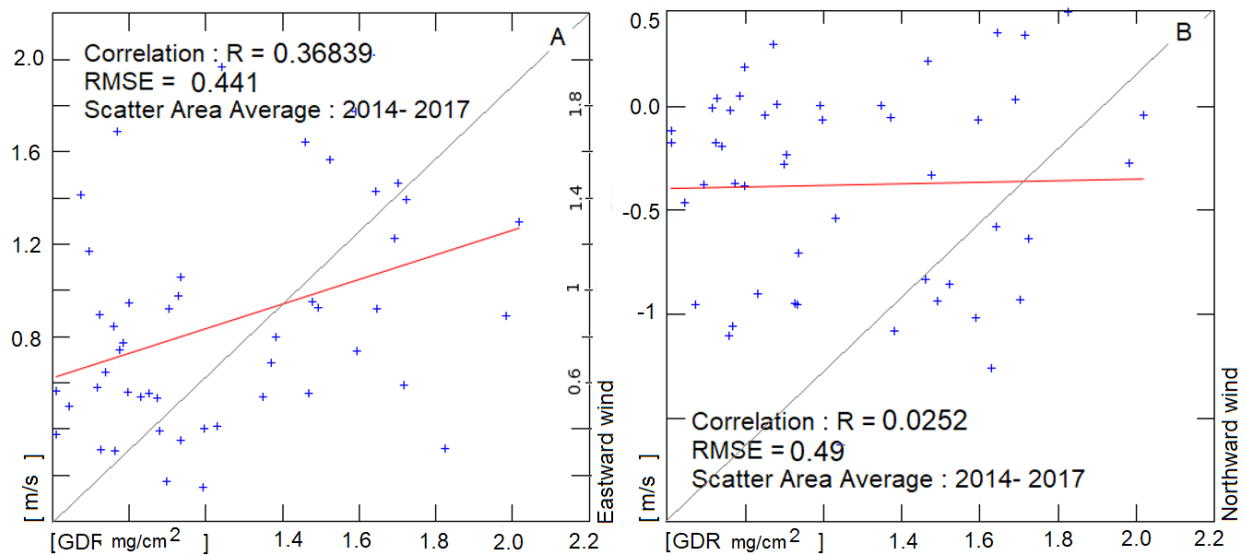


Figure 7.6 Correlation of wind velocity against the aeolian deposition rate; A. Eastward; B. Northward

According to the correlation plot in Figure 7.6, the wind speed is usually weak, so during the 90% dust deposition rate, the wind speed is less than 1.4 m/s. Traveling away from the surface produces a vertical velocity with units of length per second that are almost positive.

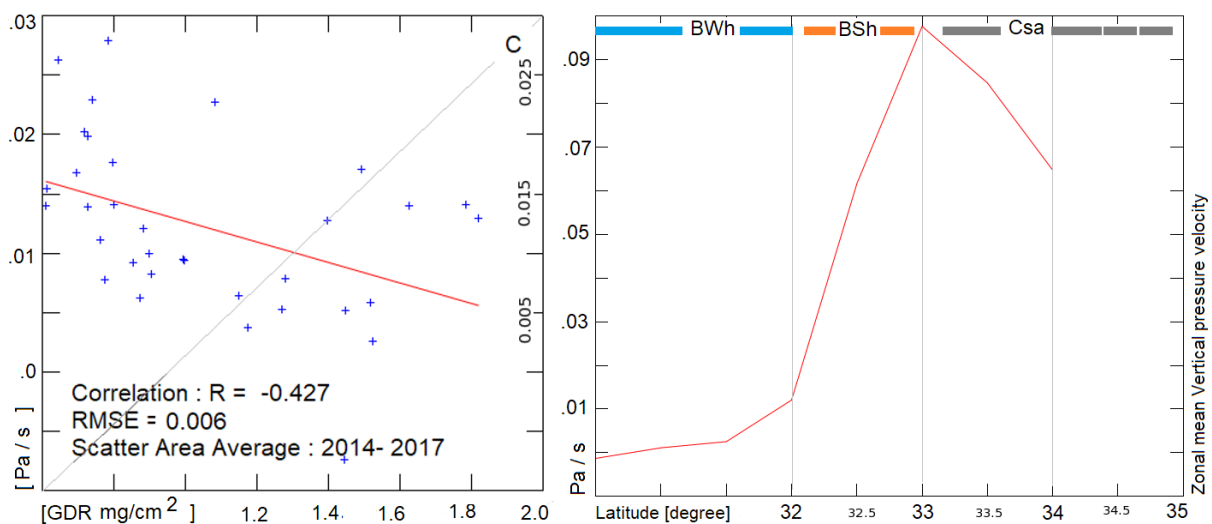


Figure 7.7 Correlation of Vertical pressure velocity against the aeolian deposition rate

Thus, negative and statistically significant correlations were expected from the deposition rate to wind vertical pressure velocity (-42%, $p < 0.01$). Lower values in the pressure's vertical velocity led more particles to deposition (Fig. 7.7). In accordance with the correlation plot from this contribution, the dust-in-suspension and deposition rate events do not require wind speeds. The vertical profiles of the monsoon, Shamal and Levant winds are especially important for the dust accumulation (Rashki et al., 2019). In the following, we examine the typical weather pattern for the study area relative to deposition rate as seen in Table 7.3. The table shows the minimum, maximum, average and standard value of temperature, precipitation and GDR in the regions [BWh], [BSh], and [Csa] from 2014 to 2017. Specifically, the correlation between the weather pattern and the main parameter of the climate zone (Geiger and Cooper, 2010) indicate that high temperatures, precipitation, and the direction of the wind are the strongest factors underlying the classification zone. With this assumption in mind, the high dust deposition rate in the spring (mg/cm²) ranges from 1.6 to 2.1 with a mean value of 1.8 per month in the [BWh] zone. The mean deposition rate value of 1.0 mg/cm², recorded for the [BSh] zone, is also considerably high. The lowest amounts of dust deposition with an almost zero value are recorded for

the [Csa] region. Again, the seasonal variations in dust deposition rates and their different climate zone responses to wind and precipitation are, in some cases, relatively weak, and the wind speed can reach 10 m/s. At such wind speeds, dust-in-suspension predominantly occurs (Song et al., 2007; Hoffmann et al., 2008). In region [BWh], the vertical pressure velocity is relatively weak and can reach less than 0.01 Pa/s. Under such wind pressure (minimum vertical speed) values, dust-in-suspension occurs and is in accordance with a previous review's (Trenberth et al., 2007; Zhang et al., 2014; Shao, 2008) deposition that reached maximum rate. Higher temperatures have also led to droughts in the subtropical dry zones of warmer climates (Previdi and Liepert, 2007; Lucas et al., 2014; Alizadeh-Choobari and Najafi, 2018).

Table 7.4 Typical climate patterns relative to the deposition rate

Classification	BWh (G10, G09, G08)			Bsh (G07, G01, G02)			Csa (G06, G05, G04, G03)		
Lat & Long	47.60E 29.97N			46.97E 31.99N			45.90E 33.00N		
Climate pattern	Temp °C	Pre mm/m	GDR mg/cm ²	Temp °C	Pre mm/m	GDR mg/cm ²	Temp °C	Pre mm/m	GDR mg/cm ²
Means	29.6	14,1	8.4	24.5	40,20	6.6	18.6	42.00	3.5
Std	11.60	13,0	3.6	12.20	33,30	3.4	13.80	34,00	2.3
Max	55	43	21	55	116	26	52	107	10
Min	5	null	-	3	null	-	-6	null	-

In summary, the contributions from the climate pattern, and the classification of the three zones for temperature and precipitation, have been articulated. On average, the annual minimum precipitation (13.75 mm) and temperature (37.30 °C) occurred for BWh at latitudes between 30N and 32N. Meanwhile, the minimum average temperature magnitude belonged to BSh, with the 32N to 33N monthly precipitation value (21.58 mm) increasing above 70%. Additionally, the third climate boundary from 33N-34.5N implied the maximum monthly precipitation (33.52 mm) on average but a high temperature. These results might arguably be considered as some of the positive consequences of the high deposition rate due to its higher quantities in the arid and desert zones (Al-Dousari and Al-Awadhi, 2012; Al-Harbi, 2015). In accordance with Trenberth, (2011) and Tao et al., (2012) the increasing air temperature have led to greater evaporation and drying of the surface and to decreases in precipitation. To evaluate the result from GDR, a comparison was made between MERRA-II and GDR across the research area during the period of high seasonal rate. Although those physical processes from the air to surface are complex and are dependent on the dust concentration, some results shows where the higher the dust concentration is, the higher the dust deposition will be (Slinn and Slinn, 1980; Wesely and Hicks, 2000; Petroff et al., 2008; Zhang et al., 2014). However, small changes in the statistical distributions can lead to pronounced changes in the incidence of extremes (Katz and Brown, 1992; Schär et al., 2004), as evidenced by the observed trends of the minimum and maximum deposition rates from ground surveying over the climate zonal surface since 2014.

With these suggestion in mind, the aeolian gradient from the MERRA II against the ground deposition rate was taken into account, and a positive and statistically significant correlation and relatively low RMSE ($r = 67\%$, $RMSE = 0.091$) were identified in 2014 between MERRA-II and GDR, which is provided at the $p < 0.01$ probability level. Equally important in 2015, there was a significant correlation, with r (65%), $RMSE = 0.01$, $p < 0.01$, for GDR and MERRA-II. Although the same significance correlation ($r = 66\%$, $RMSE = 0.102$) were obtained for 2016, positive and statistically significant correlations were detected in 2017 from MERRA-II and GDR data ($r = 74\%$, $RMSE = 0.08$) at the $p < 0.05$ probability level. A comparison of the deposition rates in the climate zones during the study period indicate that dust concentrations in the atmosphere can represent the dust deposition rate factors (Shao and Lu, 2000; Zhang et al., 2014). In accordance with Shao and Wang, (2003), the deposition rate affected by climate factors; specifically, the high aeolian deposition rate is in accordance with evidence from subtropical

dry zones (Previdi and Liepert, 2007). The results obtained from the correlation are consistent with those of (Shao and Wang, 2003; Rezazadeh et al., 2013; Opp et al., 2017), which show that region [BWh] had the highest annual deposition rate (25 g/m^2). Region [BSh] showed that the influence of the climate pattern had a lower deposition rate (16 g/m^2). Obviously, region [Csa], with a much lower deposition of 10 g/m^2 , is likely very different from other regions that are influenced by [BWh] and [BSh] (southwest and west). In addition to these findings, the highest magnitudes of the dust deposition rate in the study region are identified in the order of $\text{BWh} > \text{BSh} > \text{Csa}$ during the research period.

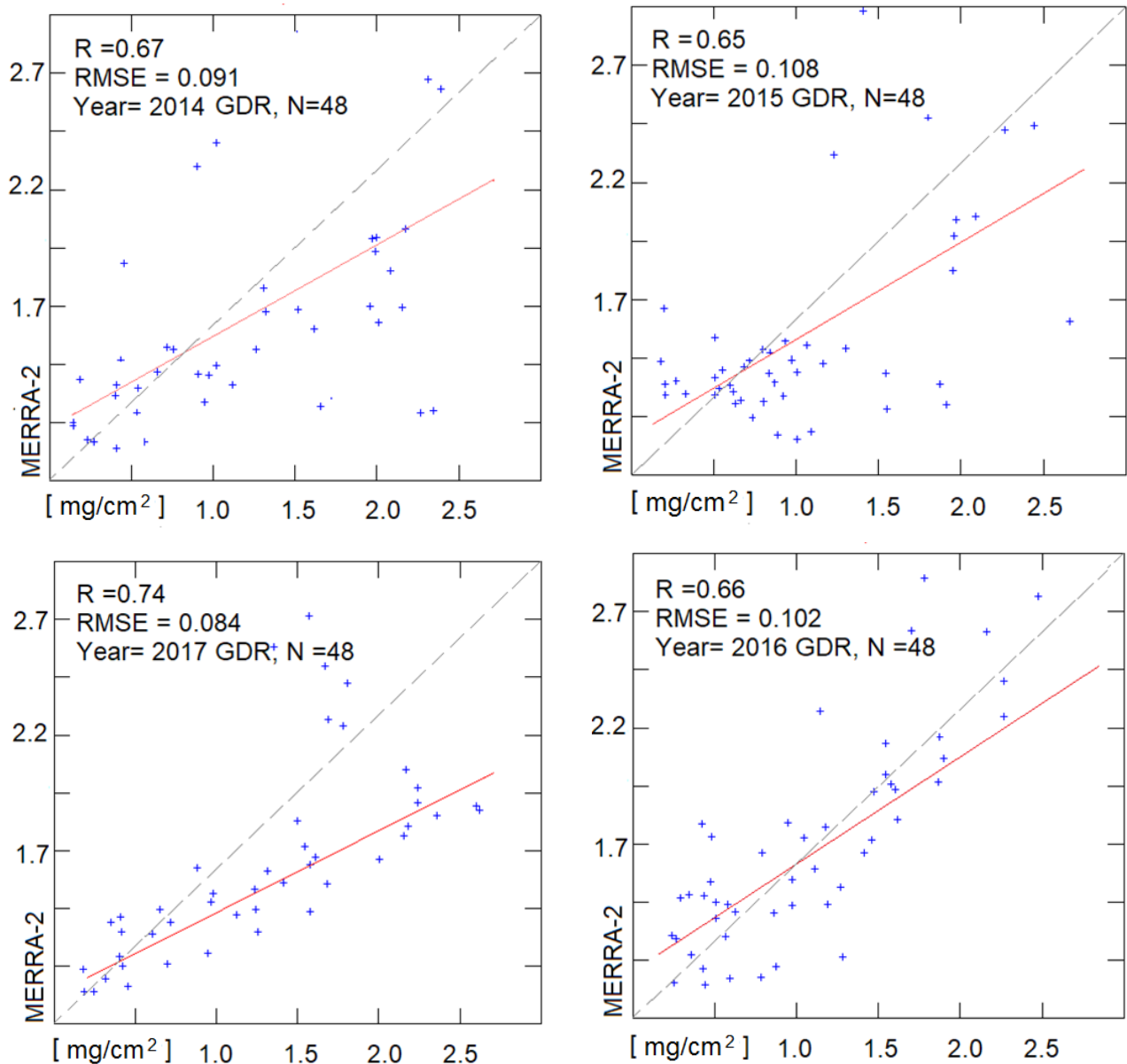


Figure 7.8 Mapping high seasonal deposition rates over climate zones

*Deposition rates from MERRA-II and GDR

7.4 Conclusions and remarks

In order to better understand the role of aeolian dust in the climate system and its impacts on air quality, significant efforts have been realized to increase both space- and ground-based observations. This study focuses on the enhancement of dust deposition rates over the southwestern part of Iran ($45^{\circ} 30' 00''$, $49^{\circ} 30' 00''$ E and $30^{\circ} 00' 00''$, $35^{\circ} 00' 00''$ N). The ground deposition rate and geophysical variation in the dust event frequency, including the mass and weight compositions, have been thoroughly

measured. Many of the links between the dust deposition and climate pattern, although perfectly reasonable from a conceptual ground survey standpoint, have been quantitatively assessed for the GDR and the MERRA-II model. The annual mean deposition rates are 100.80 t/km²/year for [BWh], 77.27 for [BSh], and 39.60 for [Csa].

The total annual dust deposition is inversely related to the total annual precipitation and was in a positive correlation with the annual temperature. Precipitation and temperature, as two of main factors in the climate zone, have a widespread, major influence on the rates of the dust deposition in the study area. However, dust-in-suspension and the deposition rate do not require wind speeds, which was reinforced by result from the correlation coefficient between the dust-in-suspension level and deposition rate.

Finally, the knowledge gained on the processes responsible for the dust deposition rate, together with feedback from the climate pattern, will provide insights into the records of data for deposition rates and their climate offsets. Future studies should be performed to obtain precise information on dust plumes by using additional observation data on climate regimes.

Acknowledge

The authors would like to gratefully acknowledge the NOAA Air Resources Laboratory team (ARL), MODIS Giovanni and NEO/NASA for their technical assistance and useful data.

** The Giovanni online data system, developed by the NASA GES DISC, has been used to obtain the surface AOT values test.

References

- Al-Dousari, A.M., Al-Awadhi, J., 2012. Dust fallout in northern Kuwait, major sources and characteristics. *Kuwait J. Sci.* 39, 171–187.
- Al-Harbi, M., 2015. Characteristics and composition of the falling dust in urban environment. *Int. J. Environ. Sci. Technol.* 12, 641–652.
- Alizadeh Choobari, O., Zawar-Reza, P., Sturman, A., 2013. Low level jet intensification by mineral dust aerosols. *Ann. Geophys.* 09927689 31.
- Alizadeh-Choobari, O., Najafi, M., 2018. Extreme weather events in Iran under a changing climate. *Clim. Dyn.* 50, 249–260.
- Allen, R.J., Landuyt, W., Rumbold, S.T., 2016. An increase in aerosol burden and radiative effects in a warmer world. *Nat. Clim. Change* 6, 269–274. <https://doi.org/10.1038/Nclimate2827>
- Barkan, J., Kutiel, H., Alpert, P., 2004. Climatology of dust sources in North Africa and the Arabian Peninsula, based on TOMS data. *Indoor Built Environ.* 13, 407–419.
- Bayat, A., Kholesifard, H., Masoumi, A., 2013. Retrieval of aerosol single-scattering albedo and polarized phase function from polarized sun-photometer measurements for Zanjan's atmosphere. *Atmospheric Meas. Tech.* 6, 2659–2669.
- Beck, H.E., Zimmermann, N.E., McVicar, T.R., Vergopolan, N., Berg, A., Wood, E.F., 2018. Present and future Köppen-Geiger climate classification maps at 1-km resolution. *Sci. Data* 5, 180214.
- Christensen, J.H., Hewitson, B., Busiuc, A., Chen, A., Gao, X., Held, R., Jones, R., Kolli, R.K., Kwon, W., Laprise, R., 2007. Regional climate projections, in: *Climate Change, 2007: The Physical Science Basis. Contribution of Working Group I to the Fourth Assessment Report of the Intergovernmental Panel on Climate Change*, University Press, Cambridge, Chapter 11. pp. 847–940.
- Claiborn, C.S., Finn, D., Larson, T.V., Koenig, J.Q., 2000. Windblown dust contributes to high PM_{2.5} concentrations. *J. Air Waste Manag. Assoc.* 50, 1440–1445.
- Dawson, J.P., Bloomer, B.J., Winner, D.A., Weaver, C.P., 2014. Understanding the meteorological drivers of US particulate matter concentrations in a changing climate. *Bull. Am. Meteorol. Soc.* 95, 521–532.
- Doabi, S.A., Afyuni, M., Karami, M., 2017. Multivariate statistical analysis of heavy metals contamination in atmospheric dust of Kermanshah province, western Iran, during the spring and summer 2013. *J. Geochem. Explor.* 180, 61–70.
- Duce, R., 1995. Sources, distributions, and fluxes of mineral aerosols and their relationship to climate. *Aerosol Forcing Clim.* 6, 43–72.
- Duce, R., Unni, C., Ray, B., Prospero, J., Merrill, J., 1980. Long-range atmospheric transport of soil dust from Asia to the tropical North Pacific: Temporal variability. *Science* 209, 1522–1524.
- Evan, A.T., Flamant, C., Gaetani, M., Guichard, F., 2016. The past, present and future of African dust. *Nature* 531, 493–5. <https://doi.org/10.1038/nature17149>
- Falkowski, P.G., Barber, R.T., Smetacek, V., 1998. Biogeochemical controls and feedbacks on ocean primary production. *Science* 281, 200–206.
- Feng, J., Liao, H., Li, J., 2016. The impact of monthly variation of the Pacific–North America (PNA) teleconnection pattern on wintertime surface-layer aerosol concentrations in the United States. *Atmospheric Chem. Phys.* 16, 4927.
- Fiedler, S., Kaplan, M., Knippertz, P., 2015. The importance of Harmattan surges for the emission of North African dust aerosol. *Geophys. Res. Lett.* 42, 9495–9504.
- Furman, H.K.H., 2003. Dust storms in the Middle East: sources of origin and their temporal characteristics. *Indoor Built Environ.* 12, 419–426.
- Geiger, A., Cooper, J., 2010. Overview of Airborne Metals Regulations, Exposure Limits, Health Effects, and Contemporary Research. US Environ. Prot. Agency Accessed August 25, 2015.
- Goudie, A., Middleton, N., 2001. Saharan dust storms: nature and consequences. *Earth-Sci. Rev.* 56, 179–204.
- Griffin, D.W., Kubilay, N., Koçak, M., Gray, M.A., Borden, T.C., Shinn, E.A., 2007. Airborne desert dust and aeromicrobiology over the Turkish Mediterranean coastline. *Atmos. Environ.* 41, 4050–4062.

- Groll, M., Opp, C., Aslanov, I., 2013. Spatial and temporal distribution of the dust deposition in Central Asia—results from a long term monitoring program. *Aeolian Res.* 9, 49–62.
- Haywood, J., Boucher, O., 2000. Estimates of the direct and indirect radiative forcing due to tropospheric aerosols: A review. *Rev. Geophys.* 38, 513–543.
- Haywood, J.M., Allan, R.P., Culverwell, I., Slingo, T., Milton, S., Edwards, J., Clerbaux, N., 2005. Can desert dust explain the outgoing longwave radiation anomaly over the Sahara during July 2003? *J. Geophys. Res. Atmospheres* 110. <https://doi.org/10.1029/2004JD005232>
- Hoffmann, C., Funk, R., Sommer, M., Li, Y., 2008. Temporal variations in PM10 and particle size distribution during Asian dust storms in Inner Mongolia. *Atmos. Environ.* 42, 8422–8431.
- Hojati, S., Khademi, H., Cano, A.F., Landi, A., 2012. Characteristics of dust deposited along a transect between central Iran and the Zagros Mountains. *Catena* 88, 27–36.
- Huneus, N., Schulz, M., Balkanski, Y., Griesfeller, J., Kinne, S., Prospero, J., Bauer, S., Boucher, O., Chin, M., Dentener, F., 2010. Global dust model intercomparison in AeroCom phase I. *Atmospheric Chem. Phys. Discuss.* 10.
- Jacob, D.J., Winner, D.A., 2009. Effect of climate change on air quality. *Atmos. Environ.* 43, 51–63.
- Jickells, T., An, Z., Andersen, K.K., Baker, A., Bergametti, G., Brooks, N., Cao, J., Boyd, P., Duce, R., Hunter, K., 2005. Global iron connections between desert dust, ocean biogeochemistry, and climate. *science* 308, 67–71.
- Jouzel, J., Waelbroeck, C., Malaize, B., Bender, M., Petit, J., Stievenard, M., Barkov, N., Barnola, J., King, T., Kotlyakov, V., 1996. Climatic interpretation of the recently extended Vostok ice records. *Clim. Dyn.* 12, 513–521.
- Katz, R.W., Brown, B.G., 1992. Extreme events in a changing climate: variability is more important than averages. *Clim. Change* 21, 289–302.
- Khalaf, F., Al-Hashash, M., 1983. Aeolian sedimentation in the north-western part of the Arabian Gulf. *J. Arid Environ.* 6, 319–332.
- Khoshsima, M., Bidokhti, A., Ahmadi-Givi, F., 2014. Variations of aerosol optical depth and Angstrom parameters at a suburban location in Iran during 2009–2010. *J. Earth Syst. Sci.* 123, 187–199.
- Kim, S.-W., Yoon, S.-C., Kim, J., 2008. Columnar Asian dust particle properties observed by sun/sky radiometers from 2000 to 2006 in Korea. *Atmos. Environ.* 42, 492–504.
- Kipling, Z., Stier, P., Johnson, C.E., Mann, G.W., Bellouin, N., Bauer, S.E., Bergman, T., Chin, M., Diehl, T., Ghan, S.J., 2016. What controls the vertical distribution of aerosol? Relationships between process sensitivity in HadGEM3–UKCA and inter-model variation from AeroCom Phase II. *Atmospheric Chem. Phys.* 16, 2221–2241.
- Lambert, F., Kug, J.S., Park, R.J., Mahowald, N., Winckler, G., Abe-Ouchi, A., O'ishi, R., Takemura, T., Lee, J.H., 2013. The role of mineral-dust aerosols in polar temperature amplification. *Nat. Clim. Change* 3, 487–491. <https://doi.org/10.1038/Nclimate1785>
- Léon, J., Legrand, M., 2003. Mineral dust sources in the surroundings of the north Indian Ocean. *Geophys. Res. Lett.* 30.
- Levin, Z., Ganor, E., Gladstein, V., 1996. The effects of desert particles coated with sulfate on rain formation in the eastern Mediterranean. *J. Appl. Meteorol.* 35, 1511–1523.
- Lin, C.-Y., Lee, Y.-H., Kuo, C.-Y., Chen, W.-C., Sheng, Y.-F., Su, C.-J., 2018. Impact of river-dust events on air quality of western Taiwan during winter monsoon: Observed evidence and model simulation. *Atmos. Environ.* 192, 160–172. <https://doi.org/10.1016/j.atmosenv.2018.08.048>
- Lin, Y.-C., Feng, J.-L., 2015. Aeolian dust contribution to the formation of alpine soils at Amdo (Northern Tibetan Plateau). *Geoderma* 259, 104–115.
- Lucas, C., Timbal, B., Nguyen, H., 2014. The expanding tropics: a critical assessment of the observational and modeling studies. *Wiley Interdiscip. Rev. Clim. Change* 5, 89–112.
- Mahowald, N.M., Engelstaedter, S., Luo, C., Sealy, A., Artaxo, P., Benitez-Nelson, C., Bonnet, S., Chen, Y., Chuang, P.Y., Cohen, D.D., 2008. Atmospheric iron deposition: global distribution, variability, and human perturbations.

- Maleki, H., Sorooshian, A., Goudarzi, G., Nikfal, A., Baneshi, M.M., 2016. Temporal profile of PM₁₀ and associated health effects in one of the most polluted cities of the world (Ahvaz, Iran) between 2009 and 2014. *Aeolian Res.* 22, 135–140.
- Maley, J., 1982. Dust, clouds, rain types, and climatic variations in tropical North Africa. *Quat. Res.* 18, 1–16.
- Martin, J.H., Gordon, R.M., 1988. Northeast Pacific iron distributions in relation to phytoplankton productivity. *Deep Sea Res. Part Oceanogr. Res. Pap.* 35, 177–196.
- Masoumi, A., Khalesifard, H., Bayat, A., Moradhaseli, R., 2013. Retrieval of aerosol optical and physical properties from ground-based measurements for Zanjan, a city in Northwest Iran. *Atmospheric Res.* 120, 343–355.
- McTainsh, G., Strong, C., 2007. The role of aeolian dust in ecosystems. 36th Binghamt. Geomorphol. Symp. 89, 39–54. <https://doi.org/10.1016/j.geomorph.2006.07.028>
- Modaihsh, A., 1997. Characteristics and composition of the falling dust sediments on Riyadh city, Saudi Arabia. *J. Arid Environ.* 36, 211–223.
- Moulin, C., Lambert, C.E., Dulac, F., Dayan, U., 1997. Control of atmospheric export of dust from North Africa by the North Atlantic Oscillation. *Nature* 387, 691.
- Norouzi, S., Khademi, H., Ayoubi, S., Cano, A.F., Acosta, J.A., 2017. Seasonal and spatial variations in dust deposition rate and concentrations of dust-borne heavy metals, a case study from Isfahan, central Iran. *Atmospheric Pollut. Res.* 8, 686–699.
- Oduber, F., Calvo, A.I., Blanco-Alegre, C., Castro, A., Nunes, T., Alves, C., Sorribas, M., Fernández-González, D., Vega-Maray, A.M., Valencia-Barrera, R.M., Lucarelli, F., Nava, S., Calzolari, G., Alonso-Blanco, E., Fraile, B., Fialho, P., Coz, E., Prevot, A.S.H., Pont, V., Fraile, R., 2019. Unusual winter Saharan dust intrusions at Northwest Spain: Air quality, radiative and health impacts. *Sci. Total Environ.* 669, 213–228. <https://doi.org/10.1016/j.scitotenv.2019.02.305>
- O'hara, S.L., Wiggs, G.F., Mamedov, B., Davidson, G., Hubbard, R.B., 2000. Exposure to airborne dust contaminated with pesticide in the Aral Sea region. *The Lancet* 355, 627–628.
- Opp, C., Groll, M., Aslanov, I., Lotz, T., Vereshagina, N., 2017. Aeolian dust deposition in the southern Aral Sea region (Uzbekistan): Ground-based monitoring results from the LUCA project. *Quat. Int.* 429, 86–99.
- Orlovsky, L., Orlovsky, N., Durdyev, A., 2005. Dust storms in Turkmenistan. *J. Arid Environ.* 60, 83–97.
- Peng, J., Hu, M., Guo, S., Du, Z., Zheng, J., Shang, D., Zamora, M.L., Zeng, L., Shao, M., Wu, Y.-S., 2016. Markedly enhanced absorption and direct radiative forcing of black carbon under polluted urban environments. *Proc. Natl. Acad. Sci.* 113, 4266–4271.
- Petroff, A., Mailliat, A., Amielh, M., Anselmet, F., 2008. Aerosol dry deposition on vegetative canopies. Part I: review of present knowledge. *Atmos. Environ.* 42, 3625–3653.
- Péwé, T.L., American Association for the Advancement of Science, 1981. Desert dust: origin, characteristics, and effect on man. Geological Society of America.
- Popov, V., 1998. The Role of Salt Migration in Landscape Genesis of the Cis-Aral region. *Probl. DESERT Dev. CC Probl. OSVOENIIA PUSTYN* 68–71.
- Previdi, M., Liepert, B.G., 2007. Annular modes and Hadley cell expansion under global warming. *Geophys. Res. Lett.* 34.
- Prospero, J.M., 1999. Long-term measurements of the transport of African mineral dust to the southeastern United States: Implications for regional air quality. *J. Geophys. Res. Atmospheres* 104, 15917–15927.
- Prospero, J.M., 1981. Arid regions as sources of mineral aerosols in the marine atmosphere. *Geol. Soc. Am. Spec. Pap.* 186, 71–86.
- Prospero, J.M., Ginoux, P., Torres, O., Nicholson, S.E., Gill, T.E., 2002. Environmental characterization of global sources of atmospheric soil dust identified with the Nimbus 7 Total Ozone Mapping Spectrometer (TOMS) absorbing aerosol product. *Rev. Geophys.* 40.
- Prospero, J.M., Lamb, P.J., 2003. African droughts and dust transport to the Caribbean: Climate change implications. *Science* 302, 1024–1027.
- Pye, K., 1987a. Aeolian dust and dust deposits. Academic.
- Pye, K., 1987b. Aeolian dust and dust deposits. Academic.

- Ramanathan, V., Chung, C., Kim, D., Bettge, T., Buja, L., Kiehl, J., Washington, W., Fu, Q., Sikka, D., Wild, M., 2005. Atmospheric brown clouds: Impacts on South Asian climate and hydrological cycle. *Proc. Natl. Acad. Sci.* 102, 5326–5333.
- Rashki, A., Arjmand, M., Kaskaoutis, D., 2017. Assessment of dust activity and dust-plume pathways over Jazmurian Basin, southeast Iran. *Aeolian Res.* 24, 145–160.
- Rashki, A., Eriksson, P.G., Rautenbach, C. de W., Kaskaoutis, D.G., Grote, W., Dykstra, J., 2013. Assessment of chemical and mineralogical characteristics of airborne dust in the Sistan region, Iran. *Chemosphere* 90, 227–236.
- Rashki, A., Kaskaoutis, D.G., Mofidi, A., Minvielle, F., Chiapello, I., Legrand, M., Dumka, U.C., Francois, P., 2019. Effects of Monsoon, Shamal and Levar winds on dust accumulation over the Arabian Sea during summer – The July 2016 case. *Aeolian Res.* 36, 27–44. <https://doi.org/10.1016/j.aeolia.2018.11.002>
- Razakov, R., Kosnazarov, K., 1996. Dust and salt transfer from the exposed bed of the Aral Sea and measures to decrease its environmental impact, in: *The Aral Sea Basin*. Springer, pp. 95–102.
- Reheis, Marith C., Kihl, R., 1995. Dust deposition in southern Nevada and California, 1984–1989: Relations to climate, source area, and source lithology. *J. Geophys. Res. Atmospheres* 100, 8893–8918. <https://doi.org/10.1029/94JD03245>
- Reheis, Marith C., Kihl, R., 1995. Dust deposition in southern Nevada and California, 1984–1989: Relations to climate, source area, and source lithology. *J. Geophys. Res. Atmospheres* 100, 8893–8918.
- Rezazadeh, M., Irannejad, P., Shao, Y., 2013. Climatology of the Middle East dust events. *Aeolian Res.* 10, 103–109.
- Schär, C., Vidale, P.L., Lüthi, D., Frei, C., Häberli, C., Liniger, M.A., Appenzeller, C., 2004. The role of increasing temperature variability in European summer heatwaves. *Nature* 427, 332.
- Shao, Y., 2008. *Physics and modelling of wind erosion*. Springer Science & Business Media.
- Shao, Y., Dong, C., 2006. A review on East Asian dust storm climate, modelling and monitoring. *Glob. Planet. Change* 52, 1–22.
- Shao, Y., Lu, H., 2000. A simple expression for wind erosion threshold friction velocity. *J. Geophys. Res. Atmospheres* 105, 22437–22443.
- Shao, Y., Wang, J., 2003. A climatology of Northeast Asian dust events. *Meteorol. Z.* 12, 187–196. <https://doi.org/10.1127/0941-2948/2003/0012-0187>
- Shao, Y., Wyrwoll, K.-H., Chappell, A., Huang, J., Lin, Z., McTainsh, G.H., Mikami, M., Tanaka, T.Y., Wang, X., Yoon, S., 2011. Dust cycle: An emerging core theme in Earth system science. *Aeolian Res.* 2, 181–204.
- Shinn, E.A., Griffin, D.W., Seba, D.B., 2003. Atmospheric transport of mold spores in clouds of desert dust. *Arch. Environ. Health* 58, 498–504.
- Simonson, R.W., 1995. Airborne dust and its significance to soils. *Geoderma* 65, 1–43.
- Slinn, S., Slinn, W., 1980. Predictions for particle deposition on natural waters. *Atmospheric Environ.* 1967 14, 1013–1016.
- Smalley, I., Jefferson, I., Dijkstra, T., Derbyshire, E., 2001. Some major events in the development of the scientific study of loess. *Earth-Sci. Rev.* 54, 5–18.
- Sokolik, I., Winker, D., Bergametti, G., Gillette, D., Carmichael, G., Kaufman, Y., Gomes, L., Schuetz, L., Penner, J., 2001. Introduction to special section: Outstanding problems in quantifying the radiative impacts of mineral dust. *J. Geophys. Res. Atmospheres* 106, 18015–18027.
- Song, H., Wang, K., Zhang, Y., Hong, C., Zhou, S., 2017. Simulation and evaluation of dust emissions with WRF-Chem (v3. 7.1) and its relationship to the changing climate over East Asia from 1980 to 2015. *Atmos. Environ.* 167, 511–522.
- Song, Z., Wang, J., Wang, S., 2007. Quantitative classification of northeast Asian dust events. *J. Geophys. Res. Atmospheres* 112.
- Stone, R., 1999. Coming to grips with the Aral Sea's grim legacy.
- Swap, R., Garstang, M., Greco, S., Talbot, R., Kållberg, P., 1992. Saharan dust in the Amazon Basin. *Tellus B* 44, 133–149.
- Ta, W., Xiao, H., Qu, J., Xiao, Z., Yang, G., Wang, T., Zhang, X., 2004. Measurements of dust deposition in Gansu Province, China, 1986–2000. *Geomorphology* 57, 41–51.

- Tao, W., Chen, J., Li, Z., Wang, C., Zhang, C., 2012. Impact of aerosols on convective clouds and precipitation. *Rev. Geophys.* 50.
- Tegen, I., Fung, I., 1994. Modeling of mineral dust in the atmosphere: Sources, transport, and optical thickness. *J. Geophys. Res. Atmospheres* 99, 22897–22914. <https://doi.org/10.1029/94JD01928>
- Tegen, I., Hollrig, P., Chin, M., Fung, I., Jacob, D., Penner, J., 1997. Contribution of different aerosol species to the global aerosol extinction optical thickness: Estimates from model results. *J. Geophys. Res. Atmospheres* 102, 23895–23915. <https://doi.org/10.1029/97JD01864>
- Tegen, I., Miller, R., 1998. A general circulation model study on the interannual variability of soil dust aerosol. *J. Geophys. Res. Atmospheres* 103, 25975–25995.
- Trenberth, K., Jones, P., Ambenje, P., Bojariu, R., Easterling, D., Klein Tank, A., Parker, D., Rahimzadeh, F., Renwick, J., Rusticucci, M., 2007. Observations: surface and atmospheric climate change. Chapter 3. *Clim. Change* 235–336.
- Trenberth, K.E., 2011. Changes in precipitation with climate change. *Clim. Res.* 47, 123–138.
- Tucker, C.J., Nicholson, S.E., 1999. Variations in the size of the Sahara Desert from 1980 to 1997. *Ambio* 587–591.
- Varga, G., Cserhádi, C., Kovács, J., Szalai, Z., 2016. Saharan dust deposition in the Carpathian Basin and its possible effects on interglacial soil formation. *Aeolian Res.* 22, 1–12.
- Wei, L., Qi, F., Tao, W., Yanwu, Z., Jianhua, S., 2004. Physicochemistry and mineralogy of storm dust and dust sediment in northern China. *Adv. Atmospheric Sci.* 21, 775–783.
- Wesely, M.L., Hicks, B.B., 2000. A review of the current status of knowledge on dry deposition. *Atmos. Environ.* 34, 2261–2282. [https://doi.org/10.1016/S1352-2310\(99\)00467-7](https://doi.org/10.1016/S1352-2310(99)00467-7)
- Westervelt, D., Horowitz, L., Naik, V., Tai, A., Fiore, A., Mauzerall, D.L., 2016. Quantifying PM_{2.5}-meteorology sensitivities in a global climate model. *Atmos. Environ.* 142, 43–56.
- Wiggs, G.F., O'hara, S.L., Wegerdt, J., Van Der Meer, J., Small, I., Hubbard, R., 2003. The dynamics and characteristics of aeolian dust in dryland Central Asia: possible impacts on human exposure and respiratory health in the Aral Sea basin. *Geogr. J.* 169, 142–157.
- Wurzler, S., Reisin, T.G., Levin, Z., 2000. Modification of mineral dust particles by cloud processing and subsequent effects on drop size distributions. *J. Geophys. Res. Atmospheres* 105, 4501–4512.
- Yaalon, D., Ganor, E., 1975. Rates of aeolian dust accretion in the Mediterranean and desert fringe environments of Israel. Presented at the 9th International Sedimentological Congress, Nice, France, pp. 169–174.
- Zender, C.S., Kwon, E.Y., 2005. Regional contrasts in dust emission responses to climate. *J. Geophys. Res. Atmospheres* 110.
- Zhang, J., Shao, Y., Huang, N., 2014. Measurements of dust deposition velocity in a wind-tunnel experiment. *Atmospheric Chem. Phys.* 14, 8869–8882.
- Zhang, XX, Shi, P., Liu, L., Tang, Y., Cao, H., Zhang, XN, Hu, X., Guo, L., Lue, Y., Qu, Z., 2010. Ambient TSP concentration and dustfall in major cities of China: spatial distribution and temporal variability. *Atmos. Environ.* 44, 1641–1648.

8. Conclusion and Recommendation

8.1 Introduction

In this thesis, aeolian dust passive sample rates were analyzed to retrieve data on three main goals. Therefore, significant conclusion for the thesis will be adjusted from dust deposition rates between 2014 and 2017. According to the first objective fields measurements are used for detecting the spatial and temporal variability of dust deposition rates in the study area. The next objective is linked to the results from the correlation analysis techniques combined with an element concentrations classification based on airborne metal regulations (AMR) in order to discriminate chemical gradients through identical events. The last part is allied to results related to the third objective. Data from a model analysis (MERRA-II) was compared with ground observation for dust deposition rates (GDRs) to understand both the spatio-temporal pattern of dust distribution and the variability of dust deposition rates in relation to climate zones.

A statistically significant variations observed in seasonal GDRs values appear to be in response to changes in meteorological parameters and climate zone. The maximum range of 85.11–88.44 t/km²/month for the dust deposited in spring and summer season might be attributed to the prevailing west to east and south to north dusty winds when the temperature is also high. Higher rainfall and relative humidity as well as cultivated vegetation tend to suppress dust flux in wet and cold seasons with the minimum dust flux of 53.34 t/km²/month in the fall and winter. The spatial pattern of annual GDR further with a mean value (t/km²/year) of 68.72-94.38 within the south against 45.23-73.89 within the west showed that dust particles are deposited more in the southern part of the study area where uncover and barren desert lands are located.

Seasonal variations were observed in the concentrations of most dust-borne elements, with the lowest observed in the summer and fall and the highest in the winter and spring. All the elements investigated, exhibited higher concentrations in the dust samples (Ba, Cd, Ni, Zn, Al, and Na within the south Cu, Cr, Co, Ni, Zn, K, Al, Si, and Sr within the west) than average values. The spatial distribution of dust-borne further, Mn, Ni, Al, and Zn followed identical patterns.

8.2 Conclusions

This study focuses on the enhancement of dust deposition rates over the southwestern part of Iran (30° 00' 00" and 35° 00' 00"N, 45° 30' 00" and 49° 30' 00" E). Both the ground deposition and the dust event frequency have been well measured. Conclusions allied to the first objective also identified and analyzed dust load and dust distribution correlated with GDR. In the first place, the composite product data from the MODIS and MISR on Terra has been addressed. Under the four layer conditions of aerosol thickness: Clean [1], Thin [2], Thick [3] and Strong Thick [4], the standard MODIS aerosol products were applied at regional scales to monitor dust distributions and transports direction. However, the 1.0 degree and even the 0.5 degree spatial resolution data are insufficient to depict the deposition rate at local scales due to inherent dust variabilities, as well as the complexity of the land surfaces. Afterward, the results from MODIS and MISR were compared. The study area divided by three geographical parts, and gauge sties classified within three parts. The first part [a], covered G01, G02, G03, and G04. The second part however enclosed G05, and G06 as [b]. The last part [c] assigned to G07, G08, G09, and G10. The findings suggested that, when the part [a], [b], and [c] are affected by a

number of dust events, in comparison with MISR, MODIS showed the better performance overall. But many differences in monthly AOT variation have been observed during spring and summer, when the seasonal load and concentration have been compared with GDR. The comparison of MODIS AOT with GDR over the study area shows a good agreement and approximately 65% of GDR falls within AOT limitations with uncertainty.

The HYSPLIT model output further was run for ending point location in each of the three parts [a], [b], and [c] back to the 4 days trajectories that influenced the observed AOT spatial distribution and transport direction. The model output confirmed that, the dust belt stretches from the Sahara desert in Africa to the East Asia, conquered southwestern Iran which is being recognized as one of the global hotspots of aeolian dust through southwest of Iran including Kermanshah, Lorestan, and Khuzestan provinces.

The results from this contribution were also capable of tracking dust events rather than monitoring the local and regional deposition rate. The measurement values of the 3rd [3] and 4th [4] layers were apparently higher in part [c] and part [a]. Therefore, the mountainous characteristics of part [b] and its geographical characteristics should be considered as an important factor when attempting to discriminate separate layers of aeolian dust from other layers of aerosols. In general, AOT retrieval can represent the strong seasonal and geographical variations in the dust deposition rates and their regional distribution. However, the possibilities to further our knowledge of dust deposition rates and frequencies in a high spatio-temporal resolution are limited so significant uncertainties remain, due to the methodological limitations of these remote sensing approaches. Finally yet importantly, concluded the essentiality of ground observation methods. Although high spatial resolution products with a chronological record are suitable basics for the improvement of dust deposition analyses and ecosystem effect assessments, ground surveys are still a key point for analyzing airborne deposition. However, deposition rate based on space model algorithms (AOT) remain the method of choice, even though they are relatively complicated and less accurate than ground observations (GDR), due to the lack of continuous atmospheric data at required scale over the area of interest.

Associated with the second key objective, the sites receiving dust deposition were classified into broad categories based on natural and anthropogenic features. The element concentration analysis is carried out with the help of an Inductively Coupled Plasma-Mass Spectrometer (ICP-MS) for 20 elements. Geometric values for each element in the southern part (n=50) and the western part (n=50) of the study area were compared. Specifically, positive, zero and negative correlations among elements and the physical parameters of dust samples adjacent to the four matrices of Airborne Metals Regulations are observed. This study comprises a perfect complement to the lessons learned from (Larssen and Carmichael 2000; Muhs and Benedict 2006) in finding dust sources by using texture similarities in dust accumulation in the area of research (G01 to G02; G09 to G10). At the same time, correlations from atmospheric reports and dust event frequency (DEF) can prove that the highest proportion of dust subjected to Airborne Metals Regulations associated with dominant sources (DS) are formed at local and regional scales rather than globally. Their hot spot areas were mainly associated with high anthropogenic activities in the western and southwestern parts of the study area. Dust-borne Cu, Cd, Ni, and As showed the same spatial distribution within western and northern areas where some industrial plants are located. The hot spot area for Ba, Cd, and Na in the dust samples was found to be within the south part, while Ni, Zn, Mn and Al showed a uniform spatial distribution throughout the study area. Based on the AMR values for all the elements in all the four seasons, anthropogenic source such as oil combustion, vegetative burning, iron and steel industry, power plants, and petroleum refinery, contribute a substantial amount of elements to dust particulates. Moreover, contamination classes based on the values of AMR in the winter season showed that atmospheric dust is significantly to very high contaminated with elements including Ni, As, Cr, Cd, and Na within the south and Cu, Sr, Co, K, Al within the west. The dust deposition rate across the study area was found to be higher in the spring and summer than in the other seasons of the year. However, summer dust appeared to be less harmful

and polluted due to the low concentrations of toxic metals. Winter, in contrast, was found to be the most problematic season with potential negative health effects because the maximum toxic metal content occurs in this season. To summarize, weathering combined with anthropogenic change influences the composition of dust transport from the source region to the local deposition; however, this composition cannot be easily controlled. Although in some cases a severity in correlation without a resulting change in the value of the element composition has been observed, elemental correlations of individual matrices are nonetheless the marked effects of dominant sources.

Conclusions from the final contribution (third key objective) focus on the enhancement of dust deposition rates. In order to better understand the role of aeolian dust in the climate system and its impacts on air quality, significant efforts have been realized to increase both space- and ground-based observations. The ground deposition rate and geophysical variation in the dust event frequency, including the mass and weight compositions, have been thoroughly measured. Many of the links between the dust deposition and climate pattern, although perfectly reasonable from a conceptual ground survey standpoint, have been quantitatively assessed for the GDR and the MERRA-2 model. Arid desert hot [BWh], arid steppe hot [BSh], and temperate hot and dry summer [Csa] climates are the three dominant climate regions with the highest average dust deposition rates in the research area. The total annual dust deposition is inversely related to the total annual precipitation and was in a positive correlation with the annual temperature. The annual mean deposition rates are 96.21 t/km²/yr for [BWh], 77.67 t/km²/yr for [BSh], and 39.18 t/km²/yr for [Csa]. Thus, precipitation and temperature, as two main factors in the climate zone, have a widespread, major influence on the rates of the dust deposition in the study area.

Finally, the knowledge gained on the processes responsible for the dust deposition rate, together with feedback from the climate pattern, will provide insights into the responses of deposition rates and their climate offsets. The findings of this study improve the understanding of the influence of climate on changes in the arid dust deposition rate in the study area. Given this point, the dust deposition rate and atmospheric concentration of dust, which has been assumed homogeneous, were considered heterogeneous within this study. Ultimately, there is no way to isolate each environment from the effects of exposure to dust due to all regions are likely to experience the adverse effect of deposition rates.

8.3 Limitations and recommendation

Results from this study, even from literature review show, that physical characteristics, and gradient distribution, are not well known globally in most of the case studies. Therefore, consistent efforts need to improve our predictions. Since aeolian deposition rates are sensitive over climate zones, even suggesting that additional observation data from GDR on climate regimes might be performed to obtain precise information on dust plumes.

Calculating ground deposition rates from AOT retrieval (load and concentration) it is still undefined. This may be due to the fact that AOT represents an integrated measurement of atmospheric dust and geographically uneven distributions over the each areas. Therefore, combining remote sensing and ground observation is, in many cases, vital to estimate real-world effects of dust on the sink regions. Thus, finding an appropriate program would be essential to estimate real-world effects in many cases. The development of ground surveying algorithms is necessary to make the estimations of the deposition rate more accurate. The current detection algorithms could be modified based on the technology of machine learning from physical characteristics, spatial and temporal distribution. So, developing guidance on the priorities of expanding projects and preventative actions towards potential dust deposition from natural and dominant sources might be next subject of institutional interest.

Although anthropogenic sources release constant amounts of metals throughout the year, differences in meteorological conditions in the study area were found to lead to differences in pollution levels during

different seasons of the year. Therefore, to reduce the harmful effects of aeolin over the area, it is essential to implement appropriate measures to reduce the concentration of heavy metals in dust. This has to be done more seriously in the wintertime when stable and cold air do not allow the rapid movement of polluted atmosphere to the neighboring areas.

Appendix I

ICP MS Result ug / g

G01	Max	Min	Median	Std
BE	4.46	2.64	3.47	0.69
Na	123.64	70.79	99.72	15.66
Mg	64.33	32.90	51.51	11.49
Al	13.64	5.19	8.84	2.73
Si	31.15	21.21	27.32	3.26
K	1440.07	530.24	904.00	305.03
Ca	0.30	0.17	0.23	0.05
V	0.53	0.17	0.31	0.12
Cr	2.77	1.55	2.27	0.30
Mn	147.69	77.84	102.86	19.71
Fe	0.10	0.05	0.08	0.02
Co	0.78	0.32	0.57	0.16
Ni	0.30	0.09	0.20	0.07
Cu	3.37	0.01	1.19	1.04
Zn	0.05	0.00	0.02	0.02
As	0.00	0.00	0.00	0.00
Se	25.93	12.72	19.71	4.01
Sr	0.00	0.00	0.00	0.00
Cd	0.68	0.25	0.45	0.12
Ba	0.10	0.05	0.08	0.01
Pb	0.00	0.00	0.00	0.00

ICP MS Result ug / g

G02	Max	Min	Median	Std
BE	4.57	2.84	3.50	0.54
Na	124.74	65.19	92.95	20.42
Mg	61.67	32.75	51.71	9.61
Al	13.90	3.64	8.99	3.42
Si	29.67	17.69	24.78	4.05
K	1367.19	593.73	1051.02	224.32
Ca	0.30	0.16	0.23	0.05
V	0.65	0.18	0.41	0.15
Cr	2.75	1.49	2.13	0.33
Mn	145.64	75.76	106.16	22.69
Fe	0.10	0.05	0.08	0.01
Co	0.74	0.37	0.58	0.12
Ni	0.28	0.09	0.17	0.06
Cu	3.66	0.01	1.85	1.01
Zn	0.05	0.00	0.02	0.02
As	0.00	0.00	0.00	0.00
Se	26.11	13.62	19.72	4.30
Sr	0.00	0.00	0.00	0.00
Cd	0.66	0.34	0.47	0.11
Ba	0.10	0.05	0.08	0.02
Pb	0.00	0.00	0.00	0.00

G03	Max	Min	Median	Std
BE	4.28	2.82	3.61	0.44
Na	119.65	66.31	88.14	18.37
Mg	61.93	33.19	49.75	9.11
Al	13.27	4.43	8.58	3.05
Si	30.20	17.02	24.30	4.83
K	1407.42	569.47	963.74	244.60
Ca	0.28	0.16	0.20	0.03
V	0.64	0.17	0.43	0.12
Cr	2.82	1.51	2.28	0.40
Mn	143.29	78.07	111.22	18.61
Fe	0.10	0.05	0.08	0.02
Co	0.77	0.37	0.56	0.12
Ni	0.27	0.10	0.19	0.06
Cu	4.06	0.24	1.96	1.29
Zn	0.05	0.00	0.02	0.02
As	0.00	0.00	0.00	0.00
Se	22.40	12.87	17.12	2.85
Sr	0.00	0.00	0.00	0.00
Cd	0.69	0.31	0.49	0.12
Ba	0.10	0.05	0.08	0.02
Pb	0.00	0.00	0.00	0.00

G04	Max	Min	Median	Std
BE	4.46	2.73	3.63	0.54
Na	127.24	68.11	98.96	21.87
Mg	63.34	35.03	45.79	9.73
Al	13.23	3.59	8.46	2.85
Si	28.22	16.67	23.15	3.94
K	1378.68	577.74	1058.36	281.40
Ca	0.30	0.15	0.21	0.05
V	0.64	0.19	0.40	0.12
Cr	2.86	1.55	2.26	0.42
Mn	146.90	93.32	125.69	16.31
Fe	0.10	0.05	0.08	0.02
Co	0.73	0.35	0.54	0.13
Ni	0.26	0.09	0.19	0.05
Cu	4.29	0.13	2.48	1.41
Zn	0.05	0.00	0.02	0.02
As	0.00	0.00	0.00	0.00
Se	24.76	12.10	17.19	3.48
Sr	0.00	0.00	0.00	0.00
Cd	0.69	0.41	0.55	0.09
Ba	0.10	0.05	0.07	0.02
Pb	0.00	0.00	0.00	0.00

ICP MS Result ug / g

G05	Max	Min	Median	Std
BE	4.53	2.69	3.61	0.58
Na	123.61	63.33	96.61	20.31
Mg	64.94	35.20	54.14	9.20
Al	13.19	4.52	8.88	2.60
Si	30.29	17.67	23.16	3.84
K	1430.04	575.74	960.92	284.84
Ca	0.29	0.19	0.25	0.03
V	0.63	0.17	0.41	0.16
Cr	2.86	1.48	2.18	0.38
Mn	138.04	74.81	99.31	20.52
Fe	0.10	0.05	0.08	0.02
Co	0.79	0.33	0.56	0.13
Ni	0.29	0.13	0.22	0.06
Cu	4.17	0.66	2.51	1.23
Zn	0.05	0.00	0.03	0.02
As	0.00	0.00	0.00	0.00
Se	26.06	15.32	20.51	3.11
Sr	0.00	0.00	0.00	0.00
Cd	0.66	0.26	0.48	0.12
Ba	0.10	0.05	0.08	0.01
Pb	0.00	0.00	0.00	0.00

ICP MS Result ug / g

G06	Max	Min	Mean	Std
BE	0.00	0.00	0.00	0.00
Na	9.52	1.92	5.62	2.68
Mg	95.01	38.65	59.35	15.54
Al	27.68	18.26	23.34	3.07
Si	2.17	0.57	1.35	0.56
K	15.35	6.52	10.65	3.21
Ca	263.46	153.46	214.19	33.60
V	0.29	0.10	0.20	0.07
Cr	0.52	0.27	0.41	0.09
Mn	1.65	0.96	1.27	0.25
Fe	83.99	47.01	63.00	13.35
Co	0.06	0.01	0.03	0.02
Ni	0.37	0.20	0.28	0.06
Cu	0.24	0.10	0.17	0.05
Zn	29.36	3.29	17.43	7.31
As	0.06	0.02	0.04	0.01
Se	0.01	0.00	0.01	0.01
Sr	0.89	0.45	0.69	0.17
Cd	0.01	0.00	0.01	0.00
Ba	0.57	0.23	0.39	0.11
Pb	0.21	0.04	0.10	0.06

G07	Max	Min	Mean	Std
BE	0.00	0.00	0.00	0.00
Na	9.22	1.83	5.39	2.45
Mg	100.41	37.91	60.01	19.38
Al	31.10	16.13	22.73	5.13
Si	1.63	-0.01	0.69	0.54
K	15.32	6.59	10.62	3.12
Ca	271.48	127.14	189.92	43.25
V	0.30	0.08	0.22	0.06
Cr	0.47	0.13	0.27	0.12
Mn	1.68	0.90	1.35	0.28
Fe	83.24	45.60	65.70	12.16
Co	0.05	0.01	0.04	0.01
Ni	0.37	0.17	0.25	0.07
Cu	0.24	0.10	0.18	0.03
Zn	26.51	4.63	18.10	6.50
As	0.06	0.02	0.04	0.02
Se	0.01	0.00	0.00	0.00
Sr	0.83	0.45	0.67	0.14
Cd	0.01	0.00	0.00	0.00
Ba	0.59	0.22	0.37	0.12
Pb	0.17	0.03	0.09	0.04

G08	Max	Min	Mean	Std
BE	0.00	0.00	0.00	0.00
Na	9.46	1.66	6.44	2.26
Mg	100.65	32.04	62.43	20.58
Al	26.86	17.63	21.68	3.41
Si	2.10	0.25	1.12	0.63
K	14.45	7.18	11.18	2.23
Ca	284.45	123.24	205.77	48.49
V	0.25	0.09	0.16	0.06
Cr	0.51	0.16	0.34	0.12
Mn	1.67	0.95	1.32	0.24
Fe	83.34	44.10	64.77	10.58
Co	0.06	0.01	0.04	0.02
Ni	0.31	0.19	0.25	0.04
Cu	0.25	0.10	0.19	0.05
Zn	28.44	2.37	15.97	8.84
As	0.06	0.03	0.04	0.01
Se	0.01	0.00	0.01	0.01
Sr	0.89	0.49	0.70	0.11
Cd	0.01	0.00	0.00	0.00
Ba	0.57	0.23	0.35	0.09
Pb	0.19	0.03	0.11	0.05

ICP MS Result ug / g

G09	Max	Min	Mean	Std
BE	0.00	0.00	0.00	0.00
Na	6.91	1.69	4.37	1.42
Mg	88.87	30.95	66.89	19.06
Al	28.89	16.09	22.75	3.59
Si	2.06	-0.05	0.86	0.80
K	15.33	7.02	11.01	2.73
Ca	251.96	118.86	208.08	48.09
V	0.28	0.09	0.17	0.06
Cr	0.51	0.22	0.35	0.08
Mn	1.62	0.96	1.22	0.24
Fe	84.32	43.11	64.75	12.43
Co	0.06	0.01	0.04	0.02
Ni	0.37	0.17	0.27	0.08
Cu	0.25	0.13	0.19	0.04
Zn	28.75	1.17	13.61	8.62
As	0.06	0.02	0.03	0.01
Se	0.01	0.00	0.00	0.00
Sr	0.84	0.45	0.61	0.12
Cd	0.01	0.00	0.01	0.01
Ba	0.51	0.26	0.40	0.09
Pb	0.21	0.03	0.10	0.05

ICP MS Result ug / g

G10	Max	Min	Mean	Std
BE	0.00	0.00	0.00	0.00
Na	9.01	1.29	5.57	2.67
Mg	100.40	35.27	68.30	21.85
Al	28.96	17.05	23.47	3.85
Si	2.25	0.00	1.13	0.77
K	14.88	6.49	11.07	2.88
Ca	261.79	116.74	183.83	46.05
V	0.28	0.12	0.19	0.05
Cr	0.42	0.14	0.28	0.09
Mn	1.66	0.99	1.34	0.20
Fe	80.48	45.62	61.14	11.11
Co	0.06	0.01	0.03	0.02
Ni	0.38	0.17	0.24	0.06
Cu	0.25	0.12	0.18	0.05
Zn	30.04	2.66	17.36	7.11
As	0.06	0.03	0.05	0.01
Se	0.01	0.00	0.00	0.00
Sr	0.90	0.47	0.68	0.14
Cd	0.01	0.00	0.01	0.01
Ba	0.59	0.23	0.37	0.11
Pb	0.20	0.03	0.12	0.06

Appendix II

Seasonal	2014 Deposition rate [mg/cm ²]										2015 Deposition rate [mg/cm ²]										Seasonal
Winter	G01	G02	G03	G04	G05	G06	G07	G08	G09	G10	G01	G02	G03	G04	G05	G06	G07	G08	G09	G10	Winter
December	0.4	0.3	0.3	0.2	0.2	0	0.6	0.5	0.4	0.5	1.5	0.2	0.1	0.2	0.2	0.2	~0.9	0.3	0.3	1	December
January	0.5	0.5	0.5	0.5	0.5	0.2	0.5	0.6	0.8	0.8	0.5	0.5	0.5	0.3	0.5	0.5	0.8	0.5	0.6	0.6	January
February	0.7	0.8	0.7	0.4	0.3	0.3	0.6	0.5	0.5	0.6	0.5	0.5	0.6	0.4	0.3	0.2	0.8	1	1	1	February
Spring										Spring										Spring	
March	0.6	0.8	0.2	0.2	0.5	0.2	0.2	0.7	0.6	1	0.4	0.5	0.6	0.4	0.3	0.6	0.8	0.9	1	1	March
April	2.6	2	0.5	~2	0.2	0.2	1	0.5	0.9	0.8	0.4	0.4	0.4	0.5	0.3	0.6	0.9	1	1.5	1.6	April
May	1	0.5	0.3	~3	0.3	0.1	0.5	0.2	0.5	0.2	1	0.9	0.9	0.8	0.4	0.6	1	1.2	1.4	1.4	May
Summer										Summer										Summer	
June	1.5	0.8	0.8	0.2	1	0.2	0.5	0.6	1	1	0.7	0.7	0.7	0.5	0.2	0.5	0.9	1	1.4	1.5	June
July	0.8	0.5	0.8	0.2	~0.9	0.3	0.6	1.9	1.2	0.9	0.9	0.8	0.8	0.6	0.4	0.4	0.8	0.9	1.5	1.4	July
August	1.5	1	0.9	0	~2	0.6	0.3	~2	1.8	2.1	0.8	0.8	0.7	0.5	0.3	0.3	0.7	0.8	1.2	1.1	August
Fall										Fall										Fall	
September	1.5	1.5	0.9	0.5	~1	~15.9	0.2	0.6	0.9	0.9	0.5	0.4	0.5	0.3	0.2	0.2	0.5	1.1	1	1.2	September
October	0.9	0.6	0.2	0.2	0.1	~9.5	0.2	0.3	0.3	0.3	0.4	0.4	0.5	0.3	0.2	0.1	0.5	0.8	0.8	0.8	October
November	2	0.9	0.2	0.2	0.1	1	0.2	0.2	0.5	0.2	0.4	0.3	0.4	0.2	0.2	0.1	0.5	0.6	0.6	0.6	November
December	1.5	0.2	0.1	0.2	0.2	0.2	~0.9	0.3	0.3	1	0.4	0.4	0.4	0.2	0	0	0.5	0.6	0.6	0.6	December

Seasonal	2016 Deposition rate [mg/cm ²]										2017	Deposition rate [mg/cm ²]										Seasonal
Winter	G01	G02	G03	G04	G05	G06	G07	G08	G09	G10		G01	G02	G03	G04	G05	G06	G07	G08	G09	G10	Winter
December	0.4	0.4	0.4	0.2	0	0	0.5	0.6	0.6	0.6		0.5	0.5	0.5	0.4	0.2	0	0.4	0.5	0.6	0.6	December
January	0.3	0.4	0.3	0.4	0.2	0.2	0.4	0.6	0.6	0.6		0.3	0.4	0.3	0.2	0.2	0	0.5	0.4	0.5	0.6	January
February	0.3	0.2	0.3	0.3	0.2	0.1	0.6	0.6	0.7	0.6		0.3	0.2	0.3	0.2	0	0	0.8	0.5	0.8	0.8	February
Spring												Spring										
March	0.4	0.4	0.4	0.2	0	0	0.5	0.6	0.6	0.6		0.5	0.5	0.5	0.4	0.2	0	0.4	0.5	0.6	0.6	March
April	0.3	0.4	0.3	0.4	0.2	0.2	0.4	0.6	0.6	0.6		0.3	0.4	0.3	0.2	0.2	0	0.5	0.4	0.5	0.6	April
May	0.3	0.2	0.3	0.3	0.2	0.1	0.6	0.6	0.7	0.6		0.3	0.2	0.3	0.2	0	0	0.8	0.5	0.8	0.8	May
Summer												Summer										
June	0.8	0.6	0.8	0.4	0.2	0	1	0.5	0.9	0.9		0.3	0.2	0.3	0.2	0.5	0.5	1	1.2	1	1.3	June
July	0.8	0.7	0.8	0.5	0.4	0.4	1	0.7	1.2	1.4		0.8	0.6	0.8	0.3	0	0.3	0.8	1	1.3	1.5	July
August	0.5	0.3	0.6	0.4	0.2	0	0.8	0.5	0.7	0.9		0.5	0.6	0.6	0.4	0.2	0.2	0.9	1	1	1.2	August
Fall												Fall										
September	0.6	0.6	0.5	0.2	0.3	0	0.7	0.5	0.7	0.7		0.6	0.4	0.5	0.2	0	0	0.7	0.5	0.7	0.8	September
October	0.4	0.3	0.4	0.2	0	0	0.3	0.4	0.3	0.5		0.5	0.4	0.2	0.3	0.2	0.2	0.6	0.6	0.8	0.9	October
November	0.3	0.2	0.3	0	0.3	0	0.3	0.6	0.5	0.6		0.2	0.2	0.2	0	0	0	0.4	0.2	0.4	0.4	November
December	0.5	0.5	0.5	0.4	0.2	0	0.4	0.5	0.6	0.6		0.4	0.3	0.3	0.2	0.2	0	0.6	0.5	0.4	0.5	December